Study of ScAlN/GaN HEMT heterostructures grown by ammonia assisted molecular beam epitaxy

Caroline Elias

Etude d'hétérostructures HEMT ScAlN/GaN élaborées par épitaxie sous jets moléculaires assistée ammoniac

Caroline ELIAS

Centre de Recherche sur l'Hétéroépitaxie et ses Applications (CRHEA)

Présentée en vue de l'obtention

du grade de docteur en Physique

d' Université Côte d'Azur

Dirigée par :

Yvon Cordier, Directeur de Recherche, CNRS, CRHEA

Co-encadrée par :

Maxime Hugues, Chargé de Recherche, CNRS, CRHEA

Soutenue le : 18/12/2023

Devant le jury, composé de :

Président du jury: Philippe Lorenzini, Professeur, Université Côte d'azur (Polytech Nice-Sophia)

Magali Morales, Maîtresse de conférence, Université de Caen Normandie, ENSICAEN (CIMAP)

Xavier Wallart, Directeur de recherche, Université de Lille (IEMN)

Stefano Leone, Docteur, Fraunhofer Institute for Applied Solid State Physics (IAF)

Maria Tchernycheva, Directrice de recherche, Université Paris-Saclay (C2N)

GaN4AP

GaNeX

Jury

Rapporteurs

Xavier Wallart
Directeur de recherche, Université de Lille (IEMN)

Magali Morales
Maîtresse de conférence, Université de Caen, Normandie, ENSICAEN (CIMAP)

Examinateurs

Philippe Lorenzini
Professeur, Université Côte d'azur (Polytech Nice-Sophia)

Stefano Leone
Docteur, Fraunhofer Institute for Applied Solid State Physics (IAF)

Maria Tchernycheva
Directrice de recherche, Université Paris-Saclay (C2N)

Remerciements

Je tiens tout d'abord à exprimer ma gratitude envers mon directeur de thèse, Yvon CORDIER, et mon co-directeur Maxime HUGUES, pour leur expertise et leur accompagnement tout au long de cette aventure de recherche.

Je souhaite également remercier les membres de mon jury de thèse, composé de Xavier WALLART, Magalie MORALES, Stefano LEONE, Maria TCHERNYCHEVA et Philippe LORENZINI, pour leur temps, leur expertise et leurs précieux commentaires lors de l'évaluation de mon travail.

Mes remerciements vont également à toutes les personnes qui m'ont soutenu dans la manipulation des équipements et leur expertise dans le domaine, notamment Sébastien CHENOT pour ses formations en salle blanche, Virginie BRANDLI pour son assistance avec le MEB, Aimeric COURVILLE pour l'AFM, et Stéfane VÉZIAN pour l'XPS. Je remercie également Frédéric GEORGI de m'avoir accueilli au laboratoire CEMEF de l'École des Mines à Sophia Antipolis pour mes travaux en XPS, ainsi que tout le personnel administratif, notamment Anne-Marie CORNUET, Michèle PEFFERKORN et Isabelle CERUTTI.

Je tiens à exprimer ma reconnaissance envers mes collègues du laboratoire, avec qui j'ai partagé des moments de travail, de discussions scientifiques et de convivialité. Un merci particulier à mon voisin et à mon ami du bureau Kilian BARIL, Renato MARTINEZ qui m'a fait connaître la culture brésilienne, Aziz et Wafa BEN YOUSSEF pour leur amitié, Léa LACOMBLEZ pour les moments de shopping !! Je tiens à remercier Antoine BARBIER CUEIL, Clément MAJOREL, Adelin PATOUX et Yanel TAHMI.

Les moments exceptionnels de rigolades avec Chiara MASTROPASQUA et Julien BOSCH, surtout pendant les conférences.

A part les moments passés ensemble au laboratoire mais aussi en dehors, comme lors des plages, des barbecues, des bars avec tous mes collègues. Et en plus les concerts de musique partagés avec Max MEUNIER, ce qui a rendu ma période de rédaction agréable.

Je remercie Béatrice WANNOUS, nous avons partagé des moments de détente sur la Côte d'Azur quand elle arrivait au CRHEA pour des campagnes de croissance.

Enfin, un grand merci à ma famille pour leur soutien inconditionnel, en particulier mes parents sans qui je n'aurais pas pu arriver ici, ma sœur et mon frère pour leurs encouragements et leur amour qui ont été essentiels dans mon parcours.

Summary

ScAlN is a wide bandgap III-Nitride semiconductor well known for its piezoelectric properties. Its spontaneous and piezoelectric polarization properties are also interesting for achieving heterojunctions with GaN in view of fabricating high electron mobility transistors (HEMTs). In these heterojunctions, the replacement of the AlGaN alloy by ScAlN presents several advantages, among them the possibility to generate two-dimensional electron gases (2DEGs) with much more carriers. It permits also to maintain a high carrier density in the channel of HEMTs with ScAlN barriers as thin as few nanometers, which allows to keep low access resistances and large saturation currents while limiting short channel effects in the submicron gate length transistors of millimeter-wave power amplifiers. Furthermore, the $Sc_{0.18}Al_{0.82}N$ alloy is lattice matched with GaN, which means that noticeably reduced stress can be induced in the devices, an advantage for their reliability. However, to benefit all these advantages, the good control of the crystal growth of ScAlN alloy on GaN is necessary in order to obtain heterojunctions with the best crystal quality and the desired electrical behavior. Recent literature has reported encouraging results on ScAlN/GaN HEMTs grown by plasma-assisted molecular beam epitaxy and metalorganic vapor phase epitaxy. In this thesis, we studied the ammonia-source molecular beam epitaxy, a technique mastered in the laboratory since more than twenty years for GaN and AlGaN compounds. For the first time to our knowledge, ScAlN alloys have been grown on GaN with this technique. The effect of growth temperature has been studied first on relatively thick (25 nm) films in the 600℃ to 800℃ range. An optimal structural quality has been obtained for a growth temperature around 670℃, whereas the amount of scandium around 14% and the thickness vary very slightly in comparison to what was reported with plasma-assisted molecular beam epitaxy. Then, the effect of barrier thickness on 2DEG concentration has been studied. A maximum concentration around $4 \times 10^{13}/cm^2$ has been obtained for a thickness of 15 nm and it remained close to $2 \times 10^{13}/cm^2$ for a nominal thickness of 5 nm. XPS, SIMS and atom probe tomography confirmed the absence of heterogeneities in alloy composition. However, X-ray diffraction and transmission electron microscopy revealed the presence of a critical thickness beyond which crystal lattice parameter modulations appear. Furthermore, this critical thickness is reduced for films grown with scandium amounts around 22% and 30%. We succeeded in elaborating ScAlN/GaN HEMTs on buffer layers developed on both Silicon and GaN-on) sapphire substrates. Our technological work consisted in the achievement of ohmic contacts with acceptable resistances ($Rc \sim 1\Omega.mm$), the device isolation with mesa etching, the fabrication of diodes, van der Paw patterns and transistors able to deliver drain current density superior to 1 A/mm. Hall effect measurements performed on Van der Paw devices confirmed the high carrier concentration of 2 to $3 \times 10^{13}/cm^2$ associated to a mobility of $500 - 600 cm^2/V.s$ in the 2DEGs of HEMTs grown on silicon. HEMTs grown on GaN-on-sapphire substrates exhibited reduced carrier densities compared to those grown on silicon substrates, but with enhanced mobility ($\sim 950 cm^2/V.s$).

Keywords: Scandium aluminum nitride (ScAlN), Molecular Beam Epitaxy (MBE), High electron mobility transistor (HEMT), Heterostructures, III-Nitride Semiconductors

Résumé

L'alliage ScAlN est un semiconducteur III-N à large bande interdite connu pour ses propriétés piézoélectriques remarquables. Ses propriétés de polarisation spontanée et piézoélectrique sont également intéressantes pour la réalisation d'hétérojonctions avec le GaN en vue de fabriquer des transistors à haute mobilité électronique (HEMTs). Dans ces hétérojonctions, remplacer le matériau barrière AlGaN habituellement utilisé par ScAlN présente plusieurs avantages, parmi lesquels la possibilité de générer des gaz bidimensionnels d'électrons (2DEGs) avec des densités bien plus importantes. En corolaire, ceci permet de maintenir de grandes densités de porteurs dans les canaux des HEMTs même avec des barrières ScAlN de très faible épaisseur (quelques nanomètres), ce qui en retour permet de conserver des résistances d'accès faibles, des courants de saturation élevés tout en limitant les effets de canal court dans les transistors à grille submicronique des amplificateurs de puissance hyperfréquence. Aussi, l'alliage $Sc_{0.18}Al_{0.82}N$ étant adapté en paramètre de maille avec GaN, la possibilité de réduire notablement les contraintes mécaniques liées au désaccord de paramètre de maille est un atout pour améliorer la fiabilité des composants. Cependant, pour bénéficier de tous ces avantages il est nécessaire de maîtriser la croissance cristalline de l'alliage ScAlN sur un film de GaN afin d'obtenir des hétérojonctions présentant la meilleure qualité cristalline possible et le comportement électrique recherché. La littérature récente a rapporté des résultats encourageants au sujet de la croissance d'hétérostructures HEMTs ScAlN/GaN par épitaxie sous jets moléculaires assistée par plasma et de la croissance par épitaxie en phase vapeur aux organo-métalliques. Dans cette thèse, nous nous intéressons à la croissance par épitaxie sous jets moléculaires à l'ammoniac, technique que le laboratoire maitrise depuis plus de vingt ans pour les composés GaN et AlGaN. Pour la première fois à notre connaissance, des alliages ScAlN ont été épitaxiés sur GaN au moyen de cette technique. L'effet de la température de croissance a tout d'abord été étudié pour des films de 25nm d'épaisseur dans une gamme allant de 600℃ à 800℃. Un optimum en termes de qualité cristalline est atteint pour 670℃, alors que la teneur en scandium autour 14% et l'épaisseur varient peu à la différence de ce qui est rapporté au sujet de l'épitaxie assistée par plasma. Différentes épaisseurs de barrière allant de 5 à 55 nm ont été étudiées et ont permis d'obtenir une densité maximale de charges dans le 2DEG, autour de $4 \times 10^{13}/cm^2$ pour une barrière épaisse de 15 nm et $2 \times 10^{13}/cm^2$ malgré une épaisseur nominale réduite à 5 nm. Les mesures XPS, SIMS et la tomographie par sonde atomique ont confirmé l'absence d'hétérogénéité de composition dans l'alliage. Cependant, la diffraction des rayons X et la microscopie électronique en transmission révèlent la présence d'une épaisseur critique à partir de laquelle des modulations du paramètre de maille apparaissent. Aussi, cette épaisseur critique diminue pour des films contenant des teneurs en scandium autour de 22% et 30%.

Nous sommes parvenus à élaborer des hétérostructures HEMTs ScAlN/GaN sur des couches tampons développées d'une part sur substrat silicium et d'autre part sur des tremplins GaN/saphir. Nos réalisations technologiques comprennent l'établissement de contacts ohmiques avec des résistances acceptable ($Rc \sim 1\Omega.mm$), la fabrication de diodes, de transistors délivrant des courants de drain jusqu'à plus de 1A/mm et des motifs de van der Pauw. Les mesures d'effet Hall réalisées sur ces derniers ont permis d'obtenir une densité d'électrons allant de 2 à $3 \times 10^{13}/cm^2$ dans le 2DEG, associée à une mobilité de $500 - 600cm^2/V.s$ dans le cas des HEMTs épitaxiés sur silicium. Les HEMT épitaxiés sur des substrats de GaN-sur-saphir ont présenté des densités de porteurs réduites par rapport à ceux épitaxiés sur des substrats de silicium, mais avec une mobilité améliorée ($\sim 950cm^2/V.s$).

Mots-clés : Nitrure de scandium aluminium (ScAlN), Epitaxie sous Jets Moléculaires (EJM), Transistor à haute mobilité électrique, Hétérostructures, Semiconducteurs Nitrures d'éléments III.

Table of contents

1 Introduction

The evolution of wireless transmissions in today's society has been marked by significant advancements and transformative changes. The first generation of massive wireless telecommunications emerged in the 1980s with analog cellular networks. These networks enabled basic voice calls and had limited capacity. The second Generation (2G) which began in the early 1990s, introduced digital cellular networks. These networks offered improved voice quality, increased capacity, and the introduction of basic data services like SMS (Short Message Service). The advent of 3G in the early 2000s, introduced high-speed data transmissions, enabling internet access, email, multimedia messaging, and basic video calling on mobile devices. The emergence of 4G networks, starting around 2009, brought about a revolution in wireless communications. 4G provided significantly faster data transmission speeds, low latency, and enhanced multimedia capabilities. It facilitated the rise of mobile apps, video streaming, social media, and more advanced mobile services. Fifth Generation (5G) represents the latest stage in the evolution of wireless transmission. It began rolling out in 2019 and continues to expand globally. 5G networks offer exponentially higher data rates, ultra-low latency, increased network capacity, and the ability to connect a massive number of devices simultaneously. 5G's advancements are expected to support transformative technologies like autonomous vehicles, augmented and virtual reality, smart cities. To achieve faster wireless telecommunications and to accommodate higher capacity, next-generation communication technologies rely on utilizing higher frequencies. Applications in the Ka to W bands are therefore conceivable, both in telecommunications and radars. This frequency range constitutes the millimeter-wave range (bands marked in red in figure 1 below). Nonetheless, as the next generation of communication technology emerges, a trade-off arises with reduced signal coverage, which is inversely proportional to the square of the operating frequency. This reduction in coverage is primarily because higher-frequency signals have shorter wavelengths and are more prone to obstacles and interference. They tend to get absorbed or scattered more easily by objects such as buildings, trees, and even the atmosphere. As a result, the signals cannot propagate as far or penetrate obstacles as effectively as lower-frequency signals. To ensure uninterrupted wide-area coverage, a higher emitted power or a substantial increase in the number of base stations is necessary.

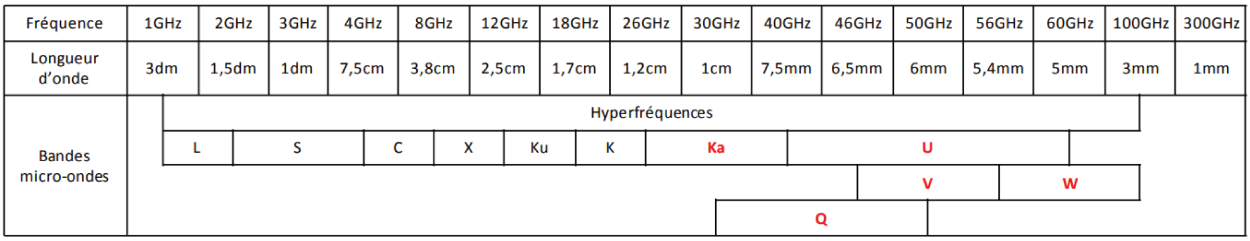

Figure 1: Electromagnetic spectrum of micro-waves.

Consequently, with an increasing number of base stations, a crucial objective from both financial and environmental perspectives is to significantly decrease their power consumption. The most impactful approach to achieve this is by enhancing the efficiency of the power amplifiers (PAE) operating at high frequencies. In 1979, Takashi Mimura, while working at Fujitsu in Japan made a groundbreaking contribution by inventing the high-electron mobility transistor [1], the basis of the HEMT was the GaAs MOSFET (metal-oxide-semiconductor fied-effect transistor). Daniel Delagebeaudeuf and Tranc Linh Nuyen, both employed at Thomson-CSF France at the time, individually submitted a patent application for a comparable field-effect transistor in 1979 [2]. HEMT contains a heterojunction to boost electron mobility, resulting in faster electron

transportation. In the case of AlGaAs/GaAs heterojunctions, doping of the AlGaAs barrier is necessary to generate a highly conductive two-dimensional electron gas in the GaAs channel. The primary constraint lies in the electron density within the 2DEG, which is below $1 \times 10^{12}/cm^2$. However, substituting GaAs with pseudomorphic InGaAs can elevate this density to approximately $2 \times 10^{12}/cm^2$. Utilizing alternative heterojunction materials such as InAlAs/InGaAs can further increase the electron density to reach levels of up to $3 \times 10^{12}/cm^2$ e-/cm² [3]. The ability to engineer the bandgap within a wide range (from 0.7 eV with InN to 6.1 eV with AlN) by combining InN, GaN, AlN and ScN makes Group III nitrides suitable for various applications in the field of RF power amplifiers, particularly in base stations for mobile communications. In 1993, Khan et al. introduced one of the first references to a GaN-based High Electron Mobility Transistor (HEMT) [4]. In contrast to GaAs HEMTs, GaN HEMTs have the advantage of not requiring doping. This is attributed to the hexagonal wurtzite structure of III-Nitride materials, which induces polarization effects. As a result, an heterostructure is formed that exhibits a high-density two-dimensional electron gas (2DEG) at the interface between the wider bandgap material (barrier) such as AlGaN, InAlN, InGaAlN and the lower bandgap one (channel) such as GaN. This unique structure enables enhanced power transistor capabilities without the need for additional doping. The initial report on the aluminum gallium nitride (AlGaN)/gallium nitride (GaN) heterojunction dates back to 1991[5], and it marked a significant milestone. This was followed by the development of the first AlGaN/GaN high-electron mobility transistor (HEMT) in 1993 [6], [7].

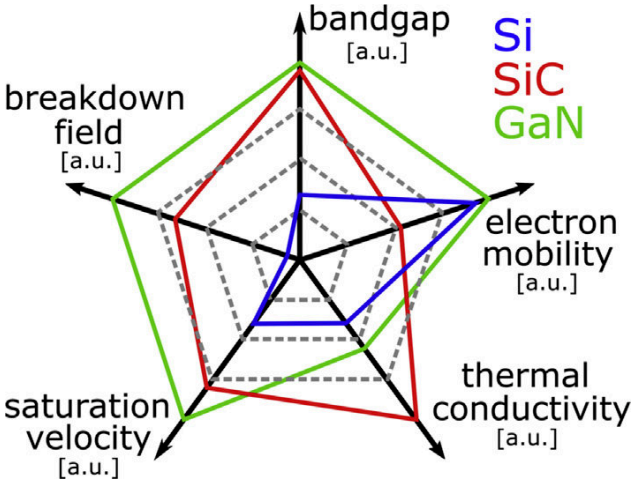

Figure 2: Differences in material properties between GaN, Si and SiC. Data from [8].

GaN-based transistors (high-electron-mobility transistor, HEMT) are increasingly replacing traditional Si-based devices such as Laterally Diffused Metal Oxide Semiconductor (LDMOS) in base stations and GaAs based transistors in radars and military applications. The large bandgap of GaN results in a high breakdown electric field of 3.5 MV/cm [9], [10] and allows for high-voltage operation and cost-effective fabrication of smaller devices and thanks to their high electron saturation velocity (up to $2.5 \times 10^7 cm^2/s$) and good thermal conductivity (1.5-2.5 W/(cm.K)), they can achieve high power and high-speed operation while reducing cooling requirements compared to other technologies (see Figure 2). Furthermore, III-Nitride HEMT heterostructures have significantly high sheet carrier concentrations (generally around $10^{13}/cm^2$) and rather high electron mobilities (1000 to 2000 $cm^2/V.s$ at 300 K).

Beyond the output power performance of the transistors, a critical parameter for applications is the power added efficiency (PAE). It is defined as the difference between RF power at the output of the device and RF power at the input, divided by the DC power used to bias the device. Such ratio gives an idea of the

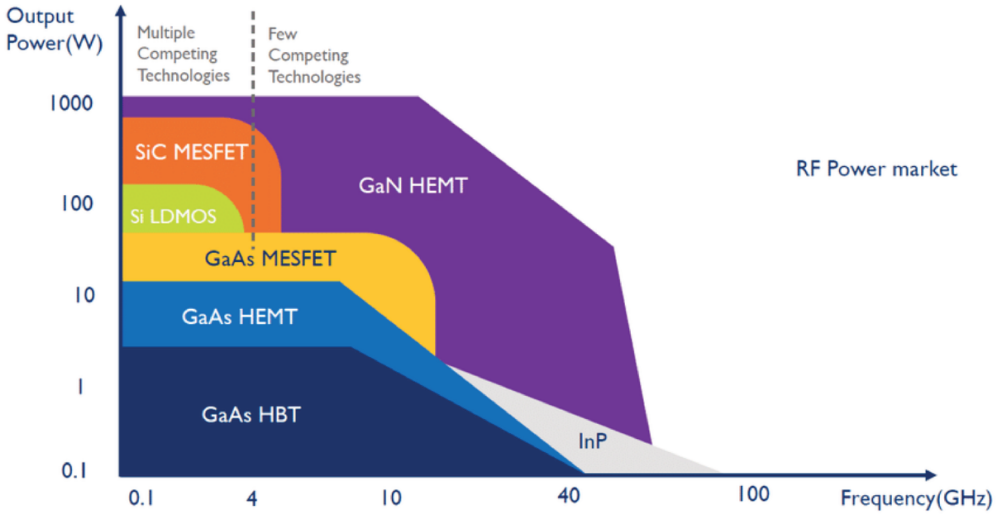

Figure 3: Output power vs frequency among different semiconductor technologies. GaN-based High Electron Mobility Transistors (HEMTs) demonstrate their suitability for operating at both high power and high frequency simultaneously[11].

energy efficiency of the transistors, which influences operation cost and also the device lifetime. In traditional $Al_xGa_{1-x}N$/GaN HEMTs, to increase the ifficiency of such transistor, it is crucial to increase the charge carrier concentration in the two-dimensional electron gas (2DEG). To enhance the operating frequency, a commonly employed technique is to decrease the gate length (Lg). By reducing Lg, the transition frequency (f_T) experiences an increase across various material systems. However, diminishing the gate length necessitates decreasing the gate-to-2DEG distance (d_{g-2DEG}) through the L_g/d_{g-2DEG} aspect ratio. In the case of nitrides (wide bandgap materials), it is crucial to maintain this aspect ratio above 15 to limit short channel effects, as indicated by a study conducted by Jessen et al. [12]. Achieving high-frequency operation in gallium nitride (GaN) devices necessitates a thin barrier layer with a high-density two-dimensional electron gas (2DEG). So far, Shinohara et al. have achieved a GaN HEMT with an impressive cutoff frequency of approximately 450 GHz [13]. $Sc_xAl_{1-x}N$ exhibits a wide and direct bandgap of greater than 5 eV for Sc molar fraction x up to x = 0.25. Additionally, it can be further tuned to 3.99 eV (indirect) for x = 0.5 [14]. This bandgap characteristic makes $Sc_xAl_{1-x}N$ suitable for serving as a barrier material in HEMT structures. By adding scandium (Sc) in the III-Nitride alloys, a remarkable increase in spontaneous polarization and a substantial fivefold enhancement in piezoelectric polarization are achieved [14], [15]. These improvements directly contribute to inducing significantly higher sheet carrier concentrations in the material. Furthermore, it is anticipated that the lattice matched growth of $Sc_xAl_{1-x}N$ with a composition of approximately $x \sim 0.18$ on GaN will result in high structural quality of the barrier layer. This high-quality structure is expected to significantly enhance the control of carriers and their transport properties within the device. The strong motivation to utilize ScAlN in HEMT structures has led to its growth using various techniques metalorganic chemical phase deposition (MOCVD)[16], and plasma-assisted molecular beam epitaxy (PA-MBE) [17]–[19]. However, there has been no investigation yet on the growth of ScAlN using ammonia source molecular beam epitaxy (NH3 MBE) growth technique. This knowledge gap provides an opportunity for CRHEA-CNRS laboratory to explore a growth technique that has proven its interest for the achievement of high performance GaN based RF devices [20].

The objective of this thesis is to establish a thorough understanding and a reliable process for the epi-

taxial growth of ternary $Sc_xAl_{1-x}N$ films by NH_3 MBE. We believe that NH_3 MBE growth permits to achieve higher resistivity GaN buffer layer which is critical for HEMT applications and thanks to their lower concentration of residual donors[21]. This involves investigating various growth parameters and systematically characterizing their impact on the structural, morphological, compositional, and electrical properties of $Sc_xAl_{1-x}N$ /GaN structures. Through a comprehensive analysis of the results, the aim is to identify the optimal growth conditions necessary for fabricating GaN-based High Electron Mobility Transistors (HEMTs) with $Sc_xAl_{1-x}N$ barrier layers.

2 Material properties of group III-Nitride materials

2.1 Group III-Nitrides main properties

2.1.1 Crystalline properties

Crystal Structures

Semiconductor materials known as nitrides of group III elements consist of elements from column III of the periodic table (Gallium Ga, Aluminium Al, Indium In, Scandium Sc) combined with nitrogen (N) from column V. The bonding between these atoms is achieved through covalent bonds. Collectively, these materials are referred to as "III-N materials" (GaN, AlN, InN, and their alloys). They can adopt three different crystal structures: two cubic structures, the zinc blende one with $F\bar{4}3m$ space group (in the Hermann–Mauguin notation), and the rocksalt one with the $Fm\bar{3}m$ space group, and one hexagonal structure (wurtzite) with the $P6_3mc$ space group.. The specific structure formed depends on various parameters, including crystal growth conditions (such as pressure, temperature, III-V ratio) and the choice of substrate with its crystallographic orientation. Among these structures, the wurtzite structure is the most thermodynamically stable and is commonly utilized in the production of electronic and optoelectronic components based on GaN. The nitrogen being more electronegative than the element III, the bond III-N is polar. The corresponding dipole moment is directed according to the bond III-V, from the most electronegative element to the least electronegative one (thus the nitrogen to the element III see Figure 4).

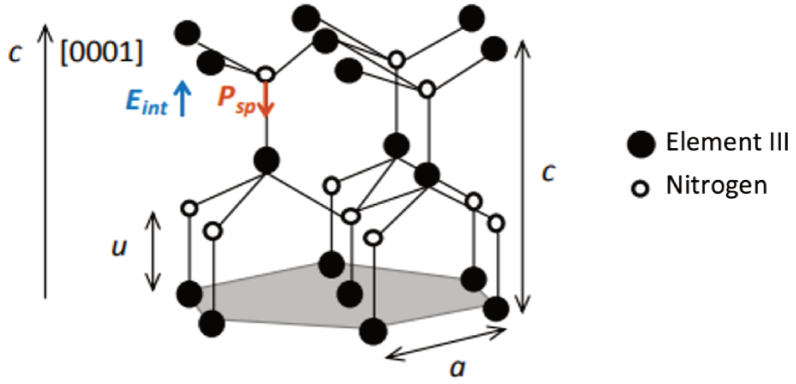

Figure 4: Wurtzite phase crytallisation of III-N materials [22].

We identify and differentiate between two separate polarities shown in Figure 5: Ga polarity and nitrogen polarity. Ga polarity is associated with GaN crystals oriented along the [0001] crystallographic axis, while nitrogen polarity corresponds to GaN crystals oriented along the $[000\bar{1}]$ axis. All the samples analyzed in this thesis exhibit Ga polarity. These orientations refer to the exposed crystal surfaces during the growth of III-N films. In GaN crystals, the Ga-face orientation, also known as the (0001) plane, is the most commonly utilized surface for epitaxial growth due to its stability and accessibility. The Ga-face has the c-axis of the crystal lattice perpendicular to the surface. GaN films grown on the Ga-face exhibit smoother surface morphology and fewer defects, attributed to the higher surface energy of the Ga-face [23]. On the other

hand, the N-face orientation exposes the surface with nitrogen atoms. The N-face orientation is less stable compared to the Ga-face due to its higher surface energy and the presence of surface polarity. However, N-face growth can yield GaN films with unique properties such as higher electron mobility and lower surface recombination velocity. In certain applications, N-face GaN is preferred due to its distinctive characteristics, including superior polarization properties, high electron mobility, and lower surface recombination velocity[24]–[26]. Nevertheless, growing N-face GaN poses challenges due to surface polarity, which can lead to the incorporation of impurities and defects in the material. Achieving N-face growth requires precise control of growth conditions and surface preparation to minimize these issues. In summary, both Ga-face and N-face orientations of III-N materials offer advantages and disadvantages. The choice of orientation depends on the specific device requirements and growth conditions, considering factors such as surface morphology, defect density, and unique properties associated with each orientation.

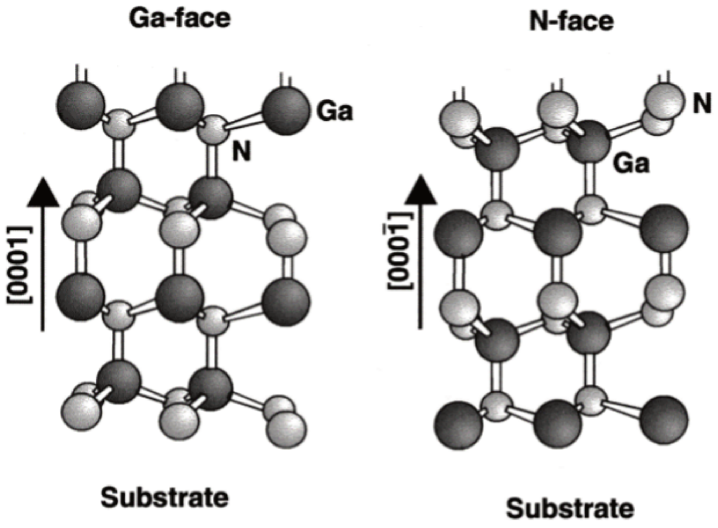

Figure 5: Ga-face and N-face in GaN [27].

The epitaxial growth of our layers predominantly occurs along the c-axis or (0001) orientation, which is the most commonly utilized direction. Nitride materials adopt a wurtzite crystal structure, which lacks inversion symmetry along this axis. This absence of inversion symmetry, coupled with the strong ionic nature of the nitrogen-metal bond, gives rise to a substantial polarization field known as spontaneous polarization. Notably, the wurtzite phase exhibits the highest level of spontaneous polarization among different crystal structures. Several factors can influence the polarity (N or Ga) during III nitride growth. First is the substrate material choice, for example, using a Ga-polar substrate may favor Ga-polarity growth, while using an N-polar substrate may promote N-polarity growth. Second, the surface preparation of the substrate before growth involves surface cleaning to remove contaminants and native oxides. Also, the growth conditions and by introducing specific layers or dopants, it is possible to manipulate the surface polarity and achieve the desired orientation [28], [29]. The asymmetrical displacement of the electron cloud towards one of the nitrogen atoms gives rise to a dipole formation. As a result, negative charges accumulate on one side of the crystal, while positive charges accumulate on the other side (Figure 6). The extent of electron accumulation is dependent on the growth polarity of the crystal.

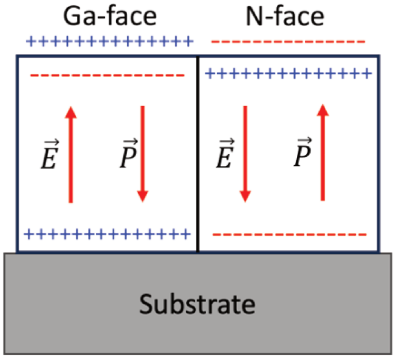

Figure 6: Crystal structure and orientation of the c-axis as well as of the macroscopic spontaneous polarization and the corresponding electric field for Ga-face and N-face GaN grown on an heterosubstrate.[30]

Lattice parameters (GaN, AlN, InN)

The lattice parameters provide important information about the crystal structure, including its symmetry, packing arrangement, and crystallographic orientations. The lattice parameters can vary slightly depending on factors such as temperature, strain, and alloy composition. The wurtzite structure is the most thermodynamically stable form of III-Nitrides. In this type of structure, there are two compact hexagonal sub-lattices, one for type III elements (Al, Ga, In) and the second for nitrogen atoms (N), shifted 5/8 along the c-axis. The lattice parameters a, c of würtzite-type crystal structures (Figure 4) for GaN, AlN and InN are shown in Table 1.

	GaN	AlN	InN
a (Å)	3.189	3.112	3.538
c (Å)	5.185	4.982	5.703
$\frac{c}{a}$ (Å)	1.626	1.600	1.612

Table 1: Lattice parameters of würtzite-type crystal structures for GaN, AlN, InN.

Vegard's rule, a linear relationship, is utilized to estimate the lattice parameters of $A_xB_{1-x}N$ alloys, where the content x acts as an independent variable.

$$a(x) = x.a_{AN} + (1-x).a_{BN}$$

$$c(x) = x.c_{AN} + (1-x).c_{BN}$$

In the case of conventional wurtzite alloys such as $Ga_xAl_{1-x}N$ and $In_xAl_{1-x}N$, the lattice parameters a and c exhibit a linear increase as the number of gallium or indium atoms replacing the aluminum atoms in AlN increases. This behavior aligns with the linear relationship predicted by Vegard's rule (deviations from Vegard's rule are obtained via bowing parameter). AlN, GaN and InN are wide-bandgap semiconductors that have similar crystal structures. They all crystallize in the wurtzite crystal structure.

ScN crystalline properties

Scandium is a group III B metal. Like Yttrium, it is a transition metal. Scandium nitride (ScN) which crystallizes in rock salt, can exhibit other crystal structures as well. While the rocksalt structure is the most commonly observed one, there have been reports of alternative crystal structures for ScN under specific conditions. ScN can also adopt wurtzite and zinc blende structure and the stability and occurrence of these alternative crystal structures for ScN may depend on factors such as growth conditions, temperature, and the presence of impurities. The rocksalt structure remains the most prevalent and well-studied crystal structure for ScN. In ScN, all the bonding states are occupied by the 8 valence electrons while keeping the non-bonding and anti-bonding states completely unocuppied and this yields to a covalent bond filling in a rock salt structure which is very stable (minimum total energy $G = E + pV - TS$) see Figure 7a and Figure 7b. Many experimental studies [34]–[36] are in agreement with theoretical investigations and reported the lattice parameter shown below in Table 2.

	ScN [34]–[36]	ScN[37]	ScN[38]	ScN[39]
ScN structure	Rocksalt NaCl	Hexagonal	Wurtzite	CsCl
a (Å)	4.54	3.660	3.49	2.81
c (Å)	-	4.417	5.58	-
$c/a(Å)$	1	1.207	1.60	1

Table 2: Structural properties of ScN reported in the literature.

In addition, other calculations have been conducted for hexagonal ScN phase which is metastable. The difference between h-ScN and w-GaN or w-InN is the number of nearest neighbors, then w-GaN and w-InN have ground state phase closer to the wurtzite structure[37].

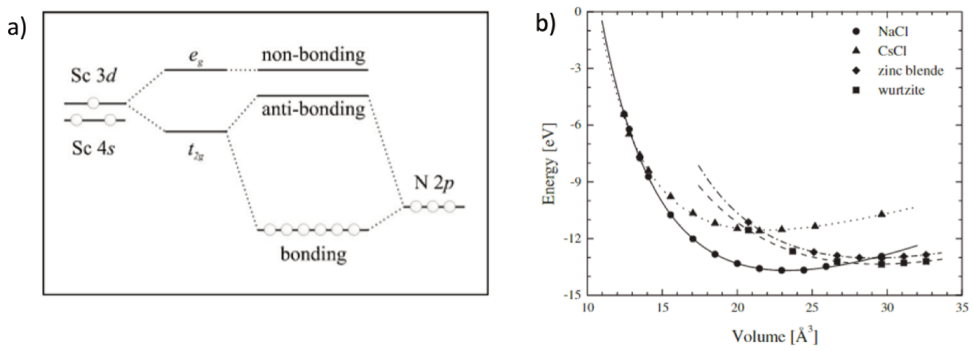

Figure 7: a) Schematic diagram of the pd bonding in rock-salt ScN [40], and b) Total energy versus atomic volume for ScN [34].

Sc has fewer valence electrons and so the Fermi level in ScN drops below the conduction band edge, leading to semi-conducting behaviour instead of the metallic properties of other rock-salt transition metal nitrides (TMNs). ScN is stable in a rock salt structure and this can be traced to the covalent bonds between N 2p and Sc 3d electrons as demonstrated by Harrison and Straub [41]. The covalent bond arrangement in ScN exhibits octahedral symmetry, reminiscent of the NaCl structure. This configuration imparts exceptional stability, as illustrated in Figure 7b, where it attains the lowest total energy within the NaCl structure. A minor electron transfer from Sc to the nitrogen atom, which has a higher electronegativity, introduces a subtle ionic character into ScN.

2.1.2 Mechanical properties

Substrates for the epitaxial growth of heterostructures

Contrary to Si, InP, GaAs... the absence of large dimeter bulk gallium nitride GaN substrates requires to use hetero-epitaxial growth [42], [43]. GaN is generally epitaxied on substrates like silicon, sapphire, Silicon carbide or aluminum nitride. Every type of substrate has advantages and drawbacks.

The advantages of growing GaN on sapphire substrates is an acceptable cost, high thermal stability, transparency specially for optoelectronics applications, and relatively simple growth process. However, due to the high lattice parameter and thermal coefficient of expansion (TCE) mismatch with GaN, this implies a strong residual compressive stress upon cooling down to 300K after the growth at 800-1050°C. This enables the growth of good crystal quality thick GaN epilayers but at the cost of large substrate curvature and resulting bow. On the other hand, sapphire is a poor thermal conductor, and this limits the development of high-power devices. Nevertheless, laser lift-off remains a possibility to separate thick GaN epilayers from the substrate as demonstrated for light-emitting devices [44] commercialized by hundreds of million pieces worldwide.

SiC presents a reasonable lattice mismatch with GaN and it is a very good thermal conductor what makes it a good choice for power devices. But SiC is expensive and absorbs a part of the visible spectrum which limits the development of optoelectronic devices. As the coefficient of thermal expansion of SiC is lower than the one of GaN, tensile stress is generated upon cooling after growth with a risk of layer cracking which limits the layer thickening.

Si substrate is known for its low cost and large size availability. Si presents a rather good thermal conduction for power applications. His large in-plane lattice parameter mismatch and large TCE mismatch with GaN results in tensile stress during cooling after growth (risk of cracking and limited layer thickening).

AlN substrate is also a potential material for GaN based devices [45]. AlN offers certain advantages compared to Silicon Carbide, such as a more favorable differential thermal expansion with GaN (33%) and a lattice mismatch with GaN that is closer to that of SiC (2.4%). Additionally, AlN exhibits nearly high thermal conductivity ($2WK^{-1}cm^{-1}$) and significantly surpasses both Silicon (Si) and sapphire, making it an appealing choice for substrates in applications involving high power or high temperatures.

	GaN	AlN	Sapphire	SiC	Si (111)
In-plane lattice parameter at 300K(Å)	a=3.189	a=3.112	a=2.747	a=3.08	a=3.84
Lattice parameter mismatch with GaN (%)	0	2.4 Compression	16 Compression	3.5 Compression	-17 Tension
Coefficient of thermal expansion ($*10^{-6}K^{-1}$)	5.59	4.2	7.5	4.7	2.59
Thermal mismatch with GaN (%)	0	33	-25.5 Compression	19 Tension	116 Tension
Thermal conductivity ($W.K^{-1}cm^{-1}$)	1.5	2	0.5	5	1.5

Table 3: The main properties associated with the growth of GaN on various substrates

Types of dislocations

Depending on the choice of the substrate, the TCE and lattice parameter mismatch can deteriorate the crystal quality of the heteroepitaxy, and crystal defects may appear by the formation of polarity inversion domains, stacking faults and dislocations. In addition, other punctual defects can appear such as interstitial or substitutional impurities. Note however that the main defects are the dislocations. The difference in lattice parameter for GaN epitaxy is of about 16% on sapphire or -17% on silicon, and the TCE mismatch is of -25.5% and 116% on sapphire and silicon (111) respectively. The nucleation of misfit dislocations is an efficient way to relax the strain due to lattice parameter mismatch. A thickness at which this occurs is defined as a critical thickness. On silicon, the critical thickness of III-Nitride thin films like AlN is about one monolayer. The heteroepitaxy of III-Nitride compounds on such substrates starts with the formation of islands of a few tens to a few hundreds of nanometers in diameter. This type of growth is said to be columnar because of the high coherence length of the grains along the growth axis [0001] and reduced in the growth plane and very small in the growth plane ($L_{//}$ assimilated to the average size of the grains crystallographic grain size). These islands coalesce rapidly, but the relative disorientations of their growth axes of growth [0001] (called tilt, see Figure 8a) and their misorientations in the plane (called twist, see Figure 8b) are responsible for the formation of threading dislocations at grain boundaries. It is possible to reduce the number of threading dislocations by bending and recombination mechanisms, but this necessitates to grow complicated structures with different materials such as AlN to achieve this goal while avoiding the risk of layer cracking after the growth[46], [47] . On the other hand, dislocation bending and annihilation in GaN grown on sapphire is easier to achieve thanks to the possibility to grow thick strain relaxed layers without the risk of crack generation after the growth.

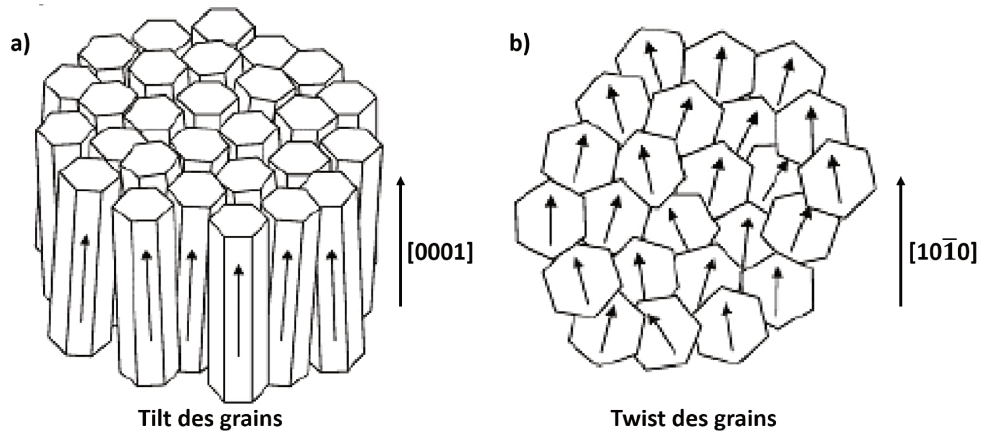

Figure 8: Grain misorientation along a) the $< 0001 >$ direction (tilt) and b) in the plane associated with columnar growth of heteroepitaxial element-III nitrides (twist) [48].

A dislocation is a line of defects in the crystal, it is defined by the unit vector $\overrightarrow{u}$, parallel to the dislocation line, and by the Burgers vector $\overrightarrow{b}$, relative to the amplitude of the local deformation of the crystal lattice. During the growth of GaN, three types of dislocations can propagate from the substrate/nitride interface to the surface through the film (threading dislocations):

1. Edge dislocation (type a): burger vector $\overrightarrow{b}$ perpendicular to unit vector $\overrightarrow{u}, b = \frac{1}{3} < 11\bar{2}0 > (= 3.189\mathring{A}$ for GaN film) so, the burger vector is in the growth plane.

2. Screw dislocation (type c): burger vector $\overrightarrow{b}$ parallel to unit vector $\overrightarrow{u}, b =< 0001 > (= 5.185\mathring{A}$ for GaN film) so the burger vector is parallel to the growth axis, perpendicular to the growth plane.

3. Mixed dislocations (type a + c): $b = \frac{1}{3} < 11\bar{2}3 > (= 6.087\mathring{A}$ for GaN film)

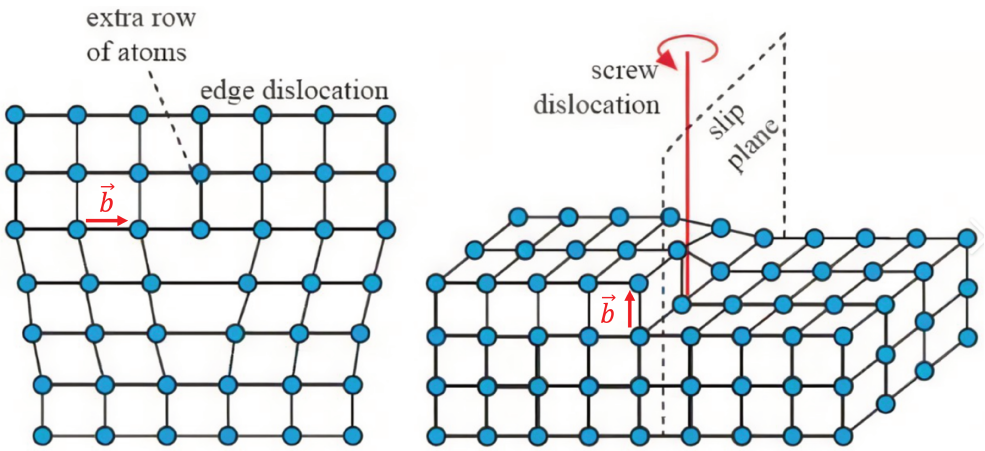

Figure 9: Schematic of edge and screw dislocations.

Stress and strain

When a film is epitaxially grown on a substrate, the crystal deforms linearly with respect to the stress provided that the strain is small, this is Hooke's law.

$$\vec{\sigma} = \widehat{C}.\vec{\varepsilon}$$

σ and ε are respectively stress and strain tensors of order 2, while C is the tensor of elastic coefficients. If the deformation exceeds a certain threshold, two behaviors are observed: Fragile materials: the rupture takes place before leaving the elastic regime thus it is characterized by the absence of plastic deformation, and by the very fast propagation of cracks. Ductile materials (Figure 10): once the yield strength is surpassed, the material enters the plastic regime where deformations become permanent. This transition occurs as the atomic planes start sliding against each other, generally facilitated by linear defects known as dislocations. From the elastic limit to the ultimate stress (ultimate strength), there is a phase of strain hardening, also referred to as plastic deformation hardening. This phenomenon is caused by the motion of dislocations. Eventually, beyond the ultimate stress, a narrowing region called necking forms in the material, leading to its fracture.

For hexagonal structures, the Hooke's law is expressed with the following matrix:

$$\begin{pmatrix} \sigma 1 \\ \sigma 2 \\ \sigma 3 \\ \sigma 4 \\ \sigma 5 \\ \sigma 6 \end{pmatrix} = \begin{pmatrix} C_{11} & C_{12} & C_{13} & 0 & 0 & 0 \\ C_{12} & C_{11} & C_{13} & 0 & 0 & 0 \\ C_{13} & C_{13} & C_{33} & 0 & 0 & 0 \\ 0 & 0 & 0 & C_{44} & 0 & 0 \\ 0 & 0 & 0 & 0 & C_{44} & 0 \\ 0 & 0 & 0 & 0 & 0 & C_{66} \end{pmatrix} \begin{pmatrix} \varepsilon 1 \\ \varepsilon 2 \\ \varepsilon 3 \\ \varepsilon 4 \\ \varepsilon 5 \\ \varepsilon 6 \end{pmatrix}$$

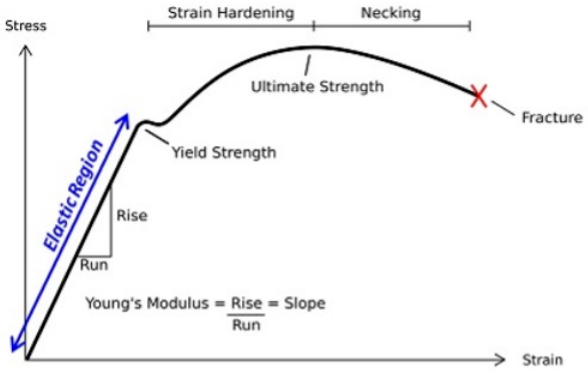

Figure 10: Schematic showing the stress vs strain in ductile material type [49].

The heteroepitaxy of GaN on a substrate induces biaxial stresses due to:

1. The difference of the in-plane lattice parameter, during the growth.
2. The difference in thermal expansion coefficient (TCE), when the system is cooled down to room temperature: this is the thermo-elastic stress.

Biaxial strain

Biaxial strain in III-N (III-nitride) materials refers to the application of strain along two perpendicular directions in the growth plane (perpendicular to growth axis). This type of strain can have a significant impact on the structural, electronic, and optical properties of III-N materials, such as gallium nitride (GaN), aluminum nitride (AlN), and indium nitride (InN). Biaxial strain is commonly induced in III-N materials by growing them on substrates with a different lattice parameter or thermal expansion coefficient. The lattice parmeter mismatch between the III-N material and the substrate leads to strain in the film. The strain can be tensile or compressive, depending on whether the lattice constant of the substrate is larger or smaller than that of the III-N material. The biaxial strain affects the physical properties of III-N materials in several ways: Band gap: Biaxial strain can modify the bandgap energy of III-N materials. Tensile strain generally leads to a smaller bandgap, while compressive strain increases the bandgap. Carrier Mobility: Biaxial strain influences the carrier mobility in III-N materials. Tensile strain can reduce the effective mass and then increase the carrier mobility. However, such effect which can be noticeable for small bandgap III-V materials is generally negligible for III-N materials. Piezoelectric Effects: III-N materials possess strong intrinsic piezoelectric properties. Biaxial strain can modify the piezoelectric polarization and strain-induced electric fields in III-N films, affecting their electronic and optical properties. For the growth of cubic or hexagonal phase materials on substrates with similar symmetry and well defined crystal orientation such as 111 or 0001 the pseudomorphic growth along c-axis (z direction), biaxial stress exists only in x and y directions, and then no stress appears on z direction. Due to crystal symmetry, the components of the strain in x and y are equal $\sigma 1 = \sigma 2$ and no component along z nor shear components $\sigma_3 = \sigma_4 = \sigma_5 = \sigma_6 = 0$.

$$\begin{pmatrix} \sigma_x x \\ \sigma_y y \\ 0 \end{pmatrix} = \begin{pmatrix} C_{11} & C_{12} & C_{13} \\ C_{12} & C_{11} & C_{13} \\ C_{13} & C_{13} & C_{33} \end{pmatrix} \begin{pmatrix} \varepsilon 1 \\ \varepsilon 2 \\ \varepsilon 3 \end{pmatrix}$$

	GaN	AlN	InN
C_{11} [GPa]	367	396	223
C_{12} [GPa]	135	137	115
C_{13} [GPa]	103	108	92
C_{33} [GPa]	405	373	224
C_{44} [GPa]	95	116	48
$E_{31}[C/m^2]$	-0.49	-0.60	-0.57
$E_{33}[C/m^2]$	0.73	1.46	0.97
$P_{SP}[C/m^2]$	-0.029	-0.081	-0.032

Table 4: Elastic constants and piezoelectric coefficients reported in [50], [51].

$$\sigma_{xx} = (C_{11} + C_{12})\varepsilon_{xx} + C_{13}\varepsilon_{zz}$$

$$\sigma_{zz} = 0 = 2C_{13}\varepsilon_{xx} + C_{33})\varepsilon_{zz}$$

Thus, the biaxial stress can be written as follows:

$$\sigma_{xx} = \varepsilon_{xx}(C_{11} + C_{12} - 2\frac{C_{13}^2}{C_{33)}})$$

$\varepsilon_{xx} = \frac{a-a_0}{a_0}$ equal to ε_{yy}, represents the in-plane biaxial strain.

$\varepsilon_{zz} = \frac{c-c_0}{c_0}$, represents the out of plane strain.

And $C_{66} = \frac{1}{2}(C_{11} - C_{12})$ for And then we identify the Poisson coefficient:

$$\nu = -\frac{\varepsilon_{zz}}{\varepsilon_{xx}} = 2\frac{C_{13}}{C_{33}}$$

Thermo elastic strain

The thermal coefficient of expansion (α) is a material-specific property that measures the degree of expansion or contraction experienced by a solid as the temperature changes. In the case of III-V materials, which are compound semiconductors made up of elements from Group III (such as aluminum, gallium, indium) and Group V (such as nitrogen, phosphorus, arsenic), the thermoelastic strain plays a significant role in determining their mechanical stability. Temperature fluctuations cause a III-V material to undergo expansion or contraction, leading to changes in its lattice parameters. Consequently, the deformation of a crystal due to temperature variations is influenced by the thermal expansion coefficient (α).

$$\alpha = \frac{1}{\alpha}\frac{\partial a}{\partial T}$$

where a is the lattice parameter of the crystal. GaN is generally grown on a foreign substrate at high T_g (growth temperature) (between 700 ℃ and 1000 ℃ depending on the growth technique used). Being given that the thermal expansion coefficients of the film and the substrate are different, thermo-elastic stress and strain appear during cooling to room temperature Ta. They are proportional to the differential of deformation undergone by the film and the substrate during the temperature change, i.e. to the quantity of strain ε_{th}, and defined classically by:

$$\varepsilon_{th} = \int_{T_C}^{T_A} (\alpha_{film} - \alpha_{substrate}) dT$$

Where α_{film} and $\alpha_{substrate}$ are the respective coefficients of thermal expansion of the film and substrate. As previously, Hooke's low can be used to calculate the residual stress as a function of the strain ε_{th}.

Strain relaxation

Due to lattice parameter mismatch, between the epitaxial film and the substrate, elastic energy is accumulated in the grown films until a relaxation occurs at a critical thickness h_c. Relaxation of an epitaxial film relaxes the stored energy by creating crystalline defects or microcracks depending on the material behavior with the substrate. The relaxation of lattice mismatched III-Nitrides is generally ductile and typically generates dislocations. The relaxation of the biaxial stress stress σ_{xx} due to the difference in lattice parameters can only take place through the edge-type dislocations (a and a+c) belonging to the slip plane (0001). They are commonly called interface dislocations or misfit dislocations. For example, growing AlGaN material on GaN with a substantial aluminum concentration is necessary to achieve a high carrier density in the 2DEG of AlGaN/GaN heterojunction components. However, as the aluminum proportion increases, the lattice parameter of AlGaN decreases, resulting in an increase in lattice mismatch. This lattice mismatch reaches its maximum at an aluminum content of 100%, corresponding to AlN, with a value of 2.4%, which is relatively high. This situation can generate significant strains in the alloys, limiting the epitaxy of an AlGaN layer on GaN to relatively small thicknesses. The primary objective is to avoid strain relaxation. In practical terms, the critical thickness of the AlGaN layer with an aluminum molar fraction of 20 to 30% typically falls between 25 and 35 nm. It's important to note that tensile strain increases proportionally with the aluminum concentration. In other words, as the aluminum concentration rises, the lattice parameter of the AlGaN material decreases even further.

2.1.3 Electronic properties

Bandgap energy

The III-N (III-nitride) materials, which include compounds such as gallium nitride (GaN), aluminum nitride (AlN), and their alloys including ones with indium, exhibit wide bandgap energies. The bandgap energy is a fundamental property of a semiconductor material that determines its optical and electronic characteristics. The bandgap energy represents the minimum energy required to excite an electron from the valence band to reach the conduction band. For exemple, Gallium nitride (GaN) has a direct bandgap energy of around 3.4 electron volts (eV) at room temperature. The bandgap of GaN can be modified by alloying it with other elements, such as aluminum (Al) or indium (In), resulting in different compounds like AlGaN or InGaN. Aluminium nitride (AlN) has a wide direct bandgap energy of about 6.0 eV at room temperature (Figure 11). It has one of the largest bandgaps among III-N materials, making it suitable for deep-ultraviolet (UV) applications. Also, indium nitride (InN) has a narrow direct bandgap energy of approximately 0.7 eV at room temperature. It possesses the smallest bandgap among the III-N materials and is typically used in the near-infrared (IR) range.

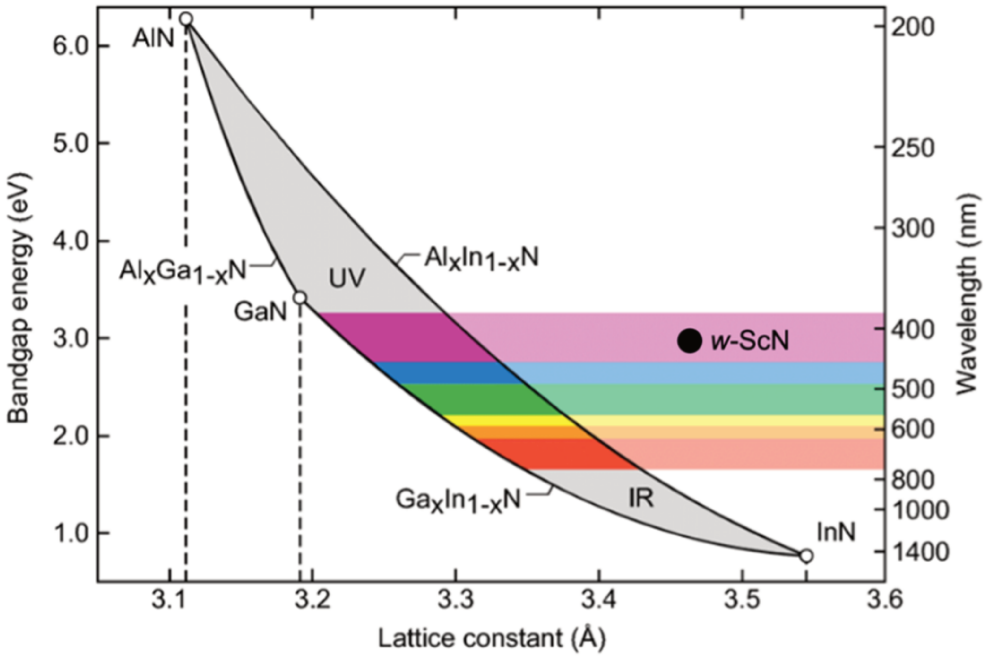

Figure 11: Bandgap energies and lattice constants for nitrides in wurtzite phase.

The bandgap energies provided above are approximate values and can vary depending on factors such as temperature, strain, and doping. For electronics, the bandgap energy is one main characteristic as wide bandgap energies allow for higher breakdown electric field and higher operating voltages [52], [53].

Rock Salt ScN is a semiconductor with a fundamental indirect gap of 0.9 eV and a direct gap of 2.4 eV, which can be incorporated directly into III-nitride structures, and which can be grown successfully using a wide range of techniques[54]–[57]. In the wurtzite phase, the presence of indirect band gap of approximately 3 eV signifies the characteristic behavior of a semiconductor. Additionally, we can discern a slender width of the valence band, which implies a frail bonding within the wurtzite structure[34].

Spontaneous and piezoelectric polarization

Spontaneous polarization in wurtzite structures is a phenomenon that arises due to the asymmetric arrangement of atoms and their electronic clouds within the crystal lattice. In the wurtzite structure, the atoms are arranged in an hexagonal lattice with alternating layers of different elements. For example, in GaN, gallium (Ga) and nitrogen (N) atoms form the lattice. However, due to the difference in electronegativity between Ga and N, there is a slight displacement of the positive Ga ions and negative N ions along the c-axis of the crystal lattice. This displacement leads to the creation of a dipole moment within each unit cell of the crystal. The dipole moment arises from the separation of positive and negative charges, creating a polarization charge. This spontaneous polarization is a bulk property of the material and does not require any external electric field. The direction and magnitude of the spontaneous polarization in wurtzite structures depend on the specific material and its crystallographic orientation. It is typically characterized by a vector pointing along the c-axis of the crystal. In GaN, for instance, the spontaneous polarization vector points from the nitrogen atom to the gallium atom as shown in Figure 4 and then from Ga-terminated surface to N-terminated surface. The presence of spontaneous polarization in wurtzite structures can have significant effects on the electronic and optical properties of these materials. Understanding and controlling the spontaneous polarization is crucial for optimizing wurtzite-based devices, such as optoelectronic devices (e.g., LEDs and laser diodes) and electronic devices (e.g., transistors). For alloys, spontaneous polarization is given as a linear variation with content according to Vegard's law, or a polynomial equation with a factor bowing as reported in [58]. For AlGaN for example: Vegard's law is as following:

$$P^{SP} = P^{SP}_{GaN} + x(P^{SP}_{AlN} - P^{SP}_{GaN})$$

While polynomial equations have reported in [58]

$$P^{SP} = -0.090x - 0.034(1)x) + 0.019x(1-x)$$

In addition to spontaneous polarization in III-N materials, also piezoelectric polarization is an important phenomenon. Piezoelectricity refers to the generation of an electric polarization in a material when subjected to mechanical strain or stress. When a III-N material is subjected to strain or stress, the atoms within the crystal lattice are displaced, leading to a redistribution of charges and the appearance of an electric polarization. The piezoelectric polarization in III-N materials arises from the relative displacement of the atoms, particularly the cations (e.g., Ga, Al, In) and anions (e.g., N), resulting in a separation of positive and negative charges. The magnitude and direction of the piezoelectric polarization depend on the specific crystal structure and the direction and magnitude of the applied strain or stress. The piezoelectric polarization in III-N materials has practical applications in various devices. For example, in piezoelectric sensors, the material can be mechanically deformed, resulting in a change in the electric polarization and generating an electrical signal. Inversely, the reverse piezoelectric effect generates a strain in presence of an electric field which can be exploited in actuators, but also can deteriorate electron devices. Combined with spontaneous polarization, the piezoelectric polarization in III-N materials significantly affects the performance of electronic devices such as high-electron-mobility transistors (HEMTs), by modifying the band structure and carrier transport properties.

The piezoelectric polarization is directly related to its strain/stress state and can be expressed as follows: [59]

$$P^{PZ} = \frac{2(a-a_0)}{a_0}(e_{31} - e_{33}\frac{C_{13}}{C_{33}}$$

Where $\varepsilon_{xx} = \frac{a-a_0}{a_0}$ is the biaxial strain generated due to the lattice parameter mismatch between the barrier material and channel material. The piezoelectric polarization is positive if the layer is stressed in compression and negative if it is stressed in extension.

2.2 Gallium Nitride based high electron mobility transistors (HEMTs)

2.2.1 What is a HEMT

A high electron mobility transistor (HEMT), also called MODFET (Modulation Doped Field Effect Transistor), TEGFET (Two-dimensional Electron Gas Field Effect Transistor) or HFET (Heterojunction Field Effect Transistor), is a field effect transistor. Is has been introduced for the first time in 1979 [1], [60], [61]. A typical HEMT device is characterized by two ohmic contacts called source and drain and a Schottky contact called gate (Figure 12). The operation principle of such transistor is based on the modulation of the density of the two-dimensional electron gas flowing in a semiconductor called channel between the source and the drain. This control is done via an electrostatic action of the gate (field effect) as shown in Figure 13. Thus, by applying a voltage between the gate and the source (Vgs), we can modulate the density of electrons in the channel and consequently the current Ids established between the drain and the source after application of a bias Vds.

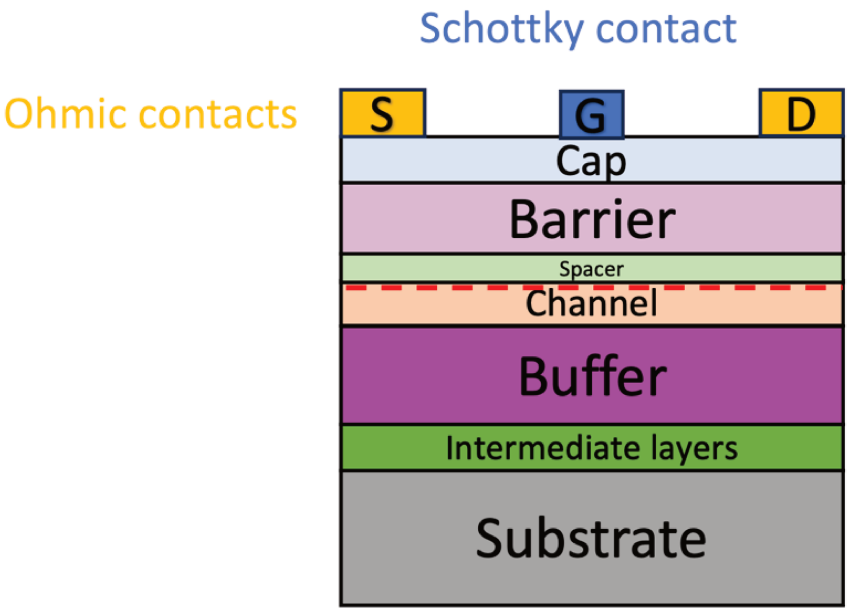

Figure 12: Schematic of a typical III-N HEMT strusture.

A HEMT structure typically consists of the stack of layers described in Figure 12. For the correct operation of the transistor, it is necessary that the buffer layer, the intermediate layers and the substrate must be insulating and also good thermal conductors in order to evacuate the heat from the component. To these conditions is added that of a good crystalline quality of the buffer layer is necessary to avoid important carrier trapping and current collapse effects.

2.2.2 Two dimensional electron gas density formation

A two-dimensional electron gas (2DEG) is formed in the channel at the interface between the barrier layer and the buffer and it is the specificity of the high electron mobility transistor. We present here the most general case of heterostructures grown with the Ga-polarity. The AlGaN/GaN heterojunction is commonly used as an illustrative model to elucidate the genesis of a Two-Dimensional Electron Gas (2DEG) within the foundational structure of a High Electron Mobility Transistor (HEMT). The emergence of this 2DEG is intricately connected to the effects of polarization and disparities in energy band alignment occurring at the AlGaN/GaN interface. This junction is the result of the stacking of two semiconductors characterized by distinct energy band properties. One of these semiconductors possesses a wider band gap, often referred to as the "barrier" region, composed of AlGaN alloy or 100% AlN and featuring a substantial band gap ranging from 3.4 to 6.2 eV. In contrast, the other region, known as the "channel," exhibits a smaller band gap, with GaN being the semiconductor in this specific context, boasting a band gap equal to 3.4 eV.

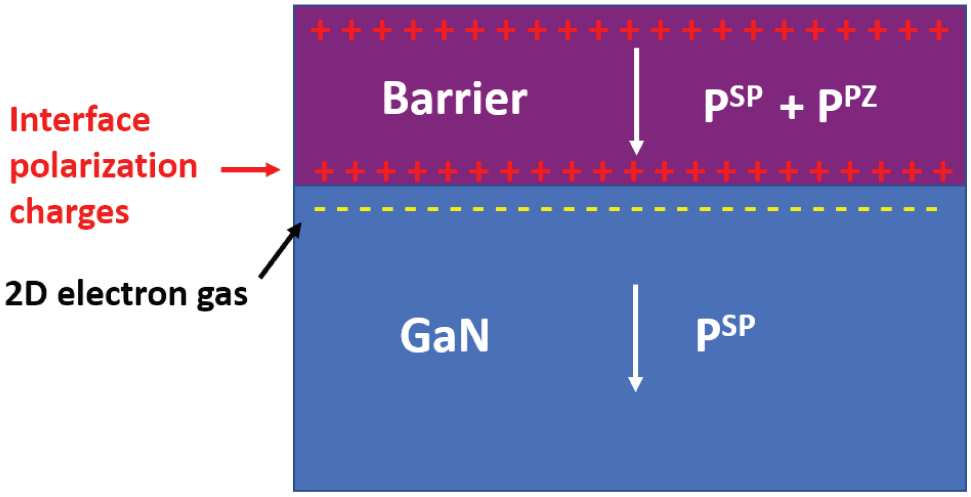

Figure 13: 2DEG formation from electrostatic point of view.

From electrostatic point of view, the two-dimensional electron gas in III element nitrides is generated by the spontaneous and piezoelectric polarization difference at the barrier/channel interface (Figure 13) which called accumulation of surface charges $\sigma_{pol}(C/m^2)$.

$$N_{pol}^{bar} = \frac{\sigma_{pol}^{bar}}{e} = \frac{\sigma_{sp}^{bar} + \sigma_{pz}^{bar}}{e}$$

$$N_{pol}^{channel} = \frac{\sigma_{pol}^{channel}}{e} = \frac{\sigma_{sp}^{bar} + \sigma_{pz}^{channel}}{e}$$

$$N_{pol} = N_{pol}^{bar} - N_{pol}^{channel}$$

Where e is the elemental electron charge. The induced electronic density refers to the discrepancy between the overall polarization of the barrier and the channel, measured per unit of surface area. The charges induced at the interface by N_{pol} attract electrons, leading to the formation of a 2DEG. The AlGaN/GaN system is used as an illustrative example to elucidate the sources of the 2D electron gas.

Temporarily disregarding the origin of the electrons, the sheet carrier concentration of the 2DEG situated

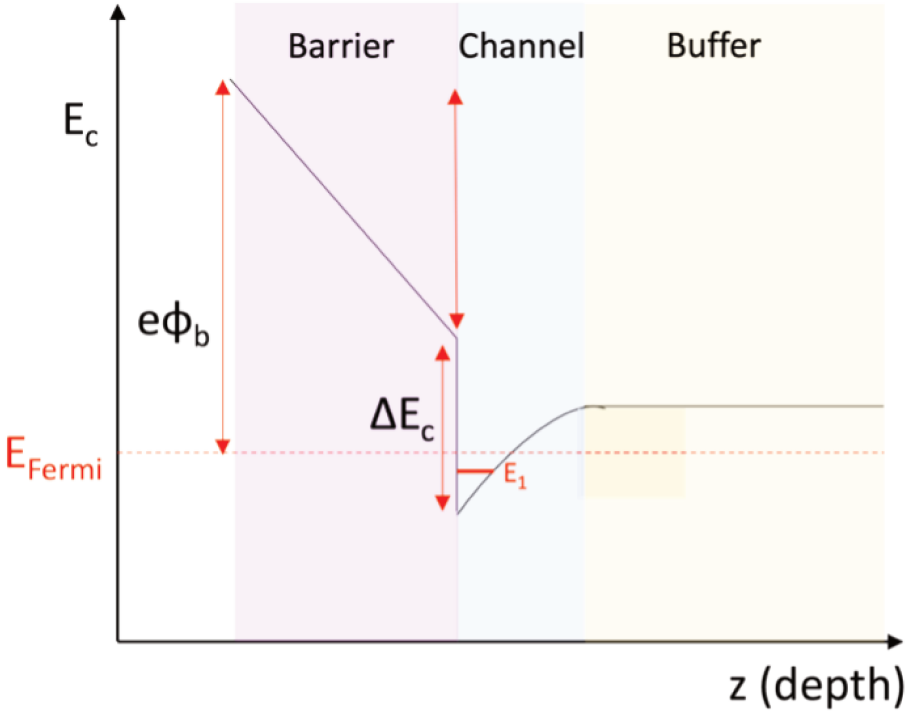

Figure 14: 2DEG band structure of HEMTs

at the AlGaN/GaN interface in the nominally undoped structures can be expressed as follows (let's assume that the 2DEG occupies only one energy level E_1 (ground state) of the triangular quantum well, which is generally 90% true):

$$N_s(x) = \frac{\sigma(x)}{e} - \frac{\varepsilon_0 \varepsilon(x)}{de^2}[e\phi_B(x) + E_F(x) - \delta E_c(x)]$$

Where $\varepsilon(x)$ is the dielectric constant, d is the AlGaN barrier width, $e\phi_B)$ is the surface barrier height, E_F is the Fermi-level position with respect to the GaN conduction-band edge, and δE_C is the conduction-band discontinuity between $Al_xGa_{1-x}N$ and GaN.

Smorchkova et al.[62][62] has demonstrated evidence for the origin of the 2DEG in nominally undoped samples. According to their findings, one possible explanation involves the presence of surface donor-like states. These states could serve as a source for both the electrons constituting the 2DEG and the positive charges that compensate for the negative polarization-induced charge at the top of the AlGaN layer. It is postulated that these donor-like surface states are positioned deep within the AlGaN bandgap and, as a result, they will be fully occupied at small values of barrier thickness d. Consequently, no 2DEG will be formed, and the electric field in the top layer will be dictated by the polarization-induced charges. [63][63] When the width of the AlGaN layer is increased, the Fermi level at the surface gradually moves downward, nearing the deep donor level (refer to the Figure 15). Once the Fermi level reaches the surface states, these states begin to transfer electrons to the 2DEG and become empty. It is important to note the position of the Fermi level in relation to the surface state in each scenario. Consequently, a 2DEG can be formed at the interface of AlGaN and GaN, leading to a reduction in the electric field within the AlGaN barrier. As the

thickness of the AlGaN layer is further increased, the density of the 2DEG tends to saturate, approaching the value of the polarization-induced charge. This assumes that the thickness of the AlGaN barrier does not reach the critical thickness at which relaxation of the mismatch strain in the ternary alloy occurs.

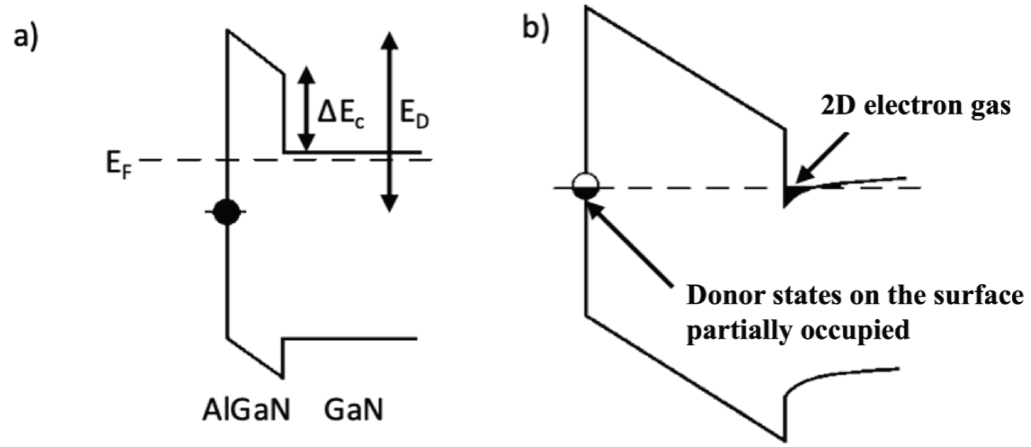

Figure 15: The band diagram illustrates the surface donor model, depicting the undoped AlGaN barrier thickness. In case "a," the barrier thickness is less than the critical thickness required for the formation of the 2DEG, while in case "b," the barrier thickness is greater than the critical thickness[63].

The density of the 2DEG is influenced not only by the thickness of the barrier but also by the composition of the alloy within the barrier. For instance, in the case of AlGaN, increasing the aluminum content in the barrier leads to a higher density of the 2DEG[64]. This is because AlN has a wider band gap and higher polarization coefficients compared to GaN, resulting in an increased density with higher aluminum content. The lattice parameter mismatch between GaN and the AlGaN barrier material causes tensile strain in the barrier layer in order to compensate for the mismatch. A tensile strain appears in AlGaN grown on GaN, causing a negative piezoelectric polarization to be induced along the c-axis for all aluminum concentrations. Consequently, this polarization accumulates with the spontaneous polarization and induces a 2DEG in the potential well formed at the interface between AlGaN and GaN. However, high aluminum concentration in AlGaN can lead to significant strain when it is grown on a GaN substrate. As the aluminum content increases, the lattice constant of AlGaN becomes smaller than that of GaN, resulting in strain. This strain can have detrimental effects on the material, including the formation of cracks on the surface or the nucleation of dislocations when the strain exceeds a critical value. These cracks can compromise the structural integrity of the device and degrade its performance. One solution to alleviate this strain is to introduce indium into the alloy, forming InAlN. InAlN has the advantage of being able to achieve lattice matching with GaN at a certain indium content, typically around 20%. This means that the lattice constant of InAlN can closely match that of GaN, reducing the strain induced during growth. By using InAlN (or InAlGaN) instead of AlGaN with high aluminum content, it is possible to mitigate the strain-related issues. Additionally, InAlN-based structures can attain elevated electron densities within the 2DEG, primarily attributable to their heightened spontaneous and piezoelectric polarization, surpassing those of typical AlGaN/GaN HEMTs. [65], [66]. In conclusion, by adjusting the thickness or the composition of the barrier we can modify the polarizations at the interface and then the induced charges at the interface and this is influencing the density of the 2DEG. The structural quality of the barrier and especially its strain state is another important

parameter influencing the 2DEG density. Furthermore, surface donor states are involved as origin of the electrons transferred from the surface to the 2DEG located at the interface between the barrier and the channel, so that other parameters like the presence of metal, oxides, or other materials at the surface like cap layers made of GaN or Silicon Nitride can also influence the number of carriers.

2.2.3 HEMT epitaxial structure

This illustration Figure 12 depicts the HEMT (High Electron Mobility Transistor) heterostructure, showcasing its distinct epitaxial layers. The subsequent section will delve into comprehensive explanations of each individual layer.

Substrate

The substrate plays a crucial role in the growth of a High Electron Mobility Transistor (HEMT) heterostructure. Some key roles of the substrate in HEMT heterostructure growth like lattice matching is very important to enable high-quality crystal growth with minimal strain and defects, leading to improved device performance, enhanced carrier mobility, reduced leakage currents, and better overall functionality. Other properties like thermal and electrical conductivity of the substrate are also critical for the operating device performance. The differences between the heteroepitaxial GaN layer and its substrate lead to the emergence of stresses, which eventually find relief by generating dislocations or at end cracks within the material. These dislocations predominantly occur as propagation of threading dislocations, meaning they extend from the substrate-epilayer interface to the surface of the epilayer. The quantity of such dislocations typically ranges from 108 to 1010 per square centimeter when GaN is epitaxially grown on a sapphire, silicon or SiC substrate. These dislocations can degrade the performance of HEMT transistors, as highlighted in reference [67]. To minimize mechanical stress, it is therefore necessary to use a substrate with a lattice parameter and a TCE as close as possible to that of GaN. Due to the significant lattice mismatch of 16% between sapphire and GaN, the incorporation of an extremely thin nucleation layer of AlN or GaN at a low temperature has been employed. This approach allows for the accommodation of the lattice mismatch by primarily confining the generation of dislocations to the bottom region of the buffer layers. However, the low thermal conductivity of sapphire poses a significant disadvantage for microwave power applications. Nevertheless, sapphire is a semi-insulating substrate and remains a relatively affordable option.

The highly resistive silicon substrate stands out as an appealing choice for GaN RF power electronics. During the growth process, the difference of lattice parameter (17%) between GaN and silicon, as well as the distinct thermal expansion coefficient (116%), lead to substrate curvature and the formation of cracks in the layers upon cooling. To address this challenge, the utilization of an AlN nucleation layer and a series of stress mitigating layers (also named lattice parameter accommodation layers) becomes necessary. These approaches help to manage stresses during both the growth and cooling phases by employing techniques such as stacking AlN/GaN layers or incorporating AlGaN layers [68], [69]. It offers significant advantages such as the availability of large wafers up to 12 inches in size, low cost, and a well-established technological framework.

Silicon carbide substrate has rapidly emerged as a highly promising option for microwave power applications. Notably, it exhibits a minimal lattice parameter mismatch of less than 4% and a relatively low difference in thermal expansion coefficient compared to GaN (25%). The outstanding thermal conductivity of silicon carbide proves to be its major advantage for power components, as it enhances heat dissipation

and mitigates current drops caused by self-heating. Additionally, the inclusion of a thin AlN nucleation layer significantly enhances GaN crystal quality due to the close lattice parameter match of AlN with SiC, which is approximately 1%. However, the main drawback of this substrate is its relatively high cost, particularly when high-resistivity substrates are required for RF applications. Today, the two most commonly used substrates in the GaN process development are sapphire (Al_2O_3) and silicon carbide (SiC), but Silicon substrate may provide lower cost solutions with acceptable performances.

Nucleation layer

The nucleation layer serves as an intermediate layer deposited on the substrate to facilitate the transition to the thicker and relaxed GaN buffer layer in most cases. The quality of this nucleation layer plays a crucial role in minimizing the density of dislocations within the HEMT structure. In the case of growth on sapphire substrates, a low-temperature GaN or AlN layer can be employed for nucleation. The nucleation layer helps to ensure a smooth and defect-free interface between the substrate and the subsequent layers, promoting the overall quality and performance of the HEMT structure. On silicon and SiC substrates, AlN is systematically used as a nucleation layer.

GaN buffer

The buffer layer in a High Electron Mobility Transistor (HEMT) is typically composed of GaN or an AlGaN alloy. This layer plays a crucial role in ensuring both good crystalline quality and electrical insulation. The crystalline quality of the buffer layer relies on the quality of the nucleation layer. To ensure reliable transistors and optimal operation, minimizing the density of dislocations, which are responsible for traps, is crucial. Once the buffer layer reaches a thickness of approximately 200 nm, it can effectively relax a significant portion of the stresses, thereby reducing the piezoelectric polarization resulting from mechanical stresses during growth. In terms of electrical insulation, acceptor dopants like iron or carbon are often employed to compensate for the residual N-type doping and enhance the resistivity of the layer. The layer above the buffer is the GaN channel, which is intentionally kept with low residual doping to improve electron mobility. The thickness of the GaN channel may vary depending on specific application requirements.

AlN interlayer

In some cases, we observe the presence of a thin layer of AlN, with a thickness on the order of 1-2 nm, between the GaN channel and the barrier in HEMT structures. This AlN exclusion or spacer layer serves the purpose of confining electrons within a two-dimensional electron gas (2D gas), thereby reducing electron penetration into the barrier region. This confinement effect is achieved because AlN has a wide band gap (approximately 6.2 eV), which increases the discontinuity of conduction bands between the barrier and the channel[70]. AlN exclusion layer helps to mitigate the effects of alloy fluctuation at the interface between the barrier and the channel[71]. This reduction in alloy fluctuation contributes to an increase in electron mobility. Moreover, the incorporation of the AlN layer increases the aluminum content within the barrier, resulting in a higher electron density within the 2DEG. Therefore, the introduction of the AlN layer in a HEMT structure serves multiple purposes: confinement of electrons within the 2DEG, reduction of electron penetration into the barrier, enhancement of electron mobility through the suppression of alloy fluctuations, and an increase in the electron density within the 2DEG.

Barrier

In a High Electron Mobility Transistor (HEMT), the barrier layer plays a crucial role in regulating the number of electrons within the device structure, forming part of the active layers. Acting as a potential barrier, the barrier layer effectively confines electrons to a specific region, enabling high electron mobility. Typically composed of a semiconductor material with a wider bandgap, such as aluminum nitride (AlN), the barrier layer establishes a potential barrier for electrons within the channel layer. This interface exhibits a discontinuity in the conduction bands due to the difference in bandgap energies. Additionally, a charge polarization discontinuity also contributes to this effect. The presence of a two-dimensional electron gas arises from the transfer of free electrons to the interface between the barrier and the GaN channel. This potential barrier layer effectively confines electrons to the channel region, preventing scattering or diffusion into neighboring layers. The primary purpose of the barrier layer in a HEMT is to enhance electron mobility by minimizing scattering and facilitating efficient electron transport. A higher barrier height results in improved confinement of electrons within the channel layer, leading to enhanced device performance. For transistor applications, the barrier has to enable an efficient control of the number of electrons flowing into the channel in the region below the gate contact. The main requirements for this purpose are the absence of electrical charge fluctuations into the barrier and a reduced leakage current through this layer. This necessitates a crystal quality as high as possible to minimize the density of electrical traps and a high energy barrier between the metal gate and the semiconductor layer.

Cap layer (SiN, GaN

A cap layer role is to protect the surface from oxidation, especially of the aluminum contained in the barrier and thus aims to protect the barrier. It is also to protect from contamination with elements like carbon which can dramatically affect surface states and are residues from the resists used for the lithography. Many studies have been carried out on different types of caps in particular GaN and SiN. The role of the GaN cap is to increase the effective height of the potential barrier thanks to the polarizations at the interface cap / barrier, and this leads to a decrease in leakage currents by tunneling effect[72]. However, the thicker this protective layer is, the higher the effective potential barrier will be, which leads to a decrease in the surface density of electrons in the potential well. It is therefore necessary to find a tradeoff between protection from oxidation of the barrier and a high electron density. In the literature, the GaN cap is very often associated with AlGaN barriers, while works that mention the use of a GaN cap on InAlN, InAlGaN or AlN barriers are rarer. At present, it is also possible to deposit another type of cap. It is a SiN cap deposited in-situ in the epitaxy reactors just after the growth of the barrier[73]. Unlike GaN, this amorphous cap does not increase the barrier height, but produces a passivation of the surface which ultimately increases the electron density in the 2DEG [74]. The surface potential decreases while using SiN as a cap layer and it may stem from the neutralization of the positive charge on the barrier surface, as suggested by Derluyn et al. [75]. Additionally, Derluyn et al. propose that the prevention of stress relaxation in AlGaN through SiNx capping could be another factor contributing to the elevated sheet carrier density.

2.2.4 Carrier mobility, sheet resistance

The high electron mobility allows for fast electron transport within the device, enabling high-frequency operation. Electron mobility refers to the ability of electrons to move through the device structure made of GaN material under the influence of an electric field. It characterizes the 2DEG. It is related to the average

relaxation time of an electron between two scattering events (diffusion) and this relaxation time is calculated according to Mathiessen's rule:

$$\frac{1}{\sigma} = \frac{1}{\sigma_1} + \frac{1}{\sigma_2} + \frac{1}{\sigma_3} + ... + \frac{1}{\sigma_n}$$

Here are a few key limitations of electron mobility in GaN HEMTs: A distinction is made between elastic scattering mechanisms (scattering by impurities, by interface roughness, by alloy disorder, by charged dislocations) and inelastic scattering mechanisms (operated by acoustic and optical phonons). Thus, the lower the mobility of one of the contributions, the greater its effect on total mobility. Furthermore, the electron density of the 2DEG often generally influences the electron mobility. Scattering by impurities: when impurities are present, they create localized energy states that scatter electrons as they traverse the material, impeding their motion and reducing their mobility. The impurity scattering arises from various interactions, such as Coulombic interactions with ionized impurities. Ionized impurities in the barrier can participate to the filling of 2DEG with electrons. Since these ionized impurities in the barrier are spatially separated from the 2DEG, this diffusion mechanism plays little part in total mobility. In addition, residual impurities in the GaN buffer layer, with densities of the order of 1014 to 1016 cm-3, affect total mobility only at low density ($N_s \sim 1 - 5 \times 10^{12} cm^{-2}$). This limiting factor is partially masked by the charge density of the free electrons, which explains an increase in mobility with charge density. Scattering through interface roughness: when electrons move close to rough interfaces, they experience scattering due to the abrupt changes in potential energy. This scattering disrupts the smooth flow of electrons, leading to a reduction in their mobility. The interface roughness scattering can increase the effective scattering cross-section, decrease electron mean free paths, and limit the overall electron transport properties in GaN-based HEMTs. Indeed, the higher the Ns, the deeper the triangular quantum well and the closer 2DEG electrons are pushed towards the barrier/channel interface. As a result, electrons in the 2DEG are more sensitive to interface defects, and mobility decreases. High charge densities, makes the contribution of interface roughness more important. Scattering through alloy disorder: alloy disorder occurs when different elements are mixed or alloyed within the material, leading to compositional variations and local fluctuations in the crystal structure. These fluctuations create localized energy states and potential fluctuations, which scatter electrons as they traverse the material. This disturbs the periodicity of the potential to which the electron gas is subjected, since some of the electrons in the 2DEG penetrate the barrier. The interaction of alloy disorder will be limited by the insertion of an AlN spacer layer at the interface between the barrier and the buffer for exemple in AlGaN/GaN HEMT. The depth of electron penetration into the barrier is reduced from 6Å to around 3 Å, and the confinement of 2DEG electrons is increased. Another possibility is to deposit, for example, an AlGaN barrier in the form of an n×(AlN/GaN) superlattice.

Scattering through dislocations: dislocations are one dimensional crystal lattice defects that appear when there are irregularities or disruptions in the arrangement of atoms. When electrons encounter dislocations, they experience scattering due to the strain fields and broken bonds associated with the dislocation lines. Threading dislocations are the first factor limiting mobility at low charge densities. Crossing dislocations, which can initially be assimilated to acceptor-type defects, will capture electrons from the conduction band. They form negatively charged lines, perpendicular to electron transport in the 2DEG plane. A zone of space charge is formed around the threading dislocations, inducing the diffusion of electrons moving across these lines. Scattering through phonons: Phonons are vibrational modes with corresponding quanta

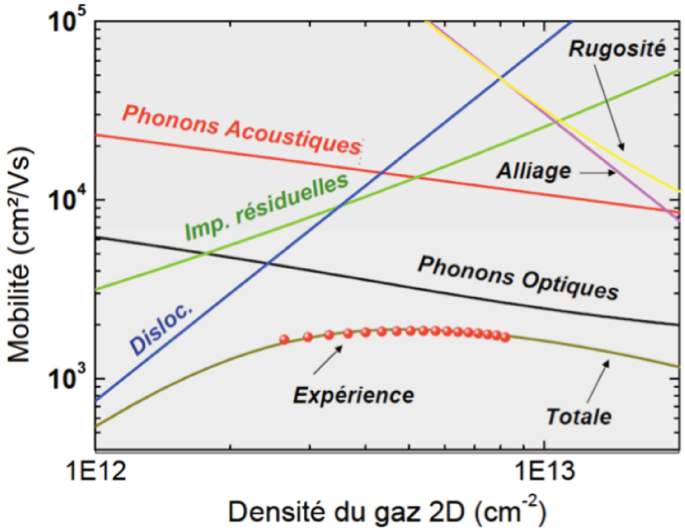

Figure 16: Experimental and simulated evolution of electron mobility at room temperature (300K) as a function of gate-modulated electron density Ns for an AlGaN/GaN HEMT-type heterostructure produced on a Silicon(111) substrate [71]

of energy associated with lattice vibrations in a crystalline material. These phonons are generated by the thermal energy available in the crystal lattice. When electrons interact with phonons, they undergo scattering as a result of momentum and energy exchanges between the electrons and the vibrating lattice. The scattering occurs due to the coupling between the electronic states and the lattice vibrations. At lower temperatures (below 200K), acoustic phonons predominantly contribute to inelastic electron scattering. As the temperature increases, optical phonons become increasingly responsible for limiting electron mobility.

Figure 16 illustrates the result of calculations fitting the experimental data obtained for an AlGaN/HEMT heterostructure grown on Silicon substrate. More details of calculation of the electron mobility are given in [49]. Finally, the last criterion for evaluating 2DEG is the sheet resistance R_{sh}, expressed in Ohm per square (Ω/sq). This value corresponds to the resistance of the electron gas and is a function of the electron density and electron mobility.

$$R_{sh} = \frac{1}{eN_s\mu}$$

The lowest possible sheet resistance is essential for an efficient transistor operation.

3 Theoretical predictions on ScAlN alloy

3.1 Crystal structure

ScAlN is known to exhibit different crystal structures, including hexagonal and rocksalt structures. The transition from the hexagonal to the rocksalt structure in ScAlN is composition dependent. ScAlN has a hexagonal crystal lattice with alternating layers of scandium, aluminum, and nitrogen atoms. The hexagonal structure is more stable for ScAlN with a lower scandium content. For certain compositions and growth conditions, ScAlN can adopt a rock salt structure[14], [76]–[79]. The exact composition range where the rock salt structure becomes favored can vary depending on experimental conditions and growth techniques. As it was reported by Moram [78], theoretical predictions showed that hexagonal phase should be maintained with Sc molar fraction up to 57%, before a transition to rock salt phase for higher Sc content.
Tasnádi et al. [80] reported with theoretical calculations on ScAlN wurtzite alloys that the N atoms are tetrahedrally bonded. While the fivefold (hexahedrally) coordinated hexagonal phase at x=0.5 correspond to an insignificant piezoelectric response making wurtzite phase more interesting for their high piezoelectric response. Figure 17 shows that the hexagonal phase of $Sc_{0.5}Al_{0.5}N$ appears at a saddle energy with a c/a ratio close to 1.27 rather than in a minimum energy like wurtzite ScAlN where $c/a = 1.47$. The preference of Sc atoms to bond hexahedrally to nitrogen results in a strong response to strain. This explains that hexagonal ScAlN is dynamically unstable and probably could not be proven experimentally.

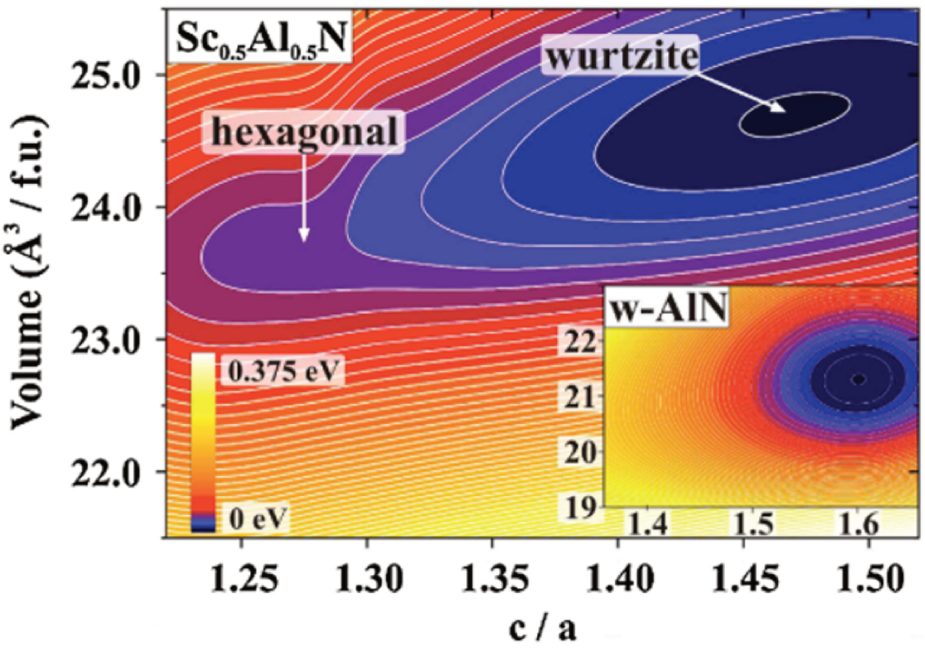

Figure 17: Energy landscape of wurtzite $Sc_{0.5}Al_{0.5}N$ as a function of c/a and volume with both wurtzite and hexagonal phase, with the inset showing the energy surface of wurtzite AlN reported by [80].

Ambacher et al. observed theoretically [77] that the structural arrangement of wurtzite $Sc_xAl_{1x}N$ gradually diverges from a perfect hexagonal crystal lattice, resembling the deformation typically seen in crystals subjected to virtual biaxial tensile strain along the basal plane. This departure from the ideal tetrahedral bonding configuration coincides with a nearly linear increase in average bond lengths and the lattice pa-

rameter a(x). Additionally, there is a non-linear alteration in bond angles and in the lattice parameter c(x) [78]. [81]–[83] experimental studies provided evidence indicating the existence of the cubic phase in ScAlN when the ScN concentration exceeded 46%. Additionally, the wurtzite phase remained stable up to a ScN concentration of 41%. Interestingly, a coexistence of both cubic and wurtzite phases was observed within the ScN concentration range of 42% to 45%. Depending on the growth conditions and growth techniques, experimental findings have indicated that cubic phases can manifest at concentrations lower than the predicted ones at 42%. [19]

3.1.1 ScAlN lattice parameters

This section provides a detailed account of the lattice parameters of the ScAlN wurtzite crystalline phase alloy. When grown by epitaxy on a foreign substrate or on another III-Nitride film, the presence of in-plane lattice mismatches gives rise to interfacial strain, ultimately leading to the formation of misfit dislocations at heterointerfaces. These dislocations have detrimental effects on the efficiency, reliability, and lifetimes for optoelectronic devices such as LEDs and lasers, as well as electronic devices like diodes or transistors. To address this issue, it is possible to reduce dislocation densities by employing nanopatterned substrates and interlayers [84], [85]. Similarly, in HEMTs, it is essential to eliminate strains in heterostructures to enhance reliability. In this thesis, we propose to reach these objectives by incorporating an additional group of wurtzite-lattice III-nitride materials based on Sc. Unlike conventional alloys such as AlGaN, $Sc_xAl_{1-x}N$ can be grown lattice matched on GaN substrates. Numerous models have been reported for the modeling of lattice parameters in ScAlN alloy, conducted by different research groups. Most of these studies focus on scandium content below 0.5 and have achieved a significant number of modelizations by density functional theory (DFT) for non-strained ScAlN. In 2013, Zhang et al. made the initial effort to determine the lattice parameters of $Sc_xAl_{1-x}N$ for in-plane lattice parameter [25]. The calculations were studied for scandium molar fraction up to 0.375.

$$a(x)[\mathring{A}] = 0.126x^2 + 0.426x + 3.1112$$

Urban et al. [76] published a study in 2021 that investigated the in-plane and out-of-plane properties of ScxAl1-xN. Notably, their research incorporated scandium molar fraction up to 0.50 into their analysis.

$$a(x)[\mathring{A}] = -0.241x^2 + 0.394x + 3.131$$

$$c(x)[\mathring{A}] = -1.120x^2 + 0.366x + 5.020$$

In the calculations performed by Ambacher et al. [65], [77] the inclusion of scandium molar fraction up to 0.50 was taken into consideration.

$$a(x)[\mathring{A}] = 0.241x^2 + 0.389x + 3.110$$

$$c(x)[\mathring{A}] = -1.114x^2 + 0.365x + 4.994$$

The relationship between the lattice parameters and increasing Sc content exhibits significant anisotropy, as observed in experimental findings [86]. The in-plane lattice parameter demonstrates a nearly linear

increase with Sc content in accordance with Vegard's rule (see Figure 18), where a_{AlN} and a_{ScN} denote the equilibrium lattice parameters of wurtzite AlN and hexagonal ScN, respectively. In contrast, the out-of-plane lattice parameter experiences minor variations and remains relatively constant across a broad range of Sc molar fraction (x up to 20%). This behavior differs significantly from other mixed wurtzite nitrides such as AlGaN and InAlN. By adjusting the $Sc_xAl_{1-x}N$ composition, it can be lattice matched to GaN when x in close to 0.2. This characteristic makes it a promising strain-free barrier material for HEMTs, espacially because it offers at the same time a higher sheet charge density compared to InAlN [66],[87].

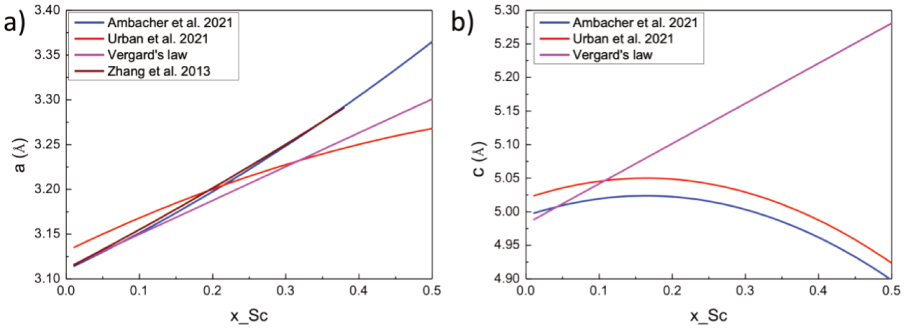

Figure 18: Simulated lattice parameter, a) a(x) (on the left) and, b) c(x) (on the right) vs alloy composition of $Sc_xAl_{1-x}N$.

The Figure 18 shows that ScAlN possesses the same in-plane lattice parameter as GaN when x is approximately 0.18 ($a_{GaN} = 3.189\text{Å}$), as indicated by the theoretical predictions in the equations provided before. The strain within the ScAlN layer fluctuates depending on the amount of scandium present, as depicted in the accompanying Figure 19:

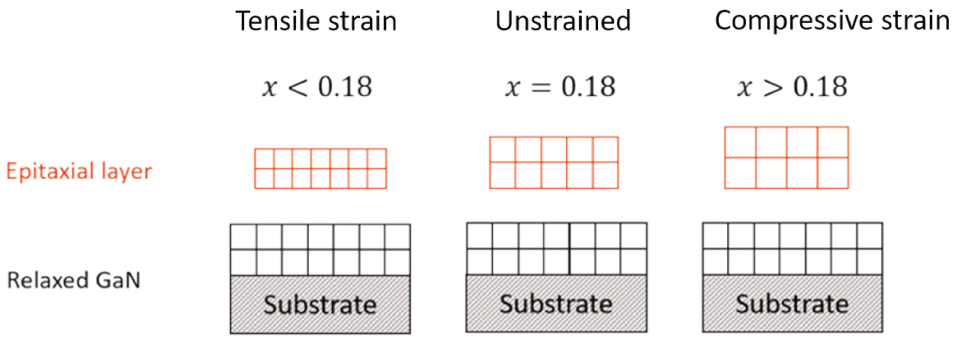

Figure 19: $Sc_xAl_{1-x}N$ epitaxy on GaN for $x < 0.18$, $x = 0.18$ and $x > 0.18$.

Moreover, the ability to grow a strain-free ScAlN on GaN leads to an infinite critical thickness, as depicted in Figure 20. This critical thickness represents the maximum thickness achievable for the epitaxial crystal before any relaxation takes place.

3.1.2 ScAlN band gap

As a result of progress in band gap engineering for optoelectronics and microelectronics, a significant amount of research has been dedicated to III-N compounds. Initially, Deng et al. [56] conducted experiments to determine the band gap energy of ScAlN using optical absorption techniques. They deposited

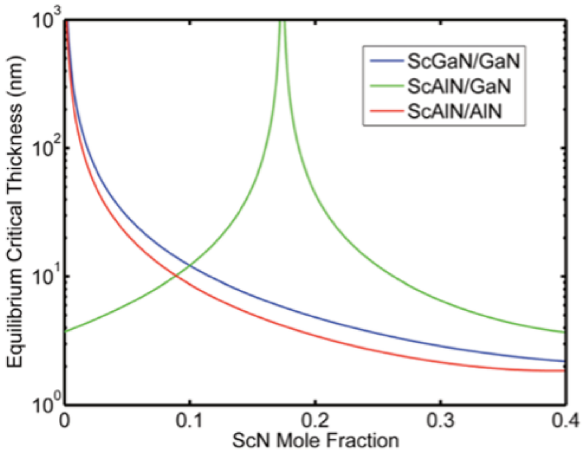

Figure 20: Critical thickness for strain relaxation of ScAlN/GaN, ScGaN/GaN and ScAlN/AlN as a function of ScN mole fraction adapted from[78].

ScAlN layers onto sapphire 0001 substrates using reactive magnetron co-sputtering. The study investigated the band gap evolution in electron volts (eV) with varying scandium molar fraction, up to 20% in ScAlN.[88]

$$E_g(x) = 6.12 - 9.32x$$

Deng et al. pointed out that for values of x less than 0.20, the band gap of ScAlN exhibits a nearly linear decrease as x increases. Specifically, when x changes from 0.20 to 0.34, the band gap drops from 4.37 eV to 2.94 eV. This drop in band gap could potentially indicate a structural transition. Additionally, it may be attributed to the absorption of segregated ScN, which reduces the apparent band gap of ScAlN. This phenomenon bears resemblance to previous findings in ScGaN, where a similar decrease in band gap was observed for x values ranging from 0.30 to 0.50 [89]. In a theoretical investigation of the ScAlN alloy [78], researchers found a decrease in the band gap as the scandium content increased. It is predicted that the band gaps of ScAlN will remain direct up to approximately 25% Sc fraction [14]. The shift in band gap arises not only from structural variations but also from strains. Moram et al. reported in their publication that compressive in-plane strains are expected to influence the magnitude of the band gap for lower Sc fraction. Furthermore, the presence of nitrogen vacancies and/or impurities may affect the measured band gap, resulting in a Moss-Burnstein shift.

In another experimental investigation[90], ScAlN samples were grown using plasma-assisted molecular beam epitaxy, with scandium fraction reaching values as high as 0.34. The researchers conducted optical absorption studies on these samples to determine their band gap. Notably, they observed a linear relationship between the band gap reduction with scandium incorporation.

$$E_g(x) = 6.1 - 3.39x$$

The optical bandgap of the wurtzite phase $Sc_xAl_{1-x}N$, where x represents the scandium fraction, aligns closely with theoretical predictions [78], [91]. Wang et al. reported also that $Sc_xAl_{1-x}N$ band gap close to 4.90 ev for x=0.33. However, in sputtered $Sc_xAl_{1-x}N$ layers, the observed bandgap is underestimated. This discrepancy can be attributed to the inferior quality of the material and the presence of a high density of defects. Notably, the formation of segregated ScN was observed as the Sc molar fraction exceeded 0.2,

further contributing to the reduced accuracy of the measured bandgap.

In summary, a 2DEG emerges at the interface between the barrier and buffer layers, primarily stemming from the discontinuity in the band gap. Specifically, GaN exhibits a lower band gap (3.4 eV) than the barrier layer, as evident from the equation provided for the ScAlN band gap. Notably, ScAlN possesses a wider band gap than GaN, especially when the scandium content is relatively low. Then a high incorporation of scandium in the alloy is reducing the barrier band gap which is not interesting for HEMTs, but as shown below, the main properties affecting the formation of a 2DEG at ScAlN/GaN interface are related to polarization.

3.1.3 ScAlN spontaneous polarization

The effectiveness of High Electron Mobility Transistors (HEMTs) in generating a high two-dimensional electron gas (2DEG) is influenced by polarizations. However, the performance of AlN and similar materials in energy harvesting applications is constrained by their piezoelectric coefficients. Consequently, there is a growing interest in exploring other tetrahedrally-bonded nitride materials that could provide additional opportunities for adjusting the piezoelectric coefficients. Such materials could potentially expand the range of lattice and polarization matching possibilities in device heterostructures. ScAlN is an emerging material in semiconductors because of its high polarization properties. Many studies have been done by modeling ScAlN with density functional theory (DFT) in order to simulate the spontaneous and piezoelectric polarizations. At first, M Caro in 2015 started to model ScAlN for alloy compositional range between 0% and 50% of scandium by ab initio methods, known as the modern or Berry-phase theory of polarization using large periodic supercells. In this study, the representation of realistic ScAlN alloys was carried out using periodic supercells containing 128 atoms, 64 cations (Sc or Al) and 64 N atoms, in a construction of 4×4×2 wurtzite primitive unit cells (each containing 4 atoms). The spontaneous polarization as a function of scandium molar fraction x reported [65], [79] up to now is in the following:

$$P_{SP} = -0.089(1-x) - 0.874x + 0.741x(1-x)$$

In the case of lattice-matched ScAlN on GaN, only spontaneous polarization is observed, with no strain-induced piezoelectric polarization occurring. The rise in Sc content leads to an increase in the average ionicity of bonds [78], as Sc–N bonds in ScN exhibit greater ionic character compared to Ga–N and Al–N bonds in GaN and AlN. This heightened ionicity, along with increased structural deformation, contributes significantly to the substantial expansion of spontaneous polarization values.

3.1.4 ScAlN piezoelectric properties

The remarkable improvement in the piezoelectric response of ScAlN, in comparison to bulk AlN, as the Sc fraction increases, has attracted significant interest for its potential application in piezoelectric and electronic devices. Since the initial experimental observation of this enhanced piezoelectric behavior by Akiyama et al. [15] in 2009, numerous experimental and theoretical investigations have consistently verified this finding [15], [80], [92].

The piezoelectric modulus d_{33} is a material property that quantifies how much electric charge is generated when a mechanical force is applied along the same axis as a material's polarization. It measures the response of a material to mechanical pressure. Materials with higher absolute values of d_{33} are more

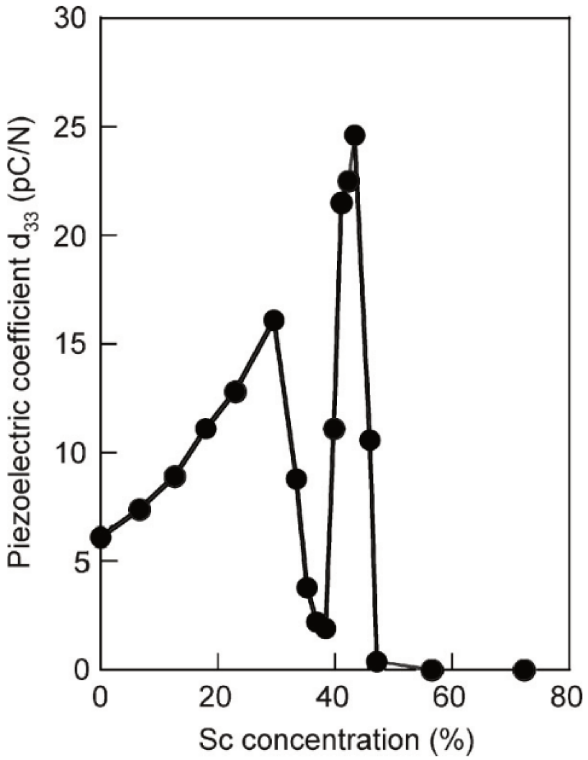

Figure 21: Piezoelectric modulus of ScAlN alloys as a function of Sc content.[15]

effective at converting mechanical energy into electrical energy and are commonly used in sensors, transducers, and other applications where accurate signal or efficient energy conversion is required. In Figure 21, piezoelectric modulus of ScAlN is presented as a function of scandium concentration. As the Sc fraction in the material is increased from 0% to 43%, the d33 value exhibits a gradual increase, d_{33} is the highest piezoelectric response among the tetrahedrally bonded semiconductors. A significant decrease in the d_{33} value becomes evident when the scandium content falls within the range of 30% to 40%. This reduction may be attributed to a misalignment of crystal orientation compared to the orientation along the c-axis. This observation has been corroborated by examining XRD rocking curves, which reveal an exceptionally broad Full Width at Half Maximum (FWHM) for scandium content within the 30% to 40% range. However, it is important to note that piezoelectric materials with higher Curie temperatures tend to exhibit lower piezoelectric coefficients (The Curie temperature represents the highest temperature at which there is no alteration in polarization properties), which could be a limitation in certain applications. Specifically, materials with higher maximum use temperatures tend to have lower piezoelectric coefficients d33. AlN is typically a high temperature piezoelectric material with the maximum operation temperature 1150℃ and $d_{33} = 5.5$ pC/N[93]. Akiyama et al. showed that ScAlN has a good balance between Curie temperature and piezoelectric response which is 400℃ and 27.6 pC/N respectively. Zinc oxide (ZnO), used in cell phones as a filter material, used to has the strongest piezoelectric response of 12.4 pC/N. At the 43% Sc molar fraction, the material reaches its peak d33 (27.6 pC/N) value, which is the highest ever reported among nitride semiconductors, which is almost 500% larger than in AlN [94]. By defining both elastic and piezoelectric coefficients, the piezoelectric polarization in ScAlN can be deduced.

ScAlN elastic coefficients are reported in GPa as follow by:

Caro [79]

$$C_{13}(x) = -78.9x^2 + 104.3x + 110.1$$

$$C_{33}(x) = 101.4x^2 - 510.2x + 385$$

Urban et al. [76]

$$C_{13} = -48.2x^2 + 79.54x + 100.3$$

$$C_{33}(x) = -86.51x^2 - 407.97x + 351.7$$

Ambacher et al.[77]

$$C_{13}(x) = -51.95x^2 + 85.65x + 108$$

$$C_{33}(x) = -95.49x^2 - 432.68x + 373$$

Zhang et al.[14]

$$C_{13}(x) = 62.072x + 108.197$$

$$C_{33}(x) = -459.210x + 364.648$$

Also piezoelectric coefficients in C/m^2 :
Caro et al. [79]

$$e_{31}(x) = -0.63(1-x) - 0.492x - 0.615x(1-x)$$

$$e_{33}(x) = 1.46(1-x) + 8.193x - 5.912x(1-x)$$

Ambacher et al.[77] and Urban et al. [76]

$$e_{31}(x) = -1.353x - 0.593(1-x) + 0.576x(1-x)$$

$$e_{33}(x) = 9.125x + 1.471(1-x) - 6.625x(1-x)$$

ScAlN provides a notable benefit in the form of a heightened piezoelectric reaction, thus amplifying the enthusiasm surrounding its application in piezoelectric devices[95]–[98]. The initial discovery of this characteristic was made by Tasnàdi et al. [99] and Tholander et al. [100], who conducted calculations specifically examining the piezoelectric properties of ScAlN along the c-axis. As depicted earlier in Figure 22, separate research groups conducted calculations that demonstrated an increase in the e_{33} value with the incorporation of Sc, attributed to internal lattice strain, while observing a decrease in C_{33}. In the following Figure 23, shows the calculated piezoelectric polarization which is derived using the formula presented in chapter 2 section Spontaneous and piezoelectric polarization, spontaneous polarization, and total polarization of epitaxial (0001) $Sc_xAl_{1-x}N$ grown on GaN (theoretical in plane lattice parameter of fully relaxed GaN value is taken into account $a_{GaN} = 3.189\text{Å}$). Piezoelectric polarization is equal to zero for x=0.18 where no strain is present in the $Sc_xAl_{1-x}N$ films on GaN. P_{PE} is negative for $x < 0.18$ where $Sc_xAl_{1-x}N$ films are tensile strain

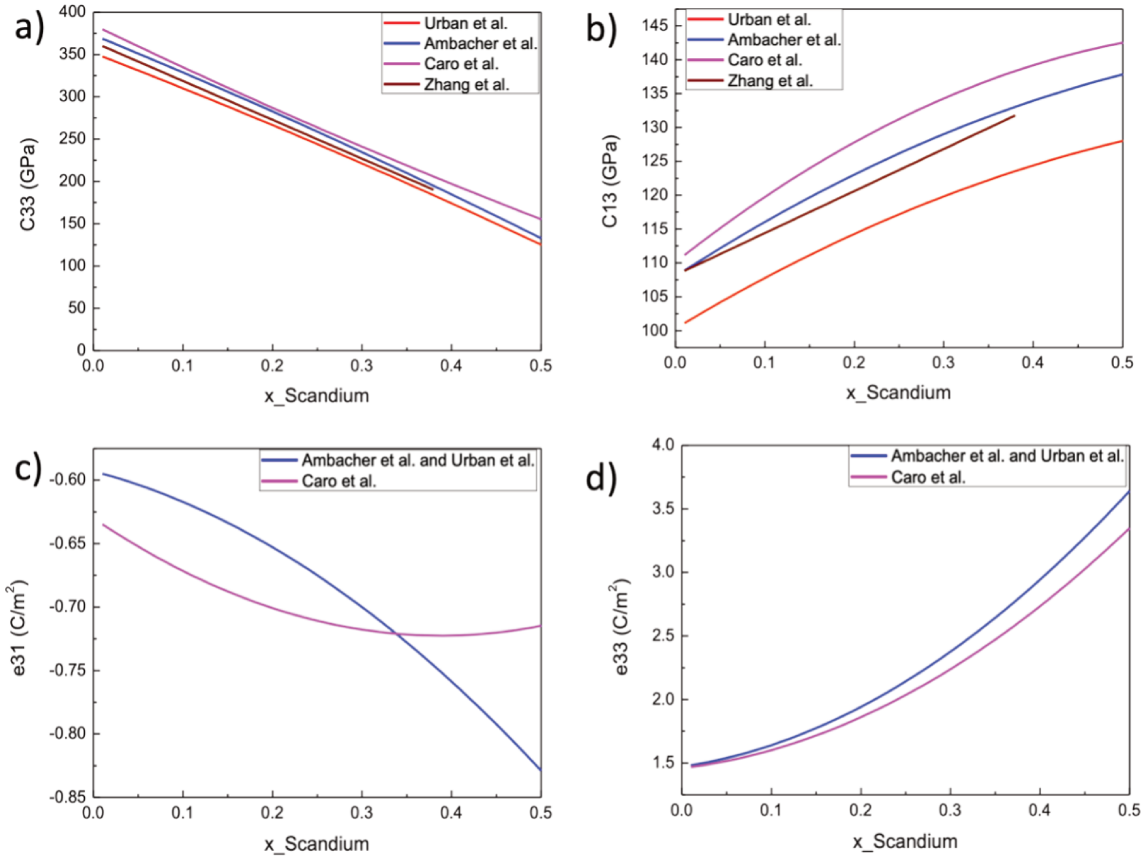

Figure 22: a) C_{13}, b) C_{33}, c) e_{31} and, d) e_{33} of ScAlN in literature.

on GaN, whereas they become compressive strain for $x > 0.18$. As a result, the spontaneous polarization in the $Sc_xAl_{1-x}N$ alloy is decreasing with x and the total polarization is crossing the spontaneous polarization ($P_{tot} = P_{SP}$) when $x = 0.18$, as no strain is present for this Sc molar fraction.

By incorporating the polarizations and coefficients of ScAlN as reported by Ambacher et al. [65], [77], and the spontaneous polarization (P_{SP}) of GaN indicated in table 4 ($P_{SP} = -0.029 C/m^2$), we can infer the polarization charge density present at the interface between both materials using the formula presented in chapter 2 section 2.b “2DEG formation”. In Figure 23b, we observe that the total polarization charge at the interface decreases with x and reaches a minimum for x approximately equal to 0.40.

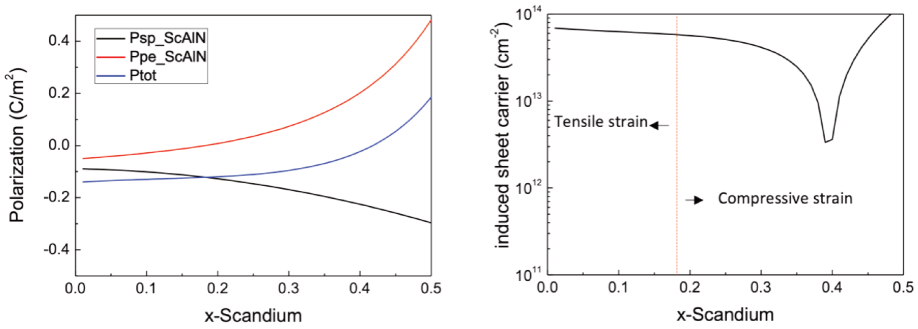

Figure 23: a) Spontaneous and piezoelectric polarization for ScAlN with quadratic equations from [65], [77], and b) The induced interface charge with the polarizatons provided from a).

Consequently, when ScAlN experiences tensile strain on GaN, it leads to an increase in the induced sheet carrier. Conversely, when ScAlN is subjected to compressive strain, it results in a reduction in the induced sheet carrier. Notably, the induced sheet carrier exhibits a sharp decline, particularly once the scandium content surpasses 30%.

3.1.5 Conclusion

In this chapter, we have explored the main structural characteristics of the ScAlN alloys. These materials exhibit spontaneous and piezoelectric polarizations, which play a crucial role in heterostructures. By attracting surface electrons, they can increase the density of a two-dimensional electron gas (2DEG) without the need for doping. Therefore, it is essential to use a wurtzite-type barrier with high spontaneous and piezoelectric polarization to maximize the density of the 2DEG.

4 ScAlN: State of art

Scandium Aluminum Nitride is a promising material in the field of advanced electronics and has garnered considerable attention due to its exceptional properties. In this chapter, we will explore the diverse applications that have emerged from this material, and we will delve into the various growth methods employed in the fabrication of this alloy.

4.1 ScAlN applications

4.1.1 Piezoelectric devices (Radio frequency (RF) filters, Surface acoustic wave (SAW), Bulk acoustic wave (BAW) resonators, . . .)

Piezoelectric devices are electronic components that leverage the piezoelectric effect to transform mechanical energy into electrical signals, or conversely, electrical energy into mechanical motion. The piezoelectric effect is a phenomenon exhibited by specific materials. Due to their capability to interchange between mechanical and electrical energy, piezoelectric devices find utility across a diverse array of fields. Several prevalent instances of piezoelectric devices encompass sensors, transducers, generators (also referred to as energy harvesters), and the utilization of piezoelectric materials in memory-related applications. Wurtzite $Sc_{0.43}Al_{0.57}N$ has shown a piezoelectric modulus d_{33} that is five times greater than the one of AlN [1]. These remarkable properties make $Sc_xAl_{1-x}N$ highly suitable for utilization in resonators for wide-bandwidth, high-frequency RF filters[2], [3],energy harvesting,[4] and lead-free high-temperature piezoelectric applications. In addition several groups verified drastic enhancement of the electromechanical coupling [5]–[8]. The growing attraction towards ScAlN is attributed to its notable piezoelectric characteristics. The piezoelectric response of ScAlN can manifest in either the wurtzite phase or the rock salt cubic phase, contingent on the amount of scandium present. However, as the scandium content increases further, the material becomes susceptible to challenges like phase separation, the introduction of cubic structures with defects at the boundary between domains with different phase, and elemental segregation, stemming from its inherent metastable nature.[9], [10].

One challenge associated with Surface Acoustic Wave (SAW) technology when used in filters is its susceptibility to environmental conditions. Specifically, SAW filters can exhibit considerable sensitivity to factors like temperature. Interestingly, certain applications consider this sensitivity advantageous. This is because the alterations in the signal resulting from changes in environmental conditions are non-random, allowing for the measurement of these variations. Consequently, over the past three decades, SAW devices have been developed for use as sensors in applications such as temperature, pressure, chemical species concentrations, and more. The fundamental operating principle of SAW devices positions them as passive components, offering the potential for wireless functionality without the need for built-in electronics or a power source. SAW devices consist of piezoelectric materials, either in the form of substrates or thin films, onto which Interdigital Transducers (IDTs) are affixed. These IDTs are applied as thin metal layers, typically with a thickness of approximately one hundred nanometers. When radiofrequency electromagnetic waves are directed at these IDTs, it results in a potential difference emerging between adjacent fingers. This voltage is then detected by the piezoelectric material, leading to the generation of a surface wave. Additionally, if a wave propagates through a piezoelectric material to reach the IDT, it experiences the polarization of the material, creating a potential difference between the fingers and consequently transmitting a signal. A reflective delayed-line SAW (Surface Acoustic Wave) device necessitates that the energy ob-

tained from both electrical-to-mechanical and mechanical-to-electrical transformations is ample to ensure signal detectability. The proportion of energy recuperated through this dual conversion process is quantified using the electromechanical coupling coefficient K^2 (in It is necessary to have a strong enough K^2 for the signal amplitude to remain sufficiently large and thus allow detection after the passage of waves. In the context of wireless measurements, the choice of a material with a strong K^2 becomes necessary. ScAlN has proven highly effective in these applications, [101] and [102] obtained a $K^2 = 3.9\%$ and $K^2 = 1.7\%$ on silicon and sapphire substrate respectively. It also reached K^2 value of 4.8% demonstrated in [103] on SiC substrate. This is primarily attributed to the exceptional shear bulk wave velocity (3920 m/s) when growing ScAlN on substrates such as 4H-SiC or diamond, enabling efficient confinement of SAW energy within the ScAlN layer. For SAW resonators fabricated with AlN, the electromechanical coupling coefficient achieves lower values than ScAlN of $K^2 = 0.12\%$ [104], 0.23 [105]. SAW resonators, based on single crystalline ScAlN layers produced through the molecular beam epitaxy (MBE) technique on silicon substrates, have demonstrated significant promise for high-frequency applications when contrasted with SAW resonators incorporating polycrystalline layers deposited through sputtering. The SAW resonators in this study [106] exhibited robust responses, featuring a high electromechanical coupling coefficient K^2 reaching an impressive 7.8% at center frequencies ranging from 3.6 to 4.0 GHz. Bulk Acoustic Wave (BAW) Filters are cost-effective, space-efficient radio frequency filters suitable for diverse applications, with a frequency range extending up to 6 GHz. SAW Filters function employs IDTs to transform electrical energy into mechanical acoustic waves, which propagate across the surface of the piezoelectric material while BAW filters enable the vertical propagation of these acoustic waves. Also ScAlN has shown interest in BAW compared to conventional AlN, [107]–[110] shows K^2 values 9.1% and even up to 19% as reported by [111]. While for AlN BAW K^2 reached 0.23% [112].

4.1.2 Ferroelectric application (memories, display, pyroelectric detection, high power transistors)

The large spontaneous polarization of ScAlN along the c lattice axis induces a ferroelectric behavior: the orientation of polarization can be altered from one stable direction to the opposite under an applied electric field. The ability to reverse spontaneous polarization in ferroelectric materials has paved the way for the development of versatile devices like FeRAM (Ferroelectric Random Access Memory) and FeFET (Ferroelectric Field Effect Transistor), which offer nonvolatile data storage solutions. Nonvolatile data storage refers to memory or storage that retains its data even without power. It differs from volatile storage, which loses its content when the power is off. Nonvolatile storage is ideal for long-term storage needs. Initially, ferroelectric perovskites like zirconate titanate (PZT) faced numerous challenges, including the requirement for buffer layers and isolated production lines due to diffusible components. Thinning the samples using certain techniques also posed scaling problems leading to the loss of ferroelectric properties. However, a significant breakthrough came with the introduction of ferroelectric hafnium oxide (HfO_2), which addressed these issues. HfO_2 could be fabricated at low temperatures while maintaining reproducible polarization down to a thickness of 3 nm. Nonetheless, it did have relatively low polarization values ($10 - 40\mu C/cm^2$). Having high polarization is crucial for achieving a maximal change in spontaneous polarization during ferroelectric switching when utilizing these materials in transistors gates. It also plays a vital role in splitting between two ferroelectric states, resulting in a high on/off current ratio in FeFETs and normally off HEMT structures. Additionally, FeRAMs benefit from higher bit density with increased polarization. Besides its high spontaneous polarization, increasing the scandium amount in ScAlN leads to a decrease in the c/a ratio[23]. This change in composition alters the coordination environment of cations from four-coordinate tetrahedrons to

five-coordinate bipyramids, resulting in a metastable layered hexagonal structure. This structural feature is beneficial for achieving a high piezoelectric constant because it creates a flat energy landscape, facilitating the movement of cations. The flat energy landscape also allows for polarization switching due to the reduced electric field required to reverse the polarization direction, keeping the coercive field (Ec) below the dielectric breakdown limit. The possibility of polarization switching in the wurtzite-type structure of ScAlN has been predicted through density functional theory calculations [24], [25]. A change in spontaneous polarization affects the internal electric dipoles of a ferroelectric material. Consequently, varying the Sc content in ScAlN can influence the ferroelectric properties of the material.

Fichtner et al.[26] first demonstrated the ferroelectric property of ScAlN experimentally, using reactive sputter deposition. Yassine et al.[27] also reported interesting results on ferroelectric ScAlN using the same growth technique. Subsequently, Yasuoka et al. and Wang et al. [28], [29] reported on the ferroelectric properties of ScAlN grown by PAMBE. Furthermore, the deposition of ScAlN on top of AlGaN barrier HEMTs has been achieved recently by sputtering method [18] and by PAMBE as well [19] with the demonstration of the modulation of the threshold voltage of the transistors by polarization effects.

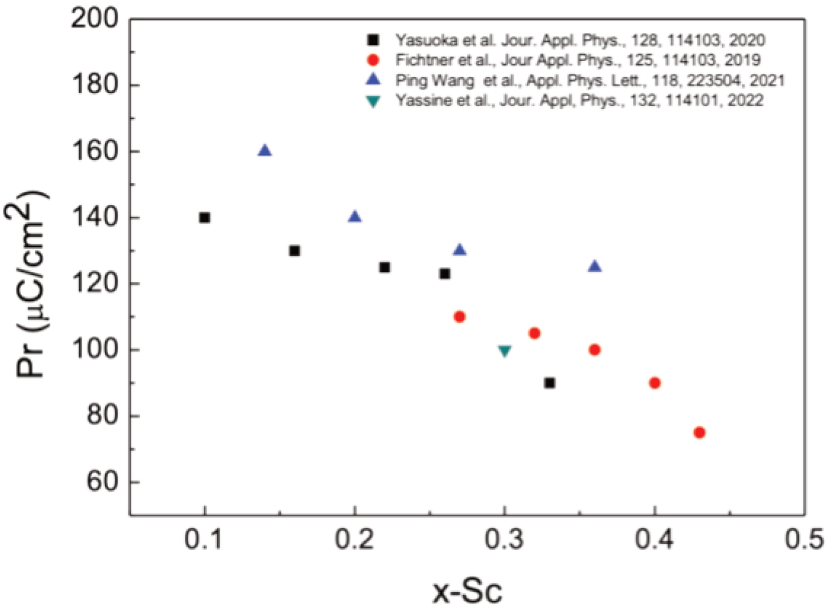

Figure 24: The figure caption illustrates the remanent polarization values reported in literature plotted against the scandium molar fraction, reaching up to 50%.

ScAlN exhibits a substantial remanent polarization ranging from 80 to 10 $\mu C/cm^2$. The tunable coercive electric field falls between 2 and 7 MV/cm, and it possesses a wide bandgap ranging from 2.9 to 5.2 eV (x=0.45 to x=0.10 respectively), all of which enhance its potential for various applications. Additionally, its high-temperature phase stability, allowing operation at up to 1100 ℃, makes it a promising candidate for advanced electronic devices, even under extreme environmental conditions.

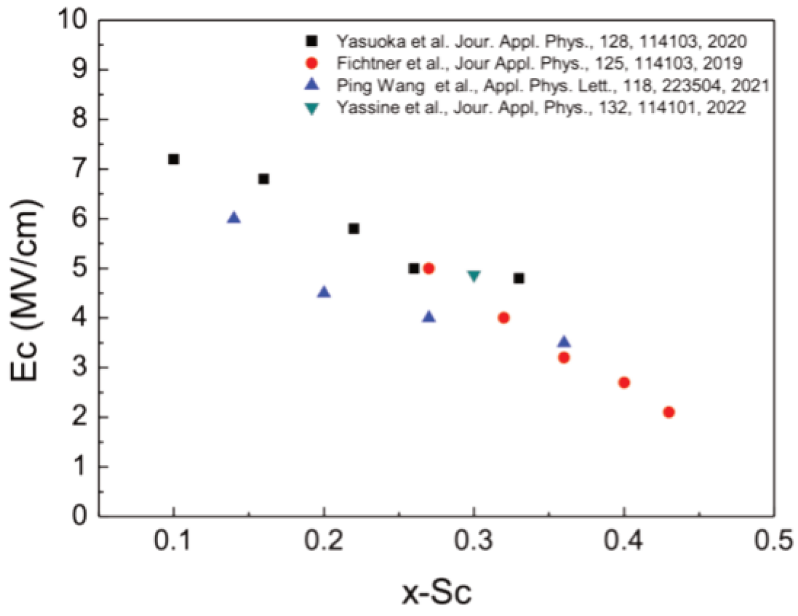

Figure 25: The legend highlights the investigation of the coercive electric field as it relates to the varying scandium molar fraction.

4.1.3 High power high frequency HEMTs

Due to its remarkable properties such as a large band gap energy, high saturated electron velocity, and a high breakdown voltage, GaN has emerged as a promising candidate for implementing circuits with superior power, efficiency, and wide operational frequency bandwidth. Over the past decade, mobile telecommunications technology has experienced rapid growth from 2G in 1990 to 5G in 2019, driven by substantial demand. Consequently, research institutions have also intensified their involvement in exploring and developing 5G/6G technologies. 5G operates at different frequency bands including the mmW range (24-71GHz), and GaN stands out as the most suitable material for this task due to its unique combination of high voltage, high power, and high-speed capabilities. GaN-based HEMTs based on III-nitride materials typically incorporate a barrier layer (AlN, InAlN, InAlGaN, or AlGaN. . .) and a GaN channel.

A HEMT structure is a junction formed by two semiconductors with different band gaps. The barrier having a larger band gap than the buffer, creating a discontinuity where the conduction band is lower than the Fermi level, confining electrons in a triangular quantum well.

Due to its high spontaneous polarization, AlN/GaN system provides a substantial sheet carrier density. However, this increased electron density coincides with a reduction in electron mobility (see Figure 26). On the other hand, AlGaN exhibits the lowest sheet carrier density among the materials mentioned, but it compensates with an exceptionally high electron mobility, reaching approximately $2200cm^2/V.s$ in the best quality heterostructures.

To increase the output power of the HEMT, it is necessary to increase the drain current I_{ds}, and the breakdown voltage V_{br}. To achieve the increase of current, it is necessary to increase the electron density in the 2DEG by increasing the polarization difference at the barrier/channel interface. While to achieve high frequencies, various techniques can be employed during the fabrication process to improve device

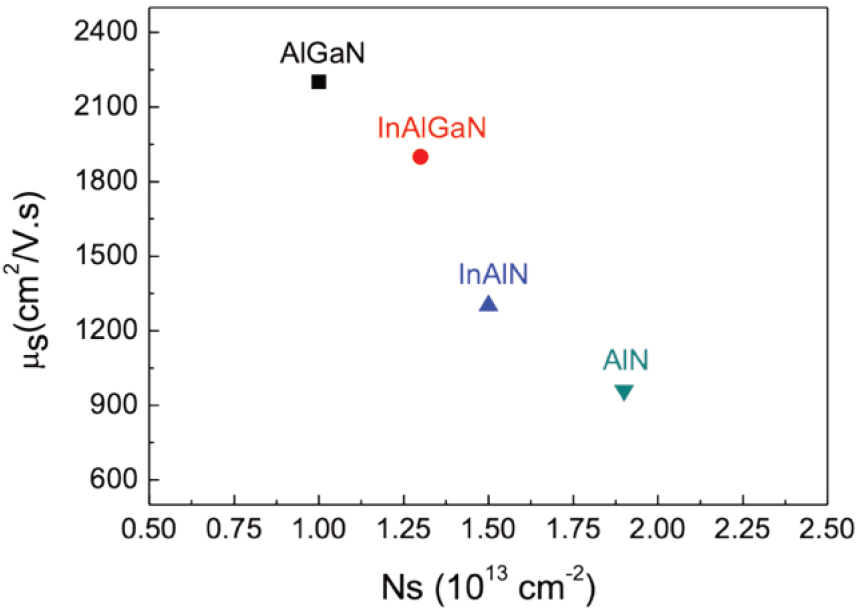

Figure 26: Typical mobility and density of electrons in the 2DEG of GaN HEMT structures based on different barrier layers grown on SiC substrate [20].

performance. There are several key factors that contribute to achieving high frequencies:

• Reducing the distance between the source and drain ohmic contacts

• Decreasing the gate length (see Figure 27)

• Minimizing contact resistance

• Ensuring effective electron confinement to limit short channel effects.

In our study, we develop heterostructures in view of enabling the reduction of the gate length to achieve high frequency performances.

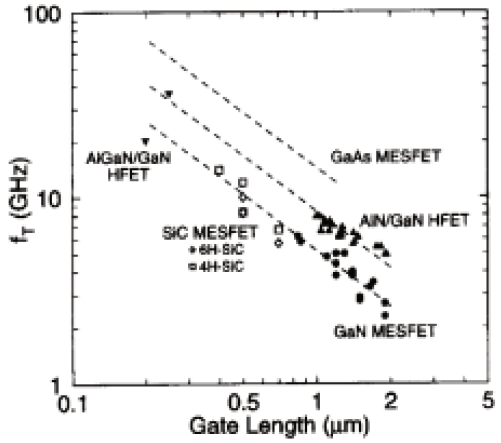

Figure 27: High cutoff frequency achieved for short gate length [21].

According to the study published by Jessen et al. [30], the aspect ratio must satisfy the following condi-

tion for GaN in order to prevent short-channel effects and keep an efficient control of the electron flow below the gate:

$$\frac{L_g}{d_{g-2DEG}} > 15$$

When the gate length is decreased, the electric field along the channel intensifies, approaching the vertical electric field that confines electrons in the 2DEG. Consequently, the depletion zone beneath the gate diminishes, enabling electrons to traverse it, giving rise to the short-channel effect. So, to achieve a high frequency with a short gate, we need to improve electron confinement in the 2DEG with a reduced barrier thickness while maintaining a high electron density in the channel. For instance, according to Figure 27, sub-100 nm gates are necessary to reach the 100 GHz frequency operation range, meaning that ideal HEMT heterostructures should be grown with barrier thickness below 6 nm.

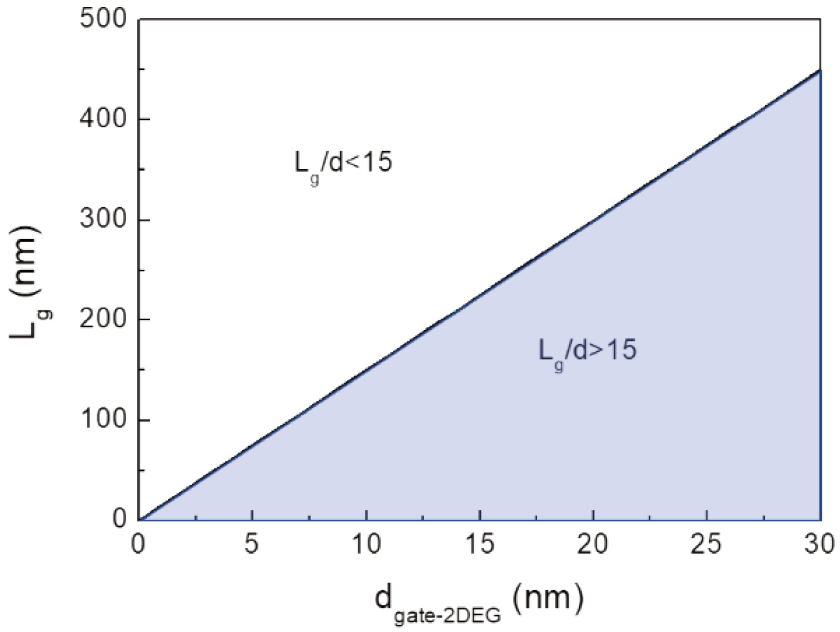

Figure 28: The critical boundary that should not be surpassed in terms of aspect ratio, aiming to mitigate short-channel effects.

Lastly, growing a lattice-matched barrier on a GaN buffer is advantageous as it should avoid the nucleation of new dislocations and minimizes the potential for cracks that may occur during the relaxation process. In this thesis, we propose that ScAlN is a promising candidate for HEMT heterostructures due to the following reasons:

1. ScAlN allows the growth of the wurtzite phase and can be lattice-matched with GaN, even with 18% scandium molar fraction.
2. The band gap energy of wurtzite ScAlN can be tuned and kept superior to the one of GaN ($E_g = 3.4eV$) within a range of 6.28 to 3.99 eV for x=0 to 0.5.
3. ScAlN exhibits high coefficients of spontaneous and piezoelectric polarization in the c orientation, further enhancing its potential for HEMT applications.

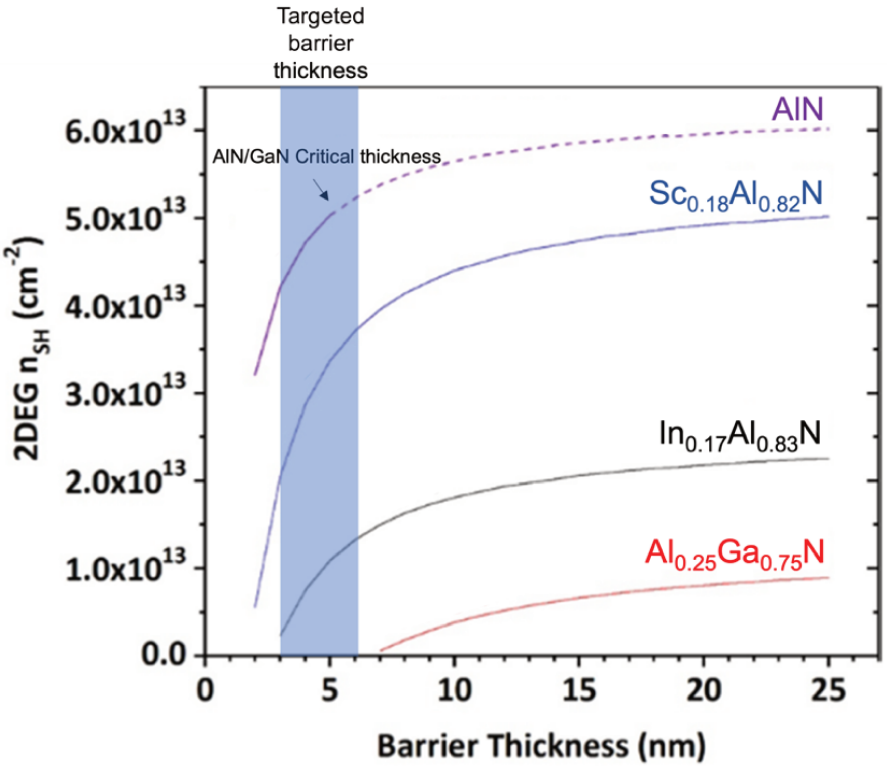

Figure 29: The graph displays the calculated sheet charge carrier concentration (n_{sh}) within the 2DEG as it varies with the thickness of the barrier layer grown on GaN. [31].

Figure 29 illustrates that AlN/GaN can reach high 2DEG densities but face limitations due to process reliability as the barrier's critical thickness is around 5 nm, which is too slender to facilitate a Schottky gate contact due to its vulnerability to Fowler-Nordheim and trap-assisted tunneling leakage current. Consequently, for the AlN/GaN heterojunction, the necessity for a gate dielectric arises.

Due to its high polarizations, we believe that ScAlN has the potential to achieve the outcome of achieving high power density at high frequency. Even with a very thin barrier layer, a strong two-dimensional electron gas (2DEG) can still form at the interface, ensuring low access source and drain resistances and resulting high drain current. In Figure 29, we observe that ScAlN can attain a density approaching $5 \times 10^{13} e^{-}/cm^2$ when it reaches a thickness of 20 nm. Furthermore, even at a thickness of approximately 5 nm, ScAlN still exhibits a high electron density of around $3 \times 10^{13} e^{-}/cm^2$. According to Frei et al, the ScAlN barrier grown using plasma-assisted MBE demonstrated remarkably high electron densities of approximately $6.2 \times 10^{13} e^{-}/cm^2$. However, the electron mobility was relatively low, measured at $340 cm^2/V$. s[32]. For such a very high carrier density, this lower mobility could be linked to the extremely reduced distance between the 2DEG and the interface that could favor alloy scattering and other effects related to the interface roughness. The absence of an AlN exclusion at the interface and so a lack of confinement of the 2DEG may also contribute to the drop of the mobility.

To our knowledge, the sheet carrier density reported for ScAlN/GaN HEMTs in all the other studies [33]–[36] falls in the range of 2.5 to $4 \times 10^{13}/cm^2$. Figure 30 shows the 2DEG densities calculated as a function of the barrier thickness for the most studied III-Nitride HEMTs grown by MBE and MOCVD [19]. In most cases, the electron mobility in these heterostructures is below $1200 cm^2/V.s$. In addition to the

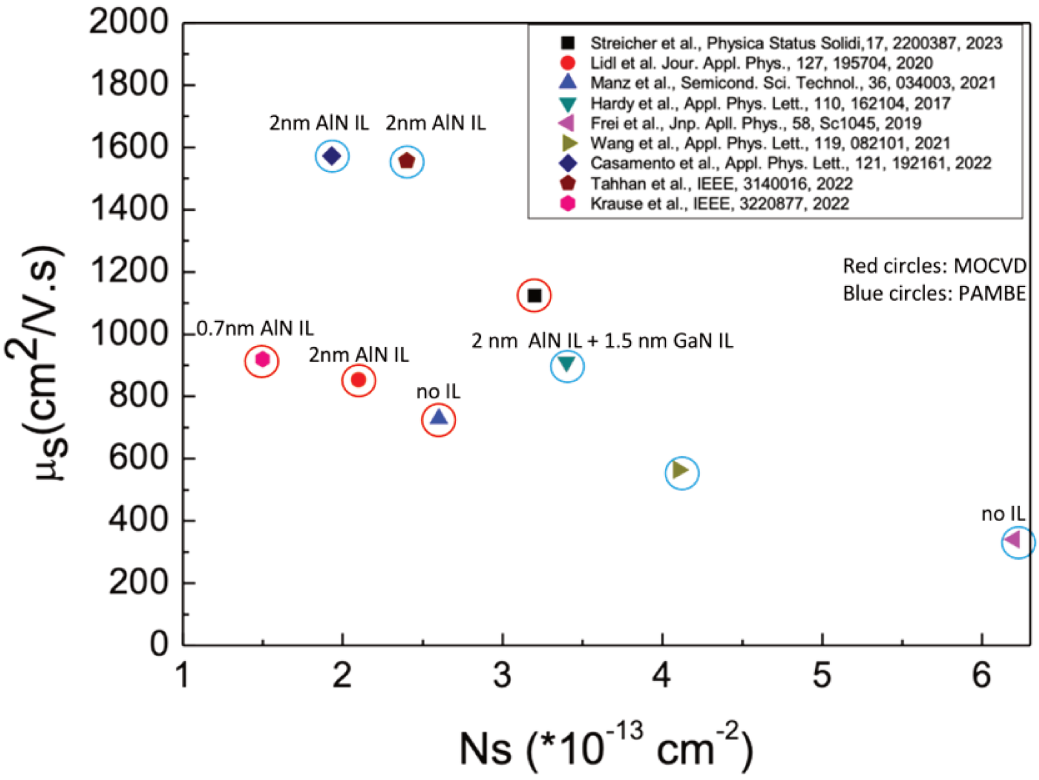

Figure 30: Mobility μ_s as a function of N_s for ScAlN barrier HEMT.

scattering effects already mentioned, the mobility could be limited by an interdiffusion effect occurring at the interface. Gallium atoms may penetrate through the interface into the ScAlN barrier, or Al atoms could diffuse into the GaN channel. In spite of a larger chemical bond energy in AlN, this diffusion effect into an AlN exclusion layer is possible too. High-temperature growth of the material can further promote atom diffusion, especially when employing very low growth rates, requiring extended growth times. To mitigate diffusion effects, a faster growth rate and a reduced temperature should be preferred. However, there is a trade-off to consider between diffusion mitigation and the nucleation of defects or the incorporation of impurities during the growth. Impurities in the scandium precursor during Metal-Organic Chemical Vapor Deposition (MOCVD) growth or effusion cells during Molecular Beam Epitaxy (MBE) growth, such as oxygen or other metal traces, can significantly impact electrical properties, leading to reduced electron mobilities, high sheet resistance, and low 2DEG concentrations. Streicher et al [34] reported a trade-off between electron mobility and 2DEG density using an AlN interlayer with a high purity scandium precursor for MOCVD growth of HEMTs.

On the other hand, AlN is introduced as an interlayer (IL) to reduce the scattering effect at the interface to enhance the electron mobility and this has been achieved by PAMBE by employing a relatively thick AlN interlayer with a thickness of 2 nm grown on SiC substrate [28], [29], an electron mobility reached $1556 cm^2/V.s$. In Figure 31, the AlN interlayer is preserved and does not interdiffuse with the GaN layer during the PAMBE growth process on a SiC substrate. It was also reported by [113], while growing only

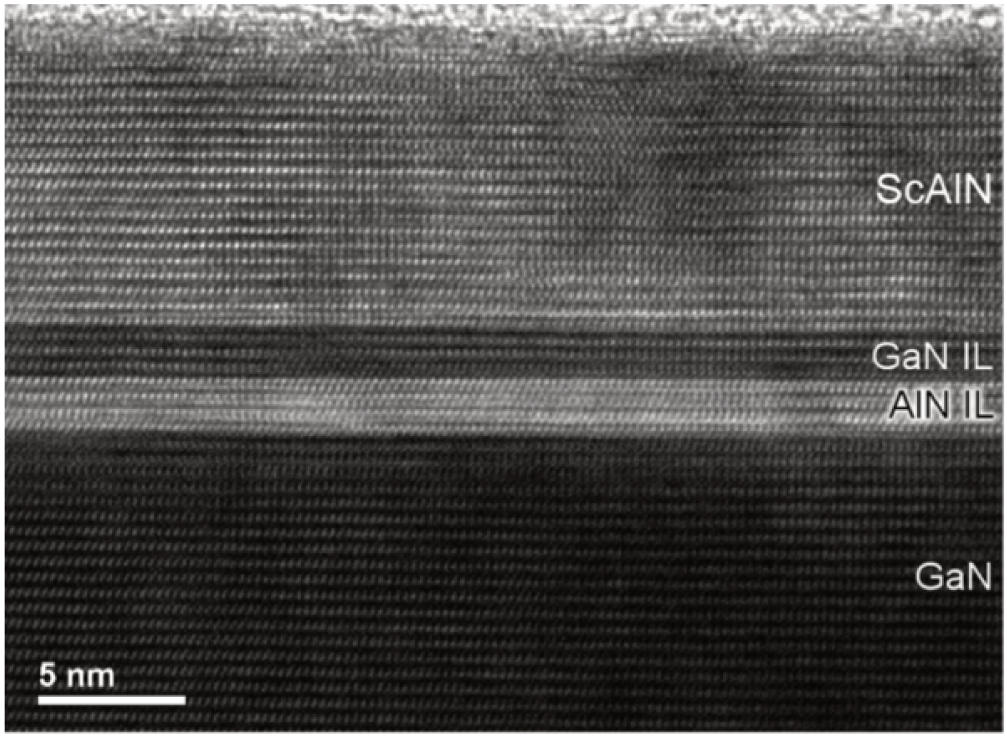

Figure 31: Cross-sectional STEM of a ScAlN-barrier HEMT grown with PAMBE on SiC substrate structure having a nominally 8-nm-thick barrier [113].

3 nm of ScAlN, a high 2DEG density was achieved with $2 \times 10^{13} e^{-}/cm^2$ and a high electron mobility of approximately $1060 cm^2/Vs$, However, MOCVD growth of a ScAlN HEMT with 2nm of AlN IL having the same 2DEG density resulted in the electron mobility drop to $900 cm^2/V.s$. The interdiffusion of scandium atoms or gallium atoms in AlN could be the reason of having a low electron mobility.

Figure 32a presents a high-resolution transmission electron microscopy (HRTEM) cross-sectional view of a thin heterostructure composed of 20 nm thick AlScN and GaN layers grown by MOCVD, with a GaN cap, grown at a temperature of 1000℃. Structural imperfections are evident at the junction between the GaN buffer layer, the AlN interlayer, and the AlScN layer. The scanning transmission electron microscopy (STEM) high-angle annular dark-field (HAADF) image reveals a significant diffusion of Ga atoms into the AlScN layer (see Figure 32b).

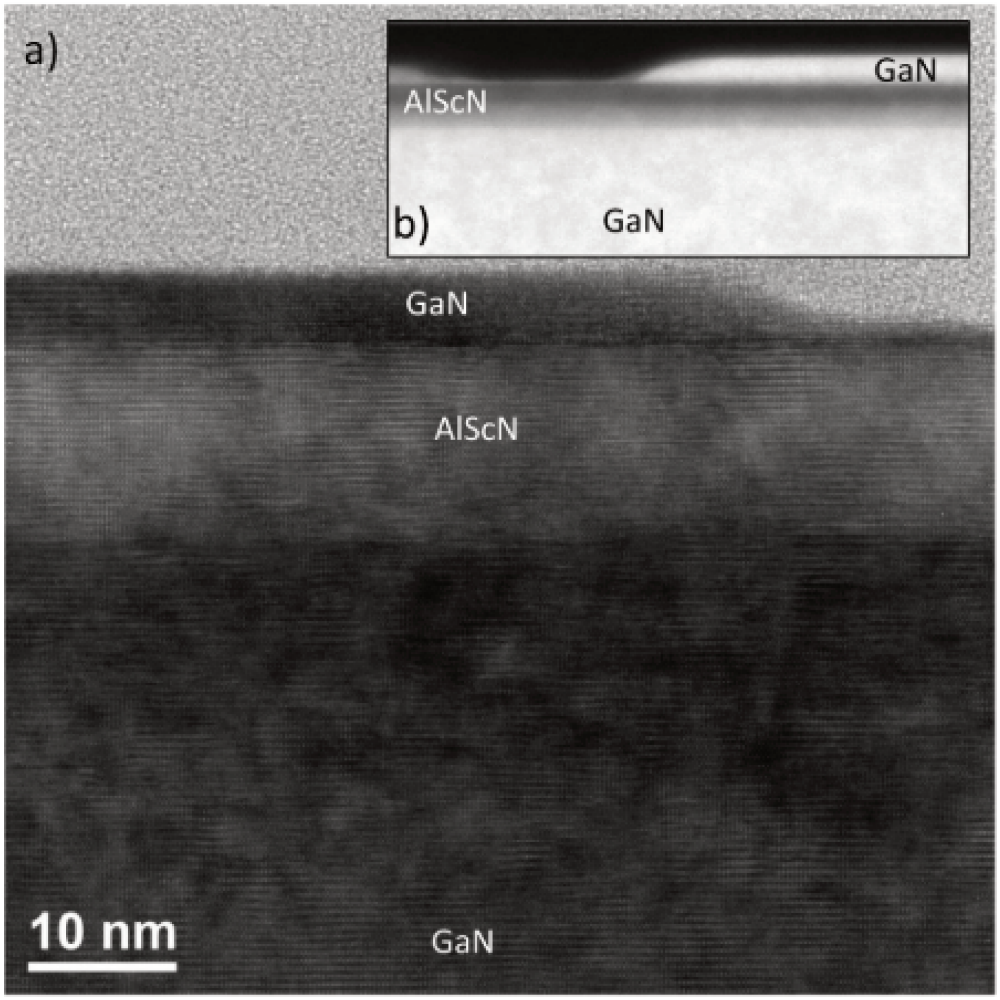

Figure 32: (a) In a cross-sectional HRTEM) and b) STEM HAADF image of ScAlN/AlN/GaN grown by MOCVD [30].

4.1.4 State of the art of ScAlN/GaN high frequency transistors :

Various research groups have achieved intriguing outcomes in the growth of ScAlN/GaN HEMTs using various growth methods [114]–[118]. Table 5 presented below illustrates the reported results, encompassing contact resistance, maximum drain current, breakdown voltages, cutoff frequencies, maximum frequencies, power-added efficiency (PAE), and transconductance.

The Bode-Fano bandwidth limit is a phenomenon where the voltage scaling alone significantly limits bandwidth (BW) [119]. Since BW (operating frequencies) decreases proportionally with transistor operating voltage, voltage scaling is limited to microwave frequencies and lower. To overcome this limitation and increase power densities at millimeter waves frequencies, one must increase transistor current density with increasing operating voltage. The challenge is to engineer a device that simultaneously supports both high current (high $I_{D,sat}$) and high operating voltage (breakdown voltage). The saturation drain current density can be described as follows:

$$I_{D,sat} = en_s v_{eff}$$

Reference	R_c ($\Omega.mm$)	I_{DS} (A/mm)	F_T(GHz)	F_{MAX} (GHz)	P_{out} (W/mm)	PAE (%)	G_m (S/mm)
Green et al. [118]	0.1	2.4	88	91		-	0.67
Kazior et al. [115]	0.1	3	50	140		-	0.5
Cheng et al. [114]	0.2	1.98	59	69		-	0.52
Tahhan et al. [116]	-	-	-	-	10.8	26	-
Krause et al. [117]	0.9	1.7	52	-	8.4	42	0.49

Table 5: Summary table displaying various transistor performance data documented in the literature.

Where e, N_s and v_{eff} are the elementary charge, sheet carrier density and the saturation drift velocity of electrons, respectively[120]. As a result, $I_{D,sat}$ can be enhanced by elevating either N_s or v_{eff}. Nonetheless, at high electric fields, v_{eff} approaches the saturation drift velocity, making it challenging to achieve significant improvements in this regard. Alternatively, boosting N_s can be achieved through appropriate engineering of the hetero junction. Also, for this purpose, low resistance ohmic contacts with the electron gas located in the channel is necessary as well as cap layers protecting the reactive alloy surface. For these reasons, highly n-type doped GaN is often regrown for high performance RF transistors resulting a Rc less than $0.1\omega.mm$ [118]. Alternatively, the initial HEMT growth sequence can be terminated by incorporating in situ GaN, AlGaN [116], or SiN cap layers [117].

4.2 ScAlN growth

4.2.1 Growth by sputtering

First ScAlN epitaxy was reported in 2009 by Akiyama et al [1] with textured ScAlN thin films deposited by reactive RF dual magnetron sputtering onto Si (001) substrates. Further studies have reported the successful growth of ScAlN with a preferred orientation along the c-axis (0001) using reactive magnetron co-sputtering. This growth has been achieved on both silicon and sapphire substrates, with scandium content reaching up to x=0.43 [8], [45]–[49] The performance of acoustic devices is significantly influenced by the crystal quality of the piezoelectric layers, as demonstrated in [50]. Previous reports have indicated a robust link between the device's crystalline structure and its piezoelectric coefficients, consequently impacting the electromechanical coupling coefficient [51]. Reactive magnetron sputtering stands as the prevalent approach for depositing AlN and ScAlN. While this technique is favored for its cost-effectiveness and reasonable growth rates, the crystal quality of the resulting layers is less optimal when contrasted with those achieved through epitaxial methods operating in a higher purity environment[52]. Indeed, AlN and ScAlN films deposited by sputtering generally contains percent or several percent of oxygen atoms. Sputtering allows to deposit AlN and ScAlN with a crystal lattice c axis-oriented perpendicular to surface of substrates like Silicon, SiC or Sapphire, which is highly required for most piezoelectric device applications. However, it is difficult to nucleate the films with a unique in-plane orientation, which results in a columnar growth with a high number of threading dislocations at grain boundaries (lattice twist). Crystal lattice tilt also exists but generally vanishes in thicker AlN films enabling the fabrication of RF BAW filters. Compared to AlN, the

growth of high crystal quality ScAlN is more difficult with the risk of nucleating new defects like abnormally oriented grains (AOG) related to multiple phases in the alloy. Nevertheless, the superiority of piezoelectric properties of such compounds elaborated by sputtering has been already demonstrated. [121] If ScAlN layers can be grown to a high standard, they could be employed in or close to the active regions of various electronic device heterostructures. These devices include HEMTs for high frequency electronics and high-power switching electronics. For this type of devices, a high crystalline quality with smooth surfaces and interfaces are required and thus, ScAlN device layers grown by molecular beam epitaxy and metal organic chemical phase deposition have been investigated[54].

4.2.2 Growth by Metal Organic Chemical Vapor Deposition (MOCVD)

MOCVD (Metalorganic Chemical Vapor Deposition) also known as MOVPE (Metal Organic Vapor Phase Epitaxy) stands as the preferred technique for large-scale industrial production due to their high growth rate compared to MBE, and various studies have demonstrated successful growth of ScAlN. MOCVD growth relies on the vapor transportation of gaseous precursor molecules. However, due to scandium's status as a transition metal in group IIIB, achieving precursors with high vapor pressure becomes crucial in contrast to metals from group IIIA, such as Al and Ga. This discrepancy has historically hindered the prosperous growth of Sc-containing nitrides through MOCVD, limiting Sc incorporation primarily through doping levels[55], [56]. Fortunately, advancements occurred with the introduction of precursors featuring high vapor pressure. Consequently, different types of scandium precursors have been subjected to testing. Initially, the Cp_3Sc precursor was employed while systematically varying growth temperature, growth mode, III/V ratio, and pressure to fine-tune the process[33], [57], [58].

The limited vapor pressure of Cp_3Sc precursor restricts the molar flow into the reactor, resulting in extremely low growth rates (GRs) around 0.006 nm/s. As a consequence, the prolonged growth times subject the epilayers to high temperatures, facilitating the diffusion of atoms at the interfaces, Figure 33 shows a noticeable diffusion of aluminum atoms into GaN even with 2 nm of AlN interlayer at $T_g = 1200C$.

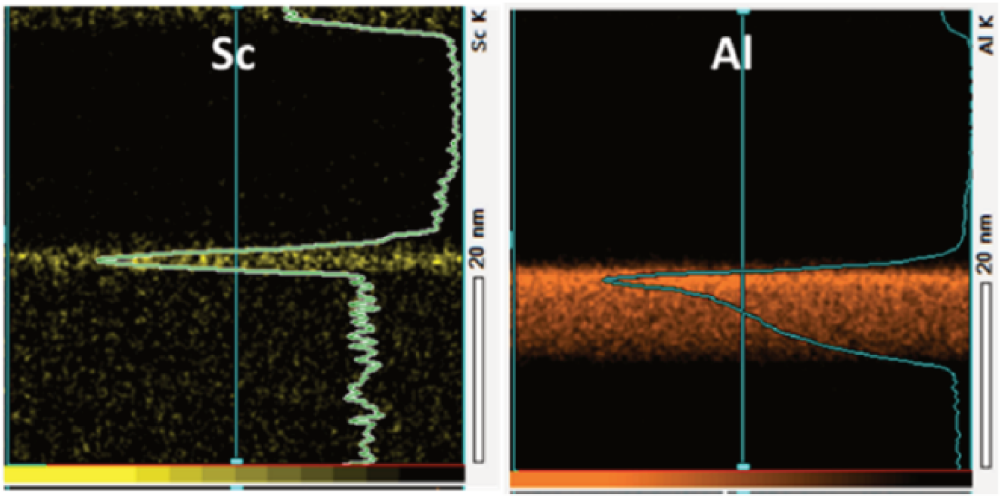

Figure 33: Elemental distrubution of STEM-EDX for ScAlN growing by MOCVD on GaN using Cp_3Sc precursor having a GR=0.006nm/s at $T_g = 1200C$ that shows a strong Al diffusion from the barrier into the GaN.

To address this issue, researchers have utilized another precursor called bis-methylcyclopentadienyl-scandium chloride $(MCp)_2ScCl$ [22], which boasts a vapor pressure ten times higher.

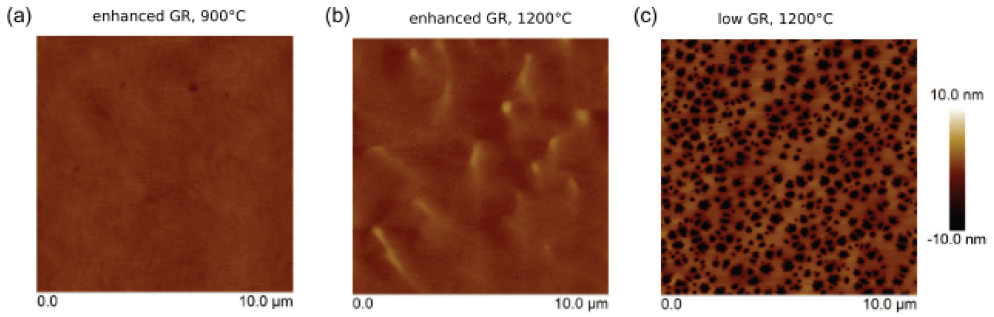

Figure 34: Atomic force microscopy (AFM) scans covering an area of $10 \times 10 \mu m^2$ reveal the surface characteristics of ScAlN high-electron-mobility transistor (HEMT) configurations grown on SiC by MOCVD with $(MCp)_2ScCl$ precursor reported by [34]. These configurations exhibit distinct growth rates (GR) as follows: a) at 900 ℃, b) at 1200 ℃ with an accelerated GR, and c) at 1200 ℃ with a lower GR for barrier growth. The root mean square (RMS) values for surface roughness are determined as: a) 0.31 nm, b) 0.58 nm, and c) 4.56 nm.

By using this alternative precursor, higher growth rates can be achieved [34], leading to a decreased thermal budget, reduced interface diffusion. Furthermore, employing a lower growth temperature range of 900-1000℃ results in smoother surface morphology especially for ScAlN grown at 900℃ as depicted in Figure 34 but it results in the inclusion of impurities like oxygen or traces of metals, which subsequently result in elevated sheet resistance, reduced electron density, and diminished electron mobility. Fascinating electrical outcomes have been attained by growing at high growth rate, especially when using lower growth temperatures for the barrier (Tg=900℃), these conditions yield a low sheet resistance of $172\Omega/sq$, a high 2DEG density of $3.2 \times 10^{13} e^-/cm^2$, and excellent mobilities of $1124 cm^2/V.s$. (reminder: When growth is conducted at lower temperatures, there is reduced interdiffusion).

4.2.3 Growth by molecular beam epitaxy (MBE)

Molecular beam epitaxy (MBE) involves the interaction of atomic or molecular beams within a chamber operating at extremely low residual pressures (base pressure of approximately $P \sim 10^{-10} torr$). This technique entails directing atomic or molecular flows onto a heated substrate for epitaxial growth. In the case of III-N compound structures, solid sources of III compounds (such as Al, Ga, In, Sc) are employed. The temperature of the crucibles containing these compounds controls the vapor pressure of the elements. Due to the extremely low pressures prevailing in the growth chamber, the evaporated atoms from the effusion cells experience negligible interactions until they reach the substrate. This molecular regime, characterized by the absence of significant atom interactions, is what gives molecular beam epitaxy its name. To introduce the nitrogen (N) component, either a source generating radicals from nitrogen N_2 (e.g., a very-high-temperature injector or RF plasma source) or a gaseous source (such as an ammonia NH3 injector) thermally cracked at the surface of the substrate is used. In the case of III-Nitrides, rather high gaseous flows are necessary to obtain smooth films, so the molecular beam regime can be altered.

MBE offers several interesting possibilities:

1. Precise control of layer thickness and composition modulation: MBE allows for rapid interruption of flows through the use of shutters placed in front of the output of the cell. This feature enables control of layer thickness and composition modulation at the molecular plane scale, providing high precision in the growth process.
2. Limitation of interdiffusion at interfaces: MBE operates at relatively low temperatures, which helps to

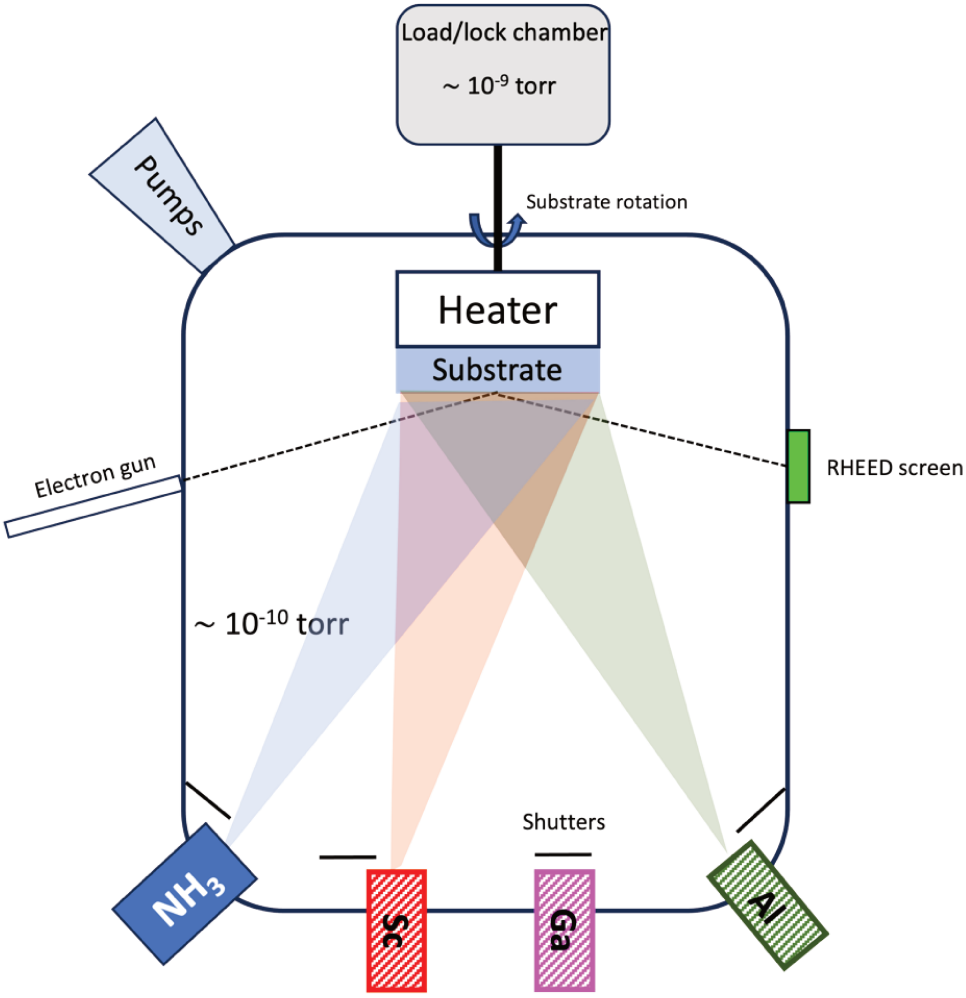

Figure 35: MBE chamber.

minimize interdiffusion at the interfaces between epitaxial layers. This temperature control is beneficial in reducing the stresses arising from the mismatch in thermal expansion coefficients between the epitaxial layers and the substrate, facilitating stress management.

3. In situ characterization tools: MBE benefits from an ultra-high-vacuum environment, allowing for the use of various in-situ growth control and surface state monitoring techniques. Reflection High-Energy Electron Diffraction (RHEED) can be employed for real-time monitoring and characterization during the growth process. Quadripole Mass Spectrometry can characterize the residual contaminants in the growth chamber and can evidence leaks or contaminations in the growth system.

4. Low impurity incorporation: MBE operates under high vacuum conditions, which minimizes the presence of impurities during growth provided that elemental sources are extremely pure.

5. Infra-red pyrometry is used to control sample temperature while laser reflectometry can help monitoring the growth rate and the film thickness. Substrate curvature measurements by optical techniques can often be implemented to follow stress evolution during the growth of lattice mismatched films and while varying the temperature. Overall, MBE is particularly well-suited for the growth of complex multilayer structures where thin elementary layers and sharp interfaces are crucial, such as in HEMTs, quantum wells or quantum dots-based structures for photodetectors, LEDs, and lasers.

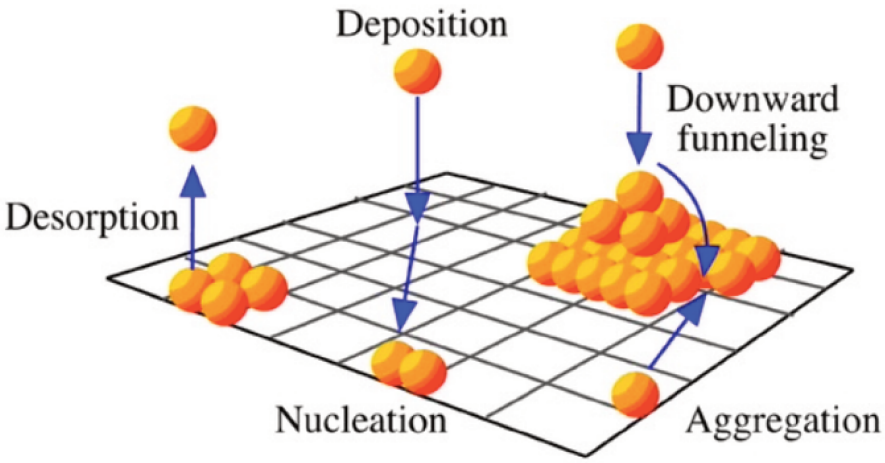

Figure 36: Physiochemical processes during MBE growth.

The growth of thin films by MBE involves several physicochemical processes. Figure 36 provides an illustration of the main phenomena:
1.Atoms and/or molecules hitting the surface undergo adsorption. There are two types of adsorptions:
a) Physisorption: this occurs when there is no transfer of electrons between the deposited atoms and the atoms of the surface crystal lattice. It is governed by attractive forces of the Van der Waals type.
b) Chemisorption: in this case, electron transfer takes place, leading to the formation of chemical bonds between the deposited atoms and the atoms in the surface crystal lattice.
2.Adsorbed atoms or molecules may undergo surface migration and dissociation.
3.Atoms are incorporated into energetically favorable crystalline sites, such as vacancies or edges.
4.Nucleation of islands occurs when atoms present on the surface come together to form small clusters.
5.Species that are not incorporated into the crystal lattice undergo thermal desorption, where they are released from the surface due to the effects of temperature. Depending on atoms and growth parameters (elements flow rates and temperature) these different mechanisms compete and result either in the growth of 3D islands, 2D islands able to coalesce and form periodically continuous films or can result in the lateral propagation of surface steps. In the case of III-Nitrides, this last regime is preferred (step flow growth), especially to grow thick smooth films. However, as it requires higher temperature and nitrogen pressure, it is sometimes difficult to achieve.

Growth by PA-MBE (Plasma Assisted Molecular Beam Epitaxy)

In 2017, researchers successfully grew single crystal ScAlN on GaN using radio frequency plasma assisted MBE, marking a significant milestone in the field [35]. According to their findings, when metal-rich growth conditions are employed, the phase purity is compromised as intermetallic Sc/Al compounds are formed alongside wurtzite ScAlN. However, it is worth noting that in the context of conventional group-III nitrides, growth under metal-rich conditions has shown to improve surface adatom mobility[59], leading to the production of high-quality films with excellent properties[60]. As a result, there is potential for utilizing these growth conditions to create superior ScAlN films suitable for electronic devices. A different research group conducted a systematic investigation of the impact of the metal and N rich on both the structural and

electrical properties of the grown ScAlN/GaN heterointerfaces [32], [35], [61]–[64]. Surface investigation by AFM demonstrated a rough surface on ScAlN in metal rich conditions exhibiting dendritic and triangular shaped surface features. The excess metal which is not incorporated during growth accumulates on the surface. It has been also demonstrated that metal-rich growth negatively impacts phase purity, which is likely due to the preferential incorporation of Al and the reaction of excess Sc with Al during the growth process.

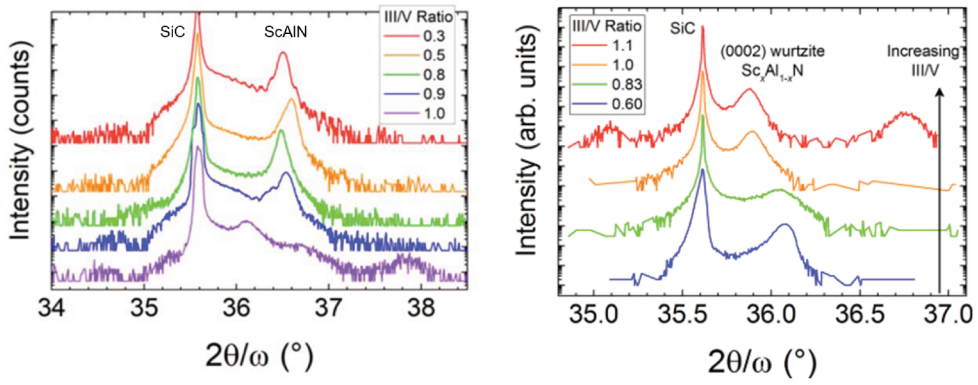

Figure 37: XRD $2\theta/\omega$ measurements for ScAlN with varying III/V ratio reported in [35], [64].

In the context of $III/V > 1$ growing at Tg=700℃ on SiC [19](indicating a growth regime rich in metal content), there is a possibility of observing an extra low-angle peak, which could correspond to either the rock salt structure of ScAlN or the perovskite structure of Sc_3AlN (Figure 37b). Additionally, the high-angle peak might be indicative of the presence of the intermetallic $ScAl_3$ phase.

In addition, metal polar and N-polar were investigated by [36] on ScAlN grown at Tg=700℃ on GaN on sapphire substrate. N-polar HEMTs featuring a $Sc_{0.18}Al_{0.82}N$ barrier have been successfully fabricated, demonstrating impressive results. These devices achieved an low sheet resistance of $271\Omega/sq$, with a sheet electron density of $4.1 \times 10^{13} e^-/cm^2$ and a mobility of $564 cm^2/V.s$. These outcomes highlight the potential of N-polar $Sc_xAl_{1-x}N$ as a promising material for the development of next-generation high-frequency and high-power electronic devices. However, the surface morphology doesn't show nano-grains or metal dendritic growths in the case of N-polar $Sc_xAl_{1-x}N$, in contrast to metal-polar $Sc_xAl_{1-x}N$ grown under similar temperature conditions. Particularly, at higher Sc content, no surface cracks were seen throughout Sc molar fraction range (0.11 to 0.38) for N-polar $Sc_xAl_{1-x}N$.

Surface acoustic wave (SAW) resonators fabricated using molecular beam epitaxy (MBE) also have been studied recently to grow single ScAlN layers on Silicon or 4H-SiC substrates [54], [65], showcased significant enhancements in acoustic performance when compared to state-of-the-art devices that had sputtered piezoelectric layers on silicon substrates. Improvements in high coupling coefficients (K^2) in ScAlN resonators were attributed to the superior crystallinity of the MBE-grown layers and the beneficial effects of scandium doping in ScAlN.

In addition, by incorporating gallium atoms into ScAlN alloy, interesting results have been observed [122]. A 12 nm thickness $Sc_{0.16}Al_{0.77}Ga_{0.07}N$ barrier has been grown by PAMBE resulting in the electrical results $N_s = 4.2 \times 10^{13} e^-/cm^2$, $R_{sh} = 171\Omega/sq$ and $\mu_s = 869 cm^2/V.s$. They showcase the successful synthesis of a homogeneous wurtzite quaternary alloy $Sc_xAl_yGa_{1xy}N$. This modification has led to several remarkable improvements, including an atomically smooth surface, enhanced crystal quality, well-defined interfaces,

and a substantial reduction in impurity incorporation. These achievements were previously elusive when working solely with $Sc_xAl_{1-x}N$, and they have been realized across a range of Sc molar fraction ($x \sim 0.16$–26) in $Sc_xAl_yGa_{1xy}N$. Furthermore, ScAlGaN has exhibited noteworthy transistor performance, achieving an output power of 5.77 W/mm and a power-added efficiency of 47% at 30 GHz [123].

Exploring NH3 MBE as a Potential Solution to Overcome Limitations in MOCVD and PAMBE Techniques

Growing ScAlN on GaN offers the potential for achieving lattice-matched growth, devoid of strains found in the barrier. This is further amplified by their notable spontaneous polarization, which can result in exceedingly elevated sheet carrier concentrations. To date, various methodologies have been explored for fabricating ScAlN barrier HEMTs, encompassing techniques such as sputtering, PAMBE, and MOCVD. PAMBE and MOCVD have demonstrated superior benefits compared to sputtering, primarily owing to their ability to yield higher crystal quality. In MOCVD a high oxygen incorporation in the barrier was noticed [33], [57]. Furthermore, the diffusion of aluminum atoms within the GaN buffer layer diminishes electron mobility in the channel due to the sluggish growth rate and this also poses a challenge. To address this aluminum diffusion issue, a potential solution involves enhancing the growth rate. This adjustment has demonstrated the potential for achieving improved electron mobility and enhanced electron confinement, as observed in the study referenced as [34]. In this context, particularly notable is the propensity of aluminum atoms to readily diffuse into the GaN substrate. This phenomenon becomes particularly pronounced when HEMT structures undergo elevated thermal conditions, either through MOCVD growth or the high-temperature annealing process of MBE samples. The capacity to grow ScAlN at comparably lower temperatures in comparison to MOCVD renders MBE a fitting choice for generating structures of elevated crystalline integrity, marked by notable phase purity and maybe minimal presence of oxygen and carbon impurities. To date, various research teams have successfully employed MBE to synthesize ScAlN, utilizing plasma assisted N2 as the source of nitrogen. Notably, it has come to light that the interplay between strain and scandium concentration is intricately linked to the growth temperature during the process of plasma-assisted MBE. In [35] study, the growth was interrupted for 90 second after GaN buffer deposition in order to evaporate completely the excess gallium present at the surface and prevent Ga incorporation in ScAlN barrier films. In spite of the high vacuum environment undesired oxygen incorporation is present in the ScAlN grown by PAMBE. It is anticipated that the undesirable incorporation of oxygen impurities can be further minimized by adopting alternative growth approaches for ScAlN, such as utilizing a higher purity scandium source and elevated growth temperatures. Within this thesis, we introduce the use of NH3 as a nitrogen source for the MBE-based fabrication of ScAlN. The use of NH3 facilitates the achievement of a GaN buffer layer with increased resistivity due to low silicon and oxygen n-type doping impurities, a crucial attribute for HEMT applications [68]. Low carbon deep acceptor concentration is achieved also. This is significant as it is expected that a similar trend could manifest in ScAlN growth. Combined with high electrical resistivity and good crystal quality of GaN buffer layers, NH3-MBE previously demonstrated well defined AlN/GaN interfaces enabling the fabrication of high-performance RF HEMTs [20], [124]. Additionally, it's worth noting that the sticking coefficients of group-III metals are nearly unity. Consequently, when employing nitrogen-rich conditions for growth, the process of monitoring growth rate and alloy composition becomes simpler within the specified temperature range. To our knowledge, so the present attempt to grow ScAlN is totally new. Till now, only the growth of ScGaN has been achieved with NH3-MBE [125], [126].

4.3 Conclusion

Due to its remarkable characteristics, ScAlN has emerged as a promising material for various advanced technologies, including RF filters, BAW (Bulk Acoustic Wave) and SAW (Surface Acoustic Wave) devices. Furthermore, its ferroelectric properties make it suitable for applications in memory devices, pyroelectric sensors, displays, and high-power transistors. Additionally, the ability to achieve lattice matching between ScAlN and GaN adds to its potential as a material for reliable power devices like for radio frequency power amplifiers, which is the focus of our current project. This chapter has highlighted the diverse techniques employed to grow lattice matched ScAlN on GaN, involving various growth environments. These methods often require precise control over parameters such as growth temperature and the III/V ratio to attain high crystalline quality which is a critical factor for HEMT (High Electron Mobility Transistor) applications. In our project, we employ MBE (Molecular Beam Epitaxy) for growth. However, unlike methods using plasma-assisted nitrogen sources, our approach involves a different nitrogen source, thermally cracked ammonia. In the forthcoming chapters, we will explore the impact of this nitrogen source on ScAlN barrier layers and its influence on transistor performance.

5 ScAlN epitaxy by NH3 MBE (Effect of the growth temperature)

For the first time, as far as our knowledge extends, we have employed ammonia source molecular beam epitaxy ($NH_3 - MBE$) to grow ScAlN. Our conjecture is that elevated growth temperatures might prompt the diffusion of gallium within the ScAlN barrier layer or the AlN interlayer, potentially resulting in the formation of AlGaN or ScGaAlN. This diffusion is attributed to the consequence of operating at relatively high temperatures during growth. This diffusion phenomenon detrimentally affects the performance of devices, particularly in terms of electron mobility within the two-dimensional electron gas (2DEG). Simultaneously, the incorporation of impurities is generally favored at lower growth temperatures. Notably, oxygen impurities might volatilize when operating at elevated temperatures. A plausible solution to mitigate oxygen-related issues involves employing high-purity sources of scandium and aluminum. It's worth highlighting that the molecular beam epitaxy chamber maintains a high vacuum with a pressure of the order of 10-10 torr. In addition, when the annealing temperature exceeds the barrier growth temperature, the increased thermal budget can promote diffusion at the interface, leading to its deterioration [127], [128]. Therefore, in this study, a temperature range of 200℃ is considered to investigate both low and high barrier growth temperatures, the latter being the usual growth temperature of GaN with NH3-MBE. This chapter focuses on the investigation of different growth temperatures to enhance surface morphology, crystal quality, and device performance. The epitaxial growth of ScAlN using MBE presents unique challenges compared to other III-Nitride (III-N) materials. In PAMBE growth, metal-rich growth regime is employed to enhance ad-atom mobility on the surface while temperature is lowered. This approach results in smoother surface morphology, reduced impurity incorporation, and minimized intrinsic stresses[129]–[132]. However, similar to AlGaN, Al has a higher tendency to incorporate preferentially over Sc in metal rich grown ScAlN. This means that when ScAlN is grown with an excess metal flux, Sc atoms tend to segregate toward the surface. Consequently, this can lead to a loss of phase purity and a degradation in crystal quality[19], [133]. To address this issue, the simplest solution is to maintain an N-rich growth regime. By ensuring a nitrogen-rich environment during the growth process, the accumulation of Sc on the surface can be prevented. This approach helps to preserve phase purity and maintain the crystal quality of the ScAlN material. However, compared to the metal-rich regime, the nitrogen-rich regime induces a lower surface mobility of ad-atoms and generally necessitates higher temperatures to counterbalance this limitation. The aim of the present study is to identify an optimum growth temperature window for such regime. The study employs metal polar GaN templates (high-quality GaN grown by MOCVD on sapphire substrates with threading dislocation density of a few $10^8/cm^2$) to achieve confinement of a two-dimensional electron layer within the GaN channel. The 300-500 nm thick GaN channel was grown first at 800℃ with a NH3 flow rate of 200 sccm and a Gallium flux resulting in a growth rate of $0.6\mu m/h$, which are the optimized growth conditions for GaN in the present reactor which is a C21T Riber system [134], [135]. A thin 1 nm AlN exclusion layer was then grown at the same temperature and in case ScAlN was grown below 800℃, a growth interruption of several minutes was used to reach the new temperature. The NH3 flow rate was kept constant for the growth of all the layers and during the cooling down up to about 450℃.

Table 6 : compiles the samples grown to study the effect of temperature. It provides an overview of the variations in growth temperature along with their respective thicknesses determined by XRR, scandium content determined by XPS, AFM surface root mean square values, and the concentration of the two-dimensional electron gas (2DEG) extracted from capacitance-voltage measurements with a mercury probe.

Sample	Tg(℃)	Thickness(nm)	Sc (%)	RMS roughness (nm)	2DEG density (e^-/cm^2)
PTC1218	620	23.75	15.9	0.43	3.10×10^{13}
PTC1217	670	22.96	14.7	0.40	3.10×10^{13}
PTC1216	720	23.06	16.1	0.32	3.00×10^{13}
PTC1220	760	22.11	15.7	0.33	2.48×10^{13}
PTC1221	800	23.42	13.9	0.24	1.56×10^{13}
PTC1269	620	n.a	n.a	n.a	2.50×10^{13}
PTC1271	800	n.a	n.a	n.a	8.24×10^{12}

Table 6: Summary of all the specimens grown at varying growth temperatures along with their corresponding analyses: ScAlN thickness was determined through X-ray reflectivity (XRR), scandium content was assessed using X-ray photoelectron spectroscopy (XPS), roughness was examined via atomic force microscopy (AFM) on a $0.5 \times 0.5 \mu m^2$ surface area, and 2DEG concentration was measured through capacitance-voltage (C(V)) assessments.

5.1 Unveiling the Scandium concentration: analytical techniques for alloy composition

5.1.1 Limitations in Scandium content determination by X-ray diffraction (XRD)

Typically, the composition of alloys like AlGaN, InAlN etc. is inferred from the lattice parameters. In these conventional alloys, Vegard's rule is a linear variation with molar content and corresponds to the lattice parameter variation of the alloy while it is not strained, in other word when the layer is fully relaxed. If the epitaxial layer is not thick enough to relax, then the layer may be strained, and the strains vary depending on the in-plane lattice parameter of the underneath layer. Then the biaxial Poisson ratio in wurtzite crystal structures, which is obtained from elastic constants C_{13} and C_{33}, is used in measuring film composition through X-ray diffraction considering the strains that may be present in the layer. The Poisson ratio defines the relationship between strains perpendicular and parallel to the (0001) plane when a film is subjected to biaxial stress in this plane, which is the growth plane. By measuring the out-of-plane lattice parameter alone, the in-plane lattice parameter can be determined using the Poisson ratio. From in plane and out of plane lattice parameters, content of an alloy can be deduced, and a strain or relaxation can be also observed by these parameters. In the case of ScAlN, the elastic constants (C_{11}, C_{33}, C_{44}, and C_{66}) decrease while C_{12} and C_{13} increase with increasing x (the Sc molar fraction)[77]. This trend differs from that observed in AlGaN, where C_{12} and C_{13} remain constant regardless of the aluminum molar fraction. In the case of InAlN, however, C_{12} and C_{13} decrease as the indium concentration increases [50]. Consequently, as x increases in $Sc_xAl_{1-x}N$, the material becomes softer. These findings are elaborated in the chapter 2 section Spontaneous and piezoelectric polarization. From C_{13} and C_{33} strained ScAlN lattice parameters can be deduced. These findings for fully relaxed crystal lattice obtained by Ambacher at al. and for strained ScAlN/GaN are presented in Figure 38.

ScAlN alloy doesn't follow Vegard's law meaning that the lattice parameters don't vary linearly with scandium molar fraction. Then studies have shown a relaxed or non-strained ScAlN with scandium molar fraction up to 25% has a constant out-of-plane lattice parameter c regardless of alloy composition, while in plane lattice parameter a of fully relaxed ScAlN increases linearly with the scandium fraction. Figure 39 displays the lattice parameters of ScAlN as documented for films produced using PAMBE, MOCVD and sputtering techniques. As it was expected from theoretical studies, the out-of-plane lattice parameters c for relaxed $Sc_xAl_{1-x}N$ is almost constant for x below 0.20. Deriving the out-of-plane lattice parameter exclusively through 2θ scan of the 0002 reflection proves challenging, particularly for scandium fraction

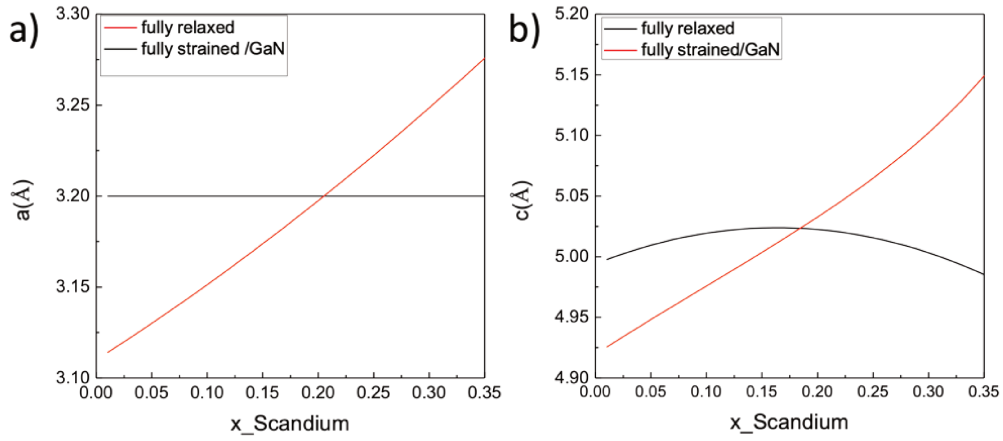

Figure 38: a) in plane and, b) out of plane lattice parameter obtained through theoretical predictions, for fully relaxed and fully strained ScAlN on GaN. [65]

below 0.2 where minimal variation is observed. Reciprocal space mapping comes to aid in determining the in-plane lattice parameter. Yet, assessing both the in-plane and out-of-plane lattice parameters allows for an estimation of the concentration in non-strained ScAlN see Figure 39.

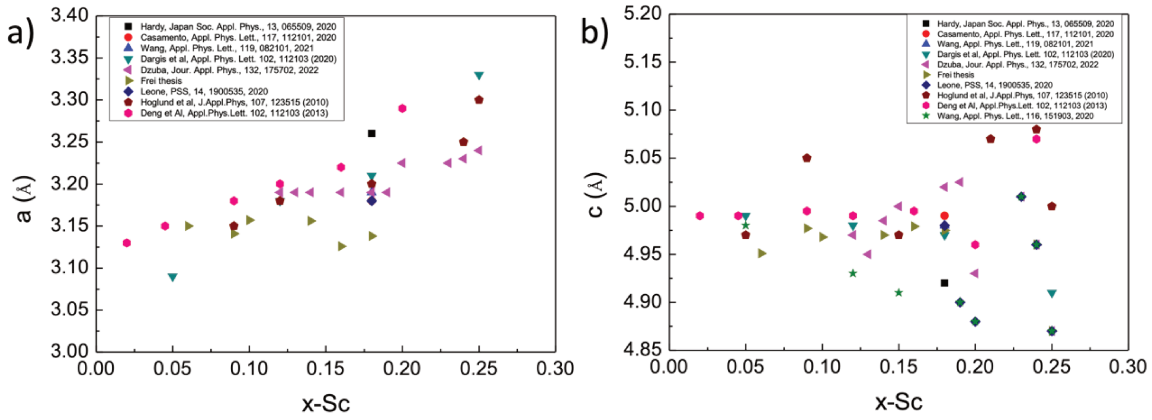

Figure 39: a) Out-of-plane and b) in-plane lattice parameters as a function of scandium molar fraction extracted from bibliography mentioned in the legend of the corresponding reference.

However, when dealing with thin ScAlN layers, the process of determining scandium composition is less obvious due to the influence of strains within the barrier layer. Relying solely on the calculations presented in Figure 38 for strained ScAlN isn't sufficient for accurate scandium molar fraction deduction. Considering the uncertainties surrounding scandium amount and material strain relaxation state, relying solely on lattice parameters (2θ scans or RSM) isn't sufficient for accurate composition evaluation. To achieve this, additional methods of chemical analysis are imperative, such as XPS, SIMS, and APT. These chemical analysis techniques are essential for obtaining reliable and detailed information about the composition.

5.1.2 X-ray photoelectron spectroscopy (XPS) measurements

The growth conditions were specifically selected to achieve an approximate scandium molar fraction of 18% in the ScAlN alloy, ensuring it remains strain-free or quasi-strain-free on GaN. In this study, we employed X-ray photoelectron spectroscopy (XPS) to determine the elemental composition of the ScAlN barrier layer. XPS is highly suitable for thin layer analysis due to its surface sensitivity, limited probing depth, and ability to identify elemental composition and chemical states. Being surface-sensitive, XPS focuses on the topmost atomic layers of a material, making it ideal for characterizing thin films where the bulk material is limited. XPS allows us to identify the atomic elements present in the films up to a depth of 10 nm depending on the binding energy of each chemical element. By conducting successive etchings using an argon ion gun, we were able to create a composition profile. In this research, an aluminum source was employed as an X-ray source, resulting in a survey spectrum where the relevant binding energies extend up to 1346 eV. Figure 40a presents the comprehensive spectrum of the ScAlN film grown at 720℃. In this spectrum, the Auger peaks for gallium, aluminum, scandium, and nitrogen are displayed across a range of high binding energies. Specifically, for binding energies below 500 eV, the most prominent peak is N 1s, followed by Ga 3s, Ga 3p1, Ga 3p3, and Ga 3d, with binding energies approximately at 160 eV, 107 eV, 104 eV, and 20 eV, respectively. Additionally, Al 2s and Al 2p peaks are observed, with binding energies of approximately 120 eV and 74 eV, respectively. Through automated identification using Advantage software, distinct peaks corresponding to scandium, aluminum, nitride, carbon, and oxygen were discerned, along with their respective Auger emissions. Figure 40b displays the XPS spectrum obtained for the same film, showing peaks corresponding to Al 2p, N 1s, Sc 2p3/2, and Sc 2p1/2 at binding energies of 75 eV, 397 eV, 401 eV, and 405 eV, respectively. In XPS measurements, we observed through quantitative analysis that the presence of nitrogen in the alloy is not in a stoichiometric ratio with aluminum and scandium. This discrepancy is likely attributed to the presence of oxygen within the alloy layer, which suggests that oxygen occupies the nitrogen's position within the lattice structure. To determine the scandium molar fraction, we opted to compare the concentration of element III, considering only the peaks of scandium, aluminum, and gallium. However, a significant challenge arises when comparing scandium to aluminum due to their markedly different binding energies. This disparity in binding energies can potentially lead to inaccurate content assessments because it affects the measurement depth. As previously mentioned, each element has its own characteristic mean free path; for instance, Al2p has a binding energy of 74 eV, whereas Sc2p has a binding energy of 401 eV. Consequently, aluminum's mean free path extends deeper into the material compared to scandium. Therefore, to achieve a quantitative study of these elements at the same depth, it is more accurate to compare scandium with nitrogen. This is why XPS is regarded as a semi-quantitative technique. Even though a comparison between scandium and nitrogen yields more accurate results, the presence of apparent non-stoichiometry constrains to focus solely on element III when conducting these comparisons. Then, the relative Sc molar fraction in ScAlN was determined by analyzing the Sc2p and Al2p peak areas using Advantage software, which considers the sensitivity factors (0.560 and 5.882 for aluminum and scandium respectively) of each atomic element and corrects for energy-dependent analysis thickness. This approach allowed us to ascertain the relative Sc molar fraction compared to Al in the ScAlN film.

Analysis using XRR revealed that the thickness of the ScAlN barrier is approximately 25 nm. Consequently, the etching rate for ScAlN containing 15% scandium is estimated at around 0.15 nm/s, while for GaN, it's approximately 0.30 nm/s (GaN etch rate deduced from XPS and XRR while taking 85s to etch 25 nm of GaN). Notably, as the x-rays begin to interact with GaN, the etching rate increases compared to

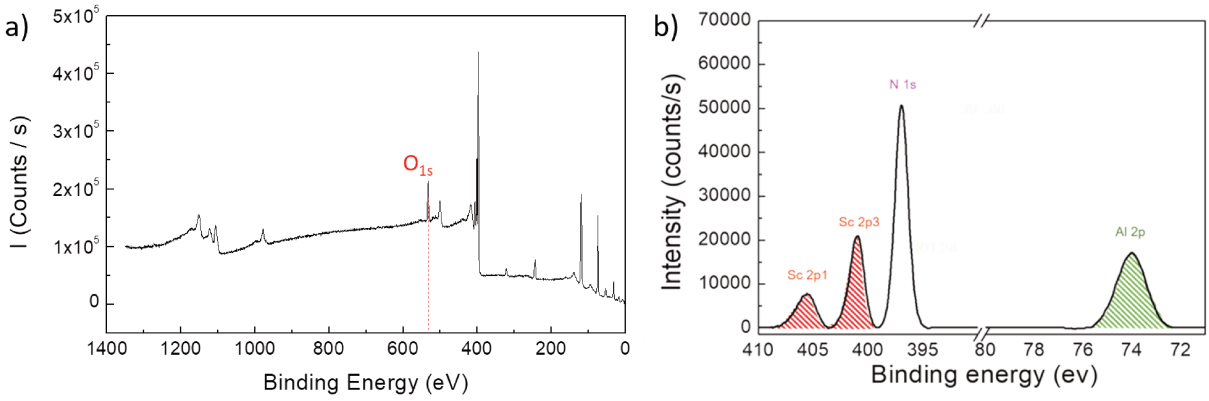

Figure 40: a) XPS survey spectrum and b) XPS profile of the ScAlN barrier layer deposited at 720 ℃.

ScAlN. To illustrate, an etching duration of 50 seconds for ScAlN corresponds to an approximate removal of 8 nm, while the same 50 seconds of etching in GaN corresponds to an approximate removal of 15 nm. Figure 41a illustrates the etching process over time for both ScAlN and GaN, subsequently converting these durations data into depth, accounting for the respective etch rates of ScAlN and GaN.

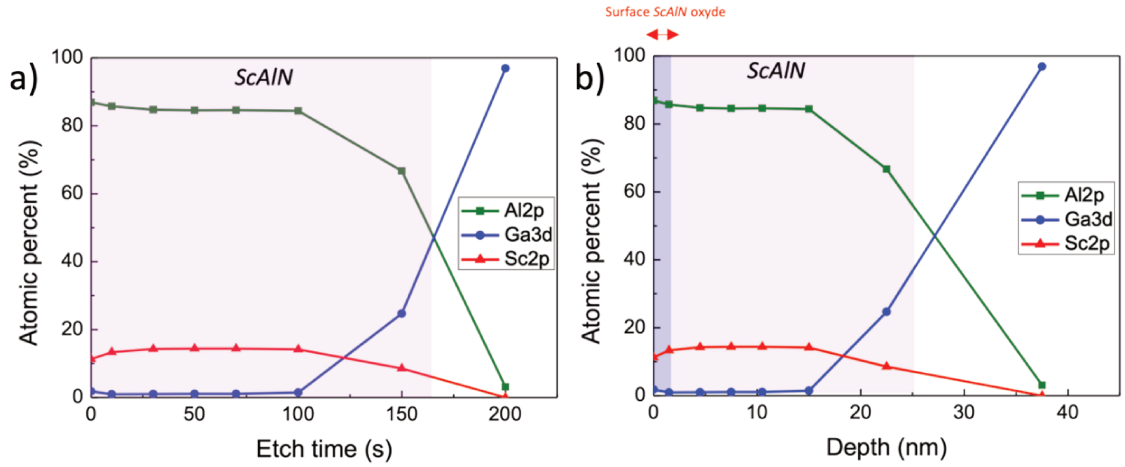

Figure 41: XPS ScAlN profile for the sample grown at 720 ℃ as a function of the a) etch time, and b) depth in nm.

During the initial surface measurement, a distinct reduction in scandium molar fraction is noticed. After the initial etching stage, the scandium content reaches a point of stability, exhibiting a constant level of scandium within the barrier layer until the x-rays begin to interact with GaN. This constancy holds true throughout the firsts 15 nm of the barrier layer. The initial two steps of this process align with surface oxidation, encompassing a range of 2-3 nm. These outcomes consistently align with XRR simulations that predict the presence of a 2-3 nm layer of ScAlN oxide on the surface. A more detailed discussion regarding this aspect will follow in the subsequent section: Understanding of the impact of growth temperature on ScAlN thickness.

In Figure 42a, an XPS deconvolution analysis was conducted to examine the potential chemical states of scandium during the oxidation process. This deconvolution analysis was performed during the initial phase

of profile measurement, prior to the commencement of the etching procedure. This illustrates chemical states linked to scandium oxides like ScO_xN, as well as scandium bonded with nitrogen in the form of ScN.

For all samples except the one grown at 670℃, the Sc molar fraction ranged between 15% and 16% see Figure 42b. As the growth temperature increased, a slight decrease in Sc content was observed. The Scandium content was calculated by averaging the values obtained for different erosion durations (t=50s, t=70s, and t=100s) for each sample. Notably, the fluctuation in the Sc concentration remained below 1.5% for each growth temperature.

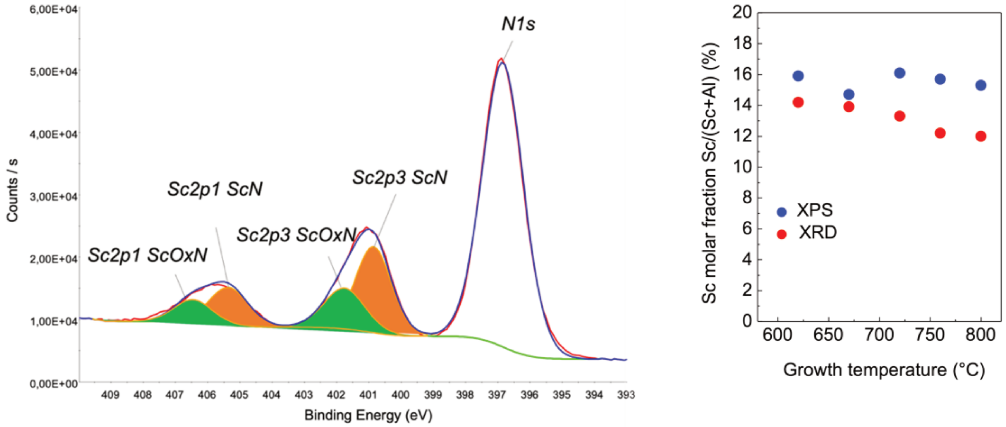

Figure 42: a) Surface chemical environment, b), Sc molar fraction as determined through XPS and XRD simulations, as investigated in relation to variations in growth temperature.

While XPS undoubtedly offers valuable insights into material composition, its utility might fall short when quantifying the scandium content within ScAlN alloys. The complex nature of ScAlN, characterized by subtle variations in chemical states and depths, can challenge the accuracy of XPS measurements alone. To confidently ascertain the scandium molar fraction, a comprehensive approach involving complementary techniques such as Secondary Ion Mass Spectrometry (SIMS) or Atom Probe Tomography (APT) becomes imperative. SIMS enables high-resolution depth profiling, allowing for a more accurate determination of elemental concentration gradients. Meanwhile, APT offers an unparalleled three-dimensional visualization of atomic arrangements, ensuring a thorough assessment of the alloy's composition.

5.1.3 Alloy's elemental composition verified by secondary ion mass spectrometry (SIMS).

A specific sample was fabricated under identical growth parameters; however, a GaN cap layer of approximately 25 nm was introduced to mitigate surface oxidation or contamination. SIMS has been performed by Probion Analysis. Subsequent SIMS measurements disclosed a Sc molar fraction of approximately 15% for this sample grown at 670℃.

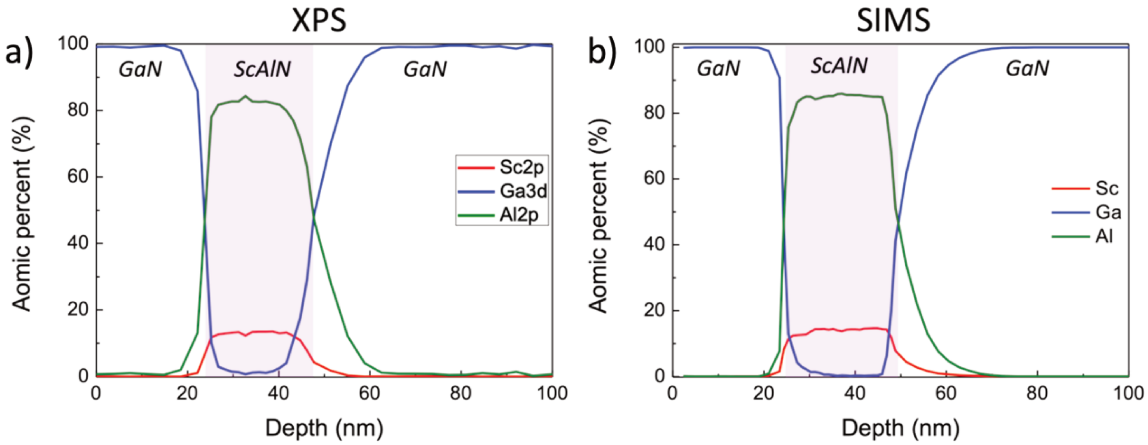

Figure 43: a) XPS and, b) SIMS comparison for ScAlN with GaN cap layer.

The results obtained from SIMS measurements corroborate the findings of XPS. This convergence between the two analytical techniques lends strong support to the accuracy of the determined scandium concentration in the alloy. The observation of aluminum appearing before scandium at the GaN/ScAlN interface (around 20 nm depth) in Figure 43, can be attributed to the distinct binding energies of Sc2p and Al2p. Specifically, the binding energy of Al2p is lower than that of Sc2p. Consequently, this implies that the mean free path associated with aluminum is greater than that of scandium. As a result, aluminum becomes discernible before scandium at the GaN/ScAlN interface. In the case of the ScAlN/GaN interface, which extends to approximately 50 nm in depth, gallium begins to become apparent at an early stage. This is evident from the detection of Ga3d with a low binding energy of approximately 20 eV, indicating a significant free mean path for gallium, thus allowing us to observe gallium presence at an early stage. In the case of scandium, we notice variations in the molar fraction at the interfaces that separate ScAlN from the GaN cap layer and the GaN buffer layer. This discrepancy arises from the more intricate etching process applied to ScAlN compared to GaN or from the initial surface roughness and the one developed with etching process, resulting in a broader profile on the GaN buffer side. This was verified by XRR in next section "Understanding of the impact of growth temperature on ScAlN thickness", where we see a sharp interfaces between ScAlN and the GaN buffer, rigid interfaces were also verified by APT (see section "APT composition analysis in ScAlN") in Figure 45.

5.1.4 Atom probe tomography (APT) composition analysis in ScAlN

In the exploration of the frontiers of materials synthesis, the contribution of nanoscale and atomic-scale microscopy techniques is crucial. These techniques not only offer a detailed understanding of materials properties but also provide valuable insights for optimizing elaboration conditions. In this context, the use of laser-assisted Atom Probe Tomography (APT) emerges as a valuable approach for characterizing epitaxial semiconductor layers. This method enables the assessment of the three-dimensional distribution of chemical species within the structure. Laser-assisted APT has found significant applications in the examination of III-N materials. Its high precision allows for accurate examination of challenges like the random distribution of alloy components [136], [137], the presence of dopant atoms [138], [139], clustering [140], and the segregation occurring at defects [141], [142]. As far as our understanding goes, there has been only one research study on ScAlN's APT characteristics. This study focused on examining the properties of ScAlN layers growing by MBE with a thickness of 100 nm, containing approximately 18% of scandium, grown at various temperatures. In this investigation, it was found that when the film was grown at a low temperature, all atomic species exhibited a uniform distribution. Conversely, at higher growth temperatures, the use of APT revealed a non-uniform distribution of aluminum atoms. [143]

APT analyses were carried out in collaboration with the Groupe de Physique des Matériaux, CNRS, University of Rouen Normandie, outside the CRHEA. We extend our gratitude to the contributors, namely Samba Ndiaye, Aïssatou Diagne, François Vurpillot, and Lorenzo Rigutti, for their valuable input in the analyses and interpretations.

The specimen under investigation is the same as previously with a 25 nm GaN cap layer and a 25 nm ScAlN barrier thickness (Figure 44a). APT needle-shaped specimens were prepared using standard lift-off and annular milling techniques utilizing a Focused Ion Beam (FIB), as depicted in Figure 44b. APT analysis was conducted using a laser-assisted wide-angle tomographic atom probe instrument at a low base temperature of T=80K. Two separate analyses were performed, employing different laser intensities ($1.1kW/m^2$ and $5.0kW/m^2$), with a detection rate of $3-4\times10^{-3}$ events per pulse.

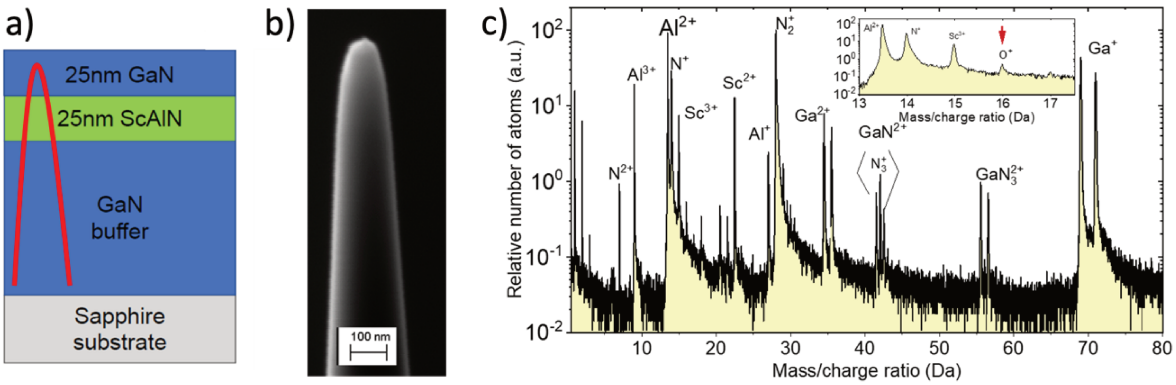

Figure 44: a) The schematic representation of the analyzed system highlights the approximate position in APT with a distinctive red color, b) The APT specimen, as produced through Focused Ion Beam (FIB) fabrication techniques, c) The mass spectrum results from an APT analysis of the $Sc_xAl_{1-x}N$ layer. In the inset, there is a closer look at the range between 13 and 17.5 Da, revealing the presence of a peak associated with O^+ (indicated by the red arrow).

Figure 44c displays the mass spectrum resulting from the analysis conducted under higher field conditions. Al appears in three ion states: Al^{+}, Al^{2+}, and Al^{3+}, like what has been observed in AlGaN [144]. In contrast, Sc is exclusively detected in the Sc^{2+} and Sc^{3+} states. Figure 44c displays the mass spectrum resulting from the analysis conducted under higher field conditions. The relative ratios of ion states for Al (expressed as the charge state ratio CSR(Al^{2+}/Al^{+}) = n(Al^{2+})/$n(Al^{+})$, where n(X) represents the count of ions of species X detected within a specific sampling volume) and Sc (charge state ratio CSR(Sc^{3+}/Sc^{2+}) = n(Sc^{3+})/$n(Sc^{2+})$) can be employed to estimate the surface electric field using the post-ionization theory framework.

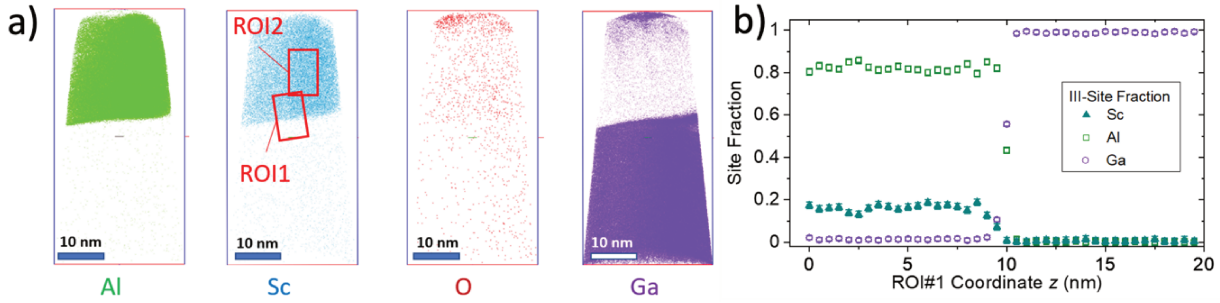

Figure 45: a) The 3D reconstructed volumes depict the spatial arrangement of atoms for Al, Sc, Ga, and O, presented in the sequence from left to right. Additionally, the positions of ROI#1 and ROI#2 are illustrated. In panel b), can be observed the site fraction profiles of Sc (represented by green filled triangles), Al (displayed as green empty squares), and Ga (indicated by violet empty circles) along the ScAlN/GaN interface, as extracted from ROI#1.

In the mass spectrum, we've detected the presence of oxygen, as depicted in the inset of Figure 44c. Figure 45a displays the 3D reconstructed volumes for the elemental species Al, Sc, Ga, and O. Notably, we observe Ga near the upper GaN/ScAlN interface, and we attribute this observation to FIB-induced damage. This is because the ScAlN film was initially covered with a 25 nm thick GaN cap layer, which was removed during the FIB preparation process. Additionally, Figure 45a highlights the positions of the regions of interest, denoted as ROI#1 ($5 \times 5 \times 7nm^3$) and ROI#2 ($5 \times 5 \times 20nm^3$). The choice of the position of the ROI#1 is to study the interface between GaN and ScAlN separated with 1nm of AlN interlayer. Figure 45b shows the profile of group III elements that are extracted by averaging the contents along the planes perpendicular to the z axis of ROI#1. The APT analysis yielded a scandium molar fraction of $x = 0.16$ ($\mp$) 0.02, which remains consistent throughout the ScAlN layer. This scandium fraction is relatively higher compared to what was determined through XPS and SIMS but falls within the error margin of the APT measurements. Furthermore, there is no indication of the existence of the 1nm AlN interlayer. But cross section TEM images reveal the presence of AlN interlayer, strain mapping using GPA analysis indicates the presence of significant strains (see section "Investigations about ScAlN strains" in chapter 6), originating from the highly strained AlN interlayer. The absence of AlN interlayer in APT could be limited by the APT resolution.

To summarize, our compositional data demonstrates metrological robustness, as evidenced by its alignment with data obtained through SIMS and XPS, as illustrated in Figure 46a. Figure 46b additionally highlights the insignificance of Ga atoms in ScAlN. This suggests that 1D compositional profiling methods like SIMS and XPS can be reliably employed in conjunction with APT.

Furthermore, compared to SIMS and XPS, APT analysis produces a more abrupt profile of scandium amount at the ScAlN/GaN interface. This emphasizes the better spatial resolution of APT and is consistent

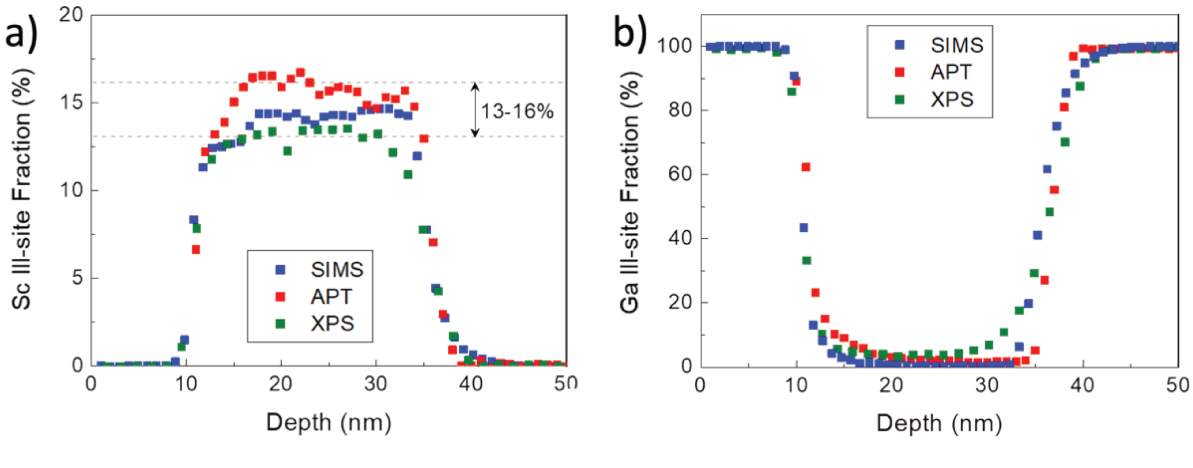

Figure 46: a) III-site fraction compared between XPS, SIMS and APT for a) Scandium and, b) Gallium.

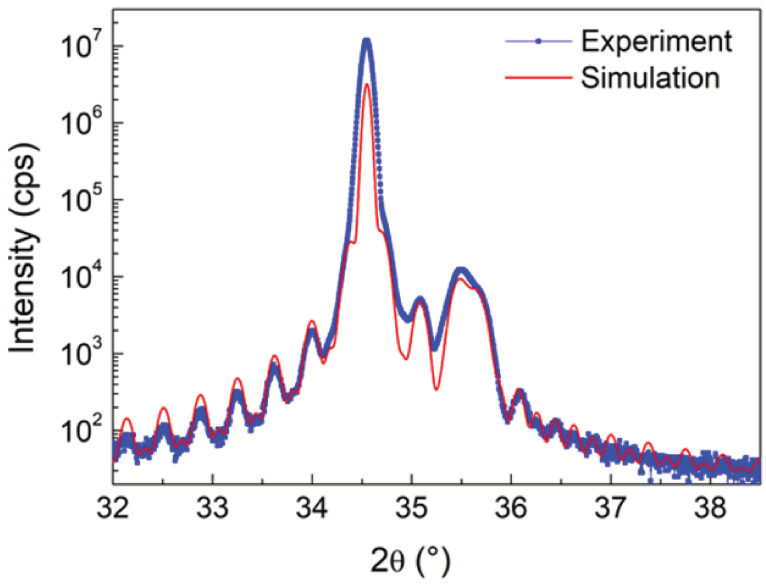

Figure 47: 2θ scan of 0002 reflection with the corresponding simulation of the studied GaN/ScAlN/GaN heterostructure.

with the fact that this interface is sufficiently abrupt to generate XRD spectra showing the oscillations with periods in agreement with the nominal thicknesses of the films corresponding to 25nm of GaN cap layer, 24 nm of ScAlN and a 1.5 nm of AlN interlayer. The simulation and the measurement are presented in Figure 47.

5.2 Crystalline quality

5.2.1 Phase purity analysis (XRD)

The HRXRD 0002 $2\theta/\omega$ scans of the studied samples with various growth temperature are shown in Figure 48 to evaluate the structural properties. In this case, the GaN measured signals encompass contributions from both MBE GaN and MOCVD, as the sample consists of a combination of these two growth methods. However, it should be noted that the GaN signals primarily reflect the properties of the MOCVD GaN layer, which has a thickness of approximately $3\mu m$, because MBE GaN layer is relatively thin (300-500 nm) and mainly replicates the crystal quality and strain of the thick layer. The asymmetry of the GaN peak plotted in a semi-log scale reveals a different strain gradient in some of the templates. However, the position of GaN peak at 34.5° indicates that the upper part of the templates is fully relaxed with an out-of-plane parameter $c = 5.189\mathring{A}$. The spectra show a second peak around 35.6° accounting for the presence of ScAlN. Within the studied growth temperature range, no additional peaks were detected, indicating the absence of any additional phases.

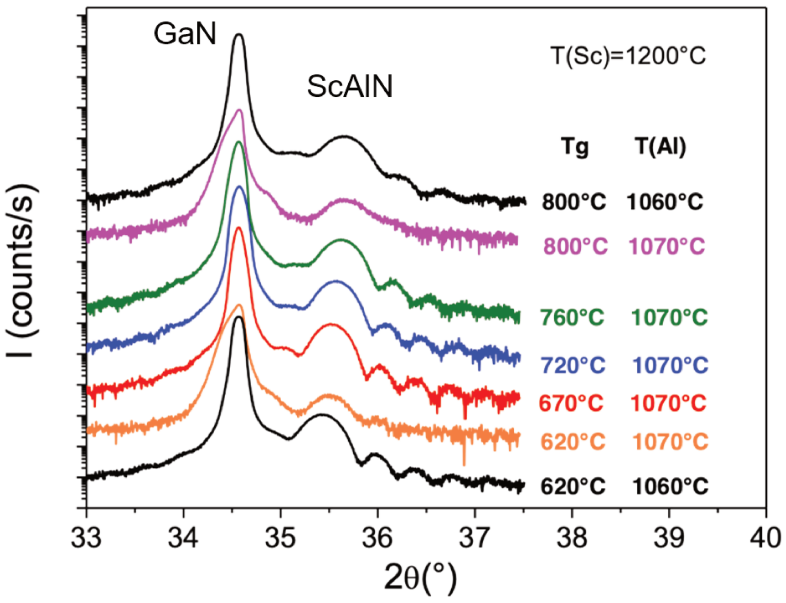

Figure 48: XRD 0002 2θ line scans of 25 nm ScAlN on GaN/sapphire as a function of growth temperature.

With an increase in the growth temperature, the ScAlN peak undergoes a continuous shift towards larger angles. This shift suggests a slight reduction in the out-of-plane lattice parameters of the ScAlN layer. This decrease can be attributed to a decrease in scandium amount within the material. These findings align with the XPS measurements presented in section " XRD Sc concentration and thickness investigations ". A comparable behavior has been noticed across a broader temperature range (from 400 to 900℃) for films produced using PAMBE on GaN. In this case, the ScAlN peaks shift from 35.6° to 36.6°, indicating a potential variation in the composition or strain of the ScAlN layer. XPS measurements did not reveal any specific trend in scandium composition change concerning the growth temperature in PAMBE. Nevertheless, the dominant characteristic peaks still validate the presence of the wurtzite structure. [90],

[145]. During the MOCVD growth of ScAlN with Cp_3Sc precursor, the temperature varies from 900℃ to 1200℃. As the temperature rises, the peaks tend to become narrower, suggesting a potential improvement in crystal quality. However, at lower temperatures ($T_g = 900C$), additional peaks emerge between the peaks of GaN and ScAlN, indicating the possible presence of Al_2O_3 [146]. Coming back to Figure 48, Pendellosung fringes are clearly observed for the films grown between 650℃ and 740℃ indicating smooth surfaces and interfaces. On the other hand, for lower and higher growth temperatures, the fringes disappear. Another growth trial was conducted several months later with sample growth at 620℃ and 800℃, however, on this occasion, fringes were observed. This observation may not necessarily be attributed to the high interface quality but could be associated with the change of the X-ray diffraction detector.

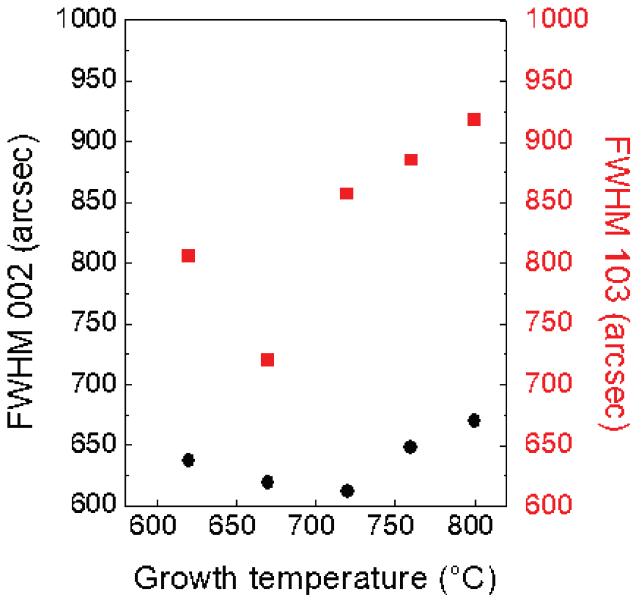

Figure 49: FWHM of rocking curves for the 0002 and $10\bar{1}3$ reflection in ScAlN.

To evaluate the crystal quality of the ScAlN film, the Full Width at Half Maximum (FWHM) values of the ω scans were extracted from the measurements (Figure 49). The FWHM of the (0002) reflection line is lower for growth temperatures (T_g) of 670℃ (620 arcsec) and 720℃ (612 arcsec), while the FWHM of the $(10\bar{1}3)$ reflection line is minimum at 720 arcsec for a T_g of 670℃. It is worth noting that the FWHM value of the $(10\bar{1}3)$ reflection obtained for T_g of 670℃ has been confirmed by multiple measurements. The beam spot size used in the measurements was around 10 mm.
Several measurements of FWHM for the (0002) and $((10\bar{1}3))$ reflections were performed on different regions of the sample, yielding a standard deviation of 7 arcsec and 14 arcsec, respectively. Furthermore, the (0002) and $((10\bar{1}3))$ reflection FWHMs of GaN were found to be very similar across all samples, approximately 360 arcsec and 430 arcsec, respectively. This indicates equivalent GaN template crystal quality, with a threading dislocation density estimated to be around $4 \times 10^8 cm^{-2}$. Based on the FWHM values, it can be concluded that the ScAlN film grown at around 670℃ exhibits the highest crystalline quality. Moreover, the evolution of both (0002) and $((10\bar{1}3))$ FWHMs is consistent with the vanishing of the Pendellösung fringes observed on $2\theta/\omega$ scans for the lowest and highest temperatures.

5.2.2 Scandium distribution in the alloy: APT analysis

According to Figure 45 and Figure 46, no lack or accumulation of scandium is noticed within the alloy and at the interfaces between the latter and the GaN layers, which indicates that no Sc segregation occurred during the growth. Furthermore, APT analysis not only provides the capability to determine the scandium amount within ScAlN but also offers insight into the nanoscale distribution of atoms within the layer.

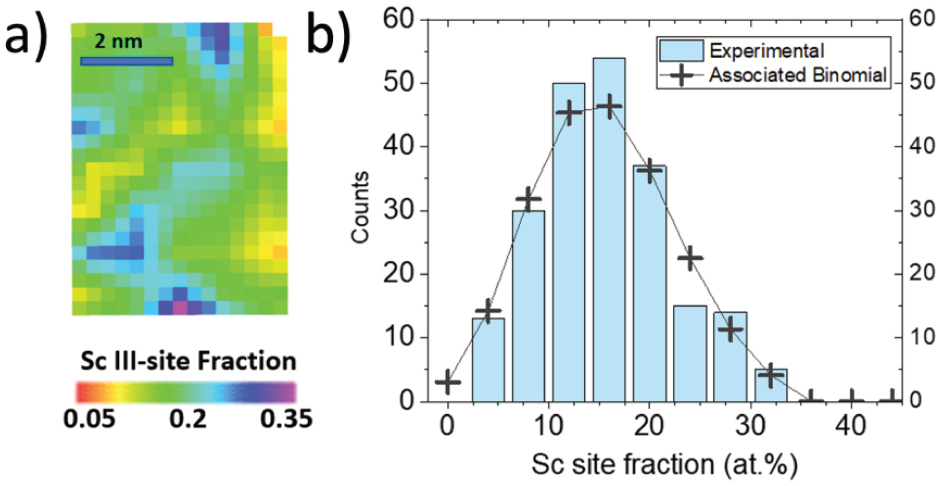

Figure 50: a) Sc site fraction map derived from data within ROI#2. B) Histogram depicting the frequency distribution of the observed Sc-site fraction, compared to the binomial distribution expected for a random alloy.

To visualize the variations in the ScAlN layer's alloy composition, Figure 50a illustrates a map of the Sc III-site fraction, obtained from a 2 nm thick section taken from ROI#2. We conducted a frequency-distribution analysis [147] on various sub-volumes extracted from the two specimens under examination. In Figure 50b is shown the III-site frequency histogram obtained from the sampling of ROI#2. Each sub volume had a base of 1x1 square nanometers and contained $N_{bin} = 25$ atoms. We then compared this resulting distribution to a binomial distribution with an expected value of $< x >= 0.16$. The comparison yielded a χ^2 value of 10.2 for $N_{DOF} = 9$ degrees of freedom, resulting in a p-value of p = 0.25. This p-value indicates that the alloy distribution aligns with a random distribution with a high degree of confidence [148]. In conclusion, we deduce that the scandium is randomly distributed into the ScAlN alloy and there is no cluster with a noticeable accumulation or lack of scandium.

5.2.3 Oxygen contamination in ScAlN barrier layer

The complementary use of SIMS, XPS and APT has provided significant insights into the elemental composition of the ScAlN alloy and its interaction with oxygen. XPS and SIMS techniques have revealed the presence of oxygen within the ScAlN alloy, suggesting a certain level of oxygen incorporation during the growth process. However, an intriguing phenomenon is revealed when comparing the ScAlN alloy to the GaN buffer layer.

Surface oxygen contamination is initially evident on the GaN cap layer but diminishes swiftly over etching time. Meanwhile, a conspicuous and abrupt rise in oxygen levels apparears throughout the entire ScAlN

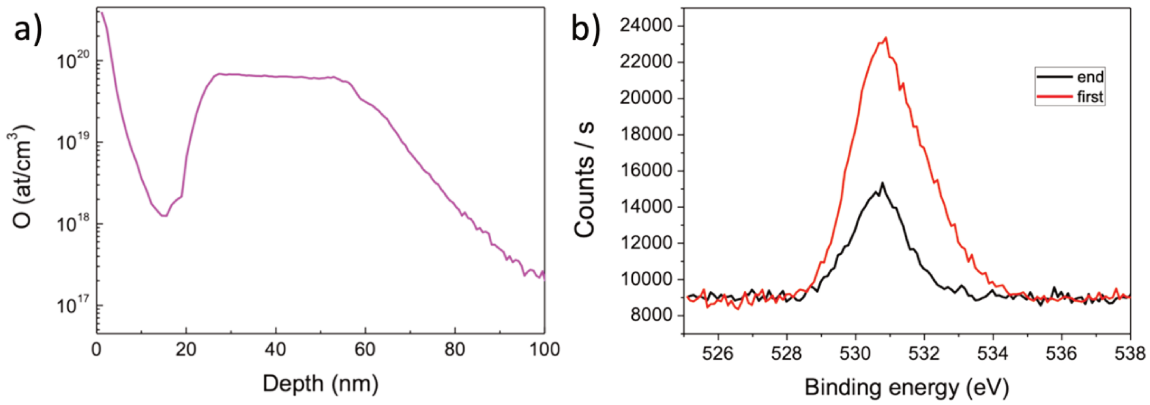

Figure 51: a) Oxygen incorporation in ScAlN observed by SIMS, and b) oxygen detection immediately after etching and 15 mins later observed by XPS.

barrier layer (see Figure 51a) followed by a slower decay of oxygen during the etching of the GaN buffer layer underneath which finally reaches the detection limit of oxygen in GaN ($10^{17}/cm^3$ for the present SIMS analysis).The decrease of oxygen signals in the GaN buffer layer points to a distinct difference in the affinity of oxygen with gallium and scandium/aluminum. Furthermore, observations indicate that as the scandium amount is elevated, there is a corresponding rise in oxygen incorporation[149] when reaching the ScAlN barrier. This phenomenon can be attributed to the pronounced propensity of scandium to undergo oxidation, a feature that surpasses even the oxidation affinity exhibited by aluminum.

The Figure 52 displays the oxygen site fraction profile (X(O)) throughout the entire reconstructed volume after APT analysis. X(O) is defined as the ratio of the number of oxygen atoms (n(O)) to the sum of oxygen, scandium (Sc), aluminum (Al), and gallium (Ga) atoms (n(O) + n(Sc) + n(Al) + n(Ga)). Notably, the surface exhibits a higher concentration of oxygen, potentially linked to sample preparation. The amorphization and damage caused by the FIB process might have increased the susceptibility of this region to oxidation. In contrast, deeper within the ScAlN layer, the oxygen concentration stabilizes. A comparison between the mass spectra of the entire dataset and that of the GaN layer demonstrates the disappearance of the 16 Da peak within GaN. This supports the notion that the 16 Da peak is associated with oxygen rather than molecular species like NH2+. Molecular species tend to become more prevalent in GaN, as GaN evaporates at lower fields, resulting in more molecular peaks [150]. Moreover, the measured oxygen concentration in GaN provides a reliable estimate of the noise level affecting the oxygen peak in the ScAlN layer. Consequently, we can assess the oxygen fraction in the ScAlN layer as approximately 0.20% ± 0.05%, which represents a significant impurity level. We speculate that the oxygen peak at the surface could be attributed to exposure to ambient air or parasitic species within the APT chamber. However, based on the current dataset, it remains challenging to definitively determine the source of oxygen within the ScAlN layer. Nonetheless, we can rule out contamination from the growth chamber, as the oxygen concentration in the lower GaN layer is below the SIMS detection limit. This observation underscores the strong affinity of ScAlN for oxygen. It is worth noting that the presence of oxygen can markedly impact the electronic properties of ScAlN layers, as previously reported by Casamento et al. [151]. Therefore, addressing this impurity issue systematically and comprehensively through further APT studies is essential. APT proves capable of accurately detecting oxygen impurities in ScAlN down to 0.1%, and even lower concentrations could be quantified in larger

sample volumes [152].

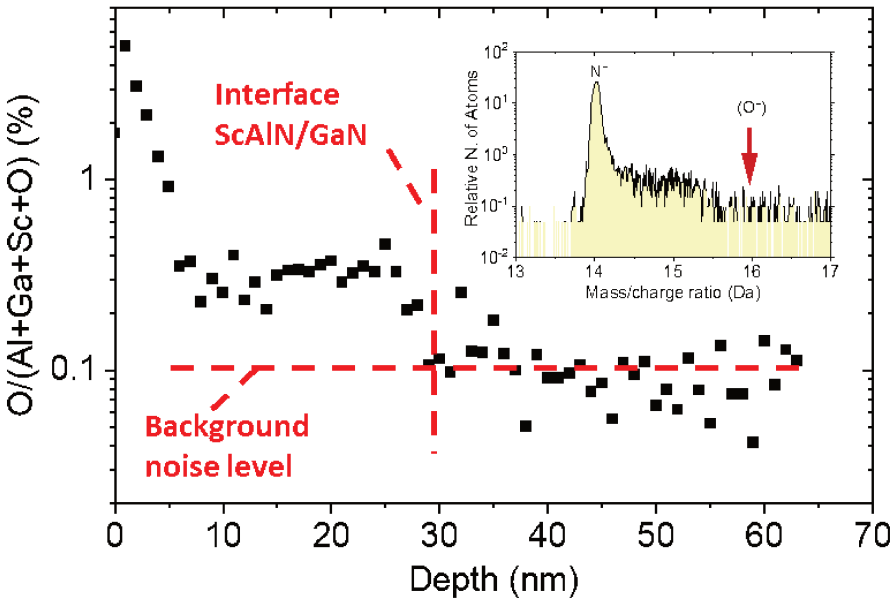

Figure 52: APT measures the oxygen fraction, relative to metallic elements, along the depth coordinate within a 3D reconstructed volume. In the inset, a close-up view of the mass spectrum (ranging from 13 to 17 Da) obtained from the GaN layer reveals a notable absence indicated by a red arrow, which corresponds to the missing O+ peak.

The presence of oxygen signals observed in SIMS, XPS and APT analyses can be attributed to various sources. Firstly, it is plausible that the initial source of impurity arises from the scandium precursor's purity. Additionally, due to scandium's heightened sensitivity to oxygen-rich environments, its detection is remarkably swift. This sensitivity is highlighted by our experimental results, where oxygen detection via XPS was conducted immediately after etching and then again after a 15-minute interval. Strikingly, the data reveals a twofold surge in oxygen content following the 15-minute duration, reinforcing the involvement of rapid oxygen adsorption onto scandium-based surfaces. This observation strongly emphasizes the critical role of environmental conditions in influencing the material's surface composition and underscores the importance of meticulous chamber management to ensure accurate analyses. (See Figure 51b). Indeed, XPS, SIMS and APT probe the surface of the alloy and necessitate an extremely pure environment to limit re-oxidation. XPS, SIMS, and APT operate within ultra-high vacuum conditions, with pressures ranging from approximately 10^{-9} to 10^{-10} mbar. To explain the significant increase in oxygen levels observed in XPS measurements (up to 5% oxygen content) compared to minimal oxygen levels in APT measurements (less than 0.2% oxygen), it is likely attributed to the utilization of a flood gun in XPS. The purpose of the flood gun is to mitigate charge buildup by emitting a controlled flow of low-energy electrons onto a specific target area. This action, however, leads to an increase in chamber pressure, raising it to around 10^{-7} mbar, thereby altering the environmental conditions significantly.

5.2.4 XRD Sc concentration and thickness investigations through theoretical calculation and simulation

In the early stages of ScAlN research at CRHEA, attempts were made to grow this alloy using NH_3 MBE, but since there were no prior studies on this specific process, determining the optimal growth conditions to achieve the desired alloy composition for HEMT barrier layers was challenging. Our study focused on achieving a lattice matched ScAlN/GaN structure with approximately 18% Scandium content, which is crucial for its application in High Electron Mobility Transistors (HEMT). While XRD measurements provide valuable information, they alone cannot accurately determine the elemental composition of the alloy. We acknowledged that calculating the alloy composition from XRD measurements can be prone to significant errors. Two main factors contribute to uncertainties in the position of the 2θ the composition of the alloy and potential strain in the thin unrelaxed layers. Hence, the insights garnered from XPS and SIMS analyses reveal a scandium molar fraction near 15%. This prompts an inquiry into the reliability of XRD measurements for accurately ascertaining the scandium content. The diagram in Figure 39 illustrates the fully relaxed ScAlN structure, which aligns with the theoretical calculations and simulations conducted by Ambacher et al. This presentation encompasses both the in-plane and out-of-plane lattice parameters for ScAlN. Furthermore, Figure 38 offers insight into the fully strained ScAlN when grown on a GaN substrate. In this configuration, the in-plane lattice parameter of ScAlN closely resembles that of GaN, hovering around $3.189\mathring{A}$ assuming that the ScAlN films are epitaxially deposited onto GaN prior to reaching the critical thickness at which ScAlN begins to relax on the GaN substrate. Since the in-plane lattice parameter conforms to the GaN substrate's properties, this also influences the out-of-plane lattice parameter. When compared to the relaxed out-of-plane lattice parameter of ScAlN, Figure 39b demonstrates an expansion along the c-axis, a phenomenon that becomes more pronounced as the scandium content increases.

Using the AMASS software, it becomes feasible to simulate both the scandium amount and the thicknesses of the ScAlN barrier. To initiate this process, the manipulation of XRD 2θ scans has been carried out across the samples grown at varying growth temperatures. The determination of ScAlN position peaks within these scans offers valuable insights into the scandium amount present in the alloy. Subsequently, the simulation of interfringes has enabled the estimation of ScAlN barrier thicknesses. This simulation procedure is carried out using [31]–[33]elastic coefficients and lattice parameters of wurtzite AlN and ScN. For AlN, $a = 3.113\mathring{A}$, $c = 4.981\mathring{A}$, $C_{13} = 10^8$ GPa and $C_{33} = 373$ GPa and for ScN, $a = 3.49\mathring{A}$, $c = 5.58\mathring{A}$, $C_{13} = 121.5$ GPa and $C_{33} = 51.3$ GPa.

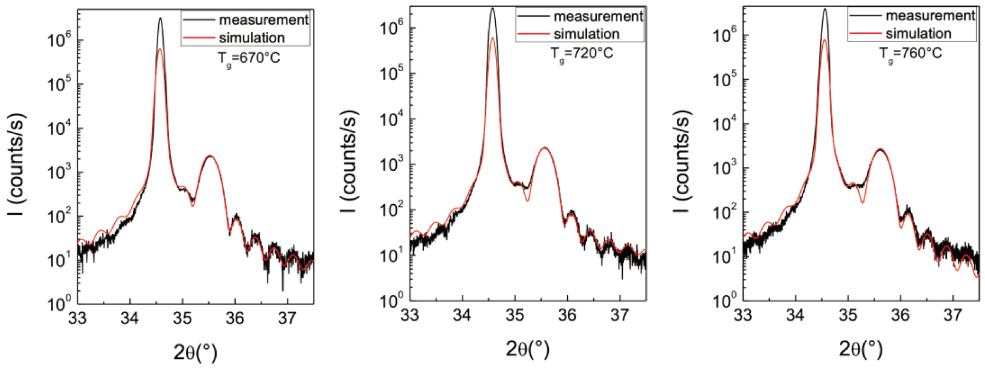

Figure 53: 2θ scan simulation for PTC 1217, PTC 1216 and PTC1220.

The simulated 2θ scans, as depicted in Figure 53 and Figure 54, serve the purpose of extracting both the scandium molar fraction and the ScAlN thickness. For the barrier thickness determination, the presence of interfringes is a prerequisite. However, as these interfringes dramatically vanish in certain scans, conducting thickness simulations becomes unfeasible. As a result, simulations have been restricted to samples PTC 1216, PTC 1217, PTC 1220, PTC 1269, and PTC 1271. Through the simulation of these patterns, the barrier thicknesses are estimated to be approximately 26 nm. This outcome reveals a consistent growth rate across different growth temperatures, thereby providing an explanation for the uniform sticking coefficient of ScAlN within this temperature range. In the context of PAMBE, evident shifts were observed in the ScAlN peaks, manifesting as a shift towards lower angles. These shifts indicate an expansion in the out-of-plane lattice parameters. In this case, XPS analyses revealed a simultaneous increase in scandium concentration. This phenomenon underscores a change where scandium atoms, replacing aluminum atoms, trigger an expansion in the unit cell dimensions. Consequently, an increase in scandium amount within the ScAlN alloy leads to an increase in the unit cell parameters. In contrast, as depicted in Figure 53, the ScAlN peaks exhibit a shift towards larger angles, indicating a reduction in the out-of-plane lattice parameters while increasing the growth temperature. Thus, the XRD simulations summarized in Figure 42b suggests a slight reduction in scandium content. This is opposite to the observations drawn from PAMBE analyses.

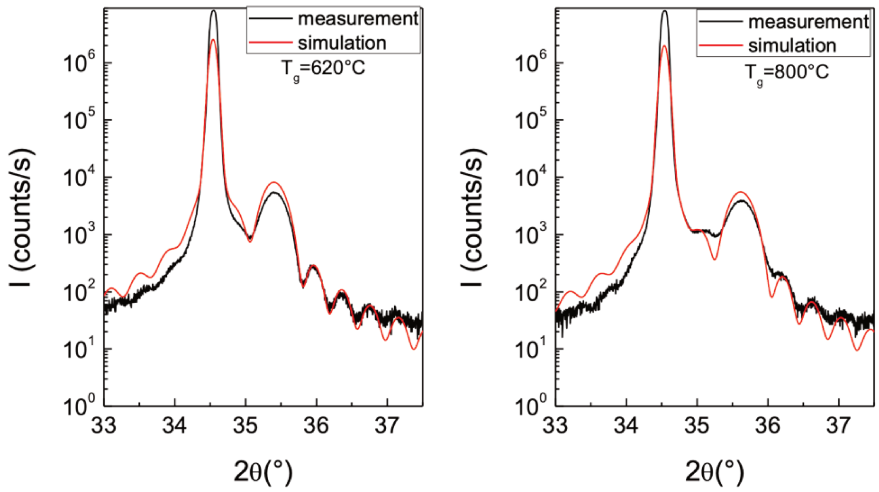

Figure 54: 2θ scan simulation for PTC 1269 and PTC1271.

Simulations were conducted on samples grown at both notably low and high temperatures, specifically for PTC1269 and PTC1271 on which we have been able to obtain interfringes and to extract thickness of approximately 26nm. The shift observed in the ScAlN peak angle, as evident in Figure 54, is pronounced, displaying a tendency towards larger angles. Through simulations, it becomes evident that this shift can be attributed to a reduction in scandium amount, a deduction corroborated by XPS analyses for the whole set of studied samples. For instance, PTC1269, derived from a sample grown at 620℃, boasts a scandium fraction of 16%, while PTC1271, originating from growth at 800℃, exhibits a scandium fraction around 12%.

In conclusion, through a combination of experimental techniques such as XRD 2θ scans, and theoretical calculations involving elastic coefficients, we have been able to successfully determine the scandium amount and thicknesses in our ScAlN layers grown on GaN. Clearly, compared with PAMBE metal-rich

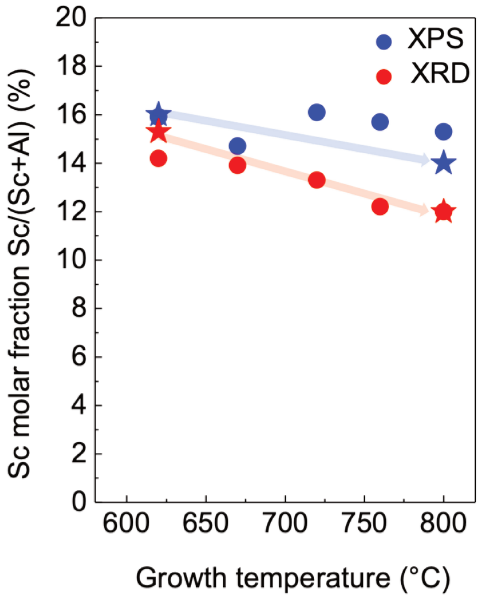

Figure 55: A comparison between XPS and XRD 2θ scan simulations for determining scandium molar fraction. The stars account for the samples PTC1269 and PTC1271.

growth, the nitrogen-rich growth regime with ammonia induces a noticeably different dependency with temperature. It results in a slow decrease of the Sc amount and almost unchanged growth rate, which are obvious advantages for the achievement of reproducible growths. However, even if the presence of oscillations in 2θ XRD scans or XRR spectra indicates the presence of smooth surface and interface, the crystal lattice matching between the alloy and the GaN buffer layer is not attested by these measurements. This information is crucial for optimizing the performance of High Electron Mobility Transistors and other potential applications.

5.2.5 Lattice matched $Sc_{0.15}Al_{0.85}N/GaN$

Reciprocal space mapping (RSM) is based on XRD. It was employed to comprehensively investigate the lattice constants and lattice strain of the grown barrier layers. A 2D reciprocal space map is shown in Figure 56 and the intensity of collected X-ray signal is plotted as a function of the scattering vector coordinates Q_x and Q_z, measured in units of $1/\lambda$ ($\AA^{-1}$). The RSM scans were specifically conducted on the $(10\bar{1}5)$ reflection of the grown samples. The corresponding crystal plane is inclined with respect to the growth direction, so that projections parallel and perpendicular to the latter can be used to calculate the lattice parameters a and c. For this purpose, the position of the diffraction intensity maxima was pointed, and the following formulas were applied (unit in nm):

$$a = \frac{2}{Q_x\sqrt{3}}(nm)$$

$$c = \frac{5}{Q_z}(nm)$$

Q_x and Q_z formulas are reported in the section dedicated to "X-ray diffraction" in Appendices.

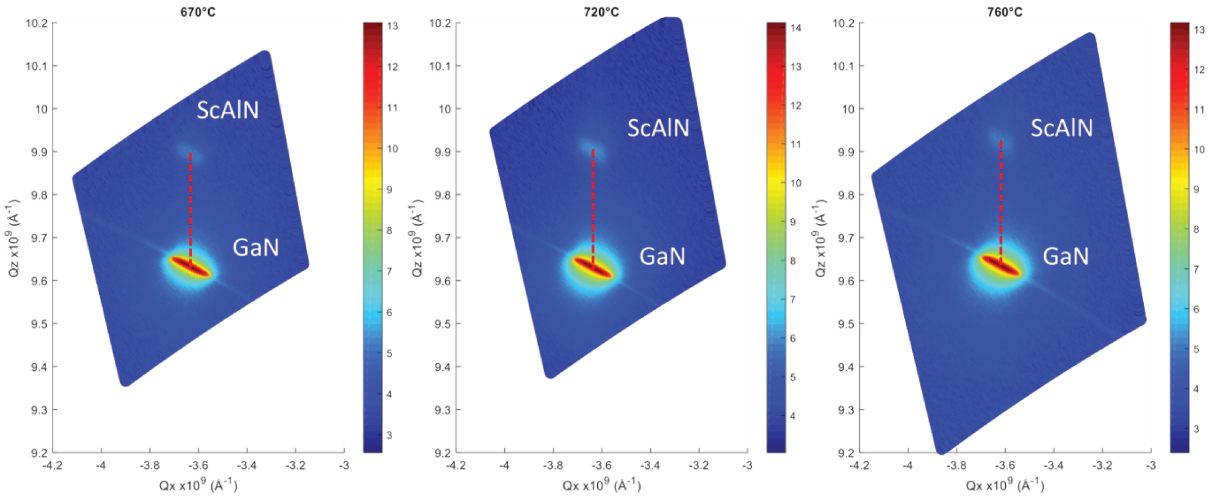

Figure 56: RSM of the $10\bar{1}5$ reflection for samples grown at 620℃, 720℃ and 760℃, indicating matching Q_x values between ScAlN and GaN, signifying identical in-plane lattice parameters.

RSM for sample grown at 670℃, 720℃ and 760℃ are shown in Figure 56. The bright pattern at $Q_x = 3.631 \times 10^9 \mathring{A}^{-1}$ and $Q_z = 9.652 \times 10^9 \mathring{A}^{-1}$ corresponds to the stain relaxed GaN film. ScAlN pattern (light blue spot) has the same Q_x as GaN showing that ScAlN layers are either lattice matched with or perfectly strained (pseudomorphic) on it. The values of lattice parameters deduced from these measurements are presented in Table 2. In the case of InAlN alloy lattice matched on GaN [153], the presence of local strain and/or compositional fluctuations can arise from the significant differences in bonding energies between AlN and InN (2.88 eV and 1.0 eV, respectively). These differences lead to challenges in maintaining a perfect lattice match and can result in strain-induced defects or compositional variations. We need to highlight that the extended broadening of RSM $10\bar{1}5$ reflections is primarily attributed to the presence of extremely thin ScAlN films.

Sample	Tg(℃)	a-GaN ($\mathring{A}$)	c-GaN($\mathring{A}$)	a-ScAlN ($\mathring{A}$)	c-ScAlN ($\mathring{A}$)	$\delta a/a$
PTC1218	620	3.19	5.19	3.18	5.06	0.003
PTC1216	670	3.19	5.18	3.20	5.05	0.003
PTC1217	720	3.19	5.19	3.19	5.04	0
PTC1220	760	3.21	5.18	3.20	5.04	0.003

Table 7: Lattice parameters for samples grown at different growth temperature for ScAlN deduced from RSM.

Consequently, the discrepancy in error between Q_x, which pertains to the in-plane lattice parameters, and Q_z, which relates to the out-of-plane lattice parameter, should be more pronounced. For the present in-plane lattice parameters of ScAlN, the error ranges between 0.0005 and 0.0008 $\mathring{A}$. Notably, this error

magnitude remains consistent for GaN as well. Figure 57 shows the extrapolation of the out-of-plane lattice parameters of ScAlN deduced from RSM as a function of scandium amount deduced from XPS compared to the Figure 38 that highlights the in-plane and out-of-plane lattice parameters deduced theoretically by [65]. This extrapolation underscores that the out-of-plane lattice parameters extend beyond the thresholds that distinguish fully relaxed configurations from fully strained ones. Based on the theoretical values, our data points appear to be approximately 22% scandium, which significantly deviates from the values obtained through XPS, SIMS, or APT measurements.

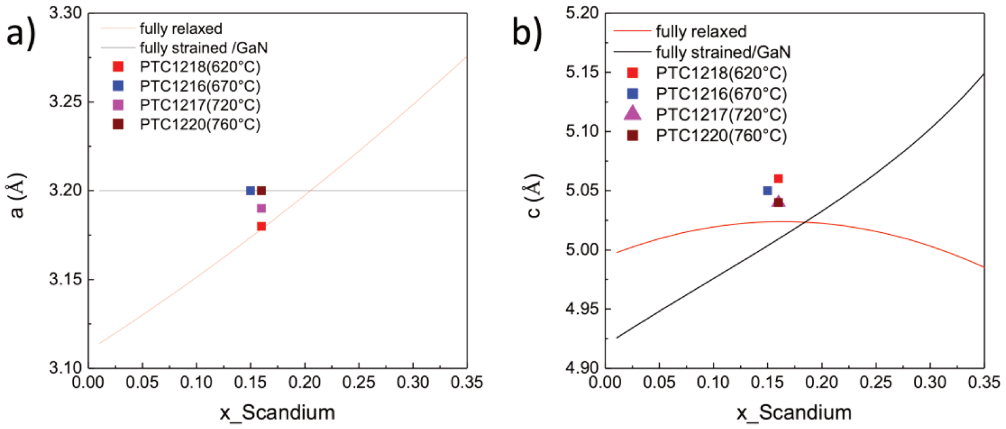

Figure 57: Data included as a result of our work and added to Figure 38.

Using RSM, we can infer the strain state of a material, whether it is under strain or relaxed. For ScAlN films with a thickness of around 25 nm, our RSM analysis reveals that no relaxation has occurred. This implies that we can determine the scandium content accurately using just 2θ scans. By employing AMASS simulation software and simulating the 2θ scan, as detailed in section "XRD Sc content and thickness investigations through theoretical calculations and simulations ", we ascertain that the in-plane lattice parameter matches that of GaN for thicknesses below 25 nm. Consequently, we can estimate the film thickness and scandium content with values closely aligned with those obtained through alternative quantitative methods.

5.2.6 Understanding of the impact of growth temperature on ScAlN thickness

HRXRD measurements discussed earlier provide layer thickness estimation with a limited accuracy. Therefore, to complement the analysis, X-ray reflectometry (XRR) was employed. This additional analysis serves to gain a more comprehensive understanding of the crystal characteristics and structural properties of the ScAlN films.

Figure 58a presents the XRR spectrum obtained for the sample grown at 670℃, along with the corresponding fit obtained using GenX software. XRR involves irradiating the sample surface with X-rays at grazing incidence angles. As the incident angle increases, the X-rays start to penetrate the material instead of being reflected. It is essential to note that the value of θ_c depends on the density of the sample material. In this series of samples, the critical angle (θ_c) falls within the range of 0.4° to 0.5°, signifying the material's density characteristics. When the incident angles exceed the critical angle (θ_c), interference fringes emerge due to interactions at the sample surface and the interfaces beneath the crystalline film being investigated.

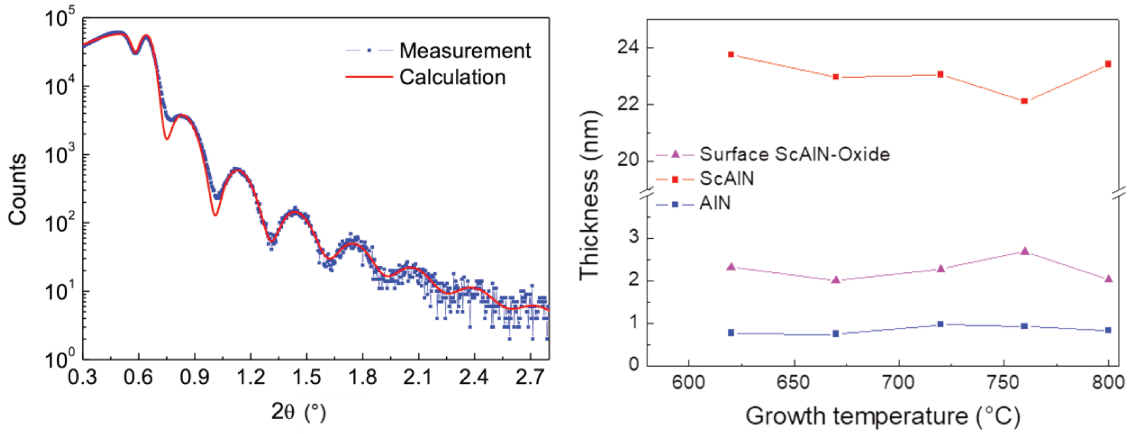

Figure 58: a) XRR scan for sample grown at 670℃, and b) Barrier thicknesses deduced from XRR for the samples grown at different temperature.

The amplitude and frequency of these fringes are directly associated with the thickness and roughness of the film. A larger roughness at the surface and/or interface of the film leads to diffuse scattering, resulting in low intensity and weak interference fringes in the XRR measurements. Remarkably, within the precision of the fitting procedure, the extracted thicknesses remain consistent across the entire temperature range under investigation. This indicates that the growth temperature has little influence on the Sc amount and the layer thickness. The stable sticking coefficients of aluminum (Al) and scandium (Sc) within this temperature range are responsible for this phenomenon. As a result, the ScAlN layer exhibits a growth rate of 150 nm/h. These findings highlight the reliable and stable growth characteristics of ScAlN, with minimal variations in thickness across the studied temperature range. This contrasts with the results obtained by MOCVD where the growth rate increased slightly at higher growth temperature[146]. The simulated AlN interlayer is approximately 0.7 nm, followed by a pure ScAlN layer of approximately 23 nm in thickness with a molar fraction of scandium equal to 15%. Notably, a better fit is obtained when an additional layer of ScAlN oxides, with a thickness ranging from 2 to 3 nm, is present on the surface. This layer's presence may have resulted from surface oxidation during the growth process or exposure to ambient conditions after deposition. The thickness of the ScAlN oxides layer can vary, but it is typically between 2 and 3 nm. The ScAlN oxide layer could influence the material's electrical properties. Indeed, it is crucial to highlight that no protective cap layer was deposited on these samples. To comprehensively explore the impact of ambient contamination on ScAlN, the implementation of a capping protective layer becomes essential. The protective layer will act as a barrier, shielding the ScAlN from external factors, such as humidity and other environmental influences.

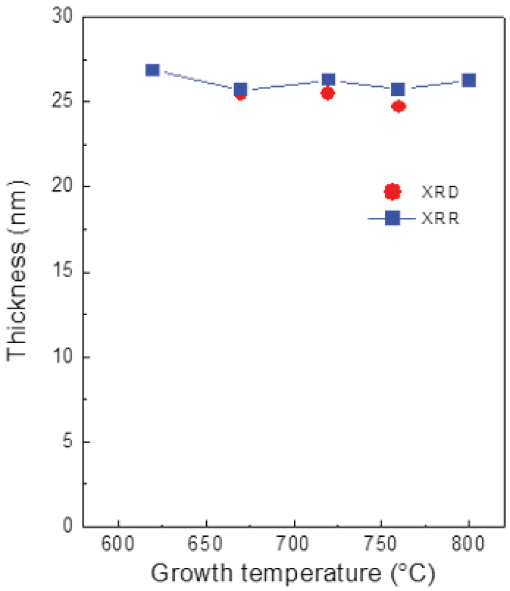

Figure 59: Thicknesses inferred from X-ray reflectivity (XRR) and X-ray diffraction (XRD) simulations, with their values varying in relation to the growth temperature.

Figure 59 illustrates the consistency of the XRD simulation conducted using the AMASS software, as previously described in the section titled " XRD Sc concentration and thickness investigations through theoretical calculation and simulation" This suggests that thickness can be accurately determined from the simulations using AMASS without the need to resort to XRR.

5.3 ScAlN surface morphology

5.3.1 Insights from reflection high energy electron diffraction (RHEED) and atom force microscopy (AFM) imaging

In-situ RHEED analysis was performed within the MBE chamber. RHEED provides instant surface morphology analysis, specifically for the few monolayers on the surface. Figure 60 illustrates the RHEED patterns obtained at the end of the growth when the deposition of scandium and aluminum was halted. Analysis of the RHEED patterns revealed a consistent 2D growth for all investigated temperatures, with no indication of 3D growth or additional spots, indicating the absence of additional phases. In N-rich PAMBE growth regime [19], [154], for extremely low growth temperatures, spotty RHEED patterns are observed, indicating the occurrence of a mixed 2D/3D growth mode. As the growth temperature increases within the range of 520℃ to 730℃, the RHEED patterns exhibit spot-modulated streaky patterns, indicating a shift towards a predominantly pure 2D growth mode. Notably, at 900℃, significant changes in the RHEED patterns are observed, characterized by the emergence of a second set of spots. This observation suggests the possible presence of rotated 111-oriented cubic phases. In our study, at Tg=620℃ some broadening of the lines appears in the RHEED patterns, indicating a less ordered surface. However, for all the other investigated

temperatures, the lines are well defined and exhibit a smoother appearance. Even at Tg=800℃ the surface morphology indicates the streakiest lines. Higher growth temperature has not been investigated in this study.

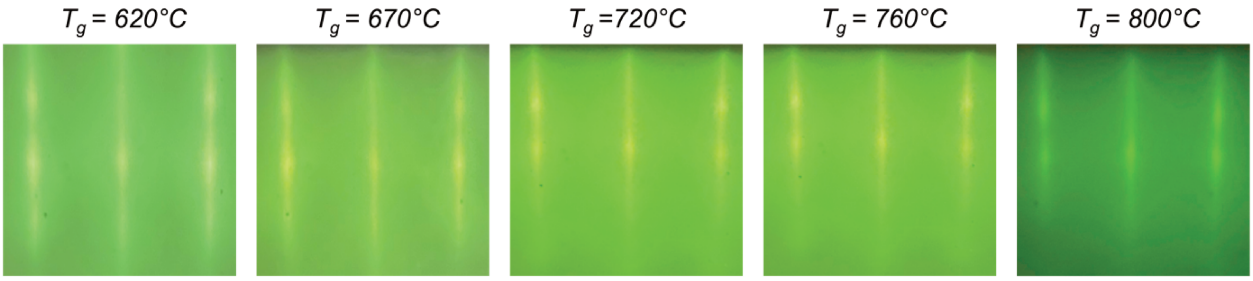

Figure 60: RHEED patterns images taking at the end of the growth process as a function of all the growth temperature range.

[36] PAMBE study shows the influence of the III/V flux ratio on surface morphology [154], it was observed, with a growth temperature about 700℃ for ScAlN layers, that with a very high N_2 flow, a growth mode characterized by a combination of 2D, and 3D growth was observed. However, as the N_2 flow was decreased, the growth mode shifted towards a predominantly pure 2D growth mode, resulting in improved surface morphology. Conversely, with very low N_2 flow, the surface morphology of ScAlN exhibited a different behavior. In this case, the material may exhibit a combination of single-crystal and polycrystalline regions, or the grains may be slightly tilted with respect to each other. These findings highlight the significance of the III/V flux ratio in determining the surface morphology of ScAlN, with high N_2 flow favoring a more 2D growth mode and low N2 flow leading to a potentially more complex morphology involving both single-crystal and polycrystalline regions or grain tilting. In our research, we have observed that the RHEED patterns appear to resemble those typically associated with a low III/V ratio, despite the fact that we are actually growing our samples in a nitrogen-rich environment.

After the samples were removed from the MBE chamber, ex-situ observations were conducted on these samples using AFM (Atomic Force Microscopy). The film grown within the temperature range of 670-760℃ provides evidence of two-dimensional growth, exhibiting a root mean square (rms) roughness below 0.4 nm over area scans of $500 \times 500nm^2$.

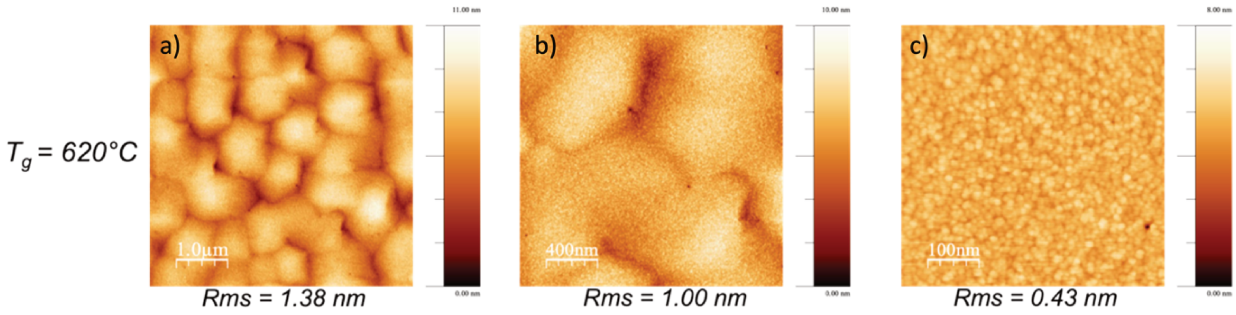

Figure 61: a) $5 \times 5\mu m^2$, b) $2 \times 2\mu m^2$ and c) $500 \times 500nm^2$ AFM image of sample grown at 620℃.

Figure 61a presents a $5 \times 5\mu m^2$ AFM image capturing the surface morphology of the sample. The image reveals the presence of large mounds with a diameter of approximately $1\mu m$, which corresponds to the growth of gallium nitride (GaN) and reveal the well-known kinetic roughening phenomena [155], [156]. When GaN is grown using nitrogen (N_2) PAMBE with a Ga-rich near stoichiometry III/V ratio, the surface exhibits a spiral growth morphology with approximately 200 nm diameter, along with the presence of atomic steps. Additionally, it is worth mentioning that the roughness of the surface, measured as the root mean square (rms), is approximately 1 nm for a $1 \times 1\mu m^2$ scan [134]. On the other hand, when GaN is grown under an N-rich regime using PAMBE, the surface is primarily characterized by the presence of hillocks with diameters ranging from 30 to 50 nm. These hillocks dominate the surface morphology in this growth condition[157].

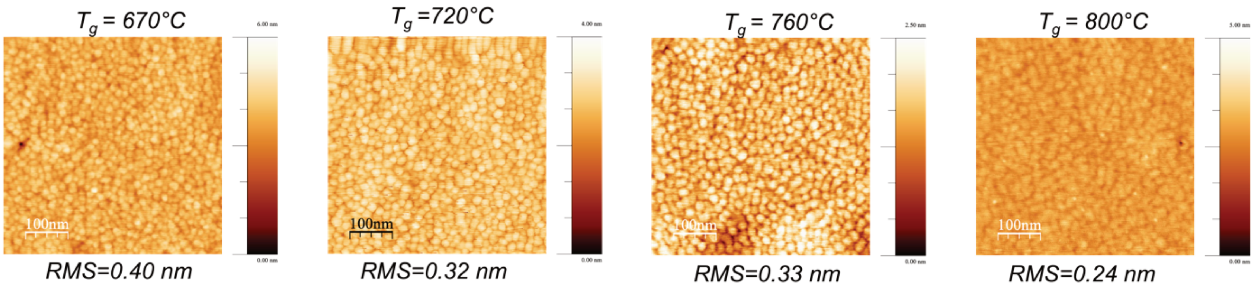

Figure 62: $500 \times 500nm^2$ AFM images of ScAlN/GaN grown at 670 ℃, 720 ℃, 760 ℃ and 800 ℃.

To examine the morphology of ScAlN, a closer look is required. Hence, a $2 \times 2\mu m^2$ image (Figure 61b) was captured, revealing the presence of grains of deposited ScAlN. To further analyze the ScAlN morphology, a smaller area of $500 \times 500nm^2$ (Figure 61c) was studied. Figure 62 demonstrates the characteristic surface morphology of the film grown within the temperature range of 670-800 ℃, showcasing homogeneous features with an average diameter of 20 nm. The periodic fluctuations in height resulting from these features account for the slight intensity modulation observed along the diffraction lines of the RHEED pattern, as depicted in Figure 60. For Tg=620 ℃ and Tg=800 ℃, the film exhibits less homogeneous features. Furthermore, for $500 \times 500nm^2$ scans, the rms roughness decreased from 0.43 ± 0.08 to 0.24 ± 0.08 nm as the growth temperature was increased from 620 ℃ to 800 ℃. For comparison, during the growth of ScAlN by PAMBE with scandium content ranging from 14% to 20% to achieve lattice matching with GaN, spiral atomic steps with a diameter of approximately 30 nm were observed[158], [159]. As the III/V ratio was increased, the diameter of these spiral atomic steps also increased, reaching up to 70 nm[154].

5.3.2 Grain size

Subsequently, as the growth temperature is increased for the samples, rms roughness decreases and well-defined grains emerge, providing an opportunity to investigate the relationship between grain sizes and growth temperature. The analysis focused on ScAlN samples with a nominal thickness of 25 nm. A specialized software was employed to exhibit distinct boundaries for each grain within the samples called SPIP (scanning probe image processor). Subsequently, a comprehensive statistical analysis was conducted to derive the precise values of the individual grain diameters.

The Figure 63 depicts the surface morphology observed through AFM, followed by the outlined boundaries of the grains as defined by the software. This visual representation offers initial insight into the grain

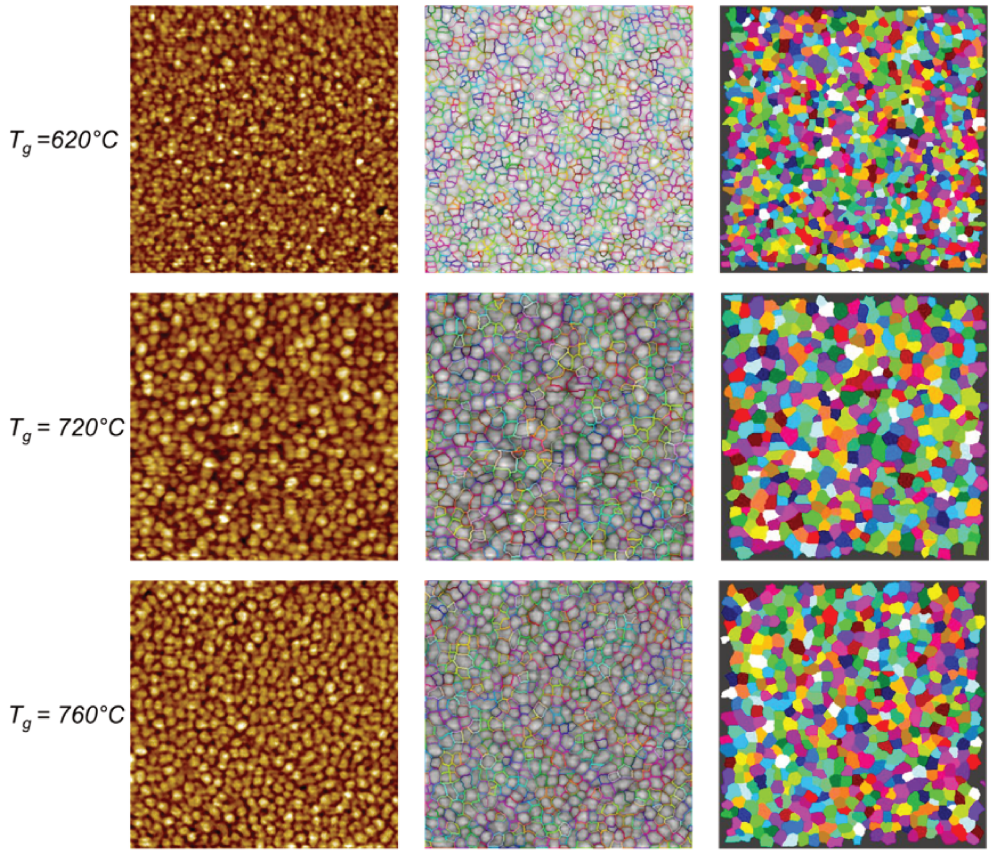

Figure 63: Grain size as a function of growth temperature.

enlargement as the growth temperature is elevated. To obtain a more comprehensive understanding of the relationship between grain sizes and growth temperature, a thorough statistical analysis was conducted. Notably, from the Figure 64, it becomes evident that at a growth temperature of 620℃, the grain area average measures approximately $170nm^2$, characterized by a small standard variation (σ) equal to $82nm^2$ which is relatively low indicating an homogeneity in the grains of the surface. Subsequently, at an increased temperature of around 720℃, the grain surface displays a bimodal distribution, indicating the coexistence of two groups of grains: one with an area around $250nm^2$ and the other around $350nm^2$. This may also be considered as a spread distribution with a mean diameter centered around $300nm^2$ with a $\sigma = 130nm^2$. Lastly, at a growth temperature of 760℃, the FWHM expands significantly, indicative of an uneven feature distribution across the surface with a mean diameter in the range of $400nm^2$ corresponding to $\sigma = 215nm^2$.

In summary, within the examined temperature range, a subtle rise in feature diameter is observed as the growth temperature is increased. According to the first APT analyses, no composition fluctuation occurs within the ScAlN alloy, so these features do not result from such a phenomenon. As a consequence, at first order, the increase of the mean diameter and the decrease of the rms roughness with the growth temperature may indicate that these grains consist of 2D islands of homogeneous composition but with size and height determined by the adatoms diffusion.

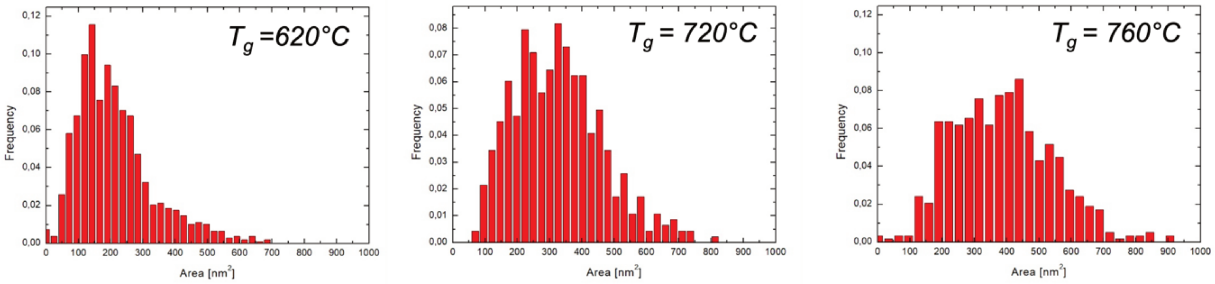

Figure 64: Histograms that depict the quantity of grains relative to their corresponding surface area measured in nm^2.

5.4 Conclusion

In this chapter, we have explored the growth conditions for ScAlN barrier layers grown on GaN on sapphire templates. Specifically, we have focused on the growth of ScAlN with a nominal thickness of 26 nm and examined the influence of growth temperature on the properties of the ScAlN barrier layer. Our investigation began with an analysis of the crystal structure of ScAlN under our growth conditions. We found that within the temperature range of 620-800℃, we were able to maintain a single wurtzite phase, which exhibited superior crystalline quality at lower growth temperatures compared to higher ones. This conclusion was substantiated by XRD omega scans, which revealed the full width at half maximum of the diffraction peaks. To gain deeper insights into the crystal structure quality, APT analysis was conducted, which demonstrated the absence of composition fluctuations within the growing layers. Additionally, we conducted a study to estimate the scandium content in the ScAlN alloy. Initially, we made theoretical predictions based on the lattice parameters of the material. However, to validate the accuracy of these calculations and simulations (including thickness and content simulations), we employed XPS, SIMS, and APT techniques to quantify the scandium amount. All three techniques consistently indicated a scandium molar fraction of approximately 15%. It is worth noting that with XPS analyses, nitrogen did not conform to stoichiometry with scandium and aluminum, making the quantitative analysis more complex. Nevertheless, we successfully determined the scandium amount by comparing the III elements together. Furthermore, we examined the surface morphology of the ScAlN films grown via NH_3 MBE and observed the presence of grains on the surface. These grains seem to be 2D islands of uniform composition alloy with a mean diameter increasing with growth temperature. Furthermore, the confirmation of scandium content through multiple analytical techniques, coupled with consistent results from simulations, underscores the reliability of estimating scandium content using simulations of the XRD 2θ 0002 scan for ScAlN thickness below 25nm.

6 Influence of the ScAlN thickness and Scandium concentration

6.1 Effect of the ScAlN barrier thickness

The primary objective is to achieve significantly reduced barrier thickness to mitigate short channel effects and enable shorter gate lengths for enhanced high-frequency performance. Considering this objective, an investigation was conducted to examine the influence of barrier thickness on both crystalline quality and the concentration of electrons in the 2DEG. To initiate this study, it was essential to exercise control over the growth process and estimate the thickness as it progressed. This estimation of thickness enabled the determination of the corresponding suitable growth duration. Considering prior reports indicating the preference for lower growth temperatures in terms of crystal quality, the samples with varying thicknesses were grown at 670℃, the optimal temperature identified for 25 nm thick films grown by NH3 MBE. Accordingly, the growth duration was adjusted for the desired thicknesses. For instance, to achieve thicknesses of 25 nm, 15 nm, 10 nm, and 5 nm, the corresponding growth durations were approximately 10 minutes, 6 minutes, 4 minutes, and 2 minutes, respectively.

6.2 ScAlN: surface morphology

Upon examining the surface morphology of ScAlN grown by NH_3 MBE using AFM, a trend emerges. As shown by the previous analyses these grains only consist in the modulation of the height, in other words a local change of the thickness of the ScAlN film. The grain size appears to be intricately linked to the thickness of the ScAlN barrier. As this barrier thickness increases, the formation of distinct grain structures becomes increasingly apparent. When observing the AFM images (see Figure 65), an evolution in grain formation becomes evident. For a barrier thickness of 5 nm, the grains remain elusive, lacking clear definition and formation. This lack of coherent structure is indicative of an early stage in the roughening process. Progressing to a thickness of 10 nm, a transformation occurs. The grains begin to take on more discernible shapes, marking the initiation of the grain formation process. Stepping further to a barrier thickness of 16 nm, the grains become perceptible; however, their overall arrangement lacks the order observed in more developed structures. Finally, the most remarkable transformation unfolds at a barrier thickness of 25 nm. Here, the surface exhibits fully formed, well-defined, and systematically organized grains. Notably, these grains maintain a uniform size and shape, demonstrating a high level of maturity in the roughening process.

In summary, the AFM analysis of ScAlN grown by NH_3 MBE underscores the significance of barrier thickness in the crystalline morphology. The distinct evolution from indistinct structures at lower thicknesses to organized and uniform grains at higher thicknesses presents similarities with the kinetic roughening process observed for GaN at larger scales and reaffirms the intricate relationship between growth conditions and resulting material characteristics [156].

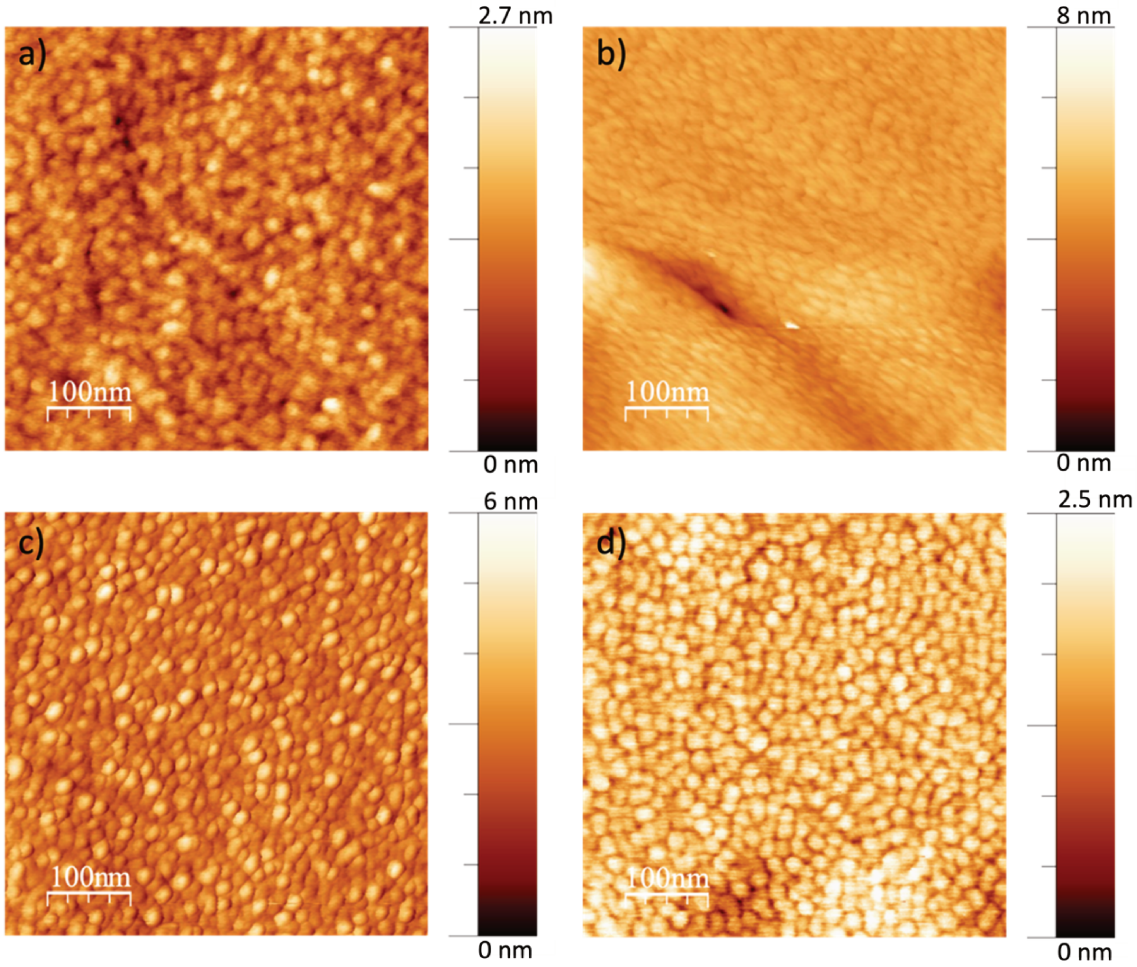

Figure 65: AFM images measuring $500 \times 500nm^2$ *for various ScAlN thicknesses: a) 5 nm, b) 10 nm, c) 16 nm, and d) 25 nm.*

6.2.1 ScAlN barrier crystal quality.

The analysis of the XRD 0002 reflection in a 2θ scan conducted on samples with ScAlN barrier thicknesses of 5 nm, 10 nm, 16 nm, and 25 nm yields noteworthy insights. In the XRD spectrum, distinct features emerge, reflecting the underlying material properties. Notably, the fully relaxed GaN template presents prominent peaks indicative of its crystalline structure. Concurrently, for thicknesses superior to 5 nm, a distinctive ScAlN peak emerges at approximately 35.5°, and remarkably, this peak position remains unchanged despite varying barrier thicknesses. Given the previously established confirmation of the simulations accuracy in predicting barrier thickness and scandium amount, these simulation techniques were subsequently applied to samples grown with varying barrier thicknesses.

The simulation of ScAlN barrier thicknesses was achieved through an analysis of the interference fringes. It is evident that as the period of the oscillations increases in breadth, this signifies a reduction in thickness. As illustrated in the Figure 66, the simulated barrier thicknesses encompass 5 nm, 9.5 nm, 14.5 nm, and 24.5 nm. The scandium molar fraction demonstrates a variation ranging between 13.4% and 15%. This observed change in scandium amount manifests at a relatively sluggish rate. However, while

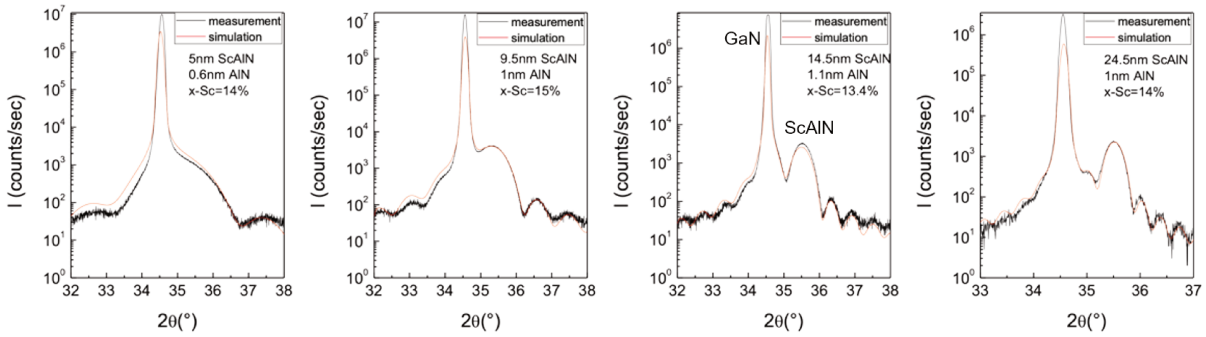

Figure 66: Simulation of thickness and scandium content variations for barriers grown at different thicknesses using AMASS.

the peak position remains stable, a conspicuous increase in peak broadening is discernible as the ScAlN barrier thickness is reduced. This phenomenon can be due to the crystal quality degradation.

6.2.2 2DEG density of 25nm of $Sc_{0.15}Al_{0.85}N/GaN/Sapphire$

To determine the density of the two-dimensional electron gas within the GaN channel, capacitance-voltage measurements were performed on various samples grown at different temperatures. In this section, we will present the capacitance-voltage profiles obtained using a mercury probe gate across various frequencies 1kHz, 10kHz and 20 kHz, all at ambient temperature. At first, we will start with the 25 nm ScAlN barrier layer. Figure 67 shows the capacitance-voltage profiles obtained on the HEMT heterostructures with ScAlN barriers grown at 620℃, 670℃, 720℃, 760℃ and 800℃. The presence of a 2DEG is confirmed by the observed capacitance plateau. Based on the evenness of this plateau, it's improbable that there's a high residual doping level within the barrier.

The capacitance measured at $V_g = 0$ V allows us to infer the distance between the gate and the 2DEG. Capacitance is inversely proportional to thickness unless trapping effects noticeably alter the measurements. The dispersion with frequency can be noticed for samples grown at lower temperatures and attests the presence of electrical defects. It's worth noting that all samples grown at different temperatures exhibit nearly the same capacitance at 1 kHz and $V_g = 0$ V and thus they have identical barrier thicknesses, and the growth rate remains constant across different growth temperatures, as determined through XRR, as discussed in the chapter 5. When increasing the growth temperature to 760℃, the pinch off voltage rapidly decreases from -20 V to reach -10 V and then at Tg= 800℃ it reaches -7 V, while the capacitance at 0 V remains unchanged. This indicates a noticeable drop of the 2DEG density. Furthermore, the lack of frequency dispersion in samples grown at 760℃ and 800℃ suggests a much smaller density of traps in the barrier and in the GaN buffer layer as well.

The sheet charge concentration, calculated by integrating the capacitance from pinch-off up to 0 V at the frequency f=10 kHz, falls within the range of $3.0 \times 10^{13}/cm^2$ to $3.5 \times 10^{13}/cm^2$ for the growth temperatures ranging from 670℃ to 720℃, and it experiences a sharp decay for higher temperatures (Figure 68a). Consistently, a concomitant drop of the pinch-off voltage from -20 V up to -7 V is noticed. The barrier grown at 620℃ exhibit more dispersed C-V and resulting 2DEG charge densities. The measured capacitance is connected to a parallel conductance. Figure 68b illustrates these measurements, where the red triangles represent the resistance (1/conductance) at $V_g = 0$ V, and the black points correspond to the resistance

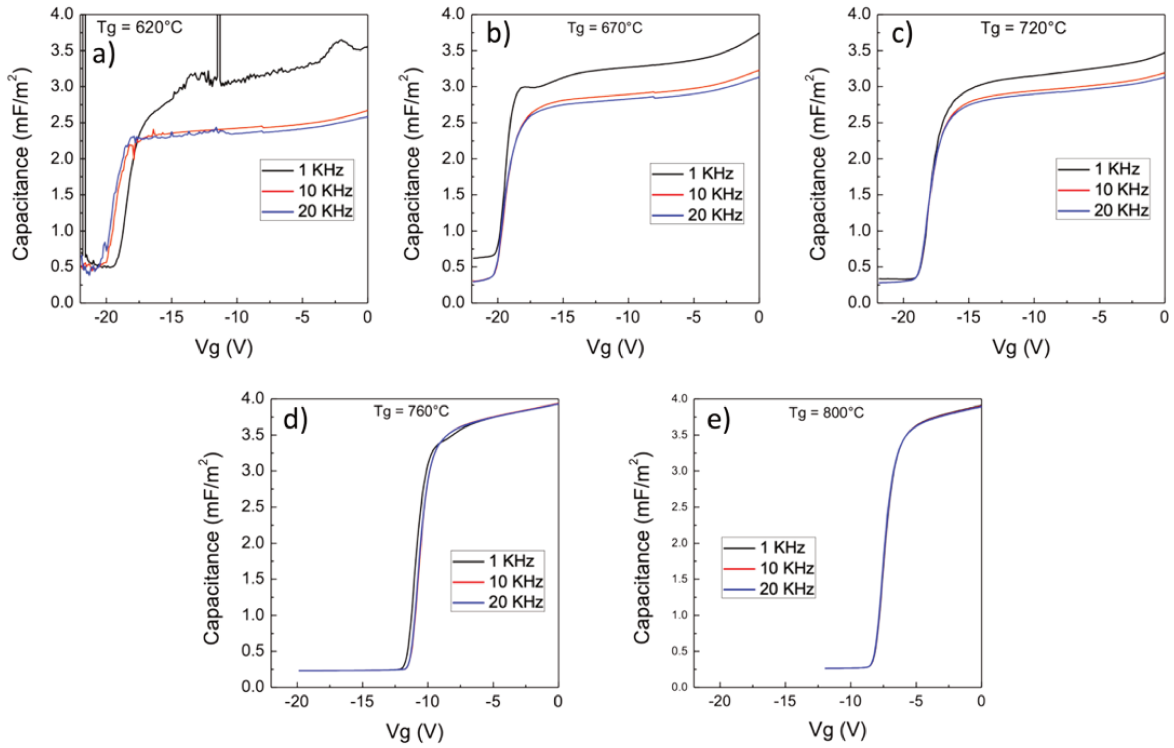

Figure 67: C(V) measurements conducted using a mercury probe on ScAlN samples with a 25 nm layer thickness. These samples were grown at various temperatures, and the measurements were performed at room temperature with frequencies ranging from 1 kHz to 20 kHz.

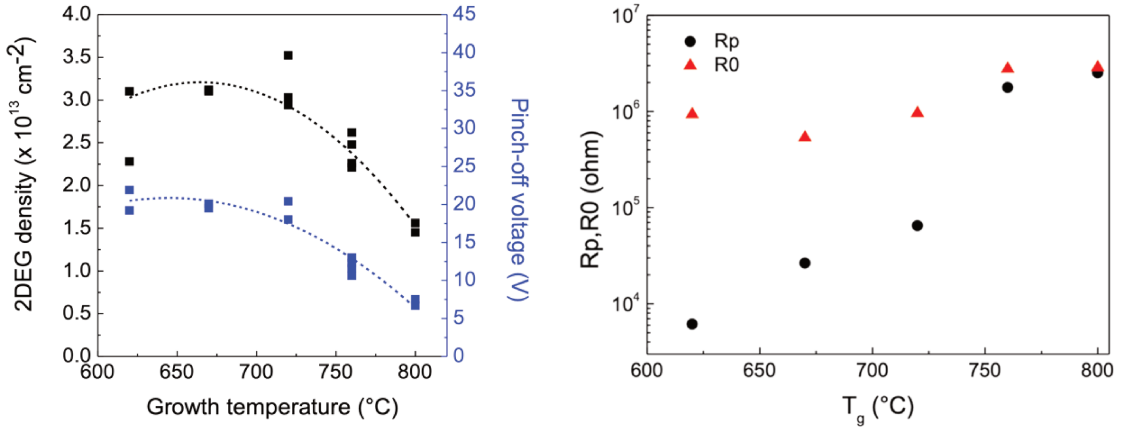

Figure 68: a) 2DEG as well as the pinch-off voltages associated with it and, b) the resistance values (R_p and R_0) for a 25 nm thick layer of ScAlN at various growth temperatures. Measurements performed at the frequency f=10 kHz.

at the respective pinch-off voltages V_p. Notably, we observed a high resistance value, denoted as R_0, around 106 ohms for all growth temperatures. In contrast, the resistance at pinch-off voltage (R_p) displayed significant variation. Samples grown at higher temperatures exhibited higher resistivity, while those grown at lower temperatures exhibited lower resistivity, reaching $6 \times 10^3 \Omega$. This suggests the occurrence of leakage

current for lower growth temperatures, aligning with frequency dispersions indicating the presence of traps at these conditions. Despite the association between high resistivity and lower leakage current at higher growth temperatures, it's important to note that lower growth temperatures result in higher 2DEG density and improved crystalline quality. Even if the measured sheet charge density is much higher than in AlGaN/GaN and InAlN/GaN systems, the present values are lower than the ones reported in [160]. XPS and XRR analyses evidenced the presence of a 2-3 nm thick scandium oxide layer (probably Sc_2O_3) at the surface of the barriers. The strong affinity of scandium with oxygen and the absence of in-situ passivation explains the presence of this oxide layer. The surface or near-surface donor states in ScAlN alloy play a role in the formation of the 2DEG. The better crystal quality revealed for lower growth temperatures probably benefits these electronic states, but the role of the surface oxide and the potential interest of in-situ passivation with GaN or SiN remain to be investigated. [161]

6.2.3 Barrier ScAlN layer below 25 nm

As previously discussed in Chapter 4, achieving high-frequency performance necessitates a reduction in gate length and the use of a thin barrier to prevent short channel effect. However, as observed with both AlGaN and InAlN barrier layers, the density of electrons in the 2DEG rapidly drops when the barrier thickness is reduced below 10 nm and the dependance of the density with the thickness has to be determined to design the HEMT structure suitable for high frequency operation.

2DEG concentration

In this thesis, the focus was on exploring methods to decrease the thickness of the ScAlN barrier. In the following section, we will delve into the measurement of the 2DEG density using a mercury probe gate. As previously noted, capacitance at 0 V demonstrates an inverse relationship with thickness. Within this series of samples featuring varying barrier thicknesses, capacitance exhibits an ascending trend as barrier thickness decreases. Specifically, for a 25 nm ScAlN barrier, the capacitance measures $3.5mF/m^2$, then escalates to $5.5mF/m^2$ for a 16 nm thickness, further increasing to $7mF/m^2$ for a 10 nm thickness, and ultimately peaking at $12mF/m^2$ for a 5 nm barrier ScAlN. As expected, as the ScAlN barrier layer thickness is reduced, a significant trend is observed in the behavior of the HEMTs. Specifically, there is a systematic reduction in the pinch-off voltages as the thickness of the ScAlN barrier layer decreases. This noteworthy phenomenon is accompanied by a concomitant decrease in the concentration of the 2DEG.

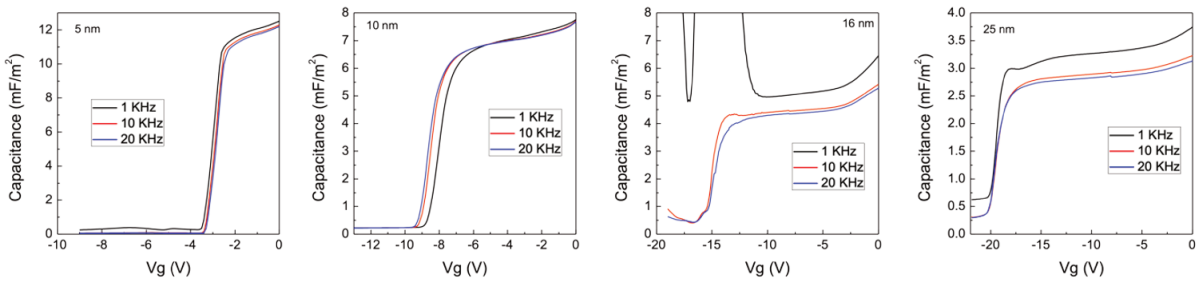

Figure 69: C(V) measurements were carried out on ScAlN samples of varying layer thickness using a mercury probe. These samples were synthesized at a temperature of 670 ℃, and the measurements were conducted at room temperature, spanning frequencies from 1 kHz to 20 kHz.

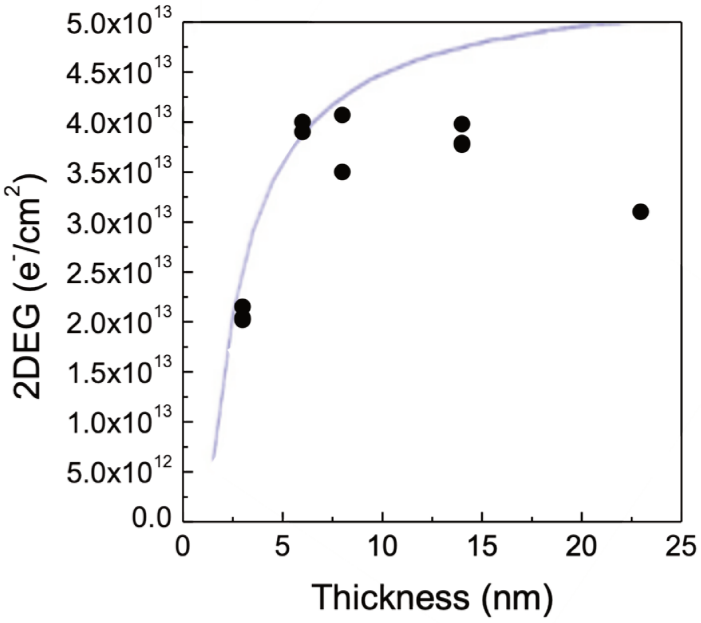

Figure 70: The black dots on the graph represent the experimental concentration of the 2DEG as it varies with the thickness of the ScAlN barrier. These measurements were obtained using C(V) measurements with a mercury probe gate, and the data was collected at a frequency of 10 kHz. Meanwhile, the blue curve corresponds to the theoretical calculations reported by [115].

Figure 70 shows the 2DEG densities obtained by integration of C-V curves from pinch-off voltage up to $V_g = 0$ V. In this figure, 2-3 nm have been subtracted from the total nominal ScAlN thickness due to the presence of the surface oxide layer. TEM images confirms the presence of oxydes on the surface which is equivalent to 2-3 nm (Figure 71). As illustrated in Figure 70, it is evident that the concentration of the 2DEG experiences distinct variations based on the ScAlN thickness. The observed trends align well with theoretical calculations[115]. Notably, even for a ScAlN thickness as low as 3 nm, the 2DEG concentration remains comparatively high, approximately $2 \times 10^{13}/cm^2$. Subsequently, an increase in thickness to 8 nm corresponds to a rise in 2DEG concentration, reaching around $4 \times 10^{13} e^-/cm^2$. Upon reaching approximately 14 nm thickness, the concentration stabilizes, aligning closely with the value observed at 8 nm, near $4 \times 10^{13}/cm^2$. However, contrary to theoretical predictions, the ScAlN barrier thickness of 23 nm (nominal 25 nm) generates a 2DEG concentration reduced to $3 \times 10^{13}/cm^2$. This behavior suggests an additional factor influencing the 2DEG concentration, likely linked to a possible degradation of the crystal characteristics of the thicker ScAlN barrier layer.

TEM images

To delve deeper into this aspect and substantiate the influence of ScAlN thickness on crystal behavior , TEM measurements were conducted on a 55 nm ScAlN sample. Through this comprehensive investigation, we seek to unravel the intricate relationship between ScAlN thickness, crystal properties, and the resulting behavior of the 2DEG concentration.

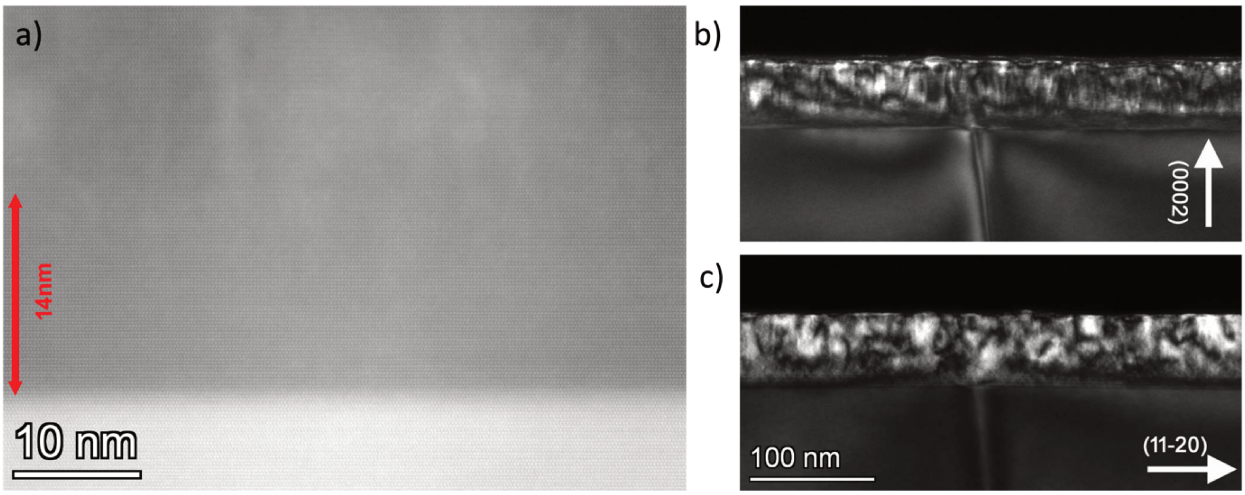

Figure 71: STEM image of the 55 nm ScAlN.

Figure 71a shows a cross-section STEM image of a 55nm ScAlN/ 1 nm AlN barrier on GaN-on-sapphire. The firsts 14 nm of the ScAlN layer exhibit a remarkable absence of atomic disorder (this is most prominently observed in Figure 72b), indicating a pristine non-defective structure. However, beyond this point, the emergence of disordered regions appear in the layer. This transition underscores the pivotal influence of thickness on the occurrence of defect formations within the ScAlN layer. This observation crucially lends itself to the explanation of the unexpected reduction in the 2DEG concentration for the 25 nm ScAlN barrier thickness. Figure 71b and Figure 71c display TEM images in dark field mode, corresponding to the diffraction spots 0002 and $11\bar{2}0$, respectively. TEM images provide insights into dislocations, including edge, screw, and mixed dislocations. It is evident from these images that there are no dislocations observed in the initial nanometers (corresponding to the first 14 nm). Nonetheless, when we examine thicknesses greater than 14 nm, we encounter differences in intensity and patterns that result from a disorder inducing a degraded crystal quality. At this stage, we haven't yet conducted a detailed analysis of the nature of these disorder.

STEM images in Figure 72 were conducted to investigate the origin of the contrasts observed in the ScAlN barrier layer. As previously mentioned, such contrasts in the ScAlN barrier layer began to appear at the 13- 15 nm thickness. In Figure 72a, we observe the chemical contrast in STEM, but there is weak variation as evidence of fluctuations in scandium content. However, in the crystallographic image shown in Figure 72b, bright features become visible starting from approximately 14 nm thickness. This suggests that these contrasts are purely structural in nature and are not linked to chemical composition or scandium amount segregation or fluctuations. In APT, no segregation of scandium or other elements such as aluminum or gallium was observed.

Therefore, both APT and STEM confirm that ScAlN does not exhibit any chemical element segregation or amount fluctuations.

Investigations about ScAlN strains

GPA, or Geometric Phase Analysis, produces comprehensive quantitative deformation and two-dimensional

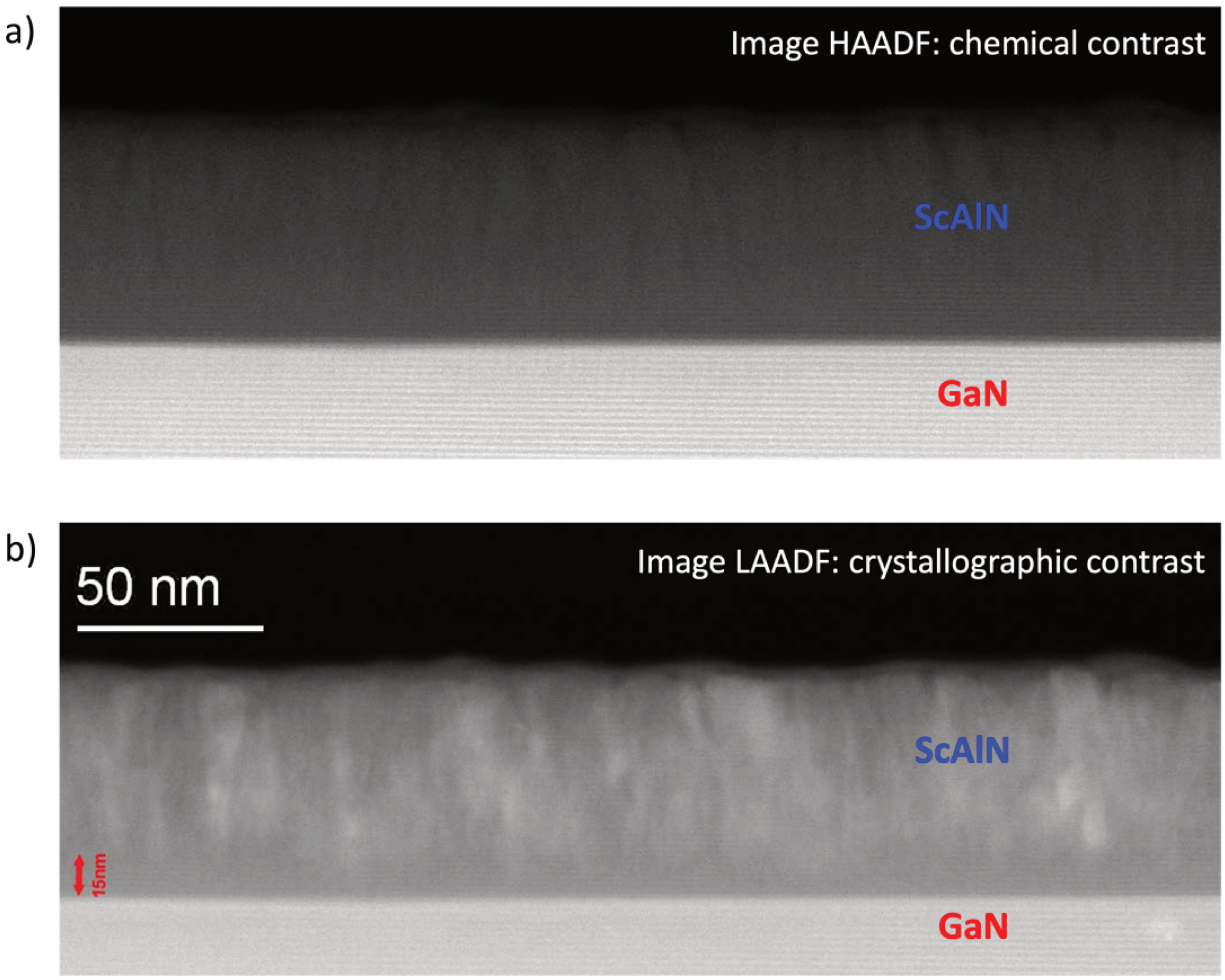

Figure 72: Image LAADF showing a) chemical contrast, and b) crystallographic contrast.

strain maps using high-resolution STEM images. GPA relies on the principles of geometric phase analysis, originally developed for this purpose. Figure 73b displays the GPA analysis, revealing that no distortion in the plane compared to GaN has been observed, which means that the in-plane lattice parameter of ScAlN matches that of GaN, indicating the absence of noticeable relaxation in the ScAlN layer grown on the fully relaxed GaN buffer layer. A similar GPA analysis was conducted for out-of-plane distortion, as depicted in the accompanying Figure 73c. In this analysis, we compare the out-of-plane parameters of AlN and ScAlN to that of GaN. The distortion in the out-of-plane direction varies in AlN and ScAlN.

The GPA analysis highlights distortions in both AlN and ScAlN layers. The AlN layer exhibits a distortion of approximately -5.5% on GaN, close the theoretical value. However, it's notable that GaN distortion exhibits fluctuations of approximately 0.5%, revealing the limits of this study. These fluctuations can help explain the discrepancies observed between theoretical predictions and the results obtained through GPA analysis.

GPA calculations indicate a distortion of approximately -3.7%, which closely matches the theoretical value for ScAlN distortion with 15% scandium fraction, as depicted in Figure 74b which is equal to -3.5%. These findings establish a consistent alignment between theoretical predictions and TEM measurements, which make the theoretical prediction of Ambacher et al. reliable for scandium content deducing. Further-

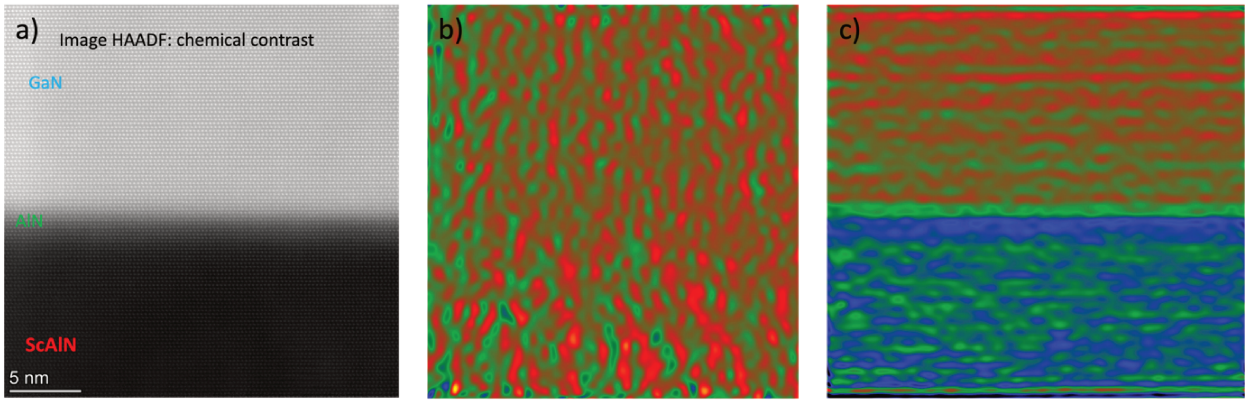

Figure 73: a) The HAADF STEM image illustrates the chemical contrast within the ScAlN/AlN/GaN structure, b) The GPA image is used to analyze in-plane distortion, and c) Another GPA image is employed to examine out-of-plane distortion.

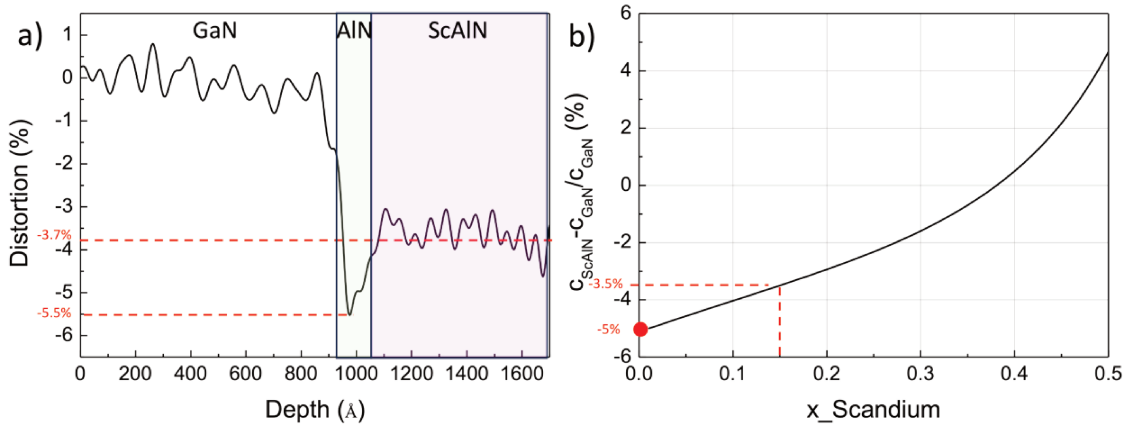

Figure 74: a) The out of plane distortion values of AlN and ScAlN on GaN have been computed using GPA analysis and are provided in the results, b) The depiction of out-of-plane distortion in ScAlN/GaN is presented as a function of scandium molar fraction. These calculations are based on parameters derived from Ambacher et al. [65] for the out-of-plane lattice parameter of ScAlN, with cGaN held at $5.185\mathring{A}$ *[31].*

more, this coherence extends to other analytical techniques such as XPS, SIMS, and APT.

6.2.4 Growth on 4 inches substrate

Up to now, the present growth study has exclusively used substrates with a diameter of 2 inches. The growth performed on these 2-inch diameter samples has exhibited notable homogeneity both in terms of layer thicknesses and the uniformity of scandium content. This uniformity is obvious from the XPS profiles, where the scandium amount demonstrates consistency across the entirety of the 2-inch diameter substrates. To expand the capacity for sample growth, thereby facilitating a more comprehensive characterization through technological processes, a transition was made to 4-inch sapphire substrates. This larger substrate size was adopted specifically for the growth of 10 nm thick ScAlN layers. This strategic choice enables an increased substrate area, thereby accommodating a greater number of samples for subsequent characterizations, an imperative step in advancing our understanding of material properties and behaviors.

Capacitance-voltage measurements were carried out on a sample grown at a temperature of 670℃ using a 4-inch GaN-on-sapphire template. The objective of these measurements was to assess the uniformity of the 2DEG concentration within the sample. To achieve this, measurements were executed at distinct locations: at the central region of the sample and subsequently at distances of 12 mm, 22 mm, 27 mm, and 32 mm from the substrate's center. The outcome of these measurements provides clear insight: Initially, we observe a trend whereas we move away from the center towards the outer regions, there is a noticeable rise in the capacitance at 0V within the plateau of the C-V profile. This increase may likely be attributed to a reduction in thickness, a hypothesis that will be substantiated through subsequent thickness simulations using XRD. Another noteworthy observation is the diminishing pinch-off voltages from the center to the periphery, suggesting a probable decrease in electron sheet carrier densities in these regions. Starting from the center and moving towards the periphery, we are placing the values of ($C_0[mF/m^2]$; Vp[Volts]) here: (6.75; -11.4), (6.70; -11.2), (7.16; -10.6), (7.85; -9), (7.95; -7.2), (8.05; -6.1) . And by integrating the C-V we had a discernible trend emerges wherein the 2DEG concentration experiences a progressive decay as the measurement points move farther away from the central region. This variation in 2DEG concentration across different locations underscores the importance of considering spatial homogeneity when evaluating the electrical characteristics of the sample. As previously demonstrated, the concentration of the 2DEG is inherently reliant on the thickness of the ScAlN barrier. Considering this, our initial approach involved conducting scans of the 0002 reflections for both GaN and ScAlN peaks using a 2θ configuration. The primary aim of these scans was to infer the thickness of the ScAlN barrier as a function of position. These scans were meticulously performed at the exact locations where the C-V measurements had been conducted. This comprehensive spatial analysis facilitates a more nuanced understanding of the relationship between ScAlN barrier thickness and its corresponding impact on the 2DEG concentration across various locations.

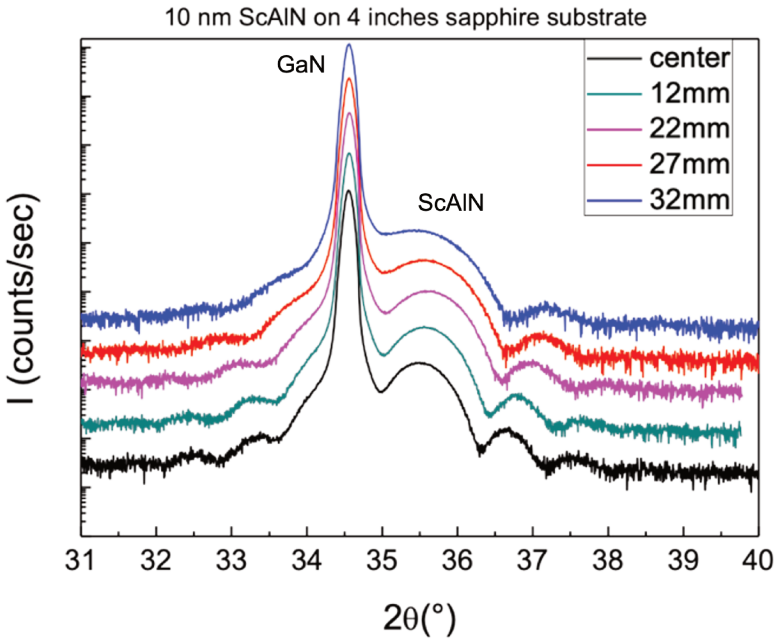

Figure 75: 2θ configurations on a 4-inch sapphire substrate, varying across different areas from the central region to the outer edges as illustrated in the inset of the diagram.

Figure 75 visually illustrates a noteworthy phenomenon: as the measurement points move progressively away from the central region, the ScAlN peak experiences a distinct broadening. This broadening trend serves as an indicative marker, suggesting a reduction in the ScAlN barrier thickness. Notably, the GaN peak exhibits full relaxation throughout the entire sample, maintaining a consistent angle of 34.57°. In pursuit of precise ScAlN thickness determination, a rigorous verification process was executed.

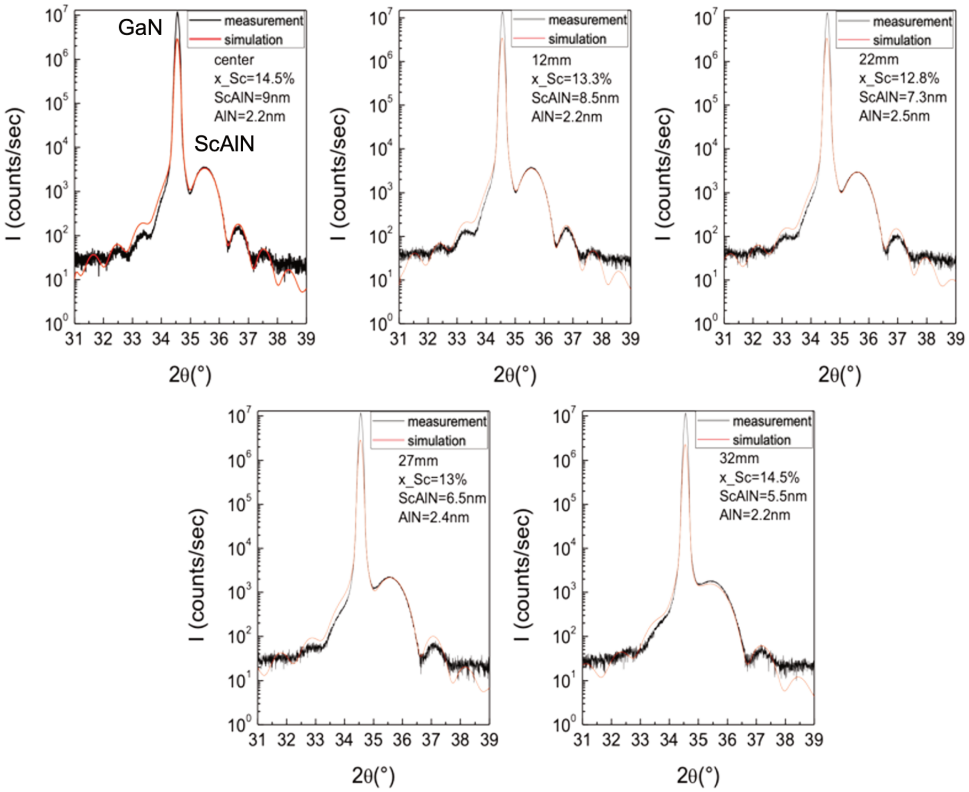

Figure 76: Simulation of thickness and scandium molar fraction variations for barriers grown at different thicknesses using AMASS.

This entailed simulating these scans using the AMASS software, as visually represented in Figure 76. This comprehensive approach strengthens the accuracy of our understanding and assessment of ScAlN thickness variations across different positions within the sample. In this sample, a 2 nm thick AlN interlayer was grown before depositing the ScAlN barrier layer. This choice was made to investigate the interlayer's impact; as previously reported by Casamento et al. [162], a higher electron mobility in the channel can be expected with high 2DEG density. As depicted in the inset of Figure 76, at the center of the sample, the best fit is with a 9 nm barrier with a 2.2 nm AlN interlayer. However, as we move away from the center to 12 mm, the barrier thickness gradually diminishes to 8.5 nm. Further along, at 22 mm, it decreases to 7.3 nm, and at 27 mm, the ScAlN thickness reaches 6.5 nm. Finally, near the substrate's edge, situated at 32 mm, the ScAlN thickness is reduced to 5.5 nm. On the other hand, the scandium molar fraction is almost constant, which indicates that the decrease in growth rate is linked to similar decays of scandium and aluminum fluxes while moving away from the center of the 4-inch substrate.

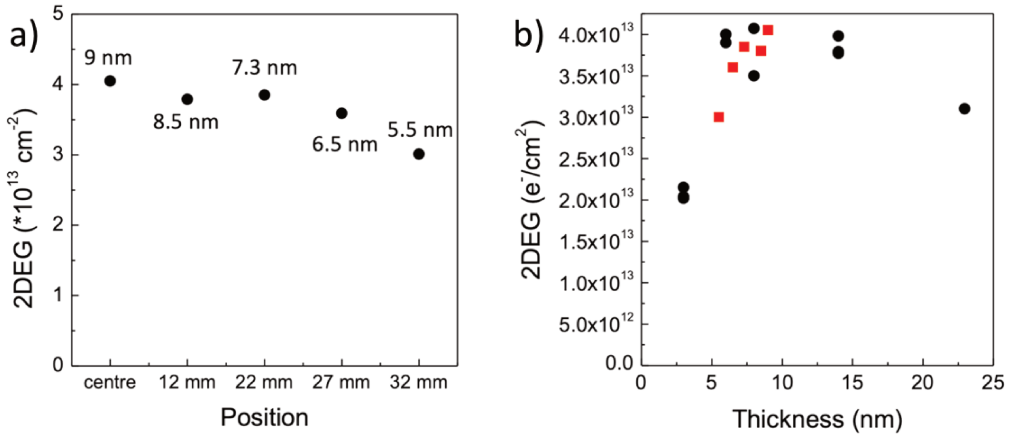

Figure 77: a)The 2DEG as a function of the C-V location and the simulated thicknesses associated with it on 4-inch sapphire substrate, and b)Comparaison of the 2DEG as a function of the thickness on 2-inch (black dots) and 4-inch (red dots) sapphire substrate.

As previously discussed in the section labeled ”Barrier ScAlN layer below 25 nm”, it is well-established that thickness significantly influences the concentration of the 2DEG. In line with this understanding, the Figure 77 illustrates a concomittant reduction in the measured 2DEG concentration via C-V measurements. This reduction is directly linked to the diminishing thickness of the barrier layer while examining it from the center to the substrate's outer edge. In the central region, with a thickness of approximately 9 nm, the electron density reaches $4 \times 10^{13}/cm^2$. Moving towards the edge, where the thickness reduces to approximately 5.5 nm, the electron density decreases to $3.0 \times 10^{13}/cm^2$.

Figure 77b illustrates how the thickness of the ScAlN barrier layer affects the 2DEG. The data combines results from varying barrier thicknesses on two different substrates: black dots represent the 2-inch substrate, while red dots represent the 4-inch substrate. This combined data highlights the consistent impact of thickness on the 2DEG, showing a similar trend in both studies.

6.3 Effect of scandium concentration

To go further in our research, we conducted experiments aimed at increasing the concentration of scandium within the barrier layer, specifically for ScAlN layers with thicknesses of 10 nm and 77 nm. In this endeavor, we raised the temperature of the scandium effusion cell, leading to a noticeable increase in the number of scandium atoms reaching the substrate surface in the MBE chamber. It's important to note that this study is not primarily focused on enhancing the performance of HEMT at high frequencies. Instead, our primary objective lies in increasing the scandium content, which has more relevance in the context of ferroelectric and piezoelectric applications. Furthermore, for these applications, a thicker ScAlN layer is required. Our experimental approach began by growing a 10 nm thick ScAlN layer to investigate the incorporation of scandium during the growth process. Subsequently, we extended the growth duration to produce thicker ScAlN layers, with the scandium content determined based on observations from the 10 nm layer growth. First, we used the optimal growth temperature, previously determined for a 15% scandium molar fraction, and found around approximately 670℃. XPS measurements revealed that the scandium content was approximately 22% for samples grown at an effusion cell temperature of scandium $T_{Sc} = 1220C$ and increased to 30% for $T_{Sc} = 1240C$.

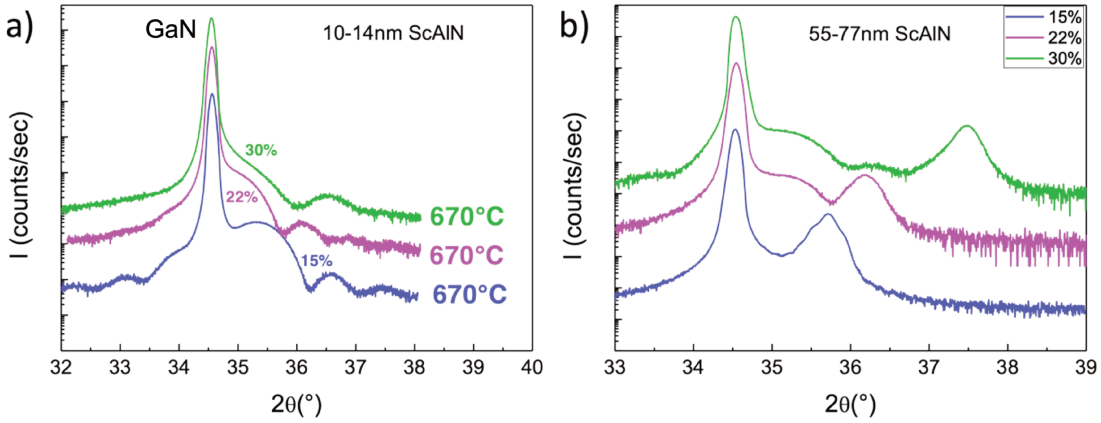

Figure 78: We conducted a 2θ scan for 0002 reflection on the following samples: a) a 10 nm ScAlN barrier layer, and b) ScAlN layers ranging from 55 nm to 77 nm, with varying scandium amount. The blue curve represents the results for the Scandium effusion cell at a temperature of 1200℃, the purple curve corresponds to a temperature of 1220℃, and the green curve corresponds to a temperature of 1240℃.

As depicted in the Figure 78a, the ScAlN peak angle demonstrates a noticeable shift towards a lower 2θ angle signifying an expansion in the out-of-plane lattice parameter. Calculations for the out-of-plane lattice parameters on ScAlN fully strained on GaN also confirm this increase in the out-of-plane lattice parameter. However, an additional peak appears on the right side; this could be due to a reduction of Sc amount in a part of the film, additional phases of ScAlN present in the layer or some strain relaxation. The growth exhibited consistent orientation along the c-axis, as evidenced by the unchanged 2θ scans while rotating the sample around the [0001] axis, suggesting a lack of varied orientations throughout the growth process (see Figure 79).

While examining the sheet carrier density in the 2DEG using C(V) measurements, Figure 80a illustrates the behavior of the 2DEG density regarding the Scandium amount. As outlined in Chapter 3, the theoretical expectation was that the induced sheet carrier concentration would decrease from 0% Scandium content

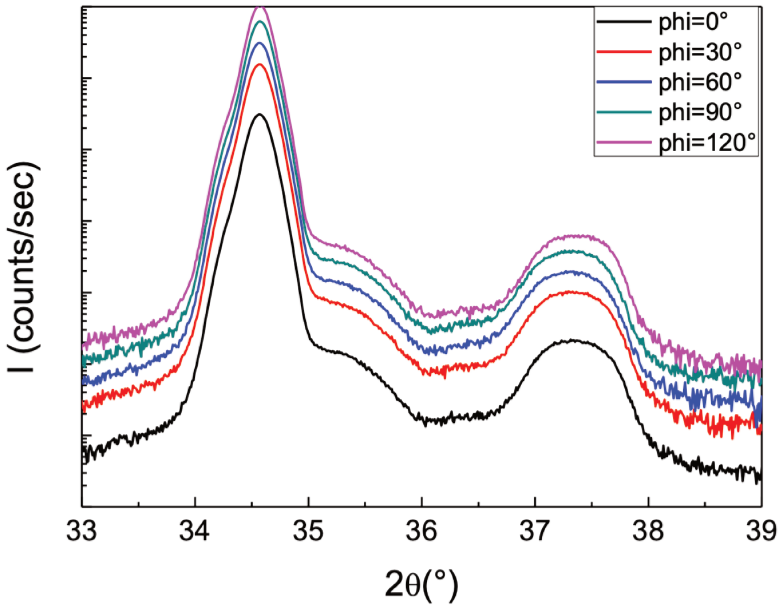

Figure 79: 2θ scans of PTC1248, changing the phi angle in increments of 30°, ranging from 0° to 120°.

up to 40%. This is in agreement with experimental analysis of our sample, where we observed a decrease in the 2DEG density when the Scandium fraction changes from 15% to 30%. But this reduction is more important, and occurs for lower Scandium concentration than what was predicted theoretically with the calculation of the induced sheet carrier at the interface. Figure 80a shows the evidence of this reduction while comparing the experimental values with the theoretical induced sheet carrier (red dashed curve). This reduction cannot be attributed to a thinner barrier layer; we used genX to simulate the thicknesses by fitting the XRR scan data and Figure 80b confirms that the barrier layer thickness increases with Scandium molar fraction. Nevertheless, drawing a parallel with our previous discussion about the ScAlN layer containing 15% Scandium, where an increase in ScAlN thickness led to a decrease in 2DEG, a similar phenomenon is observed here. Figure 82 displays the TEM cross-sections of PTC1247 ($Sc \sim 22\%$) and PTC1248 ($Sc \sim 30\%$), revealing the presence of a defective layer within the structure. This phenomenon may explain the decrease in 2DEG densities as the scandium molar fraction in the barrier layer increases.

The same duration was applied to grow all three different scandium alloys, aiming for a thickness target of approximately 50 nm in the alloy with a Sc molar fraction around 15%. The aluminum cell was maintained at the same temperature in order to keep the same equivalent AlN growth rate in the alloy. In Figure 78b, we observe the 2θ plot for the second series, which features thicker ScAlN layers. As expected for a growth limited by the flux rate of available group-III elements, the ScAlN thickness increases with amount of scandium in the alloy. Furthermore, the additional peaks shift towards higher angles. The explanation for these peaks is still unclear. However, based on previous research and the peak positions, it is possible that the peak around $2\theta = 37.5$ may correspond to the $ScAl_3$ (111) crystallographic plane, as indicated in the Table 8.

After partially etching the ScAlN barrier layer of PTC1246, as indicated by the blue portion in Figure 81, we observed that both sides of the ScAlN peaks disappeared when analyzing the XRD 2θ scan. To further

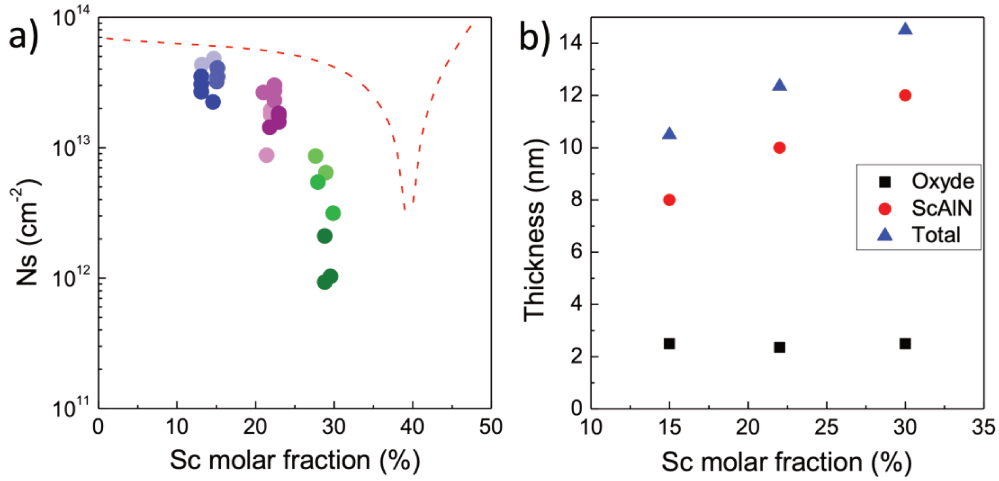

Figure 80: a)2DEG density deduced by C(V) for approximately 10 nm of ScAlN, the red dashed curve represents the calculated induced sheet carrier, and b) the corresponding thickness if the ScAlN barrier layer deduced by fitting the XRR scan.

	hkl	structure type	$d_{hkl}(\mathring{A})$	2θ
AlN	002	wurtzite	2.491	36.02
GaN	002	wurtzite	2.593	34.58
ScN	111	rocksalt	2.598	34.5
ScN	002	rocksalt	2.250	40.1
$ScAl_3$	111	$AuCu_3$	2.369	37.96
$ScAl_3$	002	$AuCu_3$	2.052	44.1

Table 8: Lattice plane distances of nitride materials taken from chapter 2 and the diffraction angle 2θ calculated with $\lambda = 1.5406\mathring{A}$, and for metallic structures $ScAl_3$ alloys taken from [163].

investigate this phenomenon, we conducted simulations, as depicted in Figure 81. For the black peak, we performed simulations by introducing multiple ScAlN layers with varying thicknesses and scandium compositions (simulations results: (x-Sc (%); ScAlN thickness(nm)); (5.3/35)/ (10/10)/ (11/12) knowing that the first two layers are fully relaxed and the 12nm are fully strained. When simulating the peak after etching, we only introduced a single layer with a scandium content of approximately 11.5% and a simulated thickness of approximately 35nm. This experimental and simulation approach confirms that some of the defective layers were indeed removed during the etching process, as evidenced by the changes observed in the XRD 2θ scans.

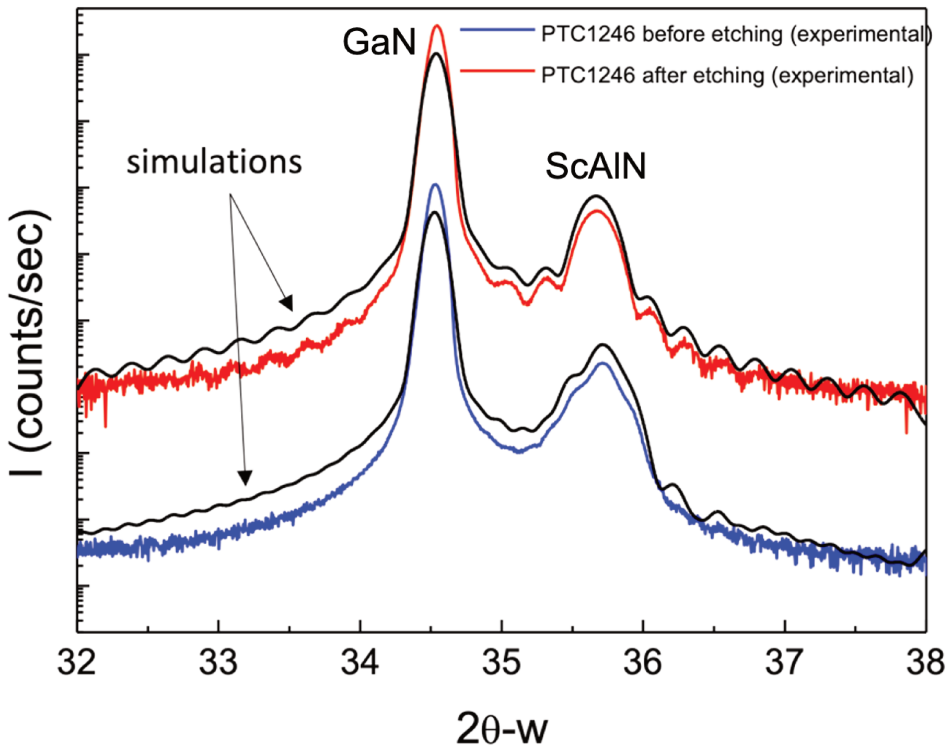

Figure 81: 2θ scans of PTC1246 before and after etching.

TEM analysis was conducted on these samples, allowing us to determine the non-defective layer thickness variations in samples with varying scandium amount.

Sample	PTC1246	PTC1247	PTC1248
Sc content (XPS %)	15	22	30
Total thickness	55	67	77
Non defective	13-15	7	4

Table 9: This table summarizes the three samples that feature a relatively thick ScAlN barrier layer, it provides information on the scandium content determined through XPS, the total thickness measured via TEM, and the thickness of the non-defective layer, also determined using TEM.

Table 9 reminds the thicknesses of the ScAlN layers and provides further confirmation of the existence of defective layers. When the Scandium concentration is approximately 22%, the non-defective layer is approximately 7 nm thick. In contrast, when the Scandium concentration is around 30%, the non-defective layer is reduced to approximately 4 nm in thickness. Figure 82 shows the crystallographic contrast and highlights the presence of defective layers.

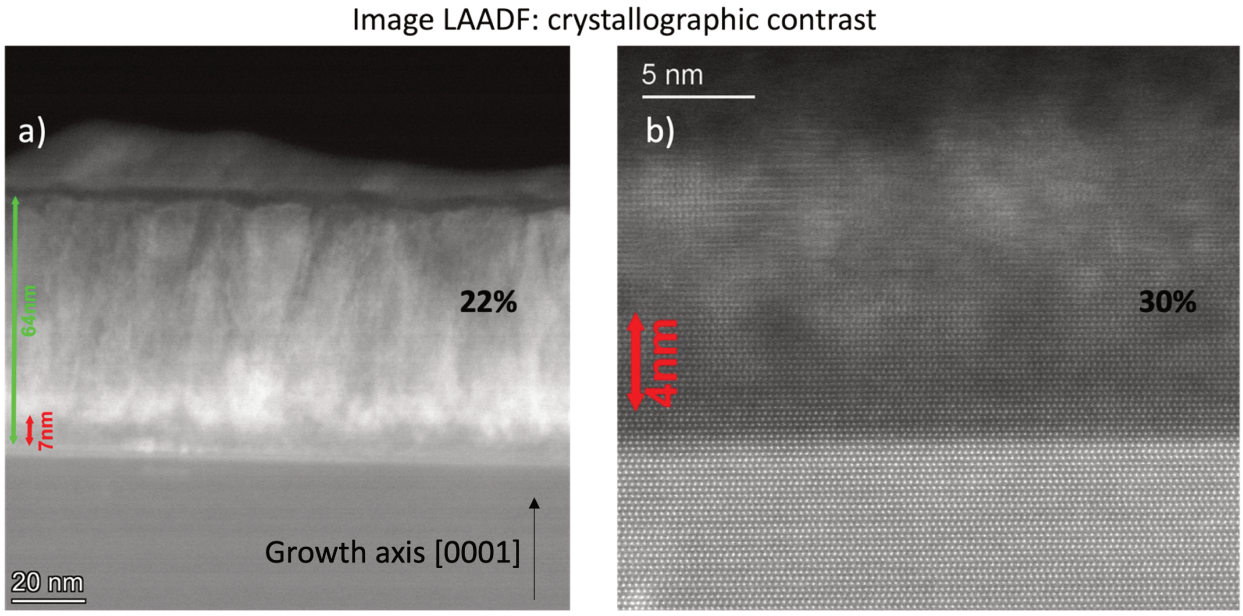

Figure 82: The LAADF image exhibits crystallographic contrast in ScAlN samples (around 50nm) with scandium fractions of 22% and 30%, showing the corresponding defective layer thickness.

This phenomenon could elucidate the reduction in the concentration of 2DEG as the scandium molar fraction increases. This may be connected to the thinner non-defective layer observed at higher scandium concentrations, potentially influencing the induced polarization within the barrier layer or introducing electrical traps and consequently affecting the density of 2DEG.

6.4 Conclusion

From this chapter, we deduced that the behavior of the 2DEG is impacted by the growth temperature. The 2DEG density is greater at lower growth temperatures in comparison to higher ones, with a temperature threshold of 720℃ that should not be surpassed. Additionally, the 2DEG density is highly responsive to changes in barrier thickness. It increases as the barrier thickness increases but starts to decline when it exceeds 10nm. A significant drop in density is noticeable at 16nm. Originally, we suspected that this decrease might be attributed to relaxation effects. However, thorough analysis, including GPA analysis, revealed no relaxation in ScAlN, even up to a thickness of 55nm. Subsequently, TEM images of the same sample indicated that the decline in 2DEG is linked to the emergence of disordered regions during growth once the thickness reaches 13-15nm for a scandium molar fraction of 15%. Therefore, the issue beyond 13-15nm pertains to the emergence of these disordered regions. Finally, we assessed how altering the scandium amount, ranging from 15% to 30% of the scandium molar fraction, led to a reduction in 2DEG density when compared to theoretical expectations. We delved into this phenomenon using TEM analysis, which revealed a substantial decline in non-defective layers. Specifically, at 22% scandium molar fraction, the non-defective layer thickness decreased to 7nm, while at 30% scandium molar fraction, the latter decreased to 4nm.

7 Technological processes

Some of the samples underwent various technological processes, as detailed in the Annexes chapter. These samples were epitaxially grown either on Si (111) or sapphire substrates. Numerous studies were conducted, involving different barrier layer thicknesses, including 25nm, 10nm, and 5nm. The research proceeded in several stages. Initially, the isolation of the buffer layer was examined (mesa). Subsequently, realization and measurements of contact resistance (ohmic contacts) were performed alongside sheet resistance using TLM patterns. Hall measurements were then conducted to determine sheet resistance again, as well as the 2D gas density and the electron mobility. The evaporation of Ni/Au metal stack as Schottky contact for circular diodes was performed, allowing the comparison of capacitance measurements with ones previously achieved on the as-grown samples. Finally, I-V measurements show the feasibility of functional transistors on a part of the samples.

7.1 Process challenges

It's worth noting that our technological process remained mostly unchanged for all samples due to time constraints. However, we intend to address this in future work by focusing on optimizing the process, specifically with respect to photoresist removal after mesa etching and metal deposition by lift-off. After the mesa etching process, we observed that the photoresist was not removed easily through cleaning with acetone and isopropanol in ultrasonic bath. This is evident in the SEM picture below Figure 83a where the photoresist remains stickled to the mesas even after the cleaning process and this also was observed after the metal lift-off procedure.

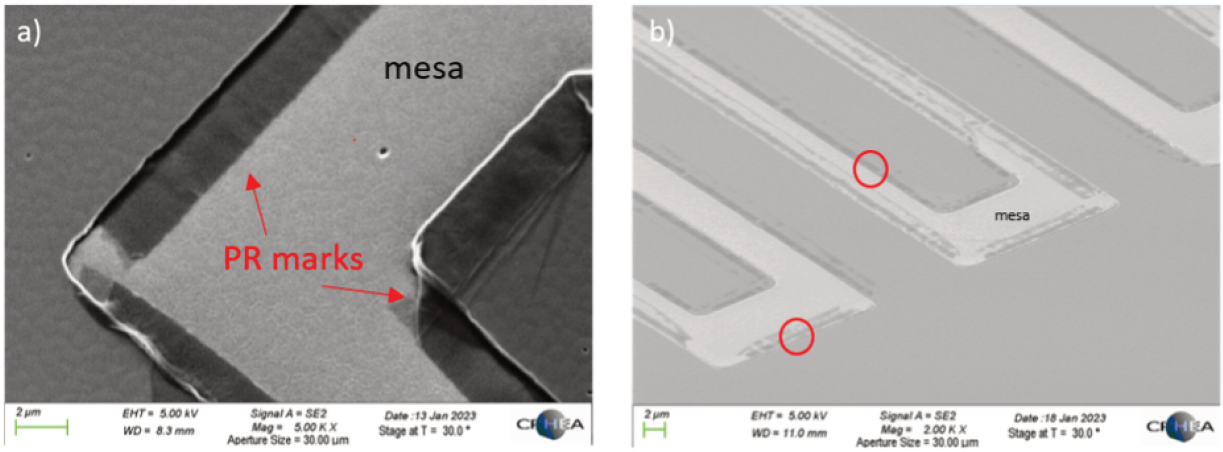

Figure 83: a) SEM image post-mesa etching and subsequent photoresist removal, and b) SEM image depicting post UV ozone cleaner showing in red the sticking photoresist (PR).

The presence of residual photoresist on the patterns was found to necessitate extended duration for the lift-off process. To address this issue, we conducted experiments using alternative solvents like PG remover instead of acetone and a UV ozone cleaner (see Figure 83b). However, it was noted that UV ozone cleaner had the drawback of potentially oxidizing the surface, making it less preferred. Even when employing these techniques, residual photoresist persisted. Ultimately, we attempted to eliminate it using Buffered Oxide Etchant (BOE), which proved successful removed photoresist on the surface as illustrated in Figure 84a. The drawback of employing the BOE treatment stems to pose issues for very thin barrier layers due to the

rapid oxidation of the topmost monolayers and the etching process that can be involved from BOE and can etch completely the thin barrier layers when the thickness is going down to 5nm.

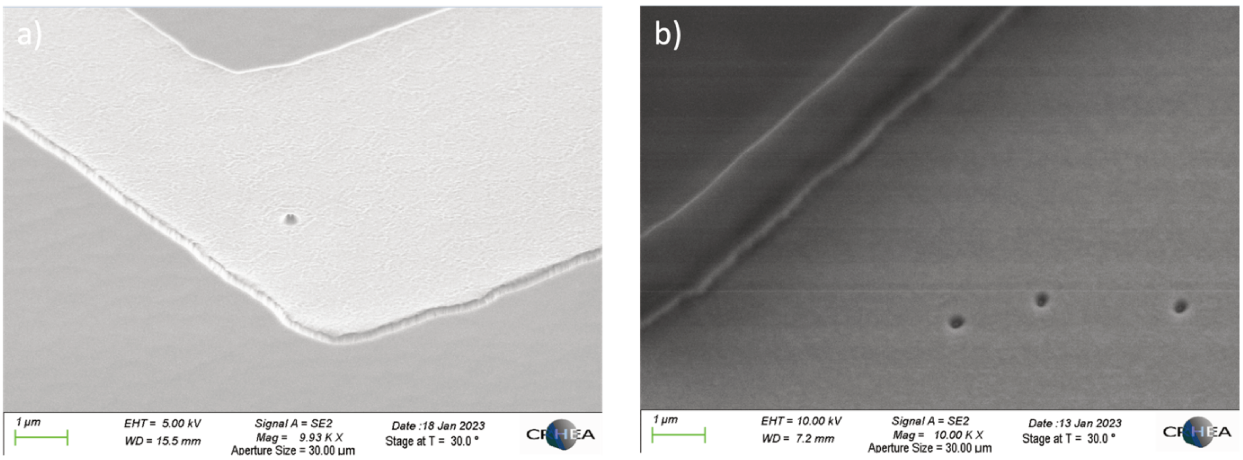

Figure 84: a). SEM image after BOE surface treatment, and b) SEM image showing the defects presented in the bottom after mesa etching.

Furthermore, in order to enhance the etching process, there is a requirement for the optimization of the etching recipes or techniques. For instance, a process limiting the revelation of defects such as threading dislocations (Figure 84b) is often preferred. A different solvent, diméthylsulfoxyde (DMSO), was utilized for cleaning photoresist, demonstrating its effective ability to remove it.

7.2 Isolation - GaN buffer leakage current

The technological processes start with mesa etching through an ICP RIE (Inductively Coupled Plasma Reactive Ion Etching) procedure. This process employed a specific recipe composed of gases in precise flow rates: Cl_2 at 15 standard cubic centimeters per minute (sccm), BCl_3 at 2 sccm, Ar at 2 sccm, and N_2 at 2 sccm. It's worth noting that this particular recipe was also selected for barrier etching prior to the deposition of ohmic contacts. During this process, a bias of 20 watts was applied, and the chamber was maintained at a pressure of 5 mTorr. Additionally, a chiller was used to maintain a temperature of 5°C to prevent the photoresist material from overheating and burning. From isolation standard and circular patterns described in the annexe section "Device Process and Electrical Characterizations of HEMTs", we can study the leakage current flowing through the GaN buffer layer. As indicated in Table 10, certain samples were grown on sapphire templates, while others were grown on silicon substrates. During our assessment of the GaN buffer isolation, we observed a significant leakage current originating from the GaN buffer layer when the samples were grown on GaN-on-sapphire templates. This phenomenon can be attributed to the incorporation of oxygen during the GaN growth process using MOCVD on sapphire, and the presence of silicon contamination at the regrowth interface. [164] In contrast, for samples grown on silicon substrates, the buffer layer is noticeably more resistive. Sample PTC1215 demonstrates the ability to limit the leakage current to 1 mA/mm for voltages up to about 100 V applied to contacts separated by $10\mu m$ spacing. Moreover, PTC1251 exhibits even better resistivity, allowing for a voltage of 120-130V in spite of total thicknesses of the order of $1\mu m$.

7.3 Ohmic contact optimization - TLM measurements.

The ohmic contact process is critical for several reasons. The main is that few data are available in the literature and ScAlN seems highly reactive with oxygen. Furthermore, our HEMT heterostructures have no protective cap layer, which can exacerbate surface degradation effects. The chosen ohmic contact metal stack is identical to the one previously developed in the laboratory for AlGaN/GaN HEMTs (Ti/Al/Ni/Au 30/180/40/160 nm respectively). Also, previous studies have shown the benefit of locally reducing the thickness of the barrier layer to deposit metals closer to the 2DEG. Thus, the partial etching of the barrier within the ohmic contact regions was performed. The purpose of our first trials was to find preparation procedure and an annealing temperature window suitable for the achievement of contacts allowing to the assessment of the 2DEG transport and charge control. The measurement of sheet and contact resistance involves multiple measurements on the rectangular TLM structure, varying the spacing between the patterns. A comprehensive explanation of this procedure can be found in the annexe, specifically in the section titled "Device Process and Electrical Characterizations of HEMTs."

Sample	Substrate	Thickness (nm)	T_a (℃)	$R_c(\Omega.mm)$	$R_{sh}(\Omega/sq)$
PTC1221	Sapphire	25	750	0.60-0.90	20
PTC1215-1	Si (111)	25	800	1.75	528
PTC1215-2	Si (111)	25	750	9	300
PTC1215-3	Si (111)	25	750	1.1-1.4	310-330
PTC1215-4	Si (111)	25	750	0.9-1.30	320-360
PTC1251	Si (111)	10	750	4.75-14.20	670-718
PTC1263-1	Sapphire	10	750	0.90-1.18	486-521
PTC1263-2	Sapphire	10	800	0.80-1.11	427-451
PTC1263-3	Sapphire	10	850	3.04-4.05	360-386
PTC1264-1	Sapphire	10	750	0.53-0.90	267-295
PTC1264-2	Sapphire	10	800	0.62-1.63	224-338
PTC1264-3	Sapphire	10	850	2.05-2.84	266-317
PTC1223	Sapphire	10	750	-n.a	-n.a
PTC1253	Sapphire	5	750	n.a	5100-6500

Table 10: Samples subjected to technological processing involving ScAlN were used to determine both the contact resistance Rc and sheet resistance Rsh through the analysis of TLM measurements. Ta is the contact annealing temperature.

Prior to these measurements, I-V curves were recorded to check the ohmic behavior of the contacts. An initial experiment was conducted using PTC1221 on a sapphire substrate. The contacts were annealed for 30 s at 750℃ under nitrogen. It was observed that the GaN buffer exhibited important current leakage. Nevertheless, an ohmic contact behavior and a quasi-linear dependence of the resistance with contact spacing was noticed, leading to a contact resistance of $0.6-0.9\Omega.mm$. On the other hand, the sheet resistance was too low to account for the 2DEG resistance. To limit buffer parallel conduction and leakage, samples grown on a Si (111) substrate are preferred (PTC1215, PTC1251). PTC1215-1 has been first annealed at 740℃ and this has not shown an ohmic behavior of the contacts. For this sample, 2/3 of the barrier layer have been etched by ICP RIE prior to the deposition of the metal stack. Then a second annealing step at 800℃ resulted in linear I-V curves and an ohmic contact resistance $R_c = 1.75\Omega.mm$ has been extracted. Another trial has been done on another piece of the same PTC1215 sample which is called now PTC1215-2, but this time the barrier was half etched, and the annealing temperature was 750℃. It resulted

in a high contact resistance $R_c = 9\Omega.mm$. PTC1215-3 and PTC1215-4 exhibited residual photoresist remaining on their surfaces after the mesas etching process. Subsequently, they were followed by a 5 minutes BOE cleaning procedure to remove the remaining photoresist and it achieved success (see Figure 84a). The PTC1215-4 process was performed with a BOE pre-treatment for 2 minutes to remove surface oxides before etching the ohmic contact (after ohmic contact photolithography) the metal deposition step and this was compared to the sample PTC1215-3 where the BOE was not used before contact depositioncontact etching. but no big difference has been observed and we continued without the BOE treatment. PTC1215-3 led to $R_c = 1.1 - 1.4\Omega.mm$ and a $R_{sh} = 310 - 330\Omega/sq$. PTC 1215-4 led to $R_c = 0.9 - 1.3\Omega.mm$ with a sheet resistance $R_{sh} = 320 - 360\Omega/sq$. No difference has been observed between PTC1215-3 and PTC1215-4 and accordingly we continued without the BOE treatment. The reduce contact resistance between PTC1215-2 and PTC1215-3 (or PTC1215-4) could be due to the 5 minutes BOE cleaning after mesa etching. The current between contacts clearly scales with their spacings and shows the capability of the HEMT structure to deliver saturation currents superior to 1 A/mm as depicted in Figure 85.

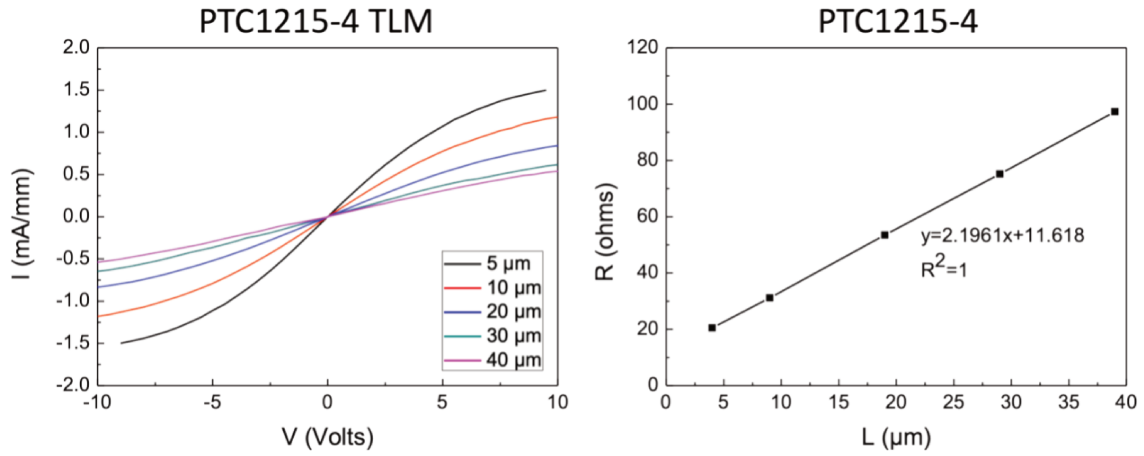

Figure 85: Left I-V measurements performed on a TLM pattern of sample PTC1215-4. Right resistance measurements performed on of the same TLM pattern.

Until now, the ScAlN barrier thickness has remained at 25nm. In this latest development, a 10 nm ScAlN barrier layer (sample PTC1251) was processed using a half-barrier etching for the ohmic contacts. Despite promising CV profiles ($N_s \sim 3 \times 10^{13}/cm^2$; $V_p \sim -6.5V$) extracted with the mercury probe shown in chapter 6 Figure 69, deceiving results have been obtained: the majority of the contacts present very high resistances. Only a reduced area of the sample exhibited a contact resistance below $10\Omega.mm$ ($R_c = 4.75\Omega.mm$) and $R_{sh} = 718\Omega/sq$ meaning that the process is far from optimized. A maximum saturation current below 300 mA/mm was measured. On the other hand, experiments on sapphire substrates were conducted to explore the impact of annealing temperature on the resistance of ohmic contacts. We tested three samples, PTC1263-1, PTC1263-2, and PTC1263-3 with annealing temperatures of 750℃, 800℃, and 850℃, respectively. Initially, we achieved a contact resistance of less than $1\Omega.mm$ for 750℃ and 800℃. However, as the annealing temperature increased to 850℃, the contact resistance also increased significantly, reaching $3.57\Omega.mm$. A similar investigation was carried out on another set of samples, PTC1264-1, PTC1264-2, and PTC1264-3, which confirmed that at lower annealing temperatures, we were able to achieve the lowest contact resistance, $R_c = 0.5 - 0.9\Omega/mm$ and saturation currents superior to 1A/mm could be obtained (Figure 86). During the annealing process at elevated temperatures (850℃), we observed a similar behavior to that

of PTC1263-3, with a resistance value of $R_c = 2.27\Omega.mm$.

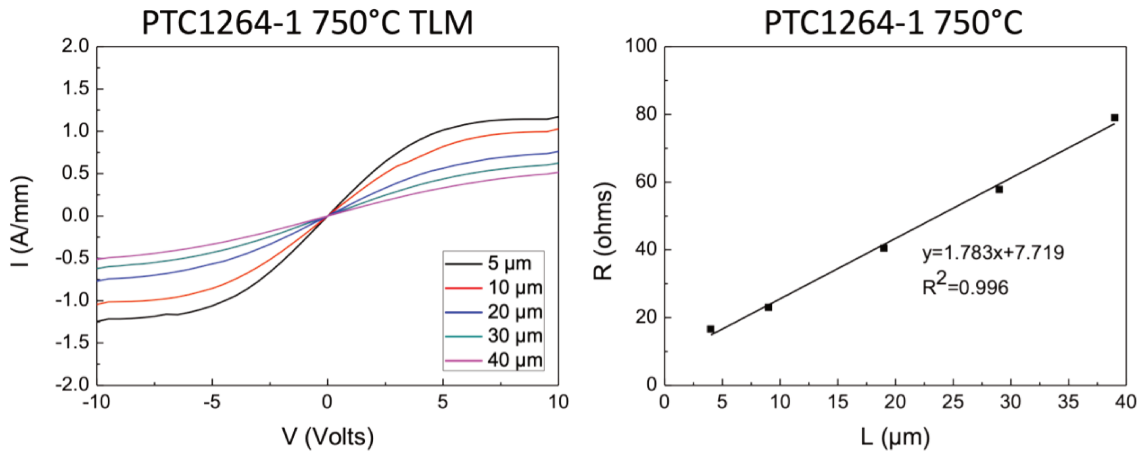

Figure 86: Left I-V measurements performed on a TLM pattern of sample PTC1264-1. Right resistance measurements performed on the same TLM pattern.

Another sample has undergone processing, featuring a ScAlN layer approximately 5 nm thick (PTC1253). It's crucial to note that there's an oxide layer on the surface measuring around 2 nm in thickness. Consequently, only 3 nm of the ScAlN layer remain as the barrier layer. The I-V measurements showed a noticeable reduction of the saturation current compared to the 25 nm ScAlN barrier sample PTC1215 (Figure 87) and the contact resistance was not sufficiently uniform to enable a clear extraction of a contact resistance. The rapid drop of the saturation current while increasing the contact spacing from $5\mu m$ to $10\mu m$ emphasized the sensitivity of the TLM pattern to surface depletion effects. Nevertheless, the $5\mu m$ spacing pattern exhibits a saturation current which is of the same order of magnitude as the one of conventional AlGaN/GaN HEMT heterostructures with much thicker barriers ($> 10nm$) processed in our laboratory [165].

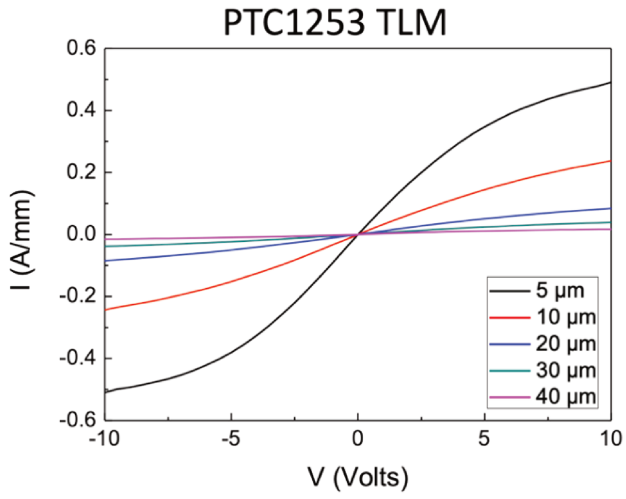

Figure 87: I-V measurements performed on the TLM patterns of sample PTC1253.

To address the issue of high oxidation on ScAlN when exposed to air, we implemented a chemical treatment step before the deposition of ohmic contacts. This treatment involved BOE to remove the oxide

layer from the surface. This specific procedure was performed on sample PTC1215-4. Comparison with PTC1215-3, indicates that this treatment had no big impact on the contact resistance. This might be attributed to the rapid oxidation of the surface in contact with the air after the treatment. The sample was not shielded from exposure to the atmosphere during the few minutes period between the BOE application and its placement in the e-beam evaporator.

Sheet resistance values were determined through TLM measurements and are reported in Table 10 . When the sheet resistance is low, it indicates a relatively high 2DEG density. We will discuss the 2DEG density in more detail in the next section where the sheet resistance was extracted from van der Paw measurements.

7.4 Van der Paw and Hall effect Measurements (sheet resistance, 2DEG density and electron mobilities).

It's imperative to keep in mind that our objective is to pinpoint extremely thin barrier layers characterized by a substantial 2DEG density and reasonable electron mobility, ultimately leading to the achievement of the lowest attainable sheet resistance. Table 112 compares the sheet resistance previously extracted from TLM patterns with the ones determined with van der Pauw devices. In almost all of the cases, the van der Pauw devices reveal a sheet resistance superior to the one extracted from TLM patterns. The discrepancy is less than 20% for PTC1215 and negligible for PTC1251. Both samples were grown with a highly resistive buffer on Si (111), which explains the similarities in the results. Hall effect revealed 2DEG carrier density and mobility in the range of $1.74-3.05\times10^{13}/cm^2$ and $450-608cm^2/V.s$respectively. The sample PTC1263-1 grown on Sapphire shows sheet resistances in the range of $400-560\Omega/sq$ but the huge carrier density ($1014/cm^2$) and the low mobility ($90cm^2/V.s$) translate a large contribution from carriers located in the buffer. The sample PTC1223 exhibits a similar behavior. On the other hand, the GaN regrowth process of sample PTC1264 did not produce such a parasitic conduction and 2DEG carrier density and mobility of $2.3\times10^{13}/cm^2$ and $950cm^2/V.s$ were extracted. This may be due to a partial or total compensation of regrowth interface contamination thanks to the presence of iron dopant in this specific template.

Sample	$R_{sh}^{TLM}(\Omega/sq)$	$R_{sh}^{vdP}(\Omega/sq)$	$N_h\times10^{13}(/cm^2)$	$\mu(cm^2/V.s)$
PTC1215-1	528	518-901	1.55-2.30	450-527
PTC1215-2	300	347-374	2.65-3.00	580-632
PTC1215-4	320-360	342-606	2.00-3.05	514-608
PTC1251	670-718	614-720	1.75-2.00	469-530
PTC1263-1	486-521	400-560	4-17.5	90-190
PTC1264-1	267-295	303-420	2.10-2.70	560-965
PTC1264-2	224-338	282-555	1.65-3.15	356-996
PTC1223	n.a	1160-1320	4.10-6.70	74-130

Table 11: Comparaison between sheet resistances deduced from TLM and Van der Pauw configuration,in addition, 2DEG density, and electron mobility deduced from Hall measurements.

Numerous research groups have documented measurements of mobilities and densities in ScAlN barrier HEMTs, as indicated in references [19], [116], [133], [146], [158], [162], [166]–[168]. These investigations encompass samples grown using both PAMBE and MOCVD methods. The reported mobilities have consistently achieved a peak value of approximately $1600cm^2/Vs$, while the associated density has remained

consistently around $2 \times 10^{13}/cm^2$. Figure 88 displays the electron mobility as a function of the 2DEG density, including previously reported data as well as our own findings. Most of these heterostructures contain an AlN interlayer to enhance the electron confinement into the GaN channel.

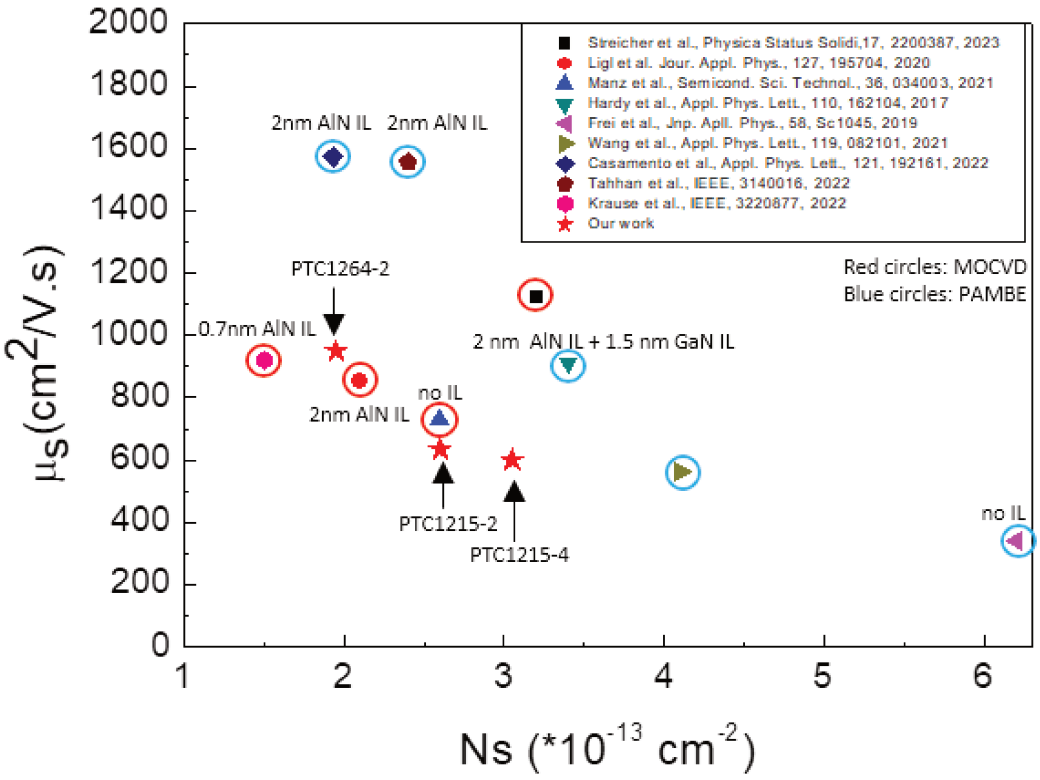

Figure 88: The graph presents a comparison of electron mobility against 2DEG density, combining data from existing literature and our newly obtained results.

It's evident that in PAMBE-grown samples, both electron mobility and 2DEG density are notably more responsive to changes in the interlayer, whereas in MOCVD-grown samples, the AlN interlayer has a comparatively negligible impact on mobility compared to PAMBE-grown samples. The highest mobility attained through MOCVD stands at approximately $1150cm^2/Vs$. These samples were grown on either SiC or sapphire substrates. The SiC substrate choice led to excellent electrical results, resulting in a remarkable mobility of $1600cm^2/Vs$. In contrast, for samples grown on sapphire substrates, the highest mobility attained was limited to $850cm^2/Vs$. One may suppose that GaN epitaxy on SiC has consistently exhibited superior crystalline quality compared to its growth on sapphireas reported in [169]. In contrast to other studies where the barrier layer thickness was typically less than 10nm, Frei et al. [133] reported a significantly thicker ScAlN barrier layer of 25nm grown on sapphire substrate by PAMBE. Despite achieving a high 2DEG density of approximately $6.2 \times 10^{13}/cm^2$, their mobility was comparatively low, measuring around $300cm^2/Vs$. Notably, it's important to mention that no interlayer was introduced before the growth of the ScAlN layer in their work. In our research, we incorporated a thin AlN interlayer of approximately 1nm thickness before growing the ScAlN layer. This was carried out on either sapphire or silicon substrates. Notably, to the best of our knowledge, our study marks the first instance of ScAlN barrier HEMT being grown on a silicon substrate

(PTC1215-PTC1251). In this diagram, we've incorporated data points for the samples PTC1215, PTC1251 and PTC1264-1. It's evident that the sample grown on sapphire (PTC1264) exhibits greater electron mobility compared to the one grown on silicon reaching a mobility close to $1000 cm^2/V.s$. However, the silicon-grown sample PTC1215-4 demonstrates a higher 2DEG density up to $3 \times 10^{13}/cm^2$. In summary, when we compare our findings to the state-of-the-art results, it becomes evident that our data aligns closely with the trend illustrated in the accompanying Figure 88 (especially for PTC1215-1 and PTC1215-4), showing that the mobilities are decreasing when the 2DEG density is increasing. This trend is observed because when the 2DEG density rises, the influence of electron-electron interactions becomes more pronounced. Electrons, which carry negative charges, tend to push each other away due to their like charges. This electron repulsion leads to increased scattering, making it more challenging for electrons to move freely, and this effect becomes more noticeable as the 2DEG density increases. Consequently, electron mobility decreases. The observed higher electron mobility in the sample grown on sapphire (PTC1264-2) compared to samples grown on Si (PTC1215-2 and PTC1215-4, see Figure 88) can primarily be attributed to the higher crystalline quality of the GaN material in the samples grown on sapphire substrates. However, it's important to note that PTC1264 still exhibits lower mobility compared to what is reported in the literature. In this case, the reduced electron mobility does not seem to be solely caused by poor crystal quality in the GaN, as samples grown on sapphire demonstrate excellent crystal quality with a low threading dislocation density ($10^8/cm^2$). Instead, the lower mobility in PTC1264 could be due to scattering effects at the interface. This could be a result of insufficient AlN thickness ($< 1nm$), which fails to effectively limit this scattering and diffusion at the interface. It's worth noting that prior studies by Tahhan et al. and Casamento et al. introduced a 2nm thick AlN layer, which proved beneficial in reducing scattering at the interface. Therefore, the insufficient AlN thickness in PTC1264 might be a key factor contributing to the lower electron mobility in this sample.

Sample	$N_s^{Hgprobe} \times 10^{13}(/cm^2)$	$V_p(V)Hg$	$C(0V)^{Hg}(mF/m^2)$	$N_h \times 10^{13}(/cm^2)$	$V_p(V)$	C(0V) (mF/m^2)
PTC1215-2	4	-19	4	4	-10	5
PTC1215-4	4	-19	4	3	-10	4.5
PTC1251	3.2	-6.5	9.1	1.60-2.20	-3.8-3.5	7.5-10
PTC1264-1	3.7	-8	8.9	2.00-2.30	-5	6.7-7.5
PTC1264-2	3.7	-8	8.9	1.70-3.00	-5.5-4.5	6.7-7.5
PTC1223	3.5	-8	8	1.20-1.60	-3.5-3	7.5-8.2

Table 12: Comparing the C(V) measurements including the N_s, V_p and C (0 Volts) from Hg probe and diodes before and after the process.

Determining the concentration of a 2DEG using capacitance voltage measurements with a mercury probe is a valuable technique to employ prior to any manufacturing processes. Next, the 2DEG concentration was verified with C-V performed on processed circular diodes (Figure 89). The results are presented in the Table 12.

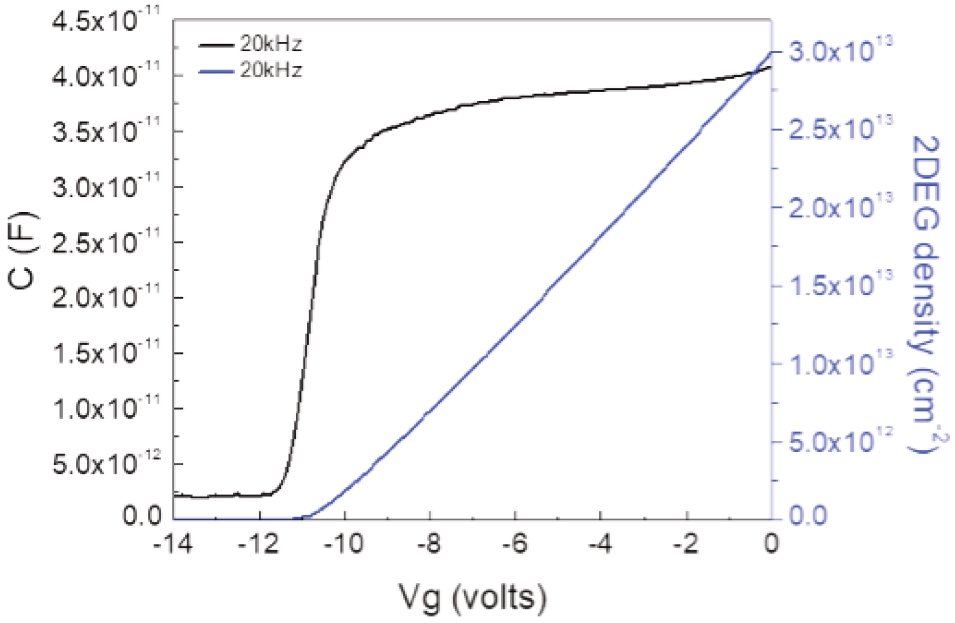

Figure 89: C-V profile recorded on a 100 µm diameter circular diode from process PTC1215-2 and associated 2DEG charge density deduced from the integration of the profile.

Following the present manufacturing process, it is expected that the 2DEG electron density will either decrease or remain unchanged. Notably, a significant decrease in 2DEG concentration is observed after

the process. For PTC 1251, PTC1264-1, PTC1264-2 and PTC1223, a drop off in terms of density by approximately a factor of 2 were observed. This decrease appear unrelated to a reduction in barrier thickness since the capacitance is not increasing. Considering the observed shift of the pinch-off voltage, a change of the effective metal/semiconductor barrier height seems not likely. This decline may be attributed to the fabrication process itself. For instance, the change in the surface states may occur during the development of the photoresist (AZ726) during the photolithography steps. A decrease of the pinch off voltage Vp of the C(V) measurements after the process can account for such an effect. On Table 12 we can notice that PTC1215-2 showed no change in 2DEG density after the process. For PTC1215-4, we noticed a small reduction in the 2DEG density that could be related to the reduction in the barrier thickness, as we observed that the capacitance at 0 volt increases from 4 to $4.5mF/m^2$. This decrease might be attributed to the treatment with the BOE.

7.5 Transistor performances

After conducting electrical tests on the samples and evaluating their contact resistance, buffer isolation, 2DEG sheet resistance and electron density, it is worth to examine transistors. This examination will involve varying the gate length and the spacing between the source and the drain. The transistor width (development) is $150\mu m$. The following Figure 90 illustrates the DC output characteristics (Ids (Vds, Vgs) of transistors with 1, 2, or 4 μm gates fabricated at CRHEA laboratory using ScAlN/GaN HEMTs on Si or sapphire substrates. The gates are centered between the ohmic contacts. We present results obtained on the following samples: PTC 1251, PTC 1215-4, PTC 1264-1, PTC 1264-2, and PTC 1253.

Figure 90 shows the DC output characteristics Ids (Vds,Vgs) of transistors fabricated on the samples processed on sapphire substrates. A compliance of 1 mA/mm (Igs=0.15 mA) was applied for the gate leakage current.

By varying the bias V_{ds} between source and drain, we can observe how the electron current flow in the GaN channel changes. For gate voltages V_{gs} ranging from +1V to -3V, increasing the V_{ds} bias results in an increase of the drain current Ids until it reaches a maximum and then slowly decreases. The maximum drain current density measured at $V_{gs} = +1V$ is similar in both process PTC1264-1 ($I_{dsmax} = 860mA/mm$) and PTC1264-2 ($I_{dsmax} = 885mA/mm$). This indicates similar contact and channel sheet resistances since distances between contacts are identical in both devices (the source to drain distance is 9 μ m and the nominal gate length 2 μ m). Furthermore, from the linear part we can deduce the resistance R_{ON}, representing the total resistance of the transistor which is in the same range of $4.8\Omega.mm$ and $5.2\Omega.mm$ for the first and the second process respectively. The possible origins of the slow decrease of the drain current in the saturation region are self-heating effect or the presence of electric traps activated for larger drain bias. The output characteristics of the device with same dimensions on sample PTC1253 exhibit clear constant drain current at saturation but for significantly lower current values ($I_{dsmax} < 160mA/mm$). This plays in the favor of thermal effects.

Despite encountering significant challenges such as high contact resistance and elevated sheet resistance, the transistor's performance did not turn out as unfavorably as initially anticipated. Despite the lack of electrical isolation in the GaN buffer, the drain leakage current in the devices processed on PTC1264 accounts for a minor fraction of the total current obtained for V_{gs} in the [-1V, +1V] range. This current directly attests the high carrier density in the 2DEG. For comparison, compared to the present ScAlN/GaN HEMT, similar devices developed in the laboratory on AlGaN/GaN heterostructures provided maximum drain cur-

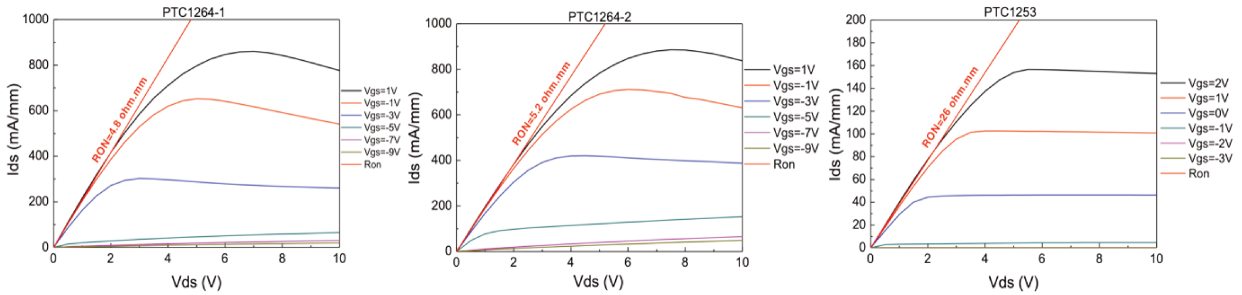

Figure 90: DC output characteristics $I_{ds}(Vds,Vgs)$ of $2\mu m \times 150\mu m$ gate transistors with $9\mu m$ source to drain spacings on ScAlN/GaN HEMTs grown on sapphire.

rents reduced by more than a factor of 2 in agreement with carrier densities at best around $10^{13}/cm^2$. [165] Furthermore, the threshold gate voltage corresponding to the pinch-off of the transistors is similar to the one deduced from C-V measurements on circular diodes and shown in Table 12. This is also the case for the devices on Silicon and attest to the uniformity of the process since the area of diode contacts is much larger than the area of the gate of transistors.

As depicted in the accompanying Figure 90, even in the case of the PTC1253 transistor, which boasts a nominal barrier thickness of just 5 nm, and if we were to exclude the oxidized surface layer, there remains a mere 3 nm of ScAlN. This reduction, as previously discussed, can likely be attributed to the surface cleaning process in absence of protection cap layer, which may unintentionally remove a few monolayers from the surface. Consequently, this procedure leads to a thinner barrier and, in turn, decreases the 2DEG density having a $R_{ON} = 26ohm.mm$ with a maximum drain current around 160 mA/mm at $V_{gs} = +2V$. Another distinct behavior appears at pinch-off. Indeed, for $V_{gs} = -2V$, the transistor is really pinched with a resulting drain current below 0.5 mA/mm. Contrary to PTC1264, the growth of the MBE GaN buffer layer started with a 200 nm thick layer doped with Mg acceptors at several $10^{18}/cm^3$, resulting in the compensation of the silicon contamination of the regrowth interface with the GaN-on-sapphire template.

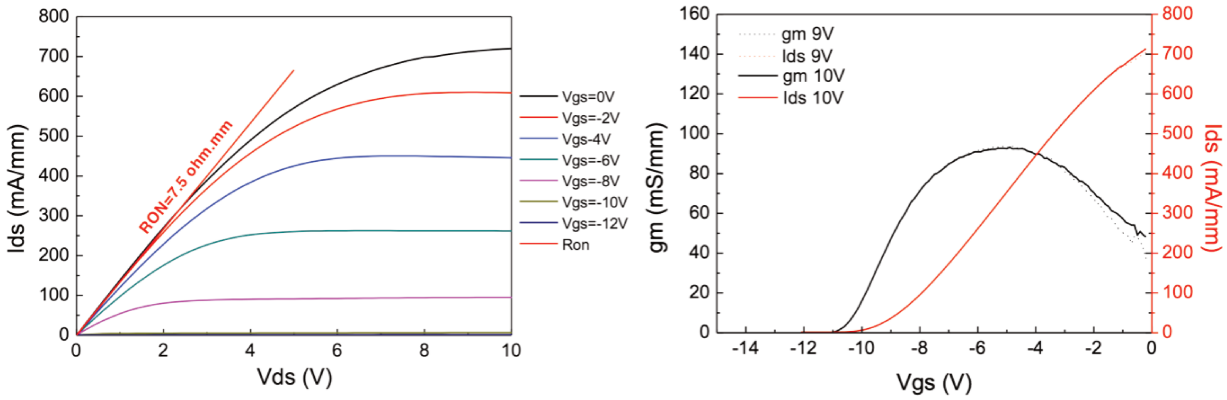

Figure 91: DC output characteristics $I_{ds}(Vds,Vgs)$ and transfer characteristics $I_{ds}(V_{gs},V_{ds})$ and $g_m(V_{gs},V_{ds})$ of a $2.8\mu m \times 150\mu m$ gate transistor with $8\mu m$ source to drain spacings on ScAlN/GaN HEMT PTC1215-1 grown on Silicon.

Figure 92 shows the results obtained on a transistor fabricated on the first HEMT grown on silicon PTC1215-1. The transistor exhibits a drain current density $I_{ds} = 700mA/mm$ at $V_{gs} = 0V$. According to the

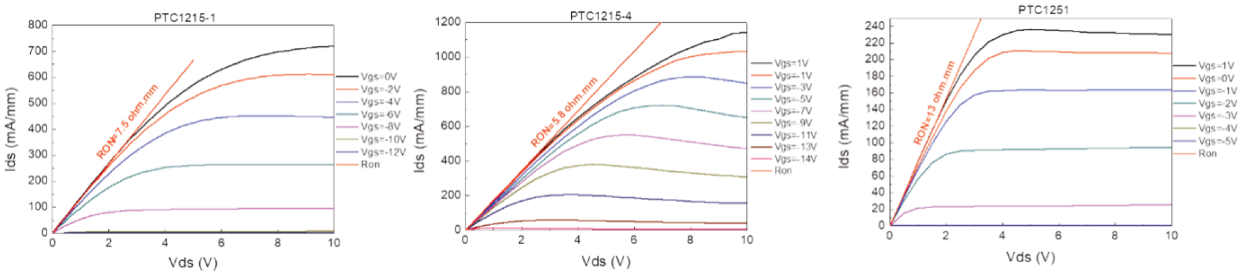

Figure 92: DC output characteristics Ids(Vds,Vgs) of 2 µm x 150 µm gate transistors with 9 µm source to drain spacings on ScAlN/GaN HEMTs grown on Silicon.

shape of the transfer curve $I_{ds}(I_{ds}(V_{gs},V_{ds})$ it should not reach much larger values at $V_{gs}=+1V$. The maximum transconductance gm is close to 100 mS/mm. The threshold voltage is around -10V, consistent with C-V measurements on circular diodes. When compared with PTC1264 (on Sapphire) the lower maximum drain current can be explained by the non-optimized process which resulted in the degradation of the 2DEG sheet resistance ($R_{sh}>500\Omega/sq$) and a contact resistance $R_c=1.75\Omega.mm$. On the other hand, the process PTC1215-4 (Figure 6) led to reduced resistances ($R_{sh}=334-400\Omega/sq$; $R_c\sim 1\Omega.mm$), to a more negative threshold voltage and a maximum drain current overpassing 1 A/mm at $V_{gs}=+1V$ although the distance between source and drain contacts was slightly larger ($L_{sd}=9\mu m$). As a consequence, the resistance RON droped from $7.5\Omega.mm$ to $5.8\Omega.mm$, which is not far from results obtained previously on the sample PTC1264. The large drain current is obtained with a ScAlN barrier thickness initially estimated at 25 nm. The reduction of the nominal barrier thickness to 10 nm was more problematic in terms of 2DEG sheet resistance and contact resistance. As discussed previously TLM provided at best a contact resistance $R_c=4.75\Omega.mm$ and a sheet resistance around $700\Omega/sq$ resulting in saturation currents of 300 mA/mm. As shown in Figure 6, such properties explain the low maximum drain current $I_{dsmax}\sim 240mA/mm$ achieved in the transistor. However, the degradation of the pinch-off voltage from -6.5V with the mercury probe to -4V presently may indicate some progress in the process compared to the one performed on the sample PTC1253.

Finally, the electrical leakage in transistors processed on PTC1251 have been measured. This sample presents a buffer breakdown voltage around 120 V as shown in Figure 93. For the transistor leakage measurements, a gate bias $V_{gs}=-6V$ was applied while the drain bias was increased up to $V_{ds}=100V$. The threshold voltage of the transistor is around $V_{gs}=-4V$ (Figure 92) and the choice of a more negative gate bias ensures a good pinch-off even at large drain voltage. As shown in Figure 92, the drain leakage current density is monotonously reaching 0.5 mA/mm at $V_{ds}=100V$ whereas the gate current density reaches 0.2 mA/mm. The leakage through ScAlN barriers is a major concern for material grown by MOCVD [170].Thus, the present result is encouraging since up to $V_{ds}=100V$, the drain leakage current is not dominated by the gate leakage and it is probably limited by the ability of the buffer to sustain large electric fields. Indeed, let's remind that the GaN buffer layer in this structure is $0.9\mu m$ thick only, which can explain the obtained breakdown voltage.

7.6 Conclusion

In summary, we have successfully fabricated electron devices such as diodes and transistors on ScAlN barrier HEMTs with GaN buffer layers grown by ammonia source molecular beam epitaxy on both silicon and sapphire substrates. Even if not fully optimized, ICP RIE etching enabled the successful achievement

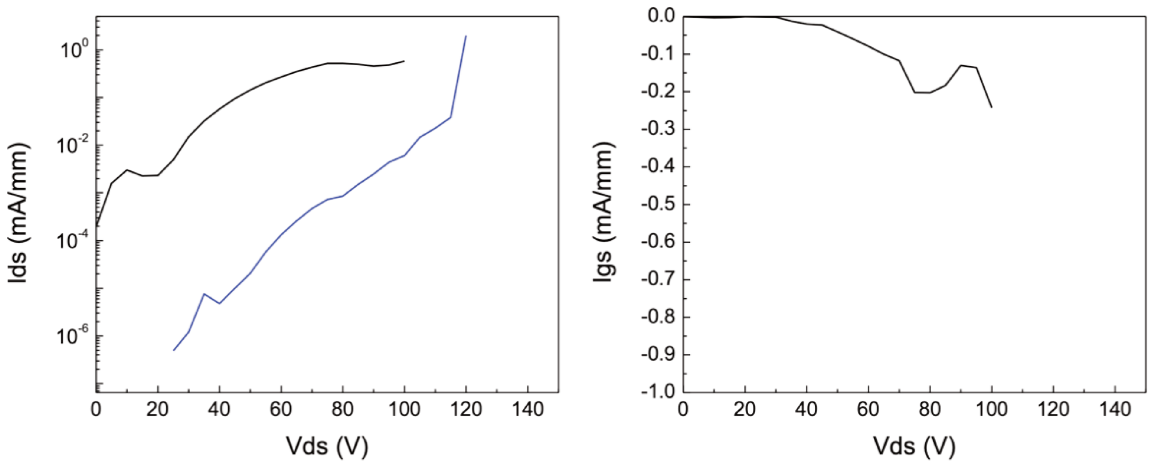

Figure 93: left: drain leakage current Ids(Vds) and right : gate leakage $I_{gs}(Vds)$ at $V_{gs} = -6V$ for a $2\mu m \times 150\mu m$ gate transistors with $9\mu m$ source to drain spacings on the ScAlN/GaN HEMTs grown on Silicon PTC1251. The blue curve on the left represents the buffer leakage current measured on an isolation pattern.

of mesas for device isolation. The realization of low resistance ohmic contacts is a challenge and the achievement of contact resistance of the order of $1\Omega.mm$ and less in some case is a first encouraging step together with the demonstration of current densities superior to 1 A/mm. The deposition of NiAu metal stack was performed as gate contact in a similar way to what is usually done to obtain Schottky contacts on AlGaN barriers. C-V measurements on diodes present a shape similar to the one obtained with a mercury probe on as grown barriers, but with differences allowing to evaluate any changes in thickness or surface donors. Such changes may be due to the reactivity of the ScAlN surface in absence of a protective cap layer. Van der Pauw patterns have been processed to confirm 2DEG carrier density and mobility. For a HEMT grown on silicon, 2DEG electron density up to $2-3\times10^{13}/cm^2$, has been measured coupled with an electron mobility of $500-600cm^2/Vs$ and a sheet resistance (R_{sh}) of 360-400 /sq. These properties explain the substantial drain current measured on transistors, with a maximum reaching 1150 mA/mm and an on-resistance of 5.8 ohm.mm for a contact distance of $9\mu m$. Furthermore, the high resistivity of GaN grown on Silicon permitted to bias a transistor close to the buffer breakdown voltage while keeping the gate leakage current below 0.2 mA/mm. This result is very encouraging considering the limitations reported with ScAlN barriers grown by other epitaxy techniques. On the other hand, the HEMTs grown on sapphire exhibited quite similar properties but with an improved electron mobility reaching $1000cm^2/Vs$. Large drain currents were achieved in transistors but the lack of resistivity of the GaN buffer regrown on GaN-on-Sapphire templates impinged a total pinching of the transistors. Nevertheless, the introduction of Mg acceptors in the MBE regrown GaN could be a solution to continue growth and device process optimizations on such templates.

8 Summary and outlooks

The primary objective of this thesis was to study the epitaxial growth of ScxAl1-xN thin films. The ultimate goal was to employ these films as an innovative barrier material in GaN-based High Electron Mobility Transistors (HEMTs) designed for high-frequency and high-power applications. In order to attain high-frequency performance, we opted to reduce the gate length and maintain a thin barrier thickness to prevent the short-channel effect. In this study, we present, for the first time to our knowledge, the successful growth of epitaxial ScAlN/GaN heterostructures using ammonia-source Molecular Beam Epitaxy (MBE) under a nitrogen-rich environment. Our investigation initiated with 25 nm thick ScAlN layers grown on GaN-on-sapphire templates. This relatively thick layer was deposited to evaluate surface morphology, crystal quality, scandium amount, and the density of 2D electron gas (2DEG) in relation to varying the growth temperatures (ranging from 620℃ to 800℃). Our findings indicated that the growth temperature had no discernible impact on the growth rate nor surface morphology (rms roughness below 0.5 nm) contrary to what happens with other epitaxy techniques. However, we observed a grain-like morphology on the surface of ScAlN films, with grains approximately 20 nm in diameter. Atomic probe tomography (APT) did not evidence the presence of heterogeneity of composition in the alloy and throughout the growth range, we consistently observed a single wurtzite phase Nevertheless, the growth temperature significantly influenced crystal quality, with the highest quality crystals obtained at lower growth temperatures (620℃ to 670℃). This trend aligned with the 2DEG density determined through capacitance-voltage measurements using a Mercury probe. The 2DEG concentration reached a peak of $3-4\times10^{13}/cm^2$ for barriers grown below 700℃ and then sharply declined at higher growth temperatures. In conclusion, these two criteria led us to consider an optimal growth temperature of approximately 670℃. We set a method to extract the scandium molar fraction from XPS measurements andnoted that in these first studied films it hovered around 15% and exhibited a slight decrease with increasing growth temperature, although this observation was subject to potential measurement errors and analysis uncertainties. Scandium molar fraction was confirmed also by SIMS and APT measurements, and from X-ray diffraction reciprocal space mapping, we figured out that ScAlN had the same i-plane lattice parameter as GaN buffer layer regardless growth temperature. Subsequently, we explored the impact of varying ScAlN barrier layer thicknesses on 2DEG concentration, aiming to reduce the barrier thickness for high-frequency performance. We grew ScAlN layers with thicknesses of 25 nm, 15 nm, 10 nm, and 5 nm observing that the 2DEG density increased with increasing barrier thickness up to 15 nm, but then experienced a sharp decline. Transmission electron microscopy (TEM) and geometric phase analysis (GPA) revealed the emergence of a defective layer starting at 13 to 15 nm ScAlN thickness, featuring atomic disorders. This phenomenon may explain the decrease in 2DEG concentration. GPA analysis corroborated that no in-plane lattice relaxation occurred even with ScAlN thicknesses of up to 55 nm.

We attempted to grow ScAlN films with higher scandium amounts, reaching up to 30%. However, this endeavor revealed additional X-ray diffraction peaks, potentially indicating the presence of extra phases, though this has not been conclusively proven. Furthermore, an observable degradation in 2DEG density accompanied the increase in scandium amount, likely due to the crystal deterioration. Additionally, the non-defective layer thickness decreased to a 4 nm for 30% scandium molar fraction.

This research has laid a solid foundation for the epitaxial growth of ScxAl1-xN films, offering valuable insights into the growth process using ammonia source MBE under a nitrogen-rich environment. The established growth parameters have facilitated the deposition of epitaxial $Sc_xAl_{1-x}N$ films matched to the lattice of GaN buffer layers. Notably, a high 2DEG density, approaching $2\times10^{13}/cm^2$ with a 5 nm nominal thickness

of ScAlN (probably 3 nm in reality due to the presence of oxides at the surface), marks significant progress in harnessing $Sc_xAl_{1-x}N$ as an innovative barrier material for GaN-based HEMTs.

A process technology was subsequently developed for samples grown on sapphire and Si (111) substrates, achieving a low contact resistance, sometimes less than $1\Omega.mm$ and a current density exceeding 1 A/mm resulting from TLM patterns and transistors. This is sufficient to assess the material properties, but future performant devices will necessitate much lower contact resistances. Our colleagues at IEMN (Univ-Lille) obtained contact resistances below $0.2\Omega.mm$ with 2 A/mm saturation current density with one of our ScAlN/GaN HEMT grown on sapphire, but the high annealing temperature required ($T > 900C$) could be an obstacle for the reliability of this process. As an alternative, the local area regrowth of n-type highly doped GaN has been reported in the literature [118].This approach already mastered for AlGaN/GaN HEMTs in our laboratory is an interesting option. Hall measurements on van der Pauw devices have shown a 2DEG density about $2-3\times10^{13}/cm^2$ with electron mobility of nearly $500-600cm^2/Vs$ for samples grown on Silicon substrates. These characteristics account for the significant drain current observed in transistors, with a peak value of 1150 mA/mm and an on-resistance of 5.8 ohm.mm at a contact distance of $9\mu m$. Moreover, the elevated resistivity of GaN when grown on Silicon enables the biasing of a transistor near the buffer breakdown voltage, while maintaining the gate leakage current below 0.2 mA/mm. HEMTs grown on GaN-on-sapphire exhibited similar carrier densities with slightly enhanced mobility ($\sim 740cm^2/V.s$). In addition, a high mobilities close to $1000cm^2/V.s$ has been reached for a sample grown on sapphire with a 2DEG density close to $2\times10^{13}/cm^2$. Based on these observations, we may anticipate that the growth of thicker GaN buffer layers with a better crystal quality could lead to higher electron mobility in HEMTs grown on Silicon substrate. On the other hand, there is room for improvement of the interface between GaN and ScAlN since the role of the thickness of the AlN interlayer grown to better confine the electrons in the 2DEG has not been extensively studied as well as a comprehensive examination of interface diffusion. C-V measurements on processed diodes present a shape similar to the one obtained with a Mercury probe on as grown barriers, but with differences allowing to evaluate any changes in thickness or surface donors. Such changes may be linked to the reactivity of the ScAlN surface in absence of a protective cap layer. The affinity of scandium for oxygen induces other problems for obtaining high purity sources, possibly for growing high purity ScAlN alloys and for analyzing the chemical purity of the as grown films as shown by our XPS analyses. As a consequence, extremely high purity analysis environments will be necessary to state on the purity of the grown ScAlN films. Passivation of the ScAlN barrier layer is needed to protect from oxidation, which can have detrimental effects on its electrical performance. To face this issue, GaN and SiN passivation layer grown by MOCVD on ScAlN have been reported [167]. The study has shown that GaN generates 3D islands resulting in a non-coalesced layer which is insufficient for surface protection (Figure 94). On the contrary, SiN passivation layer has shown a smooth surface ($rms < 0.2nm$) with a completely coalesced surface free of pits or deep valleys as seen with GaN cap layers ($rms = 1.5nm$).

However, in the context of PAMBE, it was observed that GaN cap layer grown on ScAlN/GaN exhibited a smooth surface, with a rms roughness of approximately 1.08 nm when scanned over an area of $10\times10\mu m^2$ as depicted in [162] Figure 95. Additionally, a comparative study with PAMBE [116] was conducted to assess the impact of different cap layers (GaN, AlGaN, and SiN) on the performance of ScAlN transistors. The results showed that AlGaN delivered the highest performance, achieving a power-added efficiency (PAE) of 26% with an output power (Pout) of 10.8 W/mm. In contrast, SiN demonstrated a PAE of 31% at Pout of 8 W/mm, while GaN exhibited the lowest performance, with a PAE of 27% and Pout of 4.1 W/mm. Furthermore, an analysis of the 2DEG density and mobility characteristics of an unpassivated

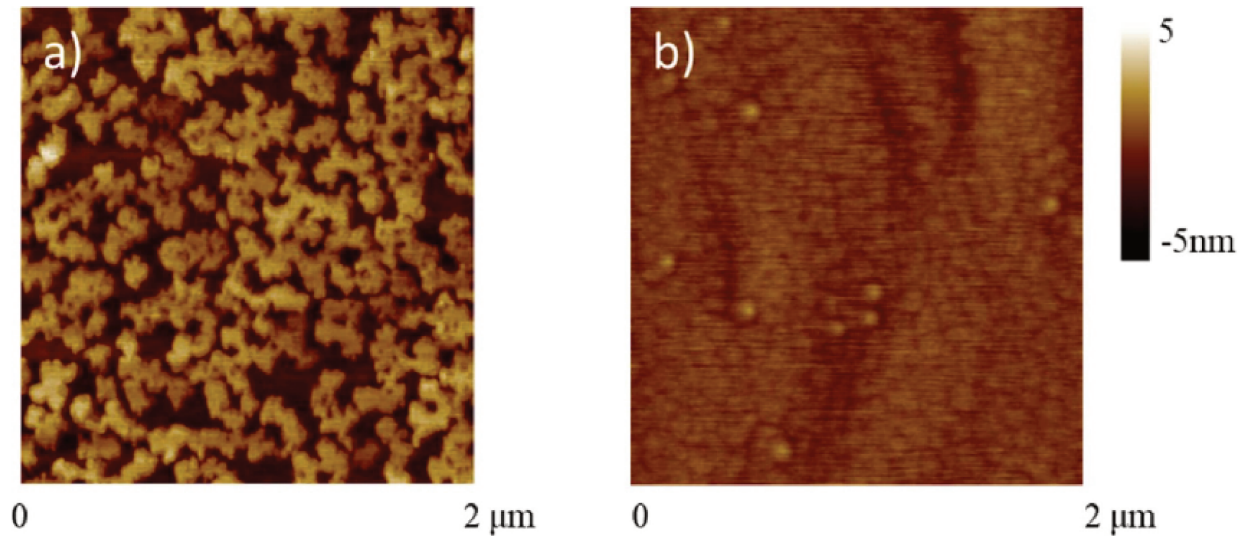

Figure 94: AFM images on $2 \times 2\mu m^2$ for GaN and SiNx cap layer grown on ScAlN/GaN/sapphire by MOCVD [167].

sample revealed initial values of $2.4 \times 10^{13} cm^{-2}$ and $1556 cm^2/V.s$, respectively. Comparatively, the in situ GaN passivated sample displayed a charge of $1.7 \times 10^{13} cm^{-2}$ and a mobility of $897 cm^2/V.s$. Finally, the in situ AlGaN passivated sample exhibited a charge of$2.1 \times 10^{13} cm^{-2}$ and a mobility of $804 cm^2/V.s$.

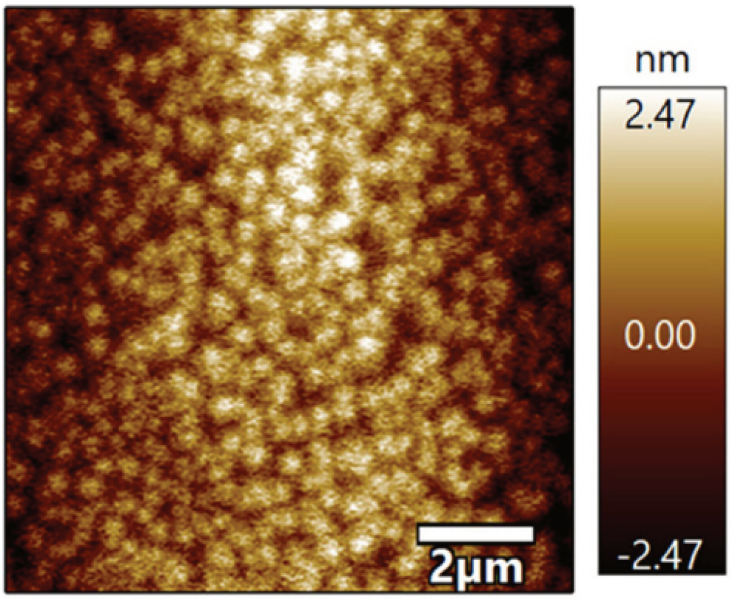

Figure 95: AFM image on $10 \times 10\mu m^2$ for GaN cap layer grown on ScAlN/GaN on SiC substrate by PAMBE [162].

In this thesis, the deposition of 2nm GaN cap layer on ScAlN by NH3 MBE has resulted in a surface with a notably rough texture showing a non-uniform protection with 3D islands and a rms roughness close to 2.2 nm for $2 \times 2\mu m^2$ AFM image scan area, as illustrated in the Figure 96. This agrees with MOCVD results [167]. Further studies on SiN cap layer growth by NH_3 MBE are needed for the passivation on ScAlN HEMT. Beyond the stabilization of the electrical behavior of transistors, a successful passivation may enable more detailed studies of the electrical properties of ScAlN, including the transport mechanisms of

electrical charges through the barrier, which are critical for applications.

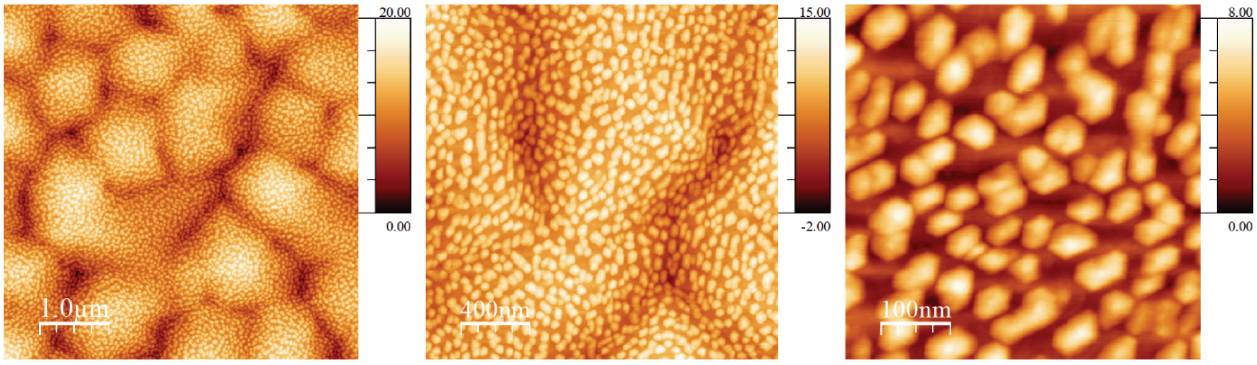

Figure 96: ScAlN/GaN with 2nm GaN cap layer having a rms roughness of 2.9nm, 2.2nm and 1.55 nm for 5×5, 2×2 *and* $0.5 \times 0.5 \mu m^2$ *scan area respectively.*

9 Appendices

9.1 Structural characterizations

9.1.1 X-ray diffraction (XRD)

Following the initial XRD experiments, a series of influential theoretical explanations were proposed by Bragg [171], Darwin [172], Ewald [173], and von Laue [174]. X-ray diffraction (XRD) is a widely used analytical technique for studying the crystal structure and properties of materials[175]. The wavelength of the X-ray photons is of the same order of magnitude as the interatomic distances of the crystal. When X-rays interact with a crystalline material, they scatter in different directions based on the periodic arrangement of atoms in the crystal lattice. The scattered X-rays produce a diffraction pattern that can be detected and analyzed. Constructive interference and, consequently, diffraction happen when the path difference ($\delta\vec{k}$) of the interfering waves is a multiple of the wavelength of radiation.

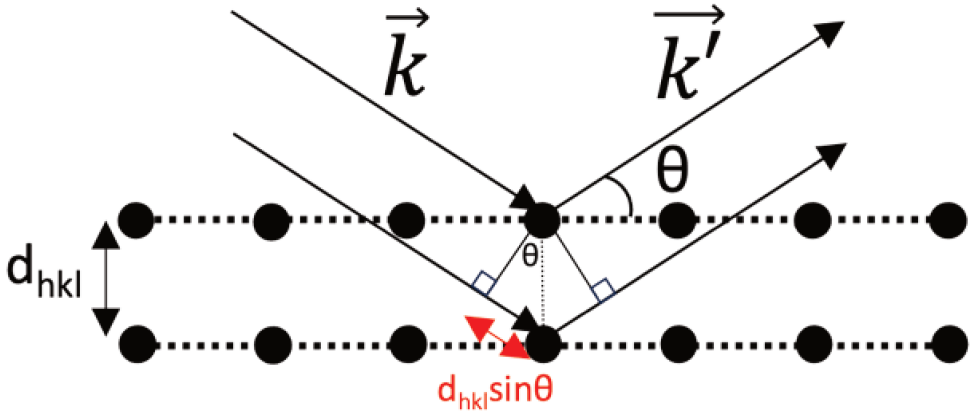

Figure 97: Path difference required for Bragg conditions in diffraction.

$$\delta\vec{k} = \vec{k} - \vec{k'} = 2d\sin\theta$$

By employing basic geometric principles, we can derive Bragg's formulation of X-ray diffraction (which also applies to electron diffraction), as described in 1913 [171].

$$n\lambda = 2d_{hkil}\sin\theta_{hkil}$$

Where n is an integer representing the order of diffraction, λ is the X-ray wavelength ($\lambda = 1.54056\text{Å}$) in our case. d is the inter-plane distance and θ is the X-ray diffraction angle.

Each miller's index (hkl) reflection from a crystal possesses a specific scattering amplitude and diffracts at a particular angle θ, determined by the interplanar distance d_{hkl}. Consequently, it is possible to construct an imaginary lattice that encompasses all the potential (hkl) reflections associated with the crystal lattice. This concept is known as reciprocal space, where the reciprocal lattice represents the Fourier transform of

the direct, real space lattice. By employing the reciprocal space concept along with the Ewald sphere construction, it becomes possible to determine the diffraction planes for a given wavelength (λ) and diffraction geometry. Figure 98 depicts an Ewald sphere construction that corresponds to the previously discussed Bragg condition. In this construction, the radius of the Ewald sphere represents the magnitude of the wave vectors $\vec{K}_{in}$ and $\vec{K}_{out}$ then $\vec{K}_{in} = \vec{K}_{out} = \frac{2\pi}{\lambda}$

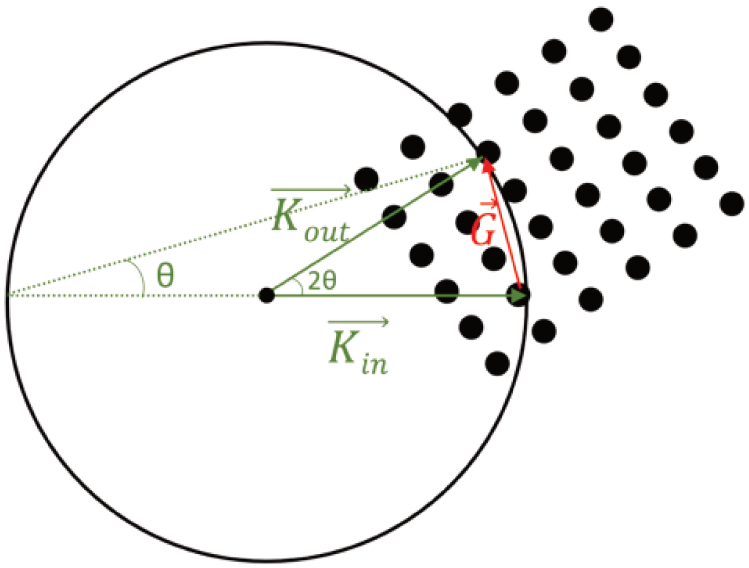

Figure 98: The Laue conditions for diffraction involve the interaction between the Ewald sphere and the reciprocal lattice points. These conditions determine when diffraction occurs.

The magnitude of the reciprocal lattice vector ($\vec{G}_{hkl}$) , which corresponds to the occurrence of diffraction, is determined when the reciprocal space vector ($\vec{G}_{hkl} = \vec{K}_{out} - \vec{K}_{in}$) terminates at a reciprocal lattice point (hkl) and the intersection of the Ewald sphere satisfies the Laue conditions. Referring to Figure 98 this geometry provides the formula for calculating ($\vec{G}_{hkl}$).

$$\vec{G}_{hkl} = \frac{4\pi \sin\theta}{\lambda}$$

In order to determine the lattice parameters of the in-plane and out-of-plane lattice structures, a reciprocal space map (RSM) is necessary where we can construct an imaginary lattice containing all possible hkl reflections, particularly in an asymmetric orientation (in our study $(10\bar{1}5)$ reflection is studied due to the high precision and intensity). The Q_x and Q_z components of ($\vec{G}_{hkl}$) (scattering vector) in reciprocal space play a crucial role in determining the corresponding a and c values.

$$Q_x = \frac{2\pi}{\lambda}(\cos(\omega) - \cos(2\theta - \omega)$$

$$Q_z = \frac{2\pi}{\lambda}(\sin(\omega) + \sin(2\theta - \omega)$$

The measurements presented in this thesis were conducted using a Panalytical X'Pert PRO MRD diffractometer. The instrument was equipped with two different detector optics (Figure 99). The first configuration involved a conventional fully open detector, while the second configuration featured a Ge crystal analyzer

in a triple axis setup. In the triple axis configuration, the diffracted beam underwent three reflections (220) before reaching the detector. To generate the incident radiation, a Cu anode, and a Ge (220) asymmetrical four-crystal monochromator were used, resulting in Cu K α_1 radiation with a wavelength of 1.54056Å. An X-ray mirror was employed to create a parallel beam with a divergence angle of less than 0.05°. For obtaining high-resolution rocking curves (transverse ω scans) and longitudinal $2\theta/\omega$ scans, the detector in the triple axis configuration was employed. On the other hand, standard measurements were carried out using the conventional detector configuration, either fully open or with a 1/4° slit in the diffraction path.

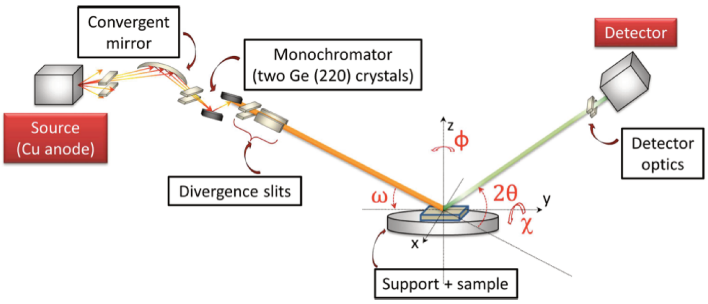

Figure 99: The schematic configuration of the diffractometer employed in this project. The angles associated with the sample movements: ω, ϕ, χ.

By rotating the sample (see Figure 100), we can adjust the angle between the sample and the beam-detector assembly. This rotation allows us to measure an intensity that is directly proportional to the number of properly oriented planes or grains at each specific angle, denoted as ω. As we vary the angle ω formed by the incident beam and the sample surface, the crystal planes of disoriented grains sequentially satisfy the diffraction condition. The width of the peak in a ω-scan reflection, measured at half of its maximum intensity, provides insights into the overall quality of the sample along the corresponding crystallographic direction indicated by the reflection (hkil). The broader the peak, the lower the overall quality of the sample and the shorter the coherence length of the crystallographic grains along the given direction. The ω scan of symmetrical reflections, specifically those denoted as (00l), provides information about the average tilt of the grains present in the sample. This tilt is associated with c-type screw-threading dislocations and a+c type mixed threading dislocations. On the other hand, the scan of asymmetrical lines, represented as (h0l), allows us to investigate all types of dislocations present in the layer, providing a comprehensive analysis of the dislocation characteristics in the sample.

In an alternative configuration known as the $2\theta/\omega$, the X-ray beam is directed onto the sample surface at an angle ω, which is equivalent to the angle θ. A diagram illustrating the sample setup is depicted in the Figure 101. The detector is positioned at an angle 2θ and records the maximum intensity when Bragg's law is satisfied. For materials such as element III nitrides that exhibit epitaxy along the [0001] direction, reflections on the (0001) planes (symmetrical lines) are particularly valuable in determining the lattice parameter c of the material using the equation provided. This lattice parameter determination enables the evaluation of crystal deformation along the growth axis as well as the concentration analysis of nitride alloys. It should be noted, however, that the obtained alloy concentration values may be affected by the stress state of the epitaxial films. For hexagonal lattices:

$$d_{hkl} = \frac{1}{\sqrt{\frac{4}{3a^2}(h^2 + k^2 + hk) + \frac{l^2}{c^2}}}$$

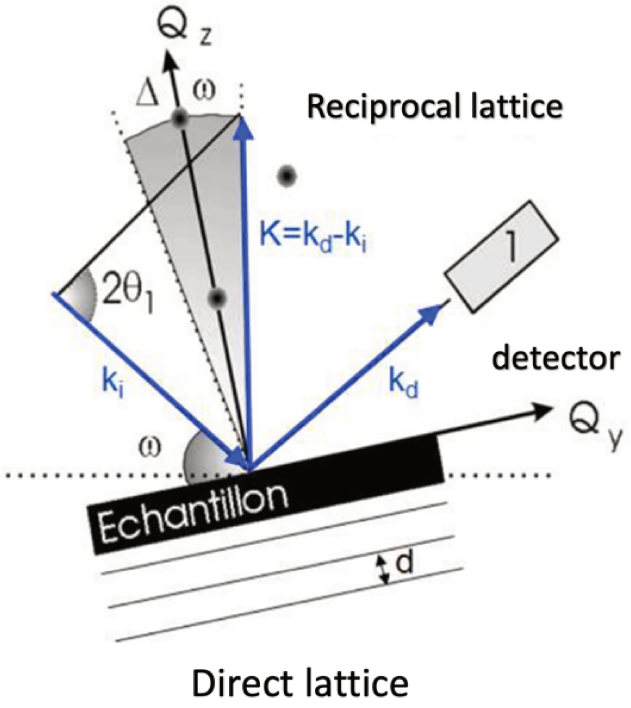

Figure 100: In a rocking curve X-ray diffraction experiment, the principle involves orienting the ω angle perpendicular to the Q_z axis of the reciprocal grating.

In symmetrical scans (when h=k=0).

$$d_{00l} = \sqrt{\frac{c^2}{l^2}} = \frac{c}{l}$$

To determine the composition of the ScAlN barriers, measurements are conducted in the $\omega_2\theta$ configuration. Additionally, simulations (AMASS and epitaxy software) of the heterostructure diffraction spectra are performed to obtain insights into the alloy's composition and thickness. However, it is important to note that there is a limitation in the system when dealing with thin layers, specifically those with a thickness below 5 nm. In such cases, the thickness fringes are either barely visible or not visible at all.

9.1.2 X-ray reflectivity (XRR)

measuring the intensity of X-rays reflected from the sample as a function of the incident angle [175]–[177]. In an X-ray reflectivity (XRR) experiment, the sample is subjected to incident X-rays at very small angles (approximately 0.2° to 5°), and the reflected X-rays are measured using the $2\theta - \omega$ configuration. Initially, total reflection occurs until a critical angle (θ_c) is reached. Beyond θ_c, the incident X-ray beam enters into the film, leading to interference between X-rays reflected from the sample surface and those reflected from the film-substrate interface. This interference results in a decrease in reflected intensity and the appearance of interference fringes as a function of the angle, as depicted in Figure 102 . The thickness (d) of the film can be determined by relating it to the angular positions of the maxima or minima, which have the order (n), using Snell's and Fresnel's laws.

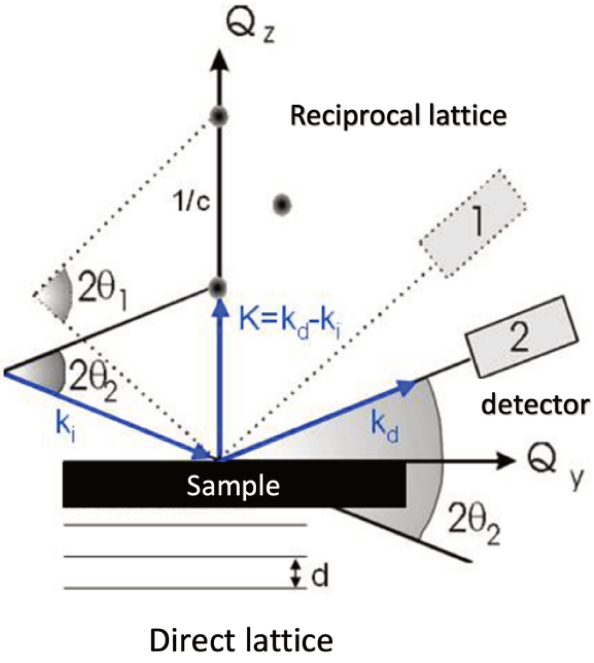

Figure 101: In a scanning X-ray diffraction experiment, the principle involves scanning the angles θ and 2θ along the Q_z axis of the reciprocal grating.

$$\theta_n^2 = (\frac{\lambda}{2d})^2 n^2 + \theta_c$$

The analysis of X-ray reflectivity data involves fitting the experimental data to a model that describes the expected behavior of the reflected X-rays based on the structure and properties of the sample. By adjusting the parameters of the model, such as layer thicknesses, roughness, and density, the best fit to the experimental data is obtained.

X-ray reflectivity is particularly useful for non-destructive analysis of samples with nanometer-scale thicknesses. X-ray reflectivity (XRR) experiments were conducted using the same diffractometer that was employed for X-ray diffraction (XRD). In these XRR experiments, the crystal analyzer detector was utilized in a triple axis configuration, allowing for the resolution of interference fringes. The curves obtained from the experiments were then fitted using the GenX [178] software.

9.1.3 Reflection High Energy Electron Diffraction (RHEED)

RHEED (Reflection High Energy Electron Diffraction) is the primary and straightforward technique used for investigating the surface morphology during growth using an MBE (Molecular Beam Epitaxy) reactor. By employing RHEED, it becomes possible to monitor the crystallographic characteristics of the surface layers in real time, while varying the growth parameters. The resulting RHEED patterns offer valuable insights into the surface structure, microstructure, and smoothness. In this method, an electron beam, generated by an electron gun and accelerated with a high voltage ranging from 10 to 50 kV, is directed towards the sample surface at a grazing incidence angle (θ) that is extremely small, usually less than 2 degrees, as illustrated

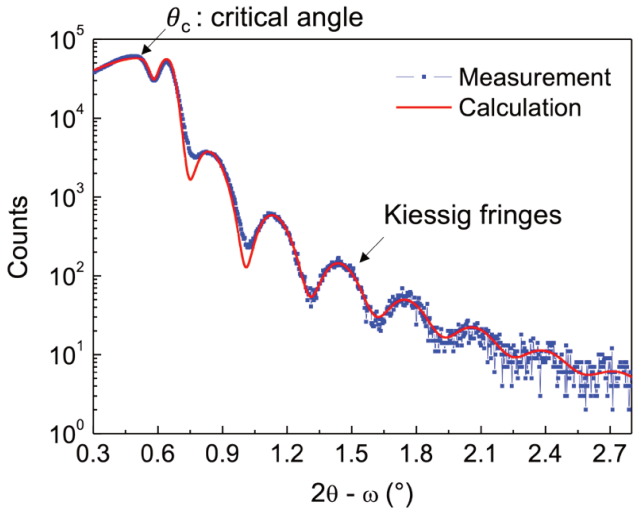

Figure 102: The red spectrum corresponds to the spectrum simulated by reflectivity to determine the thickness of the ScAlN barrier layer and the AlN interlayer.

in the accompanying Figure 103. The electron beam has a wavelength (λ) within the range of 0.06 to 0.15 $\mathring{A}$. The incident electrons strike the surface and get diffracted based on the atomic arrangement of the sample. A phosphorescent screen is used to collect the diffracted electrons. As the electrons interfere with each other, the resulting pattern provides crucial information about the positions of atoms on the sample surface. For a sufficiently flat sample surface, the electron beam penetrates the layer to a depth of only around 10 angströms, and the diffraction occurs primarily from the first atomic planes of the sample. In the quasi-2D diffraction geometry, the reciprocal lattice in X-ray reflectivity (XRR) experiments is composed of diffraction rods rather than points, which is different from X-ray diffraction (XRD). These rods are uniquely designated by two indices (hl) due to the absence of the third diffraction condition. Diffraction takes place at the point of intersection between the Ewald sphere and the diffraction rods. The radius of the Ewald sphere is determined by the magnitude of the wave vector ($\vec{K}_{in}$), which can be calculated by incorporating the de Broglie wavelength of the electrons.

$$\lambda = \frac{h}{\sqrt{2m_0E + E^2c^2}}$$

where E is the kinetic energy of the electrons, m_0 the electron mass, h the Planck constant and c the speed of light in vacuum.

In the case of a three-dimensional surface with notable roughness, the diffraction occurs when the electrons transmit through the surface's asperities. This leads to the formation of spot-like patterns in the RHEED diagram see Figure 104b. However, for amorphous materials like oxides produced through the oxidation of semiconductors in the presence of air, no diffraction is observed. Consequently, the RHEED pattern for amorphous materials solely consists of a diffuse continuous background, lacking distinct spots or lines.[179]

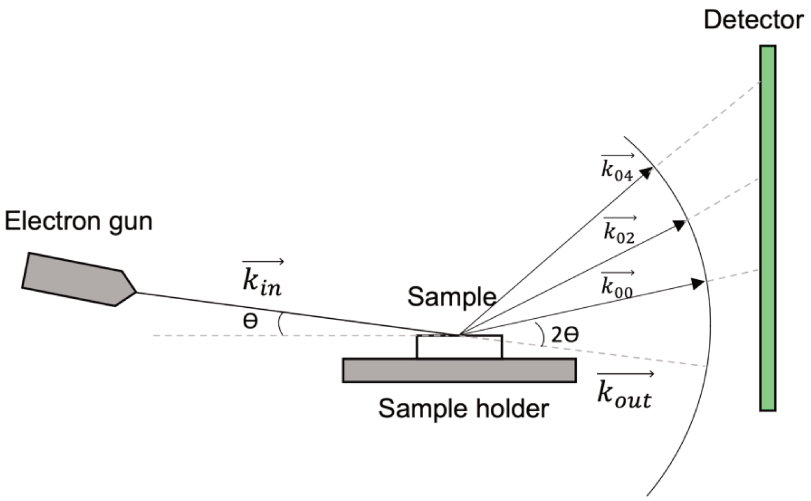

Figure 103: The RHEED pattern originates from the intersection of the Ewald sphere with the reciprocal lattice rods of a simple square lattice, as depicted in the diagram.

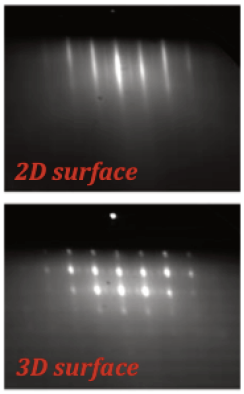

Figure 104: 2D and 3D RHEED patterns.

9.1.4 Transmission electron microscopy (TEM)

Knoll and Ruska were the inventors of the initial electron microscope in 1931. Their groundbreaking creation utilized magnetic lenses to concentrate electron beams. Ruska subsequently dedicated himself to advancing magnetic lens technology, resulting in an impressive magnification capability of over 12000 by 1934. For a comprehensive account of the evolutionary journey of transmission electron microscope (TEM) development, refer to the relevant information in the provided reference [180], [181].

The key components of a TEM setup include an electron source, electromagnetic lenses for focusing (at energies of around 100 to 300 keV, the wavelength obtained is close to that of X-rays. Note that X-rays cannot be used directly, as there is no lens to focus them. This is not the case with electrons, which are focused by electromagnetic lenses) and shaping the electron beam, a specimen holder, and a detector for capturing the transmitted electrons. The electron beam passes through the sample, and the resulting transmission image is formed due to the interaction of electrons with the sample's atomic structure. If the source produces electrons at around 100 kV, then the resulting beam has a wavelength in the picometer range, and therefore a resolution in the Å range which provide atomic-level resolution, allowing for the

visualization of individual atoms and lattice defects. TEM can be used to investigate crystal defects, grain boundaries, dislocations, interfaces, thin films, nanoparticles, and biological specimens.

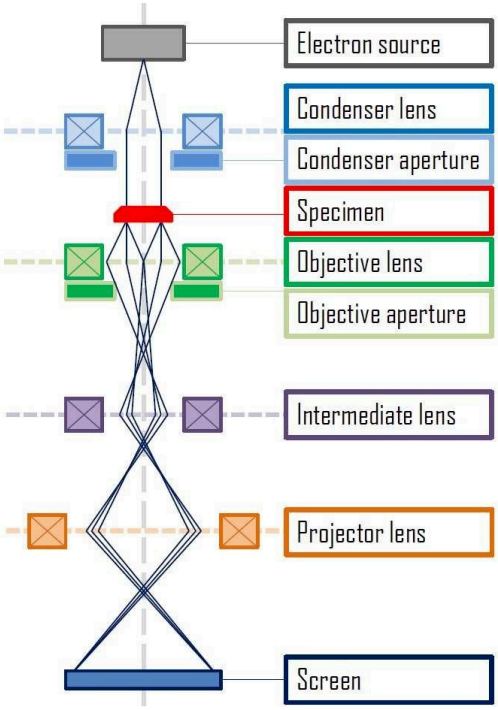

Figure 105: TEM setup [182].

Additionally, TEM can be coupled with various analytical techniques to obtain additional information. For example, energy-dispersive X-ray spectroscopy (EDS) can be used to analyze the elemental composition of the sample. High-angle annular dark-field scanning transmission electron microscopy (HAADF-STEM) is a technique within the field of scanning transmission electron microscopy (STEM) that captures inelastically scattered electrons or thermal diffuse scattering (TDS) at elevated angles using an annular dark-field (ADF) detector. In HAADF-STEM, a STEM image is generated by displaying the combined intensities of electrons in sync with the probe's position. Notably, the intensity of the HAADF image is directly related to the atomic number, with heavy atoms appearing brighter while light atoms prove challenging to distinguish.

In addition, Geometrical Phase Analysis (GPA) stands as a straightforward and effective approach for quantifying strain within nearly periodic images, with a particular emphasis on high-resolution transmission electron microscopy (HRTEM) images. In just a few simple steps, GPA conducts the averaging and optimal lattice parameter fitting within a specified region.

In this thesis, the samples were investigated using a STEM SPECTRA 200 from Thermo Fisher society (in Valbonne, France) by P. Vennéguès.

9.1.5 Atom force microscopy (AFM)

Atomic Force Microscopy (AFM) is a powerful imaging technique that allows for high-resolution imaging and characterization of surfaces at the atomic and nanoscale levels. This technique was developed by G.Binnig, CF. Quate and C.Gerber in 1986 [183]. It provides detailed topographic information and can also be used to measure various surface properties, including roughness, adhesion, and mechanical properties. During the

measurement process, a cantilever attached to a tip scans the surface of the sample line by line, with the movement facilitated by piezoelectric elements. As the tip interacts with the surface atoms, the cantilever undergoes different degrees of bending depending on the position of the tip. This bending is evaluated using a laser that is directed towards the backside of the cantilever and detected by a detector comprising multiple photodiodes, as illustrated in Figure 106. Changes in height and bending of the cantilever cause fluctuations in the intensity measured by the photodiodes. These intensity variations allow for the extraction of morphological images representing the surface features of the sample.

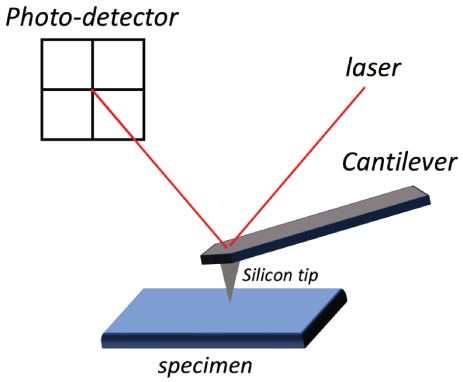

Figure 106: Representation of AFM measurement.

AFM can provide information beyond topography. By utilizing specialized probes, it is possible to measure various material properties. For example, force spectroscopy can be performed to measure the mechanical properties of the sample, such as elasticity or adhesion forces. Additionally, electrical, magnetic, and thermal properties can also be investigated with specialized AFM techniques. This technique enables surface roughness to be quantified. For roughness quantification, the Root Mean Square (RMS) parameter was used.

$$R_q = \sqrt{\frac{1}{L}\int_0^L (y(x))^2 dx}$$

In the given context, L represents the length of a line profile, while y(x) represents the variation in height for each data point relative to their average height.

As part of the thesis, AFM images were captured using a Bruker Edge system, equipped with a silicon tip. The imaging process in AFM can be performed in different modes, including contact mode, tapping mode, and non-contact mode. In this study, tapping mode was used to characterize ScAlN HEMT surface epitaxy (see Figure 107). Tapping mode, known as intermittent-contact mode, involves oscillating the cantilever at its resonant frequency while it lightly taps the surface. This mode reduces damage to the sample and to the tip, and it improves imaging resolution. Figure 107 shows the image of a ScAlN HEMT surface obtained with AFM using the tapping mode.

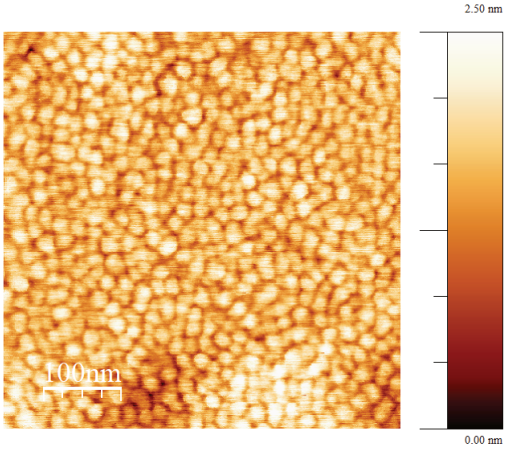

Figure 107: AFM image on a structure HEMT of ScAlN/GaN on sapphire substrate

9.2 Quantitative characterizations

9.2.1 X-ray photoelectron microscopy (XPS)

X-ray Photoelectron Spectroscopy (XPS), also known as Electron Spectroscopy for Chemical Analysis (ESCA), is a technique used to analyze the chemical composition and electronic states of a material's surface. XPS involves irradiating a sample with high-energy X-rays, which causes the emission of photoelectrons from the surface of the material. These emitted photoelectrons are then detected, and their kinetic energy is measured. The energy of the emitted photoelectrons is directly related to the binding energy of the electrons in the material, providing information about the chemical elements present and their chemical states. By analyzing the kinetic energy and intensity of the emitted photoelectrons, XPS can determine the elemental composition, chemical bonding, oxidation states, and surface contamination of the material.

When an atom absorbs a photon with an energy $h\nu$, subsequently, it can release an electron to return to a lower energy state. The ejected electron can carry on the entire energy of the incident photon, allowing it to traverse through the material, and continue moving due to its kinetic energy. In X-ray Photoelectron Spectroscopy (XPS), the incident photons typically have energies ranging from 1 to 2 kiloelectron volts (KeV). XPS commonly employs X-ray sources like magnesium and aluminum, which emit photons with energies of 1253.6 and 1486.6 electron volts (eV), respectively. The thesis focuses on the use of the Thermofisher K-Alpha 2008 XPS machine, equipped with an aluminum $K\alpha$ source and a monochromater. The relatively high energy of the incident radiation causes the emission of an electron from an inner orbital of the atom. Following this type of emission, there will be atoms with a vacancy in the original orbital of the photoelectron. This state is referred to as an ionic state, which can be de-excited through radiative emission (fluorescence) or Auger transition. By applying the principle of energy conservation, we can establish the following energy balance for the absorption of a photon with energy "hν":

$$h\nu = E_{binding} + E_{kinetic} + W$$

hν: Incident energy of the X-ray beam. $E_{kinetic}$: Kinetic energy of the electron as it leaves the sample. $E_{binding}$: Binding energy of the electron in the atom. W: work function

The distance that an ejected photoelectron will travel within a solid before encountering an obstacle

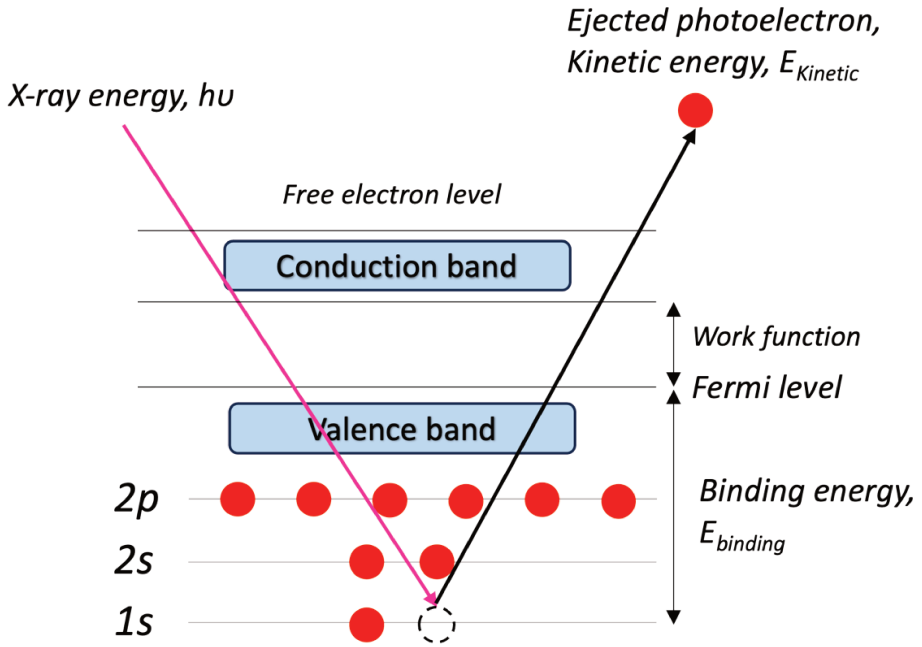

Figure 108: Principle of XPS.

is approximately around 10 nm which is about three times the value of λ (the inelastic mean free path). Beyond this distance, which is $3 \times \lambda$, the likelihood of a photoelectron emerging from the sample becomes significantly low. Consequently, the signal originating from the first layers of the sample, which may contain contaminants or surface effects, will appear enhanced in comparison. Sensitivity factors play a crucial role in X-ray Photoelectron Spectroscopy (XPS) as they help to determine the relative strength of photoelectron signals from various elements in a sample. These factors consider the differences in efficiency when it comes to emitting and detecting photoelectrons for different elements. By definition, a sensitivity factor represents the ratio of the photoelectron intensity emitted by a specific element to the number of atoms of that element present in the sample. This normalization enables meaningful comparisons of intensities across different elements within XPS spectra. The sensitivity factors can be calculated from their theoretical expression, or they can be experimentally determined from pure materials. In our case, these factors are integrated in the Avantage software. As previously mentioned, the average free path length is approximately 10 nm, and the initial few layers of the sample are typically composed with contaminants. To achieve a quantitative analysis of the sample, a compositional depth profiling technique is necessary. In our case, this can be accomplished by employing noble gas ions, such as Ar+ ions to etch the sample. The analysed surface has a spot size ellipse of 50 to $400 \mu m$.

9.2.2 Atom probe tomography (APT)

Atom Probe Tomography (APT) is an advanced technique used for examining the atomic-scale structure and composition of materials. It enables three-dimensional imaging and chemical analysis at the atomic level by combining field ion evaporation and time-of-flight spectrometry. In this method, the sample is prepared as an extremely sharp tip. This tip is cooled and subjected to a high DC voltage (ranging from 3-15 kV). Due to the very small radius of the tip and the application of high voltage, an intense electrostatic field (tens V/nm)

is generated at the surface of the tip, just below the point where atom evaporation occurs. By employing laser or high voltage pulsing, one or more atoms are evaporated from the surface, facilitated by the field effect, leading to nearly 100% ionization. These ionized atoms are then projected onto a Position Sensitive Detector (PSD) with exceptional detection efficiency. In fact, ion efficiencies can reach as high as 80%, making APT the most analytically efficient 3D microscopy technique available.

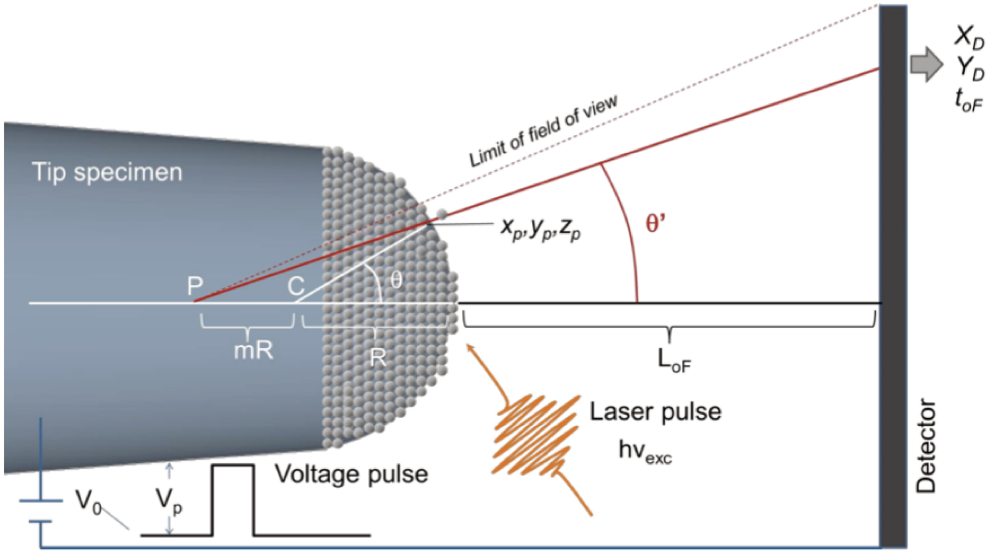

Figure 109: Schematic of APT setup.

The diagram above depicts the fundamental principle of atom probe tomography (APT), showcasing the specimen and a 2D position sensitive detector (PSD). In APT, either a laser or a voltage pulse is applied to the tip of the specimen, initiating the field evaporation of ions. Eventually, these ions reach the detector at a specific time. The detector enables simultaneous measurement of two key parameters:

- Time of Flight (t_{of}) of the ions: By measuring the time interval between the laser or voltage pulse and the arrival of ions on the PSD, the m/q ratio (mass over charge ratio) can be determined.

$$\frac{m}{n} = 2eV\frac{t_{oF}^2}{L_{oF}^2}$$

  t_{oF}^2 in the range of 10-1000 ns L_{oF}^2 in the range of 10-100 cm

- (X, Y) position of the ion impact on the detector: By measuring the X-Y position and the order of ion arrival on the PSD, the original position of the atoms on the tip can be reconstructed. By repeating this sequence, atoms are progressively removed from the tip, enabling the reconstruction of a 3D image of the material at the atomic scale.

Atom Probe Tomography (APT) or 3D Atom Probe stands out as the sole technique for material analysis that offers extensive capabilities for both 3D imaging and chemical composition measurements at the atomic scale. It achieves a remarkable resolution of approximately 0.1-0.3nm in depth and 0.3-0.5nm laterally. Since its initial developments, Atom Probe Tomography has played a significant role in advancing materials science. In this thesis, needle-shaped specimens undergo analysis using a laser-assisted wide-angle

tomographic atom probe (LaWaTAP) system, manufactured by CAMECA. This system features a straight flight path of approximately 10 cm. To facilitate detection, a custom-designed microchannel plate/advanced delay line detector (MCP/aDLD) is employed, boasting a nominal detection efficiency of $\eta MCP \sim 0.6$. The MCP/aDLD also possesses enhanced capabilities in detecting multiple events [184], [185]. The temperature of the needle tip is regulated using a closed-loop He cryostat and maintained at a fixed temperature of 80 K. To induce atom evaporation, the APT specimen is illuminated with UV laser pulses at a wavelength of 344 nm. These laser pulses have a repetition frequency of 100 kHz and a pulse duration of 350 fs.

9.2.3 Secondary ion mass spectroscopy (SIMS)

In 1910, J. J. Thomson, a physicist from Britain, made an observation of the emission of positive ions and neutral atoms from a solid surface, which was induced by the bombardment of ions[186]. In the 1940s, advancements in vacuum pump technology allowed Herzog and Viehböck to conduct the initial experimental tests on secondary ion mass spectrometry (SIMS) using a prototype setup[187]. Secondary Ion Mass Spectrometry (SIMS) is an analytical technique used to determine the elemental and isotopic composition of solid materials. SIMS is a spectroscopy technique that provides information about two to three atomic layers, roughly equivalent to 1 nm. It involves bombarding a sample with ions and detecting the resulting ions. In SIMS, a focused primary ion beam, typically composed of ions such as Cs^+, O_2^+, Ga^+, Ar^+ or O^- is directed at the surface of a sample in a vacuum. When these primary ions collide with the sample's surface, they cause the ejection of secondary ions. The secondary ions are then extracted, mass separated, and detected using a mass analyzer to isolate the ion of interest.

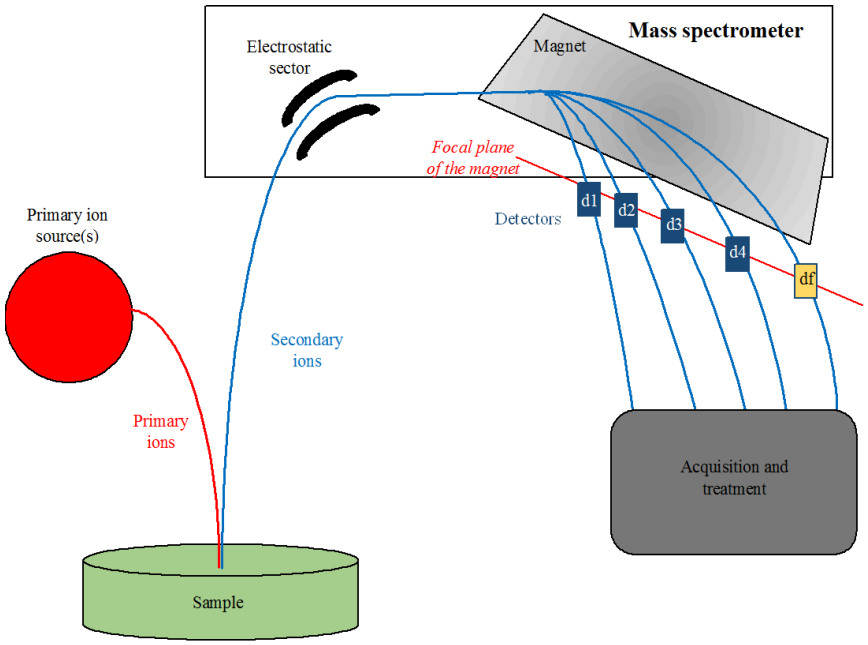

Figure 110: Principle of SIMS.

The mass analyzer measures the mass-to-charge ratio of the secondary ions, allowing for identification and quantification of the different elements present in the sample. By scanning the primary ion beam across the surface of the sample, SIMS can provide elemental maps, showing the distribution of elements on the surface. Depth profiling is another important capability of SIMS. By sputtering the surface with the primary ion beam and continuously measuring the secondary ion intensities as a function of depth, SIMS can provide information about the elemental composition as a function of depth within the material. This allows researchers to investigate layer thicknesses, interfacial compositions, and diffusion profiles. Additional information can be found in the provided reference.[188]

9.3 Electrical characterizations: Capacitance-Voltage measurements (Hg)

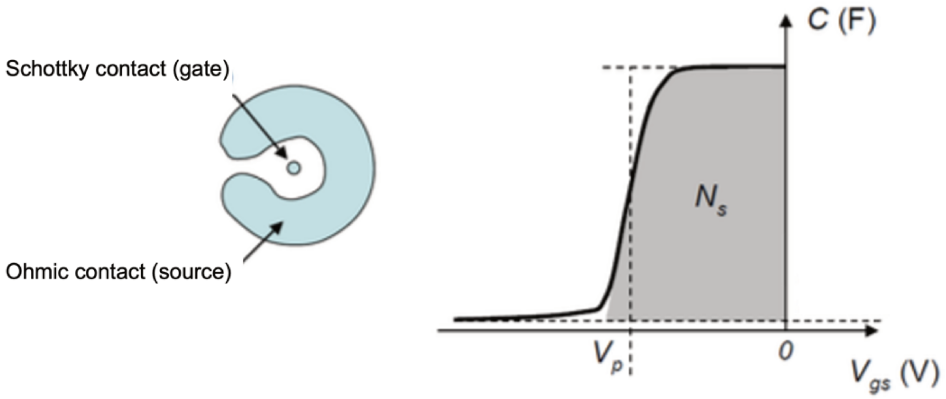

Figure 111: The diagram on the left depicts the contacts created by the mercury dot probe, illustrating both Ohmic and Schottky connections. On the right side, there is a C(V) characteristic graph for a HEMT.

The use of a mercury probe in capacitance-voltage (C-V) measurements provides a non-destructive technique for determining the density of a two-dimensional gas (2DEG) in the HEMT structure. In this method, the mercury probe acts as the first electrode, establishing a rectifying contact with the semiconductor (interface metal/semiconductor), while the second electrode, which is much larger behaves like an ohmic contact connected to the 2D electron gas. By measuring the capacitance between these two electrodes at various negative voltages (V_{gs}) applied to the first electrode, we can infer the density of the 2D gas. Notably, the applied Vgs is adjusted to a level called the ”pinch-off” voltage ($V_{gs} = V_p$), which effectively depletes the 2DEG channel. Integrating the C(V) curve from $V_{gs} = 0V$ to $V_{gs} = V_p$ yields the total surface charge density (N_s) of the 2DEG.

$$C = -\frac{dQ}{dV} = q.A.N_d.\frac{dW}{dV} = \frac{\varepsilon_r.A}{W}$$

$$N_s = \frac{1}{e.A}\int_{V_p}^{0}(C_{measured} - C_{residual}).dV$$

Additionally, assuming uniform doping within the material, it becomes possible to map the profile of the effective donor density ($N_d - N_a$) in the structure.

$$N_d = \frac{2}{e.\varepsilon_r.A^2.\frac{d(\frac{1}{(C_{measured}-C_{residual})^2})}{dV}}$$

With Q the semiconductor charge
W: the width of the space charge region
e: elemental electron charge ($\sim 1.602 \times 10^{-19} C$)
A: the area of the Schottky contact
V: the voltage applied to the Schottky contact
Nd: donor density (dNd /dV assumed negligible)
$\varepsilon_r = \varepsilon/\varepsilon_0$, ε_0 permittivity of vacuum ($\sim 8.854 \times 10^{-12} F/m$)

9.4 Device process and electrical characterizations of HEMTs

9.4.1 Technology process

To evaluate the performance of our transistors, we conducted various technological processes on the samples. The HEMTs were manufactured utilizing optical lithography. The mask utilized in the process contains a pattern of components as illustrated in Figure 112. The manufacturing procedure commences with mesa etching to isolate the components. The etchings are achieved through Corial ICP-RIE 210IL of high-density plasma etching, utilizing $Cl_2/BCl_3/Ar/N_2$ with 15/2/2/2 sccm respectively and a temperature around 5°C. The mesas have a height of approximately 150 nm. To establish Ohmic contacts, a deposition process with an e-beam evaporator called EVA 450 is employed. The deposited contacts consist of the following layered structure: Ti/Al/Ni/Au with 30//180/40/160 nm respectively. Half of the barrier layer is etched prior to the deposition of metal for ohmic contacts.

In the Ti/Al/Ni/Au stack [189], the contact layer is comprised of titanium. Titanium interacts with GaN, resulting in the formation of the TiN alloy. The formation of this alloy brings several advantages. Specifically, the diffusion of nitrogen atoms from GaN gives rise to nitrogen vacancies, which act as donors and increase the concentration of net carriers below the metal/semiconductor interface. Additionally, Ti-based ohmic contacts during annealing help to reduce the formation of the native oxide (Ga_2O_3) that naturally occurs on the GaN surface. Following the titanium layer, there is an overlayer composed of aluminum (Al), aptly named the "Overlayer." This layer of aluminum serves to reduce the reactivity of titanium with GaN or AlGaN, which is responsible for the formation of porosities at the metal-semiconductor interface [190]. The third layer in the stack is nickel (Ni), referred to as the "barrier layer." Nickel possesses a high melting point (> 1200°C), which effectively limits the inter-diffusion of other metals. The final layer, known as the cap layer, is made of gold (Au). Its primary purpose is to prevent oxidation of the underlying metals.

Subsequently, the contacts undergo RTA (Rapid Thermal Annealing) annealing for 30 seconds in an N_2 environment, forming the desired connections. Following this, gate contacts are deposited, using a combination of 20 nm Ni and 200 nm Au materials. The final step involves the deposition of contact pads, which aim to reduce contact resistance. These pads consist of a layered structure of 20 nm Ni and 200 nm Au.

The process entails the presence of: Isolation patterns: These patterns serve the purpose of evaluating unintended electrical leakage between different components or underneath them due to a lack of resistivity

of the buffer layer for instance. They consist of interdigitated combs, or circular patternswith ohmic contacts separated by 5, 10 and $20\mu m$ isolation trenches.

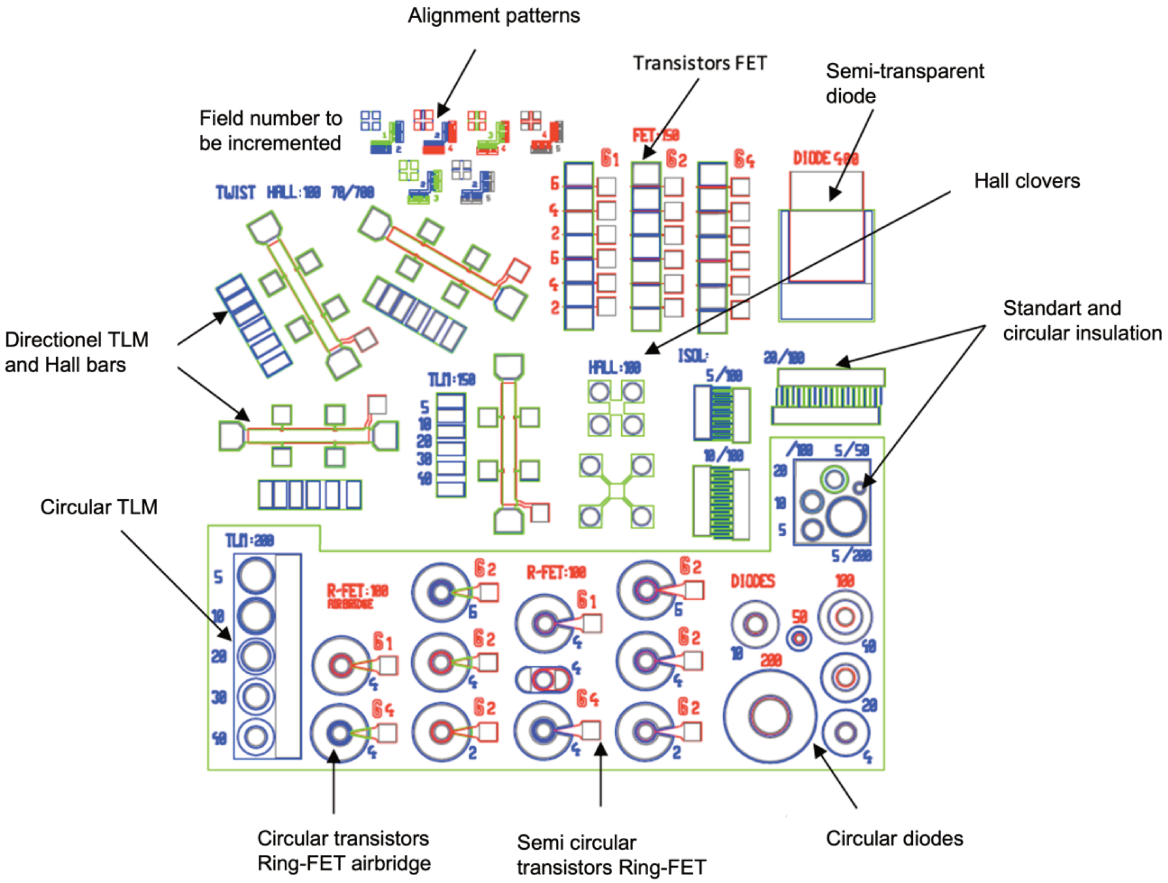

Figure 112: The mask employed for fabricating test components on epitaxial samples is characterized by its dimensions of $3700\mu m \times 3600\mu m$. Various colors on the mask indicate different mask levels: dark green represents mesas, blue represents ohmic, light green represents air bridge resin, red represents gate, and gray represents contact pads

Circular and rectangular TLM (Transfer Length Method): In the linear TLM technique, different spacing between the patterns are needed. It is employed to measure the specific contact resistance Rc between a metal contact and a semiconductor material and the 2DEG resistance R_{sheet}. The metal contacts are typically deposited using techniques like evaporation or sputtering (in our case, the metal has been deposited by e-beam evaporation). In the Circular TLM technique, circular metal contact pads of various diameters are patterned onto the semiconductor surface. Circular TLM offers several advantages over the traditional rectangular TLM method. The circular geometry allows for more symmetrical current flow, reducing the influence of edge effects that can affect the accuracy of resistance measurements. Additionally, circular TLM enables more efficient use of the available space on the semiconductor surface, allowing for a higher density of contact pads.

Van der Pauw devices: to measure layer resistance and check electron density in the 2DEG using Hall effect measurements. This allows us to deduce a value for electron mobility.

Diodes to evaluate barrier potential ϕ_b, ideality coefficient η, and reverse bias gate leakage and perform accurate C-V measurements.

Gate-centered transistors, with several gate lengths $L_g : 1, 2$ and $4\mu m$, and source-gate/gate-drain spacings $L_{sg} of 2, 4 and 6 \mu m$.

9.4.2 Sheet resistance and contact resistance.

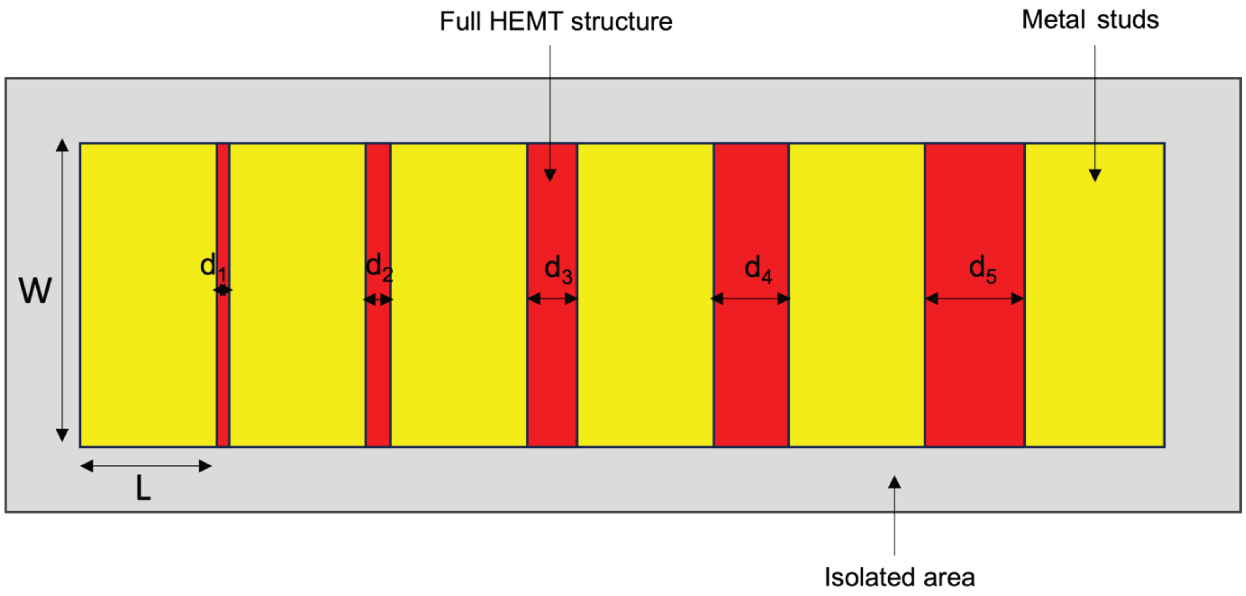

Figure 113: Schematic of a linear TLM pattern.

The quality of an ohmic contact can be determined by evaluating its contact resistance (R_c). To assess this quality, we employ the Transmission Line Method (TLM), which was introduced by Shockley in 1964. This method involves measuring the contact resistance using patterns consisting of multiple metal studs with dimensions of length (W) and width (L), spaced at increasing distances (d_i). Figure 113 provides a sketch illustrating a TLM pattern. To measure resistances, the 4-probe method is employed, offering the advantage of eliminating measurement tip resistances. In this method, a current is injected between two needle probes positioned on two adjacent contacts, while the potential difference is measured using two other probes. With the values of the injected current and the measured voltage, the total resistance can be easily calculated.

$$R_T = 2R_c + \frac{R_{sheet}}{W} d_i$$

The overall resistance (R_T) can be obtained by combining the two contact resistances (R_c) and the sheet resistance (R_{sheet}). The sheet resistance refers to the resistance of the two-dimensional electron gas in the context of a HEMT structure, or it can represent the resistance in the case of a uniformly doped layer. When calculating the total resistance, we sum the individual contact resistances with the sheet

resistance to determine the overall resistance value (R_T). The technique described allows for the extraction of contact resistances. In the case of an ohmic contact, the plot of the measured total resistance (R_T) against the distance between the metal studs (d_i) forms a straight line. The intercept of this line for a distance equal to zero corresponds to twice the contact resistance, while the slope is linked to the sheet resistance ($slope = R_{sheet}/W$). It is important to note that the current intensity and consequently the contact resistance (R_c) depend on the width of the metal pads. A wider pad width results in a lower contact resistance. To facilitate comparisons between contacts of different widths, the contact resistance is normalized by multiplying it by the width (W) of the pad:

$$R_c(\Omega.mm) = R_c(\Omega.W)$$

In the context of the thesis, characterizing ohmic contacts is essential, and the TLM method is employed for this purpose.

9.4.3 Hall effect measurements

The application of the Van Der Pauw method [191] and Hall Effect measurements allow for the direct assessment of sheet resistance (R_{sheet}) and carrier sheet concentration (N_s). Additionally, this method enables the determination of the carrier type (electrons or holes) and the calculation of mobility (μ). However, it is important to note that this technique necessitates cutting the sample into a square shape (preferably a cloverleaf) and depositing metal contacts at each corner or engaging in a series of lithography steps as descripted before. Van Der Pauw has shown that sheet resistance can be deduced from two resistances:

$$R_A = \frac{V_{43}}{I_{12}} and R_B = \frac{V_{14}}{I_{23}}$$

$$e^{\frac{\pi R_A}{R_{sheet}}} + e^{\frac{\pi R_B}{R_{sheet}}} = 1$$

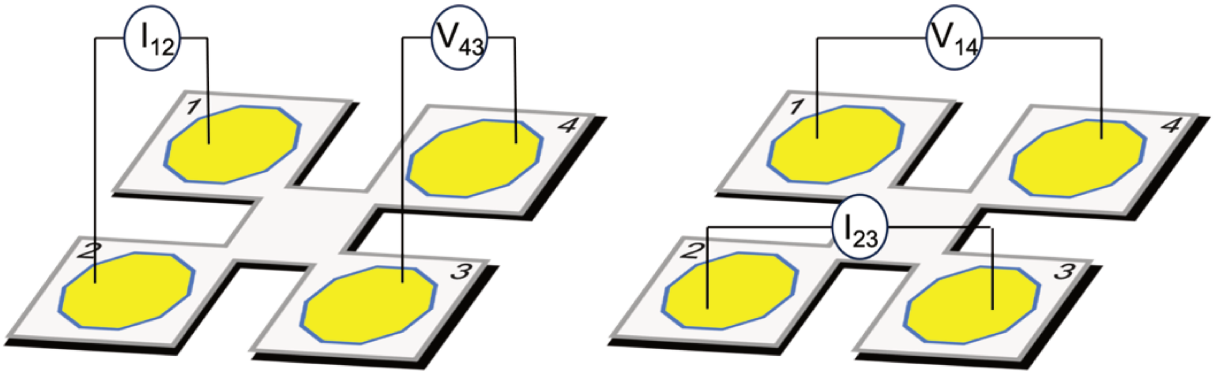

Figure 114: Schematic diagram of sheet resistance measurements using the Van der Pauw technique.

From this formula, known as the Van der Pauw formula, the sheet resistance can be extracted. And since, $R_A = R_B$;

$$R_{sheet} = \frac{\pi R_A}{ln(2)}$$

During a Hall effect measurement, a current (I) is passed through the sample, while a magnetic field ($\vec{B}$) is applied perpendicular to the direction of charge carrier movement. This setup results in the generation of a voltage called the Hall voltage (V_H), which emerges perpendicular to the displacement of the charge carriers. In Figure 115, a current is applied between contacts 1 and 3, and the Hall voltage is measured between contacts 2 and 4.

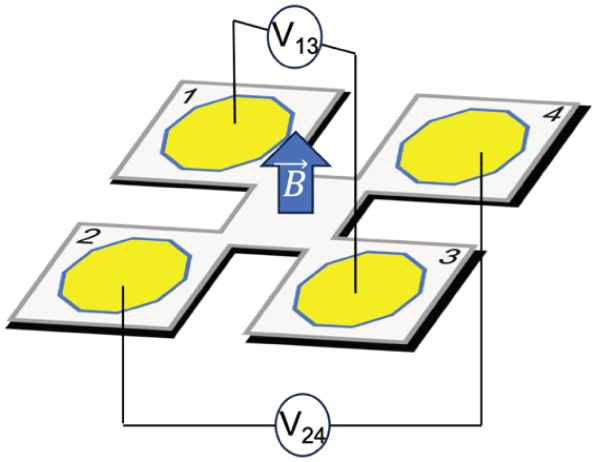

Figure 115: Schematic diagram of Hall effect measurement.

By examining the sign of the Hall voltage, it is possible to determine the type of free carriers present, distinguishing between n-type or p-type material. The carrier concentration (n_H) can be calculated using the following equation:

$$n_H = \frac{IB}{e|V_H|}$$

From (n_H) and R_{sheet}, we can calculate the mobility:

$$\mu = \frac{1}{en_H R_{sheet}}$$

In this study, the Hall effects measurements have been done with ambient temperature and a magnetic field equal to 0,35 Tesla.

10 Bibliography

[1] J. Liang et al., “A New Field-Effect Transistor with Selectively Doped GaAs/n-$Al_xGa_{1-x}As$ Heterojunctions You may also like Investigation on the interface resistance of Si/GaAs heterojunctions fabricated by surface-activated bonding Low-resistance semiconductor/semiconductor junctions with intermediate metal grids for III-V-on-Si multijunction solar cells.”

[2] “US4471366A - Field effect transistor with high cut-off frequency and process for forming same - Google Patents.” Accessed: Oct. 15, 2023. [Online].

[3] Y. Cordier, S. Bollaert, M. Zaknoune, J. Dipersio, and D. Ferre, “InAlAs/InGaAs metamorphic high electron mobility transistors on GaAs substrate: Influence of indium content on material properties and device performance,” Japanese Journal of Applied Physics, Part 1: Regular Papers and Short Notes and Review Papers, vol. 38, no. 2 B, pp. 1164–1168, Feb. 1999, doi: 10.1143/JJAP.38.1164/XML.

[4] M. Asif Khan, A. Bhattarai, J. N. Kuznia, and D. T. Olson, “High electron moility transistor based on a GaN- $Al_xGa_{1x}N$ heterojunction,” Appl Phys Lett, vol. 63, no. 9, pp. 1214–1215, Aug. 1993, doi: 10.1063/1.109775.

[5] M. A. Khan, J. M. Van Hove, J. N. Kuznia, and D. T. Olson, “High electron mobility GaN/$Al_xGa_{1-x}N$ heterostructures grown by low-pressure metalorganic chemical vapor deposition,” Appl Phys Lett, vol. 58, no. 21, pp. 2408–2410, 1991, doi: 10.1063/1.104886.

[6] M. Asif Khan, A. Bhattarai, J. N. Kuznia, and D. T. Olson, “High electron mobility transistor based on a GaN-$Al_xGa_{1-x}N$ heterojunction,” Appl Phys Lett, vol. 63, no. 9, pp. 1214–1215, 1993, doi: 10.1063/1.109775.

[7] M. Asif Khan, J. N. Kuznia, A. R. Bhattarai, and D. T. Olson, “Metal semiconductor field effect transistor based on single crystal GaN,” Appl Phys Lett, vol. 62, no. 15, pp. 1786–1787, 1993, doi: 10.1063/1.109549.

[8] “TPEL.2013.2268900”.

[9] R. S. Pengelly, S. M. Wood, J. W. Milligan, S. T. Sheppard, and W. L. Pribble, “A review of GaN on SiC high electron-mobility power transistors and MMICs,” IEEE Transactions on Microwave Theory and Techniques, vol. 60, no. 6 PART 2. pp. 1764–1783, 2012. doi: 10.1109/TMTT.2012.2187535.

[10] T. P. Chow, I. Omura, M. Higashiwaki, H. Kawarada, and V. Pala, “Smart power devices and ICs using GaAs and wide and extreme bandgap semiconductors,” IEEE Trans Electron Devices, vol. 64, no. 3, pp. 856–873, Mar. 2017, doi: 10.1109/TED.2017.2653759.

[11] M. Meneghini et al., “GaN-based power devices: Physics, reliability, and perspectives,” Journal of Applied Physics, vol. 130, no. 18. American Institute of Physics Inc., Nov. 14, 2021. doi: 10.1063/5.0061354.

[12] G. H. Jessen et al., “Short-channel effect limitations on high-frequency operation of AlGaN/ GaN HEMTs for T-gate devices,” IEEE Trans Electron Devices, vol. 54, no. 10, pp. 2589–2597, Oct. 2007, doi: 10.1109/TED.2007.904476.

[13] K. Shinohara et al., “Scaling of gan hemts and schottky diodes for submillimeter-wave mmic applications,” IEEE Trans Electron Devices, vol. 60, no. 10, pp. 2982–2996, 2013, doi: 10.1109/TED.2013.2268160.

[14] S. Zhang, W. Y. Fu, D. Holec, C. J. Humphreys, and M. A. Moram, “Elastic constants and critical thicknesses of ScGaN and ScAlN,” J Appl Phys, vol. 114, no. 24, Dec. 2013, doi: 10.1063/1.4848036.

[15] M. Akiyama, T. Kamohara, K. Kano, A. Teshigahara, Y. Takeuchi, and N. Kawahara, “Enhancement of piezoelectric response in scandium aluminum nitride alloy thin films prepared by dual reactive cosputtering,” Advanced Materials, vol. 21, no. 5, pp. 593–596, Feb. 2009, doi: 10.1002/adma.200802611.

[16] S. Leone et al., “Metal-Organic Chemical Vapor Deposition of Aluminum Scandium Nitride,” Physica Status Solidi - Rapid Research Letters, vol. 14, no. 1, Jan. 2020, doi: 10.1002/pssr.201900535.

[17] P. Wang et al., “N-polar ScAlN and HEMTs grown by molecular beam epitaxy,” Appl Phys Lett, vol. 119, no. 8, Aug. 2021, doi: 10.1063/5.0055851.

[18] M. T. Hardy et al., “Control of phase purity in high scandium fraction heteroepitaxial ScAlN grown by molecular beam epitaxy,” Applied Physics Express, vol. 13, no. 6, Jun. 2020, doi: 10.35848/1882-0786/ab916a.

[19] M. T. Hardy, B. P. Downey, N. Nepal, D. F. Storm, D. S. Katzer, and D. J. Meyer, “Epitaxial ScAlN grown by molecular beam epitaxy on GaN and SiC substrates,” Appl Phys Lett, vol. 110, no. 16, Apr. 2017, doi: 10.1063/1.4981807.

[20] Y. Cordier, “Al(Ga)N/GaN high electron mobility transistors on silicon,” physica status solidi (a), vol. 212, no. 5, pp. 1049–1058, May 2015, doi: 10.1002/PSSA.201532070.

[21] Y. Cordier et al., “Demonstration of AlGaN/GaN high-electron-mobility transistors grown by molecular beam epitaxy on Si(110),” IEEE Electron Device Letters, vol. 29, no. 11, pp. 1187–1189, 2008, doi: 10.1109/LED.2008.2005211.

[22] C. Bolognesi et al., “Jury,” 2013. [Online]. Available: https://theses.hal.science/tel-00943619v2

[23] B. Daudin, J. L. Rouvière, and M. Arlery, “The key role of polarity in the growth process of (0001) nitrides,” Materials Science and Engineering: B, vol. 43, no. 1–3, pp. 157–160, Jan. 1997, doi: 10.1016/S0921-5107(96)01854-5.

[24] S. Keller et al., “Properties of N-polar AlGaN/GaN heterostructures and field effect transistors grown by metalorganic chemical vapor deposition,” J Appl Phys, vol. 103, no. 3, Feb. 2008, doi: 10.1063/1.2838214

/902042.

[25] S. Rajan, A. Chini, M. H. Wong, J. S. Speck, and U. K. Mishra, “N-polar GaNAlGaNGaN high electron mobility transistors,” J Appl Phys, vol. 102, no. 4, Aug. 2007, doi: 10.1063/1.2769950/938715.

[26] M. H. Wong et al., “N-face high electron mobility transistors with a GaN-spacer,” physica status solidi (a), vol. 204, no. 6, pp. 2049–2053, Jun. 2007, doi: 10.1002/PSSA.200674879.

[27] O. Ambacher et al., “Two-dimensional electron gases induced by spontaneous and piezoelectric polarization charges in N- And Ga-face AlGaN/GaN heterostructures,” J Appl Phys, vol. 85, no. 6, pp. 3222–3233, Mar. 1999, doi: 10.1063/1.369664.

[28] S. F. Li et al., “Polarity and its influence on growth mechanism during MOVPE growth of GaN submicrometer rods,” Cryst Growth Des, vol. 11, no. 5, pp. 1573–1577, May 2011, doi: 10.1021/CG101537M /SUPPL-FILE/CG101537M$_5I_0$01.PDF.

[29] M. Sumiya and S. Fuke, “Review of polarity determination and control of GaN,” MRS Internet Journal of Nitride Semiconductor Research 2004 9:1, vol. 9, no. 1, pp. 1–34, Jun. 2014, doi: 10.1557/S1092578300 000363.

[30] M. Stutzmann et al., “Playing with polarity,” Physica Status Solidi (B) Basic Research, vol. 228, no. 2. pp. 505–512, Nov. 2001. doi: 10.1002/1521-3951(200111)228:2$<505::AID-PSSB505>$3.0.CO;2-U.

[31] V. Darakchieva, P. P. Paskov, T. Paskova, E. Valcheva, B. Monemar, and M. Heuken, “Lattice parameters of GaN layers grown on a-plane sapphire: Effect of in-plane strain anisotropy,” Appl Phys Lett, vol. 82, no. 5, pp. 703–705, Feb. 2003, doi: 10.1063/1.1542931.

[32] G. Martin et al., “Valence-band discontinuity between GaN and AlN measured by x-ray photoemission spectroscopy,” Appl Phys Lett, vol. 65, no. 5, pp. 610–612, 1994, doi: 10.1063/1.112247.

[33] J. Wu et al., “Small band gap bowing in In1-xGaxN alloys,” Appl Phys Lett, vol. 80, no. 25, pp. 4741–4743, Jun. 2002, doi: 10.1063/1.1489481.

[34] L. Mancera, J. A. Rodríguez, and N. Takeuchi, “Theoretical study of the stability of wurtzite, zincblende, NaCl and CsCl phases in group IIIB and IIIA nitrides,” in Physica Status Solidi (B) Basic Research, Aug. 2004, pp. 2424–2428. doi: 10.1002/pssb.200404910.

[35] C. Stampfl, W. Mannstadt, R. Asahi, and A. J. Freeman, “Electronic structure and physical properties of early transition metal mononitrides: Density-functional theory LDA, GGA, and screened-exchange LDA FLAPW calculations,” Phys Rev B Condens Matter Mater Phys, vol. 63, no. 15, Mar. 2001, doi: 10.1103/PhysRevB.63.155106.

[36] R. Deng, P. Y. Zheng, and D. Gall, “Optical and electron transport properties of rock-salt Sc1-xAlxN,”

J Appl Phys, vol. 118, no. 1, Jul. 2015, doi: 10.1063/1.4923429.

[37] N. Farrer and L. Bellaiche, “Properties of hexagonal ScN versus wurtzite GaN and InN,” Phys Rev B Condens Matter Mater Phys, vol. 66, no. 20, pp. 2012031–2012034, Nov. 2002, doi: 10.1103/PhysRevB.66.201203.

[38] L. Mancera, J. A. Rodríguez, and N. Takeuchi, “Theoretical study of the stability of wurtzite, zinc-blende, NaCl and CsCl phases in group IIIB and IIIA nitrides,” physica status solidi (b), vol. 241, no. 10, pp. 2424–2428, Aug. 2004, doi: 10.1002/PSSB.200404910.

[39] N. Takeuchi, “First-principles calculations of the ground-state properties and stability of ScN,” Phys Rev B Condens Matter Mater Phys, vol. 65, no. 4, pp. 1–4, 2002, doi: 10.1103/PhysRevB.65.045204.

[40] A. Qteish, P. Rinke, M. Scheffler, and J. Neugebauer, “Exact-exchange-based quasiparticle energy calculations for the band gap, effective masses, and deformation potentials of ScN,” Phys Rev B Condens Matter Mater Phys, vol. 74, no. 24, 2006, doi: 10.1103/PhysRevB.74.245208.

[41] “Phys. Rev. B 36, 2695 (1987) - Electronic structure and properties of d- and f-shell-metal compounds.” Accessed: Oct. 02, 2023. [Online]. Available: https://journals.aps.org/prb/abstract/10.1103/PhysRevB.36.2695

[42] E. Bellet-Amalric et al., “Plastic strain relaxation of nitride heterostructures,” J Appl Phys, vol. 95, no. 3, pp. 1127–1133, Feb. 2004, doi: 10.1063/1.1637934.

[43] A. M. Dabiran et al., “Very high channel conductivity in low-defect AlN/GaN high electron mobility transistor structures,” Appl Phys Lett, vol. 93, no. 8, 2008, doi: 10.1063/1.2970991.

[44] D. Iida et al., “Laser lift-off technique for freestanding GaN substrate using an in droplet formed by thermal decomposition of GaInN and its application to light-emitting diodes,” Appl Phys Lett, vol. 105, no. 7, p. 18, Aug. 2014, doi: 10.1063/1.4893757/133464.

[45] W. C. Mitchel, S. Elhamri, G. Landis, R. Gaska, S. B. Schujman, and L. J. Schowalter, “Electrical characterization of AlGaN/GaN on AlN substrates,” Physica Status Solidi (C) Current Topics in Solid State Physics, vol. 5, no. 6, pp. 1550–1552, 2008, doi: 10.1002/PSSC.200778470.

[46] E. Frayssinet, Y. Cordier, H. P. D. Schenk, and A. Bavard, “Growth of thick GaN layers on 4-in. and 6-in. silicon (111) by metal-organic vapor phase epitaxy,” physica status solidi c, vol. 8, no. 5, pp. 1479–1482, May 2011, doi: 10.1002/PSSC.201000885.

[47] N. Baron et al., “The critical role of growth temperature on the structural and electrical properties of AlGaN/GaN high electron mobility transistor heterostructures grown on Si(111),” J Appl Phys, vol. 105, no. 3, Feb. 2009, doi: 10.1063/1.3063698/384190.

[48] E. Feltin, “Hétéro-épitaxie de Nitrure de Gallium sur substrat de silicium (111) et applications,” http://www.theses.fr, Jan. 2003, Accessed: Sep. 25, 2023. [Online]. Available: http://www.theses.fr/2003NICE4075

[49] “Difference Between Stress and Strain in Physics — Compare the Difference Between Similar Terms.” Accessed: Sep. 25, 2023. [Online]. Available: https://www.differencebetween.com/difference-between-stress-and-strain-in-physics/

[50] A. F. Wright, “Elastic properties of zinc-blende and wurtzite AIN, GaN, and InN,” J Appl Phys, vol. 82, no. 6, pp. 2833–2839, Sep. 1997, doi: 10.1063/1.366114.

[51] F. Bernardini, V. Fiorentini, and D. Vanderbilt, “Spontaneous polarization and piezoelectric constants of III-V nitrides,” 1997.

[52] J. Wuerfl et al., “Reliability issues of GaN based high voltage power devices,” Microelectronics Reliability, vol. 51, no. 9–11, pp. 1710–1716, Sep. 2011, doi: 10.1016/J.MICROREL.2011.07.017.

[53] S. Kato, Y. Satoh, H. Sasaki, I. Masayuki, and S. Yoshida, “C-doped GaN buffer layers with high breakdown voltages for high-power operation AlGaN/GaN HFETs on 4-in Si substrates by MOVPE,” J Cryst Growth, vol. 298, no. SPEC. ISS, pp. 831–834, Jan. 2007, doi: 10.1016/J.JCRYSGRO.2006.10.192.

[54] S. Acharya, A. Chatterjee, V. Bhatia, A. I. K. Pillai, M. Garbrecht, and B. Saha, “Twinned growth of ScN thin films on lattice-matched GaN substrates,” Mater Res Bull, vol. 143, Nov. 2021, doi: 10.1016/j.materresbull.2021.111443.

[55] D. Gall et al., “Electronic structure of ScN determined using optical spectroscopy, photoemission, and ab initio calculations,” Phys Rev B Condens Matter Mater Phys, vol. 63, no. 12, pp. 1251191–1251199, 2001, doi: 10.1103/physrevb.63.125119.

[56] R. Deng, K. Jiang, and D. Gall, “Optical phonon modes in Al1-xScxN,” in Journal of Applied Physics, Jan. 2014. doi: 10.1063/1.4861034.

[57] D. Gall, I. Petrov, and J. E. Greene, “Epitaxial Sc1-xTixN(001): Optical and electronic transport properties,” J Appl Phys, vol. 89, no. 1, pp. 401–409, Jan. 2001, doi: 10.1063/1.1329348.

[58] V. Fiorentini, F. Bernardini, and O. Ambacher, “Evidence for nonlinear macroscopic polarization in III–V nitride alloy heterostructures,” Appl Phys Lett, vol. 80, no. 7, pp. 1204–1206, Feb. 2002, doi: 10.1063/1.1448668.

[59] O. Ambacher et al., “Two-dimensional electron gases induced by spontaneous and piezoelectric polarization charges in N- And Ga-face AlGaN/GaN heterostructures,” J Appl Phys, vol. 85, no. 6, pp. 3222–3233, Mar. 1999, doi: 10.1063/1.369664.

[60] H. L. Störmer, R. Dingle, A. C. Gossard, W. Wiegmann, and M. D. Sturge, “Two-dimensional electron gas at a semiconductor-semiconductor interface,” Solid State Commun, vol. 29, no. 10, pp. 705–709, Mar. 1979, doi: 10.1016/0038-1098(79)91010-X.

[61] “Field effect transistor with high cut-off frequency and process for forming same,” Mar. 1982.

[62] I. P. Smorchkova et al., “Polarization-induced charge and electron mobility in AlGaN/GaN heterostructures grown by plasma-assisted molecular-beam epitaxy,” J Appl Phys, vol. 86, no. 8, pp. 4520–4526, Oct. 1999, doi: 10.1063/1.371396.

[63] J. P. Ibbetson, P. T. Fini, K. D. Ness, S. P. DenBaars, J. S. Speck, and U. K. Mishra, “Polarization effects, surface states, and the source of electrons in AlGaN/GaN heterostructure field effect transistors,” Appl Phys Lett, vol. 77, no. 2, pp. 250–252, Jul. 2000, doi: 10.1063/1.126940.

[64] I. P. Smorchkova et al., “AlN/GaN and (Al,Ga)N/AlN/GaN two-dimensional electron gas structures grown by plasma-assisted molecular-beam epitaxy,” J Appl Phys, vol. 90, no. 10, pp. 5196–5201, Nov. 2001, doi: 10.1063/1.1412273.

[65] O. Ambacher, B. Christian, M. Yassine, M. Baeumler, S. Leone, and R. Quay, “Polarization induced interface and electron sheet charges of pseudomorphic ScAlN/GaN, GaAlN/GaN, InAlN/GaN, and InAlN/InN heterostructures,” J Appl Phys, vol. 129, no. 20, May 2021, doi: 10.1063/5.0049185.

[66] J. Kuzmík, “Power electronics on InAlN/(In)GaN: Prospect for a record performance,” IEEE Electron Device Letters, vol. 22, no. 11, pp. 510–512, Nov. 2001, doi: 10.1109/55.962646.

[67] F. A. Marino, N. Faralli, T. Palacios, D. K. Ferry, S. M. Goodnick, and M. Saraniti, “Effects of threading dislocations on AlGaN/GaN high-electron mobility transistors,” IEEE Trans Electron Devices, vol. 57, no. 1, pp. 353–360, Jan. 2010, doi: 10.1109/TED.2009.2035024.

[68] L. Pan, X. Dong, Z. Li, W. Luo, and J. Ni, “Influence of the AlN nucleation layer on the properties of AlGaN/GaN heterostructure on Si (111) substrates,” Appl Surf Sci, vol. 447, pp. 512–517, Jul. 2018, doi: 10.1016/J.APSUSC.2018.04.001.

[69] H. Ishikawa, G. Y. Zhao, N. Nakada, T. Egawa, T. Jimbo, and M. Umeno, “GaN on Si Substrate with AlGaN/AlN Intermediate Layer,” Japanese Journal of Applied Physics, Part 1: Regular Papers and Short Notes and Review Papers, vol. 38, no. 5 PART 2, pp. 492–494, May 1999, doi: 10.1143/JJAP.38.L492/XML.

[70] I. P. Smorchkova et al., “AlN/GaN and (Al,Ga)N/AlN/GaN two-dimensional electron gas structures grown by plasma-assisted molecular-beam epitaxy,” J Appl Phys, vol. 90, no. 10, pp. 5196–5201, Nov. 2001, doi: 10.1063/1.1412273.

[71] P.Lorenzini, Caractérisations des hétérostructures AlGaN/GaN : des propriétés de transport aux transistors à haute mobilité HEMT. , Habilitation à Diriger des Recherches, Université de Nice Sophia-

Antipolis, Valbonne, 2004.

[72] J. K. Sheu, M. L. Lee, and W. C. Lai, “Effect of low-temperature-grown GaN cap layer on reduced leakage current of GaN Schottky diodes,” Appl Phys Lett, vol. 86, no. 5, pp. 1–3, Jan. 2005, doi: 10.1063/1.1861113.

[73] M. Charles, Y. Baines, R. Bouis, and A. M. Papon, “The Characterization and Optimization of GaN Cap Layers and SiN Cap Layers on AlGaN/GaN HEMT Structures Grown on 200 mm GaN on Silicon,” Phys Status Solidi B Basic Res, vol. 255, no. 5, May 2018, doi: 10.1002/PSSB.201700406.

[74] T. Takizawa, S. Nakazawa, and T. Ueda, “Crystalline SiN x ultrathin films grown on AlGaN/GaN using in situ metalorganic chemical vapor deposition,” in Journal of Electronic Materials, May 2008, pp. 628–634. doi: 10.1007/s11664-008-0386-7.

[75] J. Derluyn et al., “Improvement of AlGaNGaN high electron mobility transistor structures by in situ deposition of a Si 3 N 4 surface layer,” J Appl Phys, vol. 98, no. 5, Sep. 2005, doi: 10.1063/1.2008388.

[76] D. F. Urban, O. Ambacher, and C. Elsässer, “First-principles calculation of electroacoustic properties of wurtzite (Al,Sc)N,” Phys Rev B, vol. 103, no. 11, Mar. 2021, doi: 10.1103/PhysRevB.103.115204.

[77] O. Ambacher et al., “Wurtzite ScAlN, InAlN, and GaAlN crystals, a comparison of structural, elastic, dielectric, and piezoelectric properties,” J Appl Phys, vol. 130, no. 4, Jul. 2021, doi: 10.1063/5.0048647.

[78] M. A. Moram and S. Zhang, “ScGaN and ScAlN: Emerging nitride materials,” J Mater Chem A Mater, vol. 2, no. 17, pp. 6042–6050, May 2014, doi: 10.1039/c3ta14189f.

[79] M. A. Caro et al., “Piezoelectric coefficients and spontaneous polarization of ScAlN.”

[80] F. Tasnádi et al., “Origin of the anomalous piezoelectric response in wurtzite $Sc_xAl_{1-x}N$ alloys,” Phys Rev Lett, vol. 104, no. 13, Apr. 2010, doi: 10.1103/PhysRevLett.104.137601.

[81] C. Höglund et al., “Wurtzite structure $Sc_{1-x}Al_xN$ solid solution films grown by reactive magnetron sputter epitaxy: Structural characterization and first-principles calculations,” J Appl Phys, vol. 107, no. 12, Jun. 2010, doi: 10.1063/1.3448235.

[82] H. Momida, A. Teshigahara, and T. Oguchi, “Strong enhancement of piezoelectric constants in ScxAl1- xN: First-principles calculations,” AIP Adv, vol. 6, no. 6, Jun. 2016, doi: 10.1063/1.4953856.

[83] D. Wu et al., “Characterization of Elastic Modulus Across the $(Al_{1-x}Sc_x)N$ System Using DFT and Substrate-Effect-Corrected Nanoindentation,” IEEE Trans Ultrason Ferroelectr Freq Control, vol. 65, no. 11, pp. 2167–2175, Nov. 2018, doi: 10.1109/TUFFC.2018.2862240.

[84] T. Markurt et al., “Blocking growth by an electrically active subsurface layer: The effect of si as

an antisurfactant in the growth of GaN," Phys Rev Lett, vol. 110, no. 3, Jan. 2013, doi: 10.1103/PhysRevLett.110.036103.

[85] Y. Li et al., "Defect-reduced green GaInN/GaN light-emitting diode on nanopatterned sapphire," Appl Phys Lett, vol. 98, no. 15, Apr. 2011, doi: 10.1063/1.3579255.

[86] N. Kurz et al., "Experimental determination of the electro-acoustic properties of thin film AlScN using surface acoustic wave resonators," J Appl Phys, vol. 126, no. 7, Aug. 2019, doi: 10.1063/1.5094611.

[87] S. W. Kaun et al., "GaN-based high-electron-mobility transistor structures with homogeneous lattice-matched InAlN barriers grown by plasma-assisted molecular beam epitaxy," Semicond Sci Technol, vol. 29, no. 4, p. 045011, Feb. 2014, doi: 10.1088/0268-1242/29/4/045011.

[88] R. Deng, S. R. Evans, and D. Gall, "Bandgap in $Al_{1-x}Sc_xN$," Appl Phys Lett, vol. 102, no. 11, Mar. 2013, doi: 10.1063/1.4795784.

[89] C. Constantin, H. Al-Brithen, M. B. Haider, D. Ingram, and A. R. Smith, "ScGaN alloy growth by molecular beam epitaxy: Evidence for a metastable layered hexagonal phase," Phys Rev B Condens Matter Mater Phys, vol. 70, no. 19, pp. 1–4, Nov. 2004, doi: 10.1103/PHYSREVB.70.193309/FIGURES/5/MEDIUM.

[90] P. Wang, D. A. Laleyan, A. Pandey, Y. Sun, and Z. Mi, "Molecular beam epitaxy and characterization of wurtzite $Sc_xAl_{1-x}N$," Appl Phys Lett, vol. 116, no. 15, Apr. 2020, doi: 10.1063/5.0002445.

[91] S. Zhang, W. Y. Fu, D. Holec, C. J. Humphreys, and M. A. Moram, "Elastic constants and critical thicknesses of ScGaN and ScAlN," J Appl Phys, vol. 114, no. 24, Dec. 2013, doi: 10.1063/1.4848036.

[92] P. M. Mayrhofer, H. Euchner, A. Bittner, and U. Schmid, "Circular test structure for the determination of piezoelectric constants of $Sc_xAl_{1-x}N$ thin films applying Laser Doppler Vibrometry and FEM simulations," Sens Actuators A Phys, vol. 222, pp. 301–308, Feb. 2015, doi: 10.1016/j.sna.2014.10.024.

[93] R. C. Turner, P. A. Fuierer, R. E. Newnham, and T. R. Shrout, "Materials for high temperature acoustic and vibration sensors: A review," Applied Acoustics, vol. 41, no. 4, pp. 299–324, Jan. 1994, doi: 10.1016/0003-682X(94)90091-4.

[94] H. Sun et al., "Laser Doppler vibrometry for piezoelectric coefficient (d33) measurements in irradiated aluminum nitride," Sens Actuators A Phys, vol. 347, Nov. 2022, doi: 10.1016/j.sna.2022.113886.

[95] T. Yanagitani and S. Takayanagi, "Polarization control of scaln, zno and pbtio3piezoelectric films: application to polarization-inverted multilayer bulk acoustic wave and surface acoustic wave devices," Japanese Journal of Applied Physics, vol. 60, no. SD. IOP Publishing Ltd, Jul. 01, 2021. doi: 10.35848/1347-4065/abfd95.

[96] Y. Liu et al., "Design and Performance of ScAlN/AlN Trapezoidal Cantilever-Based MEMS Piezo-

electric Energy Harvesters," IEEE Trans Electron Devices, vol. 68, no. 6, pp. 2971–2976, Jun. 2021, doi: 10.1109/TED.2021.3072612.

[97] Toshiyuki. Tsuchiya, G.-B. Lee, and Institute of Electrical and Electronics Engineers., IEEE 26th International Conference on Micro Electro Mechanical Systems (MEMS 2013): January 20-24, 2013, Taipei International Convention Center, Taipei, Taiwan.

[98] Transducer Research Foundation, Institute of Electrical and Electronics Engineers, IEEE Electron Devices Society, Alas. Transducers 18 2015.06.21-25 Anchorage, Alas. Transducers Conference 18 2015.06.21-25 Anchorage, and A. and M. 18 2015. 06. 21-25 A. International Conference on Solid-State Sensors, 2015 Transducers - 2015 18th International Conference on Solid-State Sensors, Actuators and Microsystems (Transducers) 21-25 June 2015, Anchorage, Alaska.

[99] F. Tasnádi et al., "Origin of the anomalous piezoelectric response in wurtzite $Sc_xAl_{1-x}N$ alloys," Phys Rev Lett, vol. 104, no. 13, Apr. 2010, doi: 10.1103/PhysRevLett.104.137601.

[100] C. Tholander et al., "Ab initio calculations and experimental study of piezoelectric $Y_xIn_{1-x}N$ thin films deposited using reactive magnetron sputter epitaxy," Acta Mater, vol. 105, pp. 199–206, Feb. 2016, doi: 10.1016/j.actamat.2015.11.050.

[101] S. Tokuda, S. Takayanagi, M. Matsukawa, and T. Yanagitani, "Film growth of c-axis tilted ScAlN on the sapphire substrate for SAW devices," IEEE International Ultrasonics Symposium, IUS, Oct. 2017, doi: 10.1109/ULTSYM.2017.8092072.

[102] F. Bartoli et al., "Theoretical and experimental study of ScAlN/Sapphire structure based SAW sensor," Proceedings of IEEE Sensors, vol. 2017-December, pp. 1–3, Dec. 2017, doi: 10.1109/ICSENS.2017.8233938.

[103] K. Y. Hashimoto, S. Sato, A. Teshigahara, T. Nakamura, and K. Kano, "High-performance surface acoustic wave resonators in the 1 to 3 GHz range using a ScAlN/6H-SiC structure," IEEE Trans Ultrason Ferroelectr Freq Control, vol. 60, no. 3, pp. 637–642, 2013, doi: 10.1109/TUFFC.2013.2606.

[104] M. Clement, L. Vergara, J. Sangrador, E. Iborra, and A. Sanz-Hervás, "SAW characteristics of AlN films sputtered on silicon substrates," Ultrasonics, vol. 42, no. 1–9, pp. 403–407, Apr. 2004, doi: 10.1016/J.ULTRAS.2004.01.034.

[105] C. Li, X. Liu, L. Shu, and Y. Li, "AlN-based surface acoustic wave resonators for temperature sensing applications," Materials Express, vol. 5, no. 4, pp. 367–370, Aug. 2015, doi: 10.1166/MEX.2015.1247.

[106] Z. Hao et al., "Single Crystalline ScAlN Surface Acoustic Wave Resonators with Large Figure of Merit (Q × k)," IEEE MTT-S International Microwave Symposium Digest, vol. 2019-June, pp. 786–789, Jun. 2019, doi: 10.1109/MWSYM.2019.8700824.

[107] “Surface-acoustic-wave (SAW) and bulk-acoustic-wave (BAW) Filters will be disruptor in the military RF and microwave industries – International Defense Security Technology.” Accessed: Oct. 06, 2023. [Online]. Available: https://idstch.com/technology/electronics/surface-acoustic-wave-saw-bulk-acoustic-wave-baw-filters-will-disruptor-military-rf-microwave-industries/

[108] S. Kinoshita and T. Yanagitani, “Shear Mode Polarity Inverted ScAlN Multilayer for Application to BAW Transformer in Rectifying Antenna,” IEEE International Ultrasonics Symposium, IUS, vol. 2019-October, pp. 847–848, Oct. 2019, doi: 10.1109/ULTSYM.2019.8926197.

[109] H. Igeta, M. Totsuka, M. Suzuki, and T. Yanagitani, “Temperature Characteristics of ScAlN/SiO2 BAW Resonators,” IEEE International Ultrasonics Symposium, IUS, vol. 2018-January, 2018, doi: 10.1109/ULTSYM.2018.8580165.

[110] T. Yanagitani and J. Jia, “ScAlN polarization inverted resonators and enhancement of kt2 in new YbAlN materials for BAW devices,” IEEE International Ultrasonics Symposium, IUS, vol. 2019-October, pp. 894–899, Oct. 2019, doi: 10.1109/ULTSYM.2019.8925786.

[111] K. H. Sano, R. Karasawa, and T. Yanagitani, “High electromechanical coefficient kt2=19% thick ScAlN piezoelectric films for ultrasonic transducer in low frequency of 80 MHz,” IEEE International Ultrasonics Symposium, IUS, Oct. 2017, doi: 10.1109/ULTSYM.2017.8092005.

[112] H. P. Loebl, M. Klee, C. Metzmacher, W. Brand, R. Milsom, and P. Lok, “Piezoelectric thin AlN films for bulk acoustic wave (BAW) resonators,” Mater Chem Phys, vol. 79, no. 2–3, pp. 143–146, Apr. 2003, doi: 10.1016/S0254-0584(02)00252-3.

[113] M. Hardy, D. Meyer, N. Nepal, B. Downey, D. Scott Katzer, and D. Storm, “Scandium Aluminum Nitride as an Emerging Material for High Power Transistors,” 2018 IEEE MTT-S International Microwave Workshop Series on Advanced Materials and Processes for RF and THz Applications, IMWS-AMP 2018, Sep. 2018, doi: 10.1109/IMWS-AMP.2018.8457157.

[114] J. Cheng et al., “Breakdown Voltage Enhancement in ScAlN/GaN High-Electron-Mobility Transistors by High-k Bismuth Zinc Niobate Oxide,” IEEE Trans Electron Devices, vol. 68, no. 7, pp. 3333–3338, Jul. 2021, doi: 10.1109/TED.2021.3084136.

[115] T. E. Kazior, E. M. Chumbes, B. Schultz, J. Logan, D. J. Meyer, and M. T. Hardy, “High Power Density ScAlN-Based Heterostructure FETs for mm-Wave Applications,” IEEE MTT-S International Microwave Symposium Digest, vol. 2019-June, pp. 1136–1139, Jun. 2019, doi: 10.1109/MWSYM.2019.8701055.

[116] M. B. Tahhan et al., “Passivation Schemes for ScAlN-Barrier mm-Wave High Electron Mobility Transistors,” IEEE Trans Electron Devices, vol. 69, no. 3, pp. 962–967, Mar. 2022, doi: 10.1109/TED.2021.3140016.

[117] S. Krause, I. Streicher, P. Waltereit, L. Kirste, P. Bruckner, and S. Leone, “AlScN/GaN HEMTs

Grown by Metal-Organic Chemical Vapor Deposition with 8.4 W/mm Output Power and 48 % Power-Added Efficiency at 30 GHz," IEEE Electron Device Letters, vol. 44, no. 1, pp. 17–20, Jan. 2023, doi: 10.1109/LED.2022.3220877.

[118] A. J. Green et al., "ScAlN/GaN High-Electron-Mobility Transistors with 2.4-A/mm Current Density and 0.67-S/mm Transconductance," IEEE Electron Device Letters, vol. 40, no. 7, pp. 1056–1059, Jul. 2019, doi: 10.1109/LED.2019.2915555.

[119] R. M. Fano, "Theoretical limitations on the broadband matching of arbitrary impedances," J Franklin Inst, vol. 249, no. 1, pp. 57–83, Jan. 1950, doi: 10.1016/0016-0032(50)90006-8.

[120] U. K. Mishra and J. Singh, "Semiconductor device physics and design," Semiconductor Device Physics and Design, pp. 1–559, 2008, doi: 10.1007/978-1-4020-6481-4/COVER.

[121] J. Patouillard, "Optimization of innovative AlN-based stacks and texturing on 2D-MoS2 - Applications to acoustic wave resonators and power electronics," Jun. 2023, Accessed: Oct. 09, 2023. [Online]. Available: https://theses.hal.science/tel-04207122

[122] P. Wang et al., "Quaternary alloy ScAlGaN: A promising strategy to improve the quality of ScAlN," Appl Phys Lett, vol. 120, no. 1, p. 12104, Jan. 2022, doi: 10.1063/5.0060608/2832745.

[123] A. J. Green et al., "RF Power Performance of Sc(Al,Ga)N/GaN HEMTs at Ka-Band," IEEE Electron Device Letters, vol. 41, no. 8, pp. 1181–1184, Aug. 2020, doi: 10.1109/LED.2020.3006035.

[124] S. W. Kaun, B. Mazumder, M. N. Fireman, E. C. H. Kyle, U. K. Mishra, and J. S. Speck, "Pure AlN layers in metal-polar AlGaN/AlN/GaN and AlN/GaN heterostructures grown by low-temperature ammonia-based molecular beam epitaxy," Semicond Sci Technol, vol. 30, no. 5, p. 055010, Apr. 2015, doi: 10.1088/0268-1242/30/5/055010.

[125] M. A. Moram et al., "Structural properties of wurtzitelike ScGaN films grown by NH 3-molecular beam epitaxy," J Appl Phys, vol. 106, no. 11, Dec. 2009, doi: 10.1063/1.3268466/900391.

[126] S. M. Knoll, S. Zhang, T. B. Joyce, M. J. Kappers, C. J. Humphreys, and M. A. Moram, "Growth, microstructure and morphology of epitaxial ScGaN films," physica status solidi (a), vol. 209, no. 1, pp. 33–40, Jan. 2012, doi: 10.1002/PSSA.201100158.

[127] B. J. Godejohann et al., "AlN/GaN HEMTs grown by MBE and MOCVD: Impact of Al distribution," physica status solidi (b), vol. 254, no. 8, p. 1600715, Aug. 2017, doi: 10.1002/PSSB.201600715.

[128] H. Yu et al., "Thermal budget increased alloy disorder scattering of 2DEG in III-N heterostructures," Appl Phys Lett, vol. 120, no. 21, p. 213504, May 2022, doi: 10.1063/5.0093839/2833662.

[129] H. C. L. Tsui et al., "The effect of metal-rich growth conditions on the microstructure of ScxGa1xN

films grown using molecular beam epitaxy," physica status solidi (a), vol. 212, no. 12, pp. 2837–2842, Dec. 2015, doi: 10.1002/PSSA.201532292.

[130] A. Hierro et al., "Impact of Ga/N flux ratio on trap states in n-GaN grown by plasma-assisted molecular-beam epitaxy," Appl Phys Lett, vol. 80, no. 5, pp. 805–807, Feb. 2002, doi: 10.1063/1.1445274.

[131] P. Waltereit, C. Poblenz, S. Rajan, F. Wu, U. K. Mishra, and J. S. Speck, "Structural properties of GaN buffer layers on 4H-SiC(0001) grown by plasma-assisted molecular beam epitaxy for high electron mobility transistors," Japanese Journal of Applied Physics, Part 2: Letters, vol. 43, no. 12 A, p. L1520, Dec. 2004, doi: 10.1143/JJAP.43.L1520/XML.

[132] C. D. Lee et al., "Role of Ga flux in dislocation reduction in GaN films grown on SiC(0001)," Appl Phys Lett, vol. 79, no. 21, pp. 3428–3430, Nov. 2001, doi: 10.1063/1.1421091.

[133] K. Frei et al., "Investigation of growth parameters for ScAlN-barrier HEMT structures by plasma-assisted MBE," Jpn J Appl Phys, vol. 58, no. SC, 2019, doi: 10.7567/1347-4065/ab124f.

[134] F. Natali, Y. Cordier, C. Chaix, and P. Bouchaib, "Advances in quality and uniformity of (Al,Ga)N/GaN quantum wells grown by molecular beam epitaxy with plasma source," J Cryst Growth, vol. 311, no. 7, pp. 2029–2032, Mar. 2009, doi: 10.1016/j.jcrysgro.2008.11.089.

[135] Y. Cordier, F. Natali, M. Chmielowska, M. Leroux, C. Chaix, and P. Bouchaib, "Influence of nitrogen precursor and its flow rate on the quality and the residual doping in GaN grown by molecular beam epitaxy," Physica Status Solidi (C) Current Topics in Solid State Physics, vol. 9, no. 3–4, pp. 523–526, Mar. 2012, doi: 10.1002/pssc.201100375.

[136] M. J. Galtrey et al., "Three-dimensional atom probe studies of an $In_xGa_{1-x}N$/GaN multiple quantum well structure: Assessment of possible indium clustering," Appl Phys Lett, vol. 90, no. 6, Feb. 2007, doi: 10.1063/1.2431573/327314.

[137] F. Tang et al., "Insight into the impact of atomic- and nano-scale indium distributions on the optical properties of InGaN/GaN quantum well structures grown on m -plane freestanding GaN substrates," J Appl Phys, vol. 125, no. 22, Jun. 2019, doi: 10.1063/1.5097411/346978.

[138] S. E. Bennett et al., "Atom probe tomography and transmission electron microscopy of a Mg-doped AlGaN/GaN superlattice," Ultramicroscopy, vol. 111, no. 3, pp. 207–211, Feb. 2011, doi: 10.1016/J.ULTRAMIC.2010.11.028.

[139] L. Amichi et al., "Three-dimensional measurement of Mg dopant distribution and electrical activity in GaN by correlative atom probe tomography and off-axis electron holography," J Appl Phys, vol. 127, no. 6, Feb. 2020, doi: 10.1063/1.5125188/157695.

[140] B. Bonef et al., "Composition Analysis of III-Nitrides at the Nanometer Scale: Comparison of En-

ergy Dispersive X-ray Spectroscopy and Atom Probe Tomography," Nanoscale Res Lett, vol. 11, no. 1, pp. 1–6, Dec. 2016, doi: 10.1186/S11671-016-1668-2/FIGURES/4.

[141] B. Bonef, R. D. Shah, and K. Mukherjee, "Fast Diffusion and Segregation along Threading Dislocations in Semiconductor Heterostructures," Nano Lett, vol. 19, no. 3, pp. 1428–1436, Mar. 2019, doi: 10.1021/ACS.NANOLETT.8B03734/SUPPL$_{F}ILE/NL8B03734_{S}I_{0}01.PDF$.

[142] L. Mancini et al., "Multi-microscopy study of the influence of stacking faults and three-dimensional In distribution on the optical properties of m-plane InGaN quantum wells grown on microwire sidewalls," Appl Phys Lett, vol. 108, no. 4, Jan. 2016, doi: 10.1063/1.4940748/31476.

[143] B. Dzuba et al., "Elimination of remnant phases in low-temperature growth of wurtzite ScAlN by molecular-beam epitaxy," J Appl Phys, vol. 132, no. 17, Nov. 2022, doi: 10.1063/5.0118075/2837841.

[144] L. Rigutti et al., "Statistical correction of atom probe tomography data of semiconductor alloys combined with optical spectroscopy: The case of Al0.25Ga0.75N," J Appl Phys, vol. 119, no. 10, Mar. 2016, doi: 10.1063/1.4943612/140999.

[145] M. T. Hardy, B. P. Downey, N. Nepal, D. F. Storm, D. S. Katzer, and D. J. Meyer, "Epitaxial ScAlN grown by molecular beam epitaxy on GaN and SiC substrates," Appl Phys Lett, vol. 110, no. 16, Apr. 2017, doi: 10.1063/1.4981807.

[146] J. Ligl et al., "Metalorganic chemical vapor phase deposition of AlScN/GaN heterostructures," J Appl Phys, vol. 127, no. 19, p. 195704, May 2020, doi: 10.1063/5.0003095.

[147] M. J. Galtrey et al., "Three-dimensional atom probe studies of an $In_xGa_{1-x}N$/GaN multiple quantum well structure: Assessment of possible indium clustering," Appl Phys Lett, vol. 90, no. 6, Feb. 2007, doi: 10.1063/1.2431573/327314.

[148] M. P. Moody, L. T. Stephenson, A. V. Ceguerra, and S. P. Ringer, "Quantitative binomial distribution analyses of nanoscale like-solute atom clustering and segregation in atom probe tomography data," Microsc Res Tech, vol. 71, no. 7, pp. 542–550, Jul. 2008, doi: 10.1002/JEMT.20582.

[149] R. Petrich et al., "Investigation of ScAlN for piezoelectric and ferroelectric applications."

[150] M. Thuvander et al., "Quantitative atom probe analysis of carbides," Ultramicroscopy, vol. 111, no. 6, pp. 604–608, May 2011, doi: 10.1016/J.ULTRAMIC.2010.12.024.

[151] J. Casamento et al., "Strong effect of scandium source purity on chemical and electronic properties of epitaxial $Sc_xAl_{1x}N$/GaN heterostructures," APL Mater, vol. 9, no. 9, Sep. 2021, doi: 10.1063/5.0054522/14565893/091106$_{1A}CCEPTED_{M}ANUSCRIPT.PDF$.

[152] S. Koelling et al., "Atom-by-Atom Analysis of Semiconductor Nanowires with Parts Per Million Sen-

sitivity," Nano Lett, vol. 17, no. 2, pp. 599–605, Feb. 2017, doi: 10.1021/ACS.NANOLETT.6B03109/SUPPL-FILE/NL6B03109-SI-001.PDF.

[153] H. Kim-Chauveau et al., "Growth optimization and characterization of lattice-matched Al 0.82In 0.18N optical confinement layer for edge emitting nitride laser diodes," J Cryst Growth, vol. 338, no. 1, pp. 20–29, Jan. 2012, doi: 10.1016/j.jcrysgro.2011.10.016.

[154] M. T. Hardy et al., "Control of phase purity in high scandium fraction heteroepitaxial ScAlN grown by molecular beam epitaxy," Applied Physics Express, vol. 13, no. 6, Jun. 2020, doi: 10.35848/1882-0786/ab916a.

[155] S. Vézian, F. Natali, F. Semond, and J. Massies, "From spiral growth to kinetic roughening in molecular-beam epitaxy of GaN(0001)," Phys Rev B Condens Matter Mater Phys, vol. 69, no. 12, Mar. 2004, doi: 10.1103/PhysRevB.69.125329.

[156] S. Vézian, F. Natali, F. Semond, and J. Massies, "Kinetic roughening during gas-source molecular-beam epitaxy of gallium nitride," in Applied Surface Science, Elsevier, Jul. 2004, pp. 445–450. doi: 10.1016/j.apsusc.2004.05.062.

[157] E. J. Tarsa, B. Heying, X. H. Wu, P. Fini, S. P. DenBaars, and J. S. Speck, "Homoepitaxial growth of GaN under Ga-stable and N-stable conditions by plasma-assisted molecular beam epitaxy," J Appl Phys, vol. 82, no. 11, pp. 5472–5479, Dec. 1997, doi: 10.1063/1.365575.

[158] P. Wang et al., "N-polar ScAlN and HEMTs grown by molecular beam epitaxy," Appl Phys Lett, vol. 119, no. 8, Aug. 2021, doi: 10.1063/5.0055851.

[159] R. Dargis et al., "Single-Crystal Multilayer Nitride, Metal, and Oxide Structures on Engineered Silicon for New-Generation Radio Frequency Filter Applications," Physica Status Solidi (A) Applications and Materials Science, vol. 217, no. 7, Apr. 2020, doi: 10.1002/pssa.201900813.

[160] T. E. Kazior, E. M. Chumbes, B. Schultz, J. Logan, D. J. Meyer, and M. T. Hardy, "High Power Density ScAlN-Based Heterostructure FETs for mm-Wave Applications," IEEE MTT-S International Microwave Symposium Digest, vol. 2019-June, pp. 1136–1139, Jun. 2019, doi: 10.1109/MWSYM.2019.8701055.

[161] C. Manz et al., "Improved AlScN/GaN heterostructures grown by metal-organic chemical vapor deposition," Semicond Sci Technol, vol. 36, no. 3, Mar. 2021, doi: 10.1088/1361-6641/abd924.

[162] J. Casamento et al., "Transport properties of polarization-induced 2D electron gases in epitaxial AlScN/GaN heterojunctions," Appl Phys Lett, vol. 121, no. 19, p. 192101, Nov. 2022, doi: 10.1063/5.0108475/2834639.

[163] J. Røyset and N. Ryum, "Scandium in aluminium alloys," http://dx.doi.org/10.1179/174328005X14311, vol. 50, no. 1, pp. 19–44, 2013, doi: 10.1179/174328005X14311.

[164] Y. Cordier, M. Azize, N. Baron, S. Chenot, O. Tottereau, and J. Massies, “AlGaN/GaN HEMTs regrown by MBE on epi-ready semi-insulating GaN-on-sapphire with inhibited interface contamination,” J Cryst Growth, vol. 309, no. 1, pp. 1–7, Nov. 2007, doi: 10.1016/J.JCRYSGRO.2007.09.023.

[165] E. Frayssinet et al., “Influence of metal-organic vapor phase epitaxy parameters and Si(111) substrate type on the properties of AlGaN/GaN HEMTs with thin simple buffer,” Physica Status Solidi (A) Applications and Materials Science, vol. 214, no. 4, Apr. 2017, doi: 10.1002/pssa.201600419.

[166] I. Streicher et al., “Enhanced AlScN/GaN Heterostructures Grown with a Novel Precursor by Metal–Organic Chemical Vapor Deposition,” physica status solidi (RRL) – Rapid Research Letters, vol. 17, no. 2, p. 2200387, Feb. 2023, doi: 10.1002/PSSR.202200387.

[167] C. Manz et al., “Improved AlScN/GaN heterostructures grown by metal-organic chemical vapor deposition,” Semicond Sci Technol, vol. 36, no. 3, Mar. 2021, doi: 10.1088/1361-6641/abd924.

[168] S. Krause, I. Streicher, P. Waltereit, L. Kirste, P. Bruckner, and S. Leone, “AlScN/GaN HEMTs Grown by Metal-Organic Chemical Vapor Deposition with 8.4 W/mm Output Power and 48% Power-Added Efficiency at 30 GHz,” IEEE Electron Device Letters, vol. 44, no. 1, pp. 17–20, Jan. 2023, doi: 10.1109/LED.2022.3220877.

[169] M. E. Lin, B. Sverdlov, G. L. Zhou, and H. Morkoç, “A comparative study of GaN epilayers grown on sapphire and SiC substrates by plasma-assisted molecular-beam epitaxy,” Appl Phys Lett, vol. 62, no. 26, pp. 3479–3481, Jun. 1993, doi: 10.1063/1.109026.

[170] P. Döring et al., “Voltage-margin limiting mechanisms of AlScN-based HEMTs,” Appl Phys Lett, vol. 123, no. 3, Jul. 2023, doi: 10.1063/5.0159501.

[171] M. W. L. Bragg et al., “The structure of some crystals as indicated by their diffraction of X-rays,” Proceedings of the Royal Society of London. Series A, Containing Papers of a Mathematical and Physical Character, vol. 89, no. 610, pp. 248–277, Sep. 1913, doi: 10.1098/RSPA.1913.0083.

[172] “Full text of ‘The London, Edinburgh and Dublin philosophical magazine and journal of science.’” Accessed: Jul. 03, 2023. [Online]. Available: https://archive.org/stream/londonedinburg6271914lond/londonedinburg6271914lond-djvu.txt

[173] P. P. Ewald, “Zur Begründung der Kristalloptik,” Ann Phys, vol. 359, no. 23, pp. 519–556, Jan. 1917, doi: 10.1002/ANDP.19173592305.

[174] M. v. Laue, “Röntgenstrahlinterferenz und Mischkristalle,” Ann Phys, vol. 361, no. 15, pp. 497–506, Jan. 1918, doi: 10.1002/ANDP.19183611502.

[175] M. A. Moram and M. E. Vickers, “X-ray diffraction of III-nitrides,” Reports on Progress in Physics,

vol. 72, no. 3, 2009, doi: 10.1088/0034-4885/72/3/036502.

[176] “XRRmeasurement”.

[177] S. A. Veldhuis, P. Brinks, T. M. Stawski, O. F. Göbel, and J. E. Ten Elshof, “A facile method for the density determination of ceramic thin films using X-ray reflectivity,” J Solgel Sci Technol, vol. 71, no. 1, pp. 118–128, 2014, doi: 10.1007/S10971-014-3336-2.

[178] M. Björck and G. Andersson, “GenX: An extensible X-ray reflectivity refinement program utilizing differential evolution,” J Appl Crystallogr, vol. 40, no. 6, pp. 1174–1178, Nov. 2007, doi: 10.1107/S00218898 07045086.

[179] E. H. C. Parker, The Technology and physics of molecular beam epitaxy. Plenum Press, 1985.

[180] P. J. Mestres Ventura, “The electron microscope on the eve of its first centenary,” 2023.

[181] E. Ruska, “The development of the electron microscope and of electron microscopy,” Biosci Rep, vol. 7, no. 8, pp. 607–629, 1987, doi: 10.1007/BF01127674/METRICS.

[182] N. Abrikossova, “Investigation of nanoparticle-cell interactions for development of next generation of biocompatible MRI contrast agents,” vol. 1961, Nov. 2018, doi: 10.3384/DISS.DIVA-152347.

[183] G. Binnig, C. F. Quate’ ’, E. L. Gi, and C. Gerber, “Atomic Force Microscope.”

[184] G. Da Costa et al., “Design of a delay-line position-sensitive detector with improved performance,” Review of Scientific Instruments, vol. 76, no. 1, p. 013304, Jan. 2005, doi: 10.1063/1.1829975.

[185] G. Da Costa, H. Wang, S. Duguay, A. Bostel, D. Blavette, and B. Deconihout, “Advance in multi-hit detection and quantization in atom probe tomography,” Review of Scientific Instruments, vol. 83, no. 12, Dec. 2012, doi: 10.1063/1.4770120/357454.

[186] S. J. J. Thomson, “LXXXIII. Rays of positive electricity,” https://doi.org/10.1080/14786441008636962, vol. 20, no. 118, pp. 752–767, Oct. 2009, doi: 10.1080/14786441008636962.

[187] R. F. K. Herzog and F. P. Viehböck, “Ion Source for Mass Spectrography,” Physical Review, vol. 76, no. 6, p. 855, Sep. 1949, doi: 10.1103/PhysRev.76.855.

[188] P. Williams, “Secondary Ion Mass Spectrometry,” https://doi.org/10.1146/annurev.ms.15.080185.00 2505, vol. 15, no. 1, pp. 517–548, Nov. 2003, doi: 10.1146/ANNUREV.MS.15.080185.002505.

[189] G. Greco, F. Iucolano, and F. Roccaforte, “Ohmic contacts to Gallium Nitride materials,” Appl Surf Sci, vol. 383, pp. 324–345, Oct. 2016, doi: 10.1016/j.apsusc.2016.04.016.

[190] B. Van Daele, G. Van Tendeloo, W. Ruythooren, J. Derluyn, M. R. Leys, and M. Germain, “The role of Al on Ohmic contact formation on n -type GaN and AlGaNGaN,” Appl Phys Lett, vol. 87, no. 6, 2005, doi: 10.1063/1.2008361.

[191] U. Ausserlechner, “Simple Proofs of Upper and Lower Envelopes of Van Der Pauw’s Equation for Hall-Plates with an Insulated Hole and Four Peripheral Point-Contacts,” Journal of Applied Mathematics and Physics, vol. 10, no. 03, pp. 960–999, 2022, doi: 10.4236/JAMP.2022.103066.

List of Figures

List of Tables